STUDIES OF STRATOSPHERIC AND TROPOSPHERIC OZONE, NO_2, AND BrO USING UV-VISIBLE SPECTROSCOPY IN THE ARCTIC AND AT MID-LATITUDES

by

Kristof Bognar

A thesis submitted in conformity with the requirements
for the degree of Doctor of Philosophy
Graduate Department of Physics
University of Toronto

Abstract

Studies of Stratospheric and Tropospheric Ozone, NO_2, and BrO Using UV-Visible
Spectroscopy in the Arctic and at Mid-latitudes

Kristof Bognar
Doctor of Philosophy
Graduate Department of Physics
University of Toronto
2021

This thesis utilizes UV-visible spectroscopy to develop new datasets, study Arctic and urban atmospheric composition, and validate satellite data products. The primary instruments used here (the Ground-Based Spectrometers, or GBSs) have been taking measurements at the Polar Environment Atmospheric Research Laboratory (PEARL, 80.05°N, 86.42°W) since 1999 and 2006, respectively.

The GBS dataset, combined with other measurements at PEARL, was used to validate ozone and NO_2 measurements from the Atmospheric Chemistry Experiment (ACE) and Optical Spectrograph and InfraRed Imaging System (OSIRIS) satellite instruments. Ozone from all instruments agrees to within 12.0%, while NO_2 measurements agree to within 33.2%. There are no apparent systematic changes in the observed differences between the satellite and the ground-based instruments over time.

In the winter/spring of 2020, the unusually strong and cold polar vortex led to unprecedented Arctic ozone depletion. Total column ozone was at an all-time low in the 20-year GBS dataset. Chlorine activation inside the vortex was ongoing until the end of March, resulting in mean chemical ozone loss of 111-127 DU (27-31%) over Eureka, which represents similar absolute loss and greater relative loss compared to that in spring 2011.

GBS BrO partial columns were used to investigate Arctic tropospheric ozone depletion during four bromine activation seasons. BrO enhancements show two modes differentiated by air mass history. Contact with the snowpack on sea ice corresponds to increased BrO for one of these modes only, while the other mode is related to storms that almost always bring bromine-enriched air to Eureka. The presence of coarse mode aerosols (likely sea salt aerosol) is a necessary and sufficient condition for observing BrO at Eureka, indicating that sea salt aerosols play an active role in bromine activation.

A tropospheric NO_2 profile dataset was retrieved from 2018-2020 Pandora spectrometer measurements to investigate NO_2 pollution in Toronto. Retrievals using optimal estimation and parametric algorithms show good agreement. Seasonal and diurnal variability is apparent in both the NO_2 partial column and surface concentration datasets. During the spring 2020 COVID-19 lockdown in Toronto, daily maximum NO_2 values showed substantial reductions.

Acknowledgements

My PhD work is finished, and this thesis marks the end of my long journey as a student that took me across three continents. Thank you to my supervisor, Kim Strong, for giving me this wonderful opportunity. I really enjoyed my time in your research group. I'm grateful for your support and guidance throughout the last five years, and I appreciate the time and effort you invest in helping your students succeed. Thank you to my MSc committee members, Dylan Jones and Debra Wunch, and my PhD committee members, Dylan Jones and Kaley Walker, for the support and guidance throughout my graduate studies.

The Eureka campaigns were an amazing experience, even though the GBSs can be temperamental. Thank you to Pierre Fogal and to the CANDAC operators (John Gallagher, Andrew Hall, Mike Maurice, and Peter McGovern) for helping me fix any problems, and for keeping the instruments running all year round. Thank you to everyone who travelled to Eureka with me for making those trips the highlights of my grad school years. Thank you to the Eureka Weather Station staff for hosting us and always making us feel welcome, and I appreciate the local wildlife checking in on us year after year. Thank you to Jim Drummond, Pierre Fogal, Ashley Harrett, Kim Strong, and Kaley Walker for the well-organized campaigns.

I also had the opportunity to spend a month in the Netherlands for CINDI-2. The campaign was a great learning experience, and I appreciate all the scientists and fellow students who gave me advice while we were neighbours in the CINDI-2 container town. Thank you Xiaoyi Zhao for sharing the work of preparing and deploying the PEARL-GBS, and thank you Orfeo Colebatch for all you technical support, not just for CINDI-2, but in Eureka as well.

I'd like to thank everyone on the long list of collaborators and co-authors on my projects for providing data, code, and advice. This includes (but is not limited to): Steffen Beirle, Rachel Chang, Martyn Chipperfield, Sandip Dhomse, Wuhu Feng, Udo Frieß, Florence Goutail, Patrick Hayes, Paul Jeffery, Erik Lutsch, Gloria Manney, Emily McCullough, Luis Millán, Andrea Pazmino, Xin Yang, Xiaoyi Zhao... I appreciate the time and effort you put into helping me get to this point. Thank you Jochen Stutz, Peter Taylor, and Kenjiro Toyota for accepting my invitation to give Noble seminars, and thank you Ana Sousa for making all that (and much more) possible.

Thank you Xiaoyi Zhao for teaching me everything about the GBSs, and for the continued collaboration even after you graduated. To my office mates (Paul Jeffery, Joseph Mendonca, Sebastian Roche, Dan Weaver, Xiaoyi Zhao, and others), thanks for the discussions, advice, and general camaraderie, back when all that was still possible. Thanks to the PEARL group for making PAHA meetings and CMOS Congresses the highlights of the conference season. Ramina Alwarda, thanks for taking over the GBSs, and I hope they will treat you well!

To my friends and family, in Canada, Hungary, and elsewhere: thank you for supporting me throughout this long journey. Finally, thank you Judy for bearing with me for the last five years. We ended up on opposite sides of the continent for grad school, but you moved across the country so we could spend the last three years together in Toronto. We have now ended up in Vancouver, and I'm looking forward to the next chapter of our lives together!

Table of Contents

List of Tables

List of Figures

List of Acronyms

0PAL	Zero-altitude PEARL auxiliary laboratory
ACE	Atmospheric Chemistry Experiment
AFGL	Air Force Geophysics Laboratory
AFO-XY	XY Fiber-Optic Mount
AMF	air mass factor
AOD	aerosol optical depth
APS	Aerodynamic Particle Sizer
AStrO	Arctic Stratospheric Ozone Observatory
BIRA-IASB	Belgian Institute for Space Aeronomy
BTUH	British Thermal Units per Hour
CAMS	Copernicus Atmosphere Monitoring Service
CANDAC	Canadian Network for the Detection of Atmospheric Change
CCD	charge-coupled device
CESAR	Cabauw Experimental Site for Atmospheric Research
CFS	Climate Forecast System
CINDI	Cabauw Intercomparison of Nitrogen Dioxide measuring Instruments
CINDI-2	the second Cabauw Intercomparison of Nitrogen Dioxide measuring Instruments
COVID-19	Coronavirus disease 2019
CRL	CANDAC Rayleigh-Mie-Raman Lidar
CTM	chemical transport model
DMP	derived meteorological product
DOAS	Differential Optical Absorption Spectroscopy
DOFS	degrees of freedom for signal
dSCD	differential slant column density
EASE-Grid	Equal-Area Scalable Earth Grid
ECCC	Environment and Climate Change Canada
ECMWF	European Centre for Medium-Range Weather Forecasts
ERA5	ECMWF Reanalysis 5^{th} Generation
EWS	Eureka Weather Station
FLEXPART	FLEXible PARTicle model
FOV	field-of-view

FRM4DOAS	Fiducial Reference Measurements for Ground-Based Differential Optical Absorption Spectroscopy Air-Quality Observations
FS	fixed slit
FTIR	Fourier transform infrared
FTS	Fourier Transform Spectrometer
FWHM	full width at half maximum
FYI	first-year sea ice
GBS	Ground-Based Spectrometer
GEOS-5	Goddard Earth Observing System-5
GOME	Global Ozone Monitoring Experiment
GOME-2	Global Ozone Monitoring Experiment-2
HDF	Hierarchical Data Format
HeiPro	Heidelberg remote sensing group profile retrieval code
HITEMP	high-temperature molecular spectroscopic database
HITRAN	high-resolution transmission molecular absorption database
IFS	isotopic fine structure
IUPHD	Institute of Environmental Physics, University of Heidelberg
IWG	Infrared Working Group
JETPAC	Jet and Tropopause Products for Analysis and Characterization
KNMI	Royal Netherlands Meteorological Institute
Lidar	Light Detection and Ranging
LLG	liquid light guide
LP-DOAS	long-path Differential Optical Absorption Spectroscopy
LUT	look-up table
MAESTRO	Measurements of Aerosol Extinction in the Stratosphere and Troposphere Retrieved by Occultation
MANTRA	Middle Atmosphere Nitrogen TRend Assessment
MAP	maximum a posteriori
MAPA	Mainz profile algorithm
MART	multiplicative algebraic reconstruction technique
MAX-DOAS	Multi-AXis Differential Optical Absorption Spectroscopy
MC	Monte Carlo
MERRA-2	Modern-Era Retrospective analysis for Research and Applications, version 2
MIPAS	Michelson Interferometer for Passive Atmospheric Sounding
MLS	Microwave Limb Sounder
MODIS	Moderate Resolution Imaging Spectroradiometer
MS	mechanical slit
MYI	multi-year sea ice
NAPS	National Air Pollution Surveillance
NASA	National Aeronautics and Space Administration

NAT	nitric acid trihydrate
NCEP	National Centers for Environmental Prediction
NDACC	Network for the Detection of Atmospheric Composition Change
NDSC	Network for the Detection of Stratospheric Change
ODE	ozone depletion event
ODR	orthogonal distance regression
OEM	optimal estimation method
OLS	ordinary least squares
OMI	Ozone Monitoring Instrument
OPC	Optical Particle Counter
OSIRIS	Optical Spectrograph and InfraRed Imager System
PAHA	Probing the Atmosphere of the High Arctic
PARIS-IR	Portable Atmospheric Research Interferometric Spectrometer for the InfraRed
PAX	Photoacoustic Extinctiometer
PC	principal component
PCA	principal component analysis
PEARL	Polar Environment Atmospheric Research Laboratory
PGN	Pandonia Global Network
PSC	polar stratospheric cloud
PV	potential vorticity
RCD	reference column density
RD	rapid delivery
RMA	reduced major-axis
RMS	root-mean-square
RMSD	root-mean-square deviation
RMSE	root-mean-square error
RTM	radiative transfer model
SAOZ	Systéme d'Analyse par Observation Zènithale
SCD	slant column density
SCIAMACHY	Scanning Imaging Absorption Spectrometer for Atmospheric Cartography
SMPS	Scanning Mobility Particle Sizer
SNR	signal-to-noise ratio
SSA	sea salt aerosol
SZA	solar zenith angle
STS	supercooled ternary solution
TAO	University of Toronto Atmospheric Observatory
TCA	triple colocation analysis
TCP	Transmission Control Protocol
TOAS	total optical absorption spectroscopy

TOMS	Total Ozone Mapping Spectrometer
TROPOMI	TROPOspheric Monitoring Instrument
UTC	Coordinated Universal Time
UT-GBS	University of Toronto Ground-Based Spectrometer
VCD	vertical column density
VMR	volume mixing ratio
WG	working group
WMO	World Meteorological Organization
ZSL-DOAS	zenith-scattered-light Differential Optical Absorption Spectroscopy

Chapter 1

Introduction

Ozone is a well-known and important trace gas with a range of roles in both the stratosphere and the troposphere. Ozone determines the temperature profile of the stratosphere by absorbing ultraviolet (UV) light. This absorption also shields organisms on the surface from harmful radiation, and the ozone layer received widespread scientific and public attention after the discovery of the Antarctic ozone hole in the 1980s (Farman et al., 1985). Even though the highest concentrations are found in the stratosphere, ozone is important near the surface as well, where it controls the oxidation potential (i.e., the self-cleaning capacity) of the troposphere. On the other hand, tropospheric ozone is also a pollutant and a greenhouse gas.

The interplay of the complex roles of ozone is particularly relevant in the Arctic. Stratospheric ozone depletion, while not as severe as in the Antarctic, is highly variable (WMO, 2014, 2018), and has the potential to negatively impact populations in northern regions. On smaller scales, ozone depletion occurs in the troposphere as well (Oltmans and Komhyr, 1986; Bottenheim et al., 1986), with potentially harmful impacts on the Arctic environment. A significant complicating factor is climate change, since the Arctic is one of the most affected regions. The surface is warming at the fastest rate anywhere in the world, and summer sea ice extent has been steadily declining over the past half century (IPCC, 2013). While stratospheric ozone levels are expected to recover to 1980 levels by the mid-21$^{\text{st}}$ century, climate change introduces significant uncertainty in the recovery process (WMO, 2018). The warming surface and decreasing sea ice cover might affect near-surface ozone depletion as well.

The changing Arctic atmosphere necessitates the long-term monitoring of ozone and related trace gases. While satellites provide Arctic-wide coverage, ground-based stations produce complementary, localized measurements of the stratosphere, the troposphere, and the near-surface layers. Eureka, Nunavut, Canada (80°N, 86°W) is one of the few stations in the high Arctic, and is an excellent location for Arctic atmospheric studies. Weather observations have been made at Eureka since 1947. The Arctic Stratospheric Ozone Observatory (AStrO) was established near Eureka in 1992, and the facility was subsequently expanded and renamed the Polar Environment Atmospheric Research Laboratory (PEARL) in 2005. UV-visible (UV-vis) spectrometers have been taking measurements at AStrO/PEARL since 1999, and this thesis uses data from these spectrometers (as well as other instruments at Eureka) to study ozone and related trace gases in both the stratosphere and the troposphere. This chapter presents the scientific background for, and the motivation behind, the work presented in this thesis.

1.1 Stratospheric Ozone

The presence of high ozone concentrations in the stratosphere was suggested as early as the late 19th century (Hartley, 1881a,b). Stratospheric ozone was first detected in the 1920s (Fabry and Buisson, 1921; Dobson and Harrison, 1926), and a theory, proposed by Chapman (1930), soon emerged to explain the origins of this ozone. The Chapman cycle involves rapid cycling between O and ozone (collectively called O_x or odd-oxygen), and slower cycling between O_2 and O_x. The Chapman cycle is responsible for the absorption of nearly all UV-C (100-280 nm) and most of UV-B (280-320 nm) radiation entering Earth's atmosphere, due to the wavelengths required for the photolysis of O_2 ($\lambda < 240$ nm) and ozone (mostly $\lambda < 320$ nm). While this mechanism explains the general shape of the ozone layer, it overestimates the ozone concentrations, implying that there are additional sinks. These sinks are catalytic ozone-depleting cycles, which can generally be simplified to the following reaction sequence:

$$\mathrm{X} + \mathrm{O_3} \longrightarrow \mathrm{XO} + \mathrm{O_2} \tag{R1}$$

$$\mathrm{XO} + \mathrm{O} \longrightarrow \mathrm{X} + \mathrm{O_2} \tag{R2}$$

$$\mathit{net} : \mathrm{O} + \mathrm{O_3} \longrightarrow 2 \times \mathrm{O_2},$$

where X is the catalyst that speeds up the reaction without being consumed. X might be the hydroxyl radical (OH), nitric oxide (NO), chlorine (Cl), or bromine (Br). The importance of each cycle varies with altitude, and the reactions are limited by the conversion of X into stable reservoir species.

The cycles involving hydrogen oxides and nitrogen oxides are natural ozone sinks. Stratospheric OH is produced by the oxidization of water vapor. Water vapor, in turn, is either transported from the troposphere, or produced in the stratosphere by oxidation of methane (CH_4). OH and HO_2 together are called the HO_x family, and HO_x-catalyzed cycles represent the dominant natural ozone sink in the lower stratosphere (Lary, 1997). Most stratospheric NO originates from N_2O, which is produced naturally in the biosphere. Ozone depletion by NO and NO_2 (together called NO_x) is slowed by conversion of NO_x into non-radical reservoir species: nitric acid (HNO_3) during the day and N_2O_5 at night. Taking the HO_x and NO_x cycles into account, it is possible to fully explain the missing sink in the Chapman mechanism, when considering a pristine stratosphere (Jacob, 1999).

1.1.1 Chemical Ozone Depletion

Anthropogenic influences on stratospheric ozone became a topic of active concern starting in the 1950s, first due to nuclear testing in the stratosphere, and then as a response to a proposed fleet of supersonic aircraft. Another concern was emissions of chlorofluorocarbons (CFCs), which have been in use since the 1930s in refrigeration and air conditioning. Lovelock et al. (1973) discovered that CFCs accumulate in the stratosphere, and are distributed globally. Molina and Rowland (1974) proposed that chlorine released from the photolysis of CFCs would cause a global loss of ozone in the upper stratosphere (through Reactions R1 and R2). However, the detection of the ozone hole above Antarctica by Farman et al. (1985) came as a surprise since the ozone depletion was expected to be uniform at all latitudes. In response to the perceived crisis, the Montreal Protocol on Substances that Deplete the Ozone Layer was signed in 1987 in order to phase out the production of CFCs and other ozone-depleting substances. As a result, there are signs that Antarctic ozone concentrations have now levelled off and might be starting to increase again (Solomon et al., 2016), with return to pre-CFC levels expected around the middle of the 21^{st} century (WMO, 2018).

To account for the large and unexpected sink of ozone in the Antarctic spring, two new catalytic cycles were proposed. One involves the self-reaction of ClO (Molina and Molina, 1987):

$$\mathrm{ClO + ClO + M \longrightarrow ClOOCl + M} \tag{R3}$$

$$\mathrm{ClOOCl \xrightarrow{h\nu} ClOO + Cl} \tag{R4}$$

$$\mathrm{ClOO + M \longrightarrow Cl + O_2 + M} \tag{R5}$$

$$\mathrm{2 \times (Cl + O_3 \longrightarrow ClO + O_2)} \tag{R6}$$

$$net: \mathrm{2 \times O_3 \longrightarrow 3 \times O_2},$$

where M is a non-reacting molecule, and $h\nu$ indicates photolysis. The other cycle is based on the cross-reaction of ClO with BrO (McElroy et al., 1986; Tung et al., 1986):

$$\mathrm{Cl + O_3 \longrightarrow ClO + O_2} \tag{R7}$$

$$\mathrm{Br + O_3 \longrightarrow BrO + O_2} \tag{R8}$$

$$\mathrm{BrO + ClO \longrightarrow Br + Cl + O_2} \tag{R9}$$

$$net : 2 \times \mathrm{O_3} \longrightarrow 3 \times \mathrm{O_2}.$$

One of the pathways for Reaction R9 also produces OClO, which is then rapidly photolyzed (Sander and Friedl, 1989). Sequences R3-R6 and R7-R9 both recycle chlorine faster than the simple chlorine catalytic cycle. Both the self-reaction and cross-reaction cycles, however, require exceptionally high ClO concentrations. Finding the origin of the ClO was the last major step towards understanding the Antarctic ozone hole.

Concentrations of ClO are typically kept in check due to chlorine deactivation, partly by NO_2 via conversion to $ClONO_2$. Similarly, BrO also reacts with NO_2 to form $BrONO_2$ However, if the temperature in the winter stratosphere is sufficiently cold, polar stratospheric clouds (PSCs) start to form. The stratospheric aerosol background is mainly liquid droplets composed of sulphuric acid (H_2SO_4) and water (see e.g., Kremser et al., 2016, and references therein). Below ∼195 K (T_{NAT}, a pressure-dependent threshold specific to the lower stratosphere), these droplets take up HNO_3 and water to form Type I PSCs, which further differentiate into two categories. Liquid $HNO_3/H_2SO_4/H_2O$ droplets form supercooled ternary solution (STS) PSCs (Type Ib), and these particles might freeze to solid nitric acid trihydrate (NAT) PSCs (Type Ia). If temperatures drop further, water ice freezes into Type II PSCs below ∼188 K (e.g., WMO, 2014). Since HNO_3 is one of the reservoirs of NO_2, formation of Type I PSCs ties up NO_2 and slows chlorine deactivation. In addition, sedimentation of PSC particles leads to long term loss of NO_2 from the stratosphere in a process known as denitrification (Salawitch et al., 1989; WMO, 2014). Most importantly, PSCs (along with other cold aerosols) provide a catalytic surface for the heterogeneous reaction of chlorine reservoirs HCl and $ClONO_2$ (Solomon et al., 1986):

$$\mathrm{ClONO_2 + HCl} \xrightarrow{PSC} \mathrm{Cl_2 + HNO_3}. \tag{R10}$$

Reaction R10 is fast and continues until one of the chlorine reservoirs is completely depleted. HCl also reacts with $BrONO_2$ on PSC surfaces:

$$\mathrm{BrONO_2 + HCl} \xrightarrow{PSC} \mathrm{BrCl + HNO_3}, \tag{R11}$$

providing another pathway to release both chlorine and bromine from reservoir species

(McElroy et al., 1986). Halogens in the stratosphere then build up over the winter, and once sunlight returns in the spring, Cl_2 and BrCl are rapidly photolyzed. Ozone depletion then proceeds via Reactions R3-R6 and R7-R9 as described above.

1.1.2 Arctic Ozone Loss

While the ozone hole forms every spring in Antarctica, the Arctic rarely experiences significant ozone loss. The reasons the ozone loss regimes at the two poles are so different lie in stratospheric dynamics. The heterogeneous chemistry described in Section 1.1.1 relies on low temperatures that are only reached inside the polar vortex. The vortex forms over the winter pole due to the cooling that results from the lack of sunlight. This cooling results in a meridional temperature gradient, which, in combination with geostrophic equilibrium, leads to a strong westerly flow (the polar night jet) with minimal meridional transport. The region within this circumpolar flow is called the polar vortex. In Antarctica, the jet passes over the Southern Ocean, and the lack of topography and land-ocean contrast leads to strong isolation of the vortex from mid-latitude air. Temperatures inside the vortex stay below the threshold required for Type I PSC formation for most of the winter, and ice PSCs are common (Pitts et al., 2018; Spang et al., 2018). The Antarctic vortex is typically strongly denitrified, and in the absence of NO_2 to deactivate chlorine, ozone loss can continue as long as the vortex remains cold enough for PSCs and continues to act as a transport barrier.

By contrast, in the Arctic, planetary waves propagating upward from the mid-latitude troposphere are much more common than near Antarctica, due to the complex topography at northern mid-latitudes. These planetary waves often disrupt the zonal symmetry of the northern polar night jet, and create a meandering jet stream and a less isolated polar vortex. As a consequence, the Arctic vortex is typically warmer than its southern counterpart, and the area of the vortex where PSCs might form is reduced, with large interannual variability. In some years PSCs might not form at all, and when they do, STS PSCs appear to be the dominant type (Pitts et al., 2018; Spang et al., 2018). Ice PSCs are rare in the Arctic. The reduced presence of PSCs leads to less efficient chlorine activation and less denitrification, which in turn results in more efficient deactivation of chlorine via NO_2. In addition, the Arctic vortex is often weak or already broken down by the early spring due to sudden stratospheric warmings, which are marked amplifications of planetary wave activity that warm the stratosphere and slow (or even reverse) the polar night jet in a matter of days (e.g., Charlton and Polvani, 2007).

Aside from creating the conditions for chemical ozone loss, stratospheric dynamics is responsible for transporting ozone from the tropics (where ozone production rates are the highest) to the polar regions. The main dynamical feature of the stratosphere is the Brewer-Dobson circulation (Brewer, 1949; Dobson, 1956), a wave-driven feature that involves the rise of air in the tropics and the summer hemisphere, transport towards the winter pole, and descent in the polar vortex. The Brewer-Dobson circulation transports ozone-rich air from the tropics to the winter pole, and is also responsible for the transport of CFCs and other trace gases into the polar regions. The Brewer-Dobson circulation is stronger in the Northern Hemisphere, due to the stronger wave activity that also weakens the Arctic polar vortex. The stronger circulation means that more ozone is transported into the Arctic vortex than into its Antarctic counterpart. Approximately half the interannual ozone variability in the Arctic can be explained by dynamics (Chipperfield and Jones, 1999; Tegtmeier et al., 2008). Taken together, the weaker Arctic vortex and the larger role of transport mean that ozone concentrations in the Arctic might still exhibit a weak springtime maximum despite chemical ozone depletion.

Significant ozone loss can, however, occur in the Arctic when the vortex remains strong, stable, and cold throughout the winter and spring. The best example to date (in the satellite era) was the winter of 2019/2020. While the size of the vortex was close to the average for much of the winter, it maintained a more or less constant size to become one of the largest by April. Potential vorticity (PV) gradients, a qualitative measure of the vortex stability in the lower stratosphere, set all-time records from February to April, indicating that the vortex acted as an exceptionally strong barrier to mixing and transport (Lawrence et al., 2020). Figure 1.1 shows the evolution of temperature inside the polar vortex in 2019/2020, compared to other Arctic winters. In 2020, temperatures remained below the threshold for Type I PSCs (T_{NAT}) from early December all the way to late March, the longest on record. The fraction of the vortex with temperatures below T_{NAT} was consistently high, and the mean fraction for the entire winter was the highest on record. As a result, chlorine activation was apparent by late November 2019, with high ClO concentrations persisting until the end of March (Manney et al., 2020).

Given the conditions outlined above, the winter of 2019/2020 might have had the greatest ozone loss potential ever observed in the Arctic (Lawrence et al., 2020). While various methods of estimating chemical ozone loss have large uncertainties (e.g., Griffin et al., 2019a; Manney et al., 2020), and dynamical contributions to low ozone columns need to be considered, measurements suggest that spring 2020 set new records for ozone depletion in the Arctic. Minimum lower stratospheric ozone concentrations observed from satellites (Manney et al., 2020) and ozonesondes (Wohltmann et al., 2020) were far lower than previously seen (approaching levels typical for the Antarctic ozone hole), and ozone

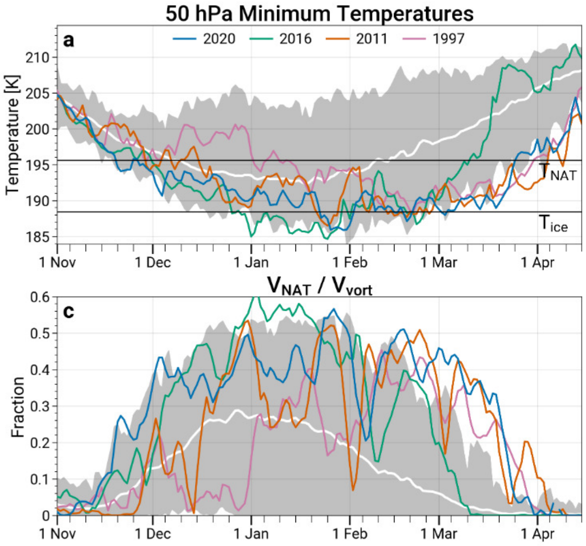

Figure 1.1: Temperatures in the Arctic vortex from reanalysis data. The left column shows **a)** daily time series of minimum temperatures at 50 hPa, and **c)** the fraction of the vortex with $T < T_{NAT}$ in the lower stratosphere. The right column shows yearly statistics of **b)** the total number of days with $T < T_{NAT}$ at 50 hPa, and **d)** the November-March averages corresponding to **c)**. Years of interest are highlighted in color. The gray areas and white lines in **a)** and **c)** represent the ranges and averages from other years, while the dashed lines in **b)** and **d)** show the mean across all available years. Reproduced from Figure 11 of Lawrence et al. (2020).

columns were anomalously low across the Arctic (Bernhard et al., 2020; Grooß and Müller, 2020; Inness et al., 2020; Lawrence et al., 2020).

The previous winter with the most significant ozone loss was 2010/2011 (Balis et al., 2011; Manney et al., 2011b; Sinnhuber et al., 2011; Adams et al., 2012b; Kuttippurath et al., 2012; Lindenmaier et al., 2012; Pommereau et al., 2013; Strahan et al., 2013; Hommel et al., 2014; Solomon et al., 2014). The two seasons were similar in many respects, with a persistent, strong, and cold vortex (Lawrence et al., 2020). While the duration of the period with temperatures below T_{NAT} was similar, a smaller fraction of the vortex was exposed to such low temperatures in 2010/2011 (Fig. 1.1). In addition, ozone depletion started later in 2010/2011 than in 2019/2020 (Manney et al., 2020). Minima in the ozone profiles in 2011 did not drop as low as in 2020, and the minima occurred at higher altitudes. As a result, the total ozone column was affected less in 2011 than in 2020 (Manney et al., 2020; Wohltmann et al., 2020). Estimates of vortex-averaged chemical loss in the ozone column for 2011 vary based on the methods, satellite instruments, and altitude ranges used. Aura Microwave Limb Sounder (MLS) measurements have been used to estimate vortex-averaged ozone loss in the lower stratospheric column, with values of 84 DU (Strahan et al., 2013) and 115-131 DU (Kuttippurath et al., 2012). Sinnhuber et al. (2011) calculated an average loss of ~120 DU for the lower stratosphere using Michelson Interferometer for Passive Atmospheric Sounding (MIPAS) measurements. For the total column, Manney et al. (2011b) estimated a vortex-averaged loss of ~120 DU using Ozone Monitoring Instrument (OMI) data, and Pommereau et al. (2013) estimated an average loss of ~170 DU based on a ground-based measurement network.

Significant ozone loss was also observed in the springs of 1996, 2000, and 2005 (Rex et al., 2004; Manney et al., 2006; Rex et al., 2006; Tilmes et al., 2006; Feng et al., 2007). The vortex during these winters was particularly cold, but ozone depletion ceased much earlier than in 2011 (Manney et al., 2011b) or 2020. The duration of the cold period (see Fig. 1.1) is key for large-scale ozone depletion, and the only year other than 2011 and 2020 with a large portion of the vortex below T_{NAT} going into March was 1997 (Coy et al., 1997; Manney et al., 1997; Newman et al., 1997). The polar vortex in 1997 (along with the vortex in 2020) was the largest on record for the March to early May period. Temperatures below T_{NAT} persisted until late March, but the volume of cold air was very limited until mid-January. This effectively delayed the depletion season by over a month compared to 2019/2020. As a result, ozone loss in 1997 was less significant than in any of the aforementioned years (Manney et al., 2011b). The 2015/2016 season started with record-breaking low temperatures, the formation of ice PSCs, and significant dehydration of the vortex (Manney and Lawrence, 2016; Matthias et al., 2016). An early final warming, however, broke up the vortex by early March, preventing ozone loss on the scale of 2011 or 2020.

While individual winters might stand out in terms of some of the parameters that determine the potential for ozone loss, it is rare that all required conditions are present and significant ozone loss actually occurs. In terms of the strength and durability of the vortex PV gradients, the springs of 2011 and 2020 remain outliers (Lawrence et al., 2020), and ozone loss in those years is the most significant on record. Ozone loss in 2011 has been described as an Arctic ‘ozone hole’ (e.g., Manney et al., 2011b), but these comparisons are controversial (Solomon et al., 2014). While the spring of 2020 was arguably much closer to a real ozone hole than 2011 (e.g., Wohltmann et al., 2020), the extremes commonly seen in the Antarctic ozone hole have never been observed in the Arctic.

1.1.3 Ozone Monitoring Networks

The need for long-term, globally distributed measurements of ozone arose in the 1960s and 1970s, in parallel with rising concerns about anthropogenic impacts on the atmosphere.

An informal network of Dobson spectrophotometers has been measuring total column ozone since the 1930s (Dobson, 1968). This network was formalized after the 1957 International Geophysical Year, under the Global Ozone Observing System established by the World Meteorological Organization (WMO)[1]. The Brewer spectrophotometers, developed in the 1980s for more accurate (and automated) measurements of ozone (Brewer, 1973; Kerr et al., 1981), were coordinated by this network as well. In 1989, WMO observational networks were consolidated into the Global Atmosphere Watch programme, with the Dobson and Brewer instruments as the standard for total column ozone. More than 100 Dobson instruments and over 230 Brewers are in operation around the world today (Zhao et al., 2020a).

Interest in establishing formal networks for systematic long-term measurements of stratospheric composition increased after the detection of the Antarctic ozone hole. In response, the Network for the Detection of Stratospheric Change (NDSC) was established in 1991[2]. To accommodate increasing measurement capabilities and a broadening focus, NDSC was renamed Detection of Atmospheric Composition Change (NDACC) in 2005. NDACC is currently composed of more than 70 stations globally, and the network coordinates data collected using numerous measurement methods and instrument types (De Mazière et al., 2018). Of particular interest here is the NDACC UV-visible Working Group (UV-vis WG), which coordinates measurements by the Differential Optical Absorption Spectroscopy (DOAS) instruments used in this thesis. These are UV-vis grating spectrometers which typically measure ozone and NO_2, as discussed in detail in Chapter 2. NDACC has several other instrument working groups, which focus, for example, on Fourier transform infrared (FTIR) spectroscopy, lidar measurements, or satellite data. In addition to collecting data from member instruments/stations, NDACC also cooperates with instrument networks. The Dobson and Brewer network has a working group of its own within NDACC. Another cooperating network is comprised of Systéme d'Analyse par Observation Zènithale (SAOZ) DOAS instruments, UV-vis grating spectrometers designed for automated monitoring of polar stratospheric ozone (Pommereau and Goutail, 1988). A new addition to NDACC is the Pandonia Global Network (PGN), which joined as a cooperating network in 2020[3]. The PGN is made up of standardized and calibrated Pandora instruments, which are UV-vis grating spectrometers capable of multiple measurement modes (Herman et al., 2009; Tzortziou et al., 2012).

In an excellent location to contribute to Arctic atmospheric monitoring, PEARL

---

[1] `https://public.wmo.int/en/programmes/global-atmosphere-watch-programme`

[2] `https://www.ndaccdemo.org/about/history`

[3] `https://www.pandonia-global-network.org/home/about/`

(Fogal et al., 2013) hosts instruments representing all of the networks discussed above. PEARL is a collection of three separate facilities operated by the Canadian Network for the Detection of Atmospheric Change (CANDAC) since 2005. The PEARL Ridge Lab (known as AStrO prior to 2005) is home to the two main instruments used here, the University of Toronto Ground-Based Spectrometer (UT-GBS) and the PEARL-GBS. Both GBS instruments are NDACC-certified, and regularly submit data to the NDACC database. A SAOZ instrument has been installed at the PEARL Ridge Lab since 2005. The lab also hosts the CANDAC Bruker IFS 125HR FTIR spectrometer (hereafter Bruker FTIR), which is part of the NDACC Infrared Working Group (IWG). Pandora #144 was installed at the Ridge Lab in 2019, and as of 2020, the instrument is officially the northernmost integrated member of the PGN. PEARL and the Environment and Climate Change Canada (ECCC) Eureka Weather Station (EWS) host several Brewer instruments as well.

1.2 Tropospheric Ozone

Ozone in the troposphere is present at far lower concentrations than in the stratosphere. Photolysis of ozone facilitates OH production, and so ozone controls the oxidation potential of the troposphere (Jacob, 1999). OH reacts with CO and CH_4, and reduces the tropospheric lifetime of these species. In the presence of NO, the oxidation of CO, CH_4, and other hydrocarbons leads to the production of ozone. The result is the remarkable fact that HO_x and NO_x catalyze ozone production in the troposphere and ozone destruction in the stratosphere. The ozone destruction cycles via reactions R1-R2 still proceed in the troposphere, but reaction rates are exceedingly low due to the low concentrations of O_x.

In parallel to growing concern about stratospheric ozone and the discovery of the ozone hole, it was discovered that upon the return of sunlight in the Arctic spring, surface ozone concentrations regularly drop from the usual ∼30 ppbv (parts per billion by volume) to a few ppbv or even below detection limits (Oltmans and Komhyr, 1986; Bottenheim et al., 1986). These ozone depletion events (ODEs) happen regularly during the months of March to May, and typically last for 1-3 days. ODEs occur mostly over the frozen Arctic Ocean, and ozone-depleted airmasses can extend over hundreds of km horizontally (e.g., Halfacre et al., 2014). The lack of ozone drastically alters the oxidation pathways available in the atmosphere, and one effect is the deposition of gas-phase mercury onto the snowpack, with potentially harmful impacts on the Arctic environment (Schroeder et al., 1998; Steffen et al., 2008; Cole and Steffen, 2010; Berg et al., 2013). Measurements in Antarctica showed that ODEs occur during the Austral spring as well (Schnell et al., 1991; Oltmans, 1993; Kalnajs and Avallone, 2006; Jones et al., 2009, 2010).

The near-surface distribution of ozone during springtime typically shows smaller ozone concentrations at the surface than aloft. Near the surface, ozone can be deposited to the snowpack, or potentially affected by snowpack photochemical NO_x production (Jones et al., 2001; Honrath et al., 2002; Grannas et al., 2007). Studies at both inland sites (Helmig et al., 2007b,a, 2009; Bocquet et al., 2011) and at the coast (Helmig et al., 2012) have shown that ozone deposition rates to the snowpack are too slow to generate springtime ODEs. Other surface-based processes are then necessary to explain near-surface ozone depletion.

1.2.1 Halogen Chemistry

It was noticed early on that ODEs were accompanied by high levels of filterable bromine, and a bromine-catalyzed cycle was suggested as the primary cause of near surface ozone depletion (Barrie et al., 1988). Bromine is thought to be released to the atmosphere from condensed phase bromide (Br^-) through heterogeneous reactions (Eigen and Kustin, 1962; Fan and Jacob, 1992; Wang et al., 2019). Once in the atmosphere, bromine destroys ozone through catalytic cycles similar to those involved in stratospheric ozone loss. The mechanisms involved in bromine release are the subject of several detailed reviews (Simpson et al., 2007; Abbatt et al., 2012; Saiz-Lopez and von Glasow, 2012; Simpson et al., 2015).

BrO forms after the initial reaction of bromine with ozone (Reaction R1). However, given the low concentrations of O_x in the troposphere, Reaction R2 cannot proceed. Instead, recycling of bromine from BrO happens through photolysis, self-reaction of BrO, cross-reaction of BrO with ClO or IO, or reaction with HO_2. Photolysis and self-reaction are slow compared to cross-reactions with other halogen oxides, but ClO and IO are generally rare in the troposphere. The key process recycling bromine is thus the reaction with HO_2:

$$\mathrm{Br} + \mathrm{O_3} \longrightarrow \mathrm{BrO} + \mathrm{O_2} \tag{R12}$$

$$\mathrm{BrO} + \mathrm{HO_2} \longrightarrow \mathrm{HOBr} + \mathrm{O_2} \tag{R13}$$

$$\mathrm{HOBr} \xrightarrow{h\nu} \mathrm{Br} + \mathrm{OH}. \tag{R14}$$

Reaction R13 is faster than the cross-reaction of BrO with other halogen oxides, and HO_2 is abundant in the troposphere since it is the product of the oxidation of CO by OH.

These cycles, however, do not increase the concentration of reactive bromine in the atmosphere, and can only proceed with sufficient amounts of Br and BrO already present. Bromine is common in sea salt, and the proposed main reaction that produces gaseous Br is the following (Eigen and Kustin, 1962; Fan and Jacob, 1992):

$$\mathrm{HOBr} + \mathrm{Br}^-_{\mathrm{aq}} + \mathrm{H}^+_{\mathrm{aq}} \xrightarrow{mp} \mathrm{H_2O} + \mathrm{Br_2} \tag{R15}$$

$$\mathrm{Br_2} \xrightarrow{h\nu} 2 \times \mathrm{Br}, \tag{R16}$$

where *mp* indicates a multi-phase (occurring in the bulk of the solution) or heterogeneous (occurring on the surface) reaction. Reaction R15 transfers bromine from high salinity liquid brine or from ice surfaces into the atmosphere. Combining Reactions R15 and R16 with Reactions R12 and R13 into the so-called “bromine explosion” cycle (Wennberg, 1999) gives the following net reaction:

$$\mathrm{Br}^-_{\mathrm{aq}} + \mathrm{H}^+_{\mathrm{aq}} + \mathrm{HO_2} + \mathrm{O_3} \xrightarrow{mp,h\nu} \mathrm{Br} + \mathrm{H_2O} + 2 \times \mathrm{O_2}. \tag{R17}$$

This sequence is autocatalytic, since each bromine atom released can produce HOBr via Reaction R13, and HOBr can then re-enter the brine solution to release more bromine. As long as Br^- and H^+ are available, bromine concentrations in the atmosphere can increase exponentially, hence the term bromine explosion.

Ozone, OH and reactive nitrogen species can also directly oxidize bromide in frozen solution via gas-surface interactions (see e.g., Abbatt et al., 2012). While these processes do not lead to an explosive increase of atmospheric bromine concentrations, they can proceed in the dark. Given that the autocatalytic cycle described above requires sunlight and some gas phase bromine already present, release via ozone, OH and nitrogen species may provide the seed bromine required for bromine explosion events.

The temporal evolution of the main species during a bromine explosion is shown in Figure 1.2. During the initial phase, ozone is still abundant, and so bromine is mostly present as BrO and HOBr. BrO, detectable using remote sensing, is therefore commonly used as an indicator of bromine activation. The lifetime of BrO is on the order of minutes due to photolysis, but Br and BrO are rapidly cycled at normal ozone levels. Once ozone is completely depleted, however, Reaction R12 cannot proceed, and BrO cannot form. Bromine is then converted to more stable species (like HBr, which is important for the redeposition of bromine into the condensed phase), or the bromine explosion might continue via reactions with nitrogen oxides (Wang et al., 2019).

While bromine chemistry is the most prominent factor in ODEs, other species might

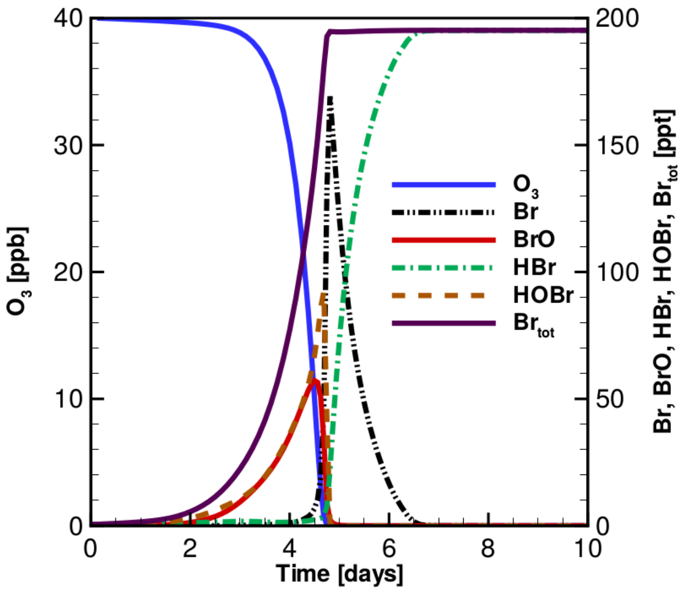

Figure 1.2: Temporal evolution of the main bromine species during a bromine explosion, simulated in a 200 m deep boundary layer. Reproduced from Figure 1 of Cao et al. (2016).

also play important roles. Snowpack chlorine production was reported by Liao et al. (2014) and Custard et al. (2017). Chlorine does not efficiently destroy ozone in the troposphere, but could enhance bromine release via BrCl production (Thompson et al., 2015; Wang and Pratt, 2017). Iodine has recently been observed in the Arctic springtime, both as IO (Zielcke, 2015), and in molecular form (Raso et al., 2017). Although far less abundant than bromine, iodine might deplete ozone much more efficiently (Thompson et al., 2015). In addition, modelling studies suggest that NO_x (emitted naturally from the snowpack and sometimes present as fresh pollution from nearby combustion emissions) could enhance bromine production if sufficient surface area is present for heterogeneous reactions (Thomas et al., 2012; Cao et al., 2014; Wang and Pratt, 2017; Wang et al., 2019). High levels of nitrogen oxides, however, might suppress BrO and reduce ozone loss (Custard et al., 2015), highlighting a potential impact of local pollution in the Arctic.

1.2.2 Bromine Activation

The reactions described in the previous section release bromine from the condensed phase into the atmosphere. The exact surfaces involved, as well as the mechanisms and conditions required, are the topics of ongoing research. The proposed reaction cycle requires the condensed phase material to have a high surface area, high salinity, and low pH. Given the early realization that bromine enhancement is connected to first-year sea ice

(FYI) (Wagner et al., 2001), frost flowers (Style and Worster, 2009; Barber et al., 2014) were initially thought to fulfill all the requirements to be a source of reactive bromine (Rankin et al., 2002; Kaleschke et al., 2004). Further research, however, showed that frost flowers have a surface area smaller than initially thought (Domine et al., 2005; Obbard et al., 2009), and their pH is likely too high (Kalnajs and Avallone, 2006; Douglas et al., 2012). The most likely contribution of frost flowers to bromine activation is their indirect influence on the nearby or overlying snowpack (Hara et al., 2017).

In parallel to the frost flower theory, the snowpack on sea ice and on land was also considered as a possible bromine source (e.g., Foster et al., 2001; Spicer et al., 2002). Using outdoor snow chambers, Pratt et al. (2013) measured emission of molecular bromine when snow samples were exposed to sunlight. They found that this process was most efficient for more acidic samples in the presence of ozone, consistent with the bromine explosion mechanism. Wren et al. (2013) arrived at similar conclusions from laboratory experiments. Flux measurements of molecular bromine from the tundra snowpack by Custard et al. (2017) indicated that the snowpack is potentially a dominant source of bromine to the atmosphere. Modelling studies, incorporating snowpack chemistry of varying complexity, corroborated the importance of the snowpack (Toyota et al., 2011, 2014; Thompson et al., 2015, 2017; Wang and Pratt, 2017). While most studies focus on coastal sites, bromine production in snow has also been observed far from marine influences (Stutz et al., 2011; Thomas et al., 2011, 2012).

Bromine release from the snowpack often occurs in the presence of weak winds and a shallow, stable boundary layer. Multi-AXis DOAS (MAX-DOAS) (Hönninger et al., 2004) measurements indicate that bromine in such conditions is restricted to the lowest 200-300 m of the atmosphere (Peterson et al., 2015; Simpson et al., 2017). Wind pumping by moderate winds enhances the transfer of bromine from the snowpack to the atmosphere (Pratt et al., 2013; Peterson et al., 2015), and strong temperature inversions typical in the Arctic spring inhibit vertical mixing. This allows bromine to build up and destroy ozone near the surface. Measurements over the Arctic Ocean showed that most of the marine boundary layer is likely to be at least partially depleted of ozone in the spring (Jacobi et al., 2010; Halfacre et al., 2014).

Other potential sources of bromine include blowing snow and aerosol particles. Yang et al. (2008) and Jones et al. (2009, 2010) argued that high wind speeds and good mixing conditions might create another set of favorable conditions for bromine release. This is in agreement with the recent results of Swanson et al. (2020), who found that the statistics of BrO measurements across the Arctic differentiate into the two sets of environmental conditions outlined above. Strong winds (7-8 m s^{-1}, Li and Pomeroy, 1997) generate blowing snow, and these particles might release bromine through a process similar to what is observed in the snowpack. MAX-DOAS measurements by Frieß et al. (2011) and in situ measurements by Liao et al. (2012) indicated that BrO levels were greater at faster wind speeds (5-6 m s^{-1}). Other studies, however, did not observe such a relationship (Peterson et al., 2015). It is important to note, however, that blizzard conditions can significantly reduce the sensitivity of MAX-DOAS measurements to BrO (Frieß et al., 2011). In situ analysis of blowing snow in Antarctica provided a range of results, with Br^- depletion (compared to seawater) reported by Lieb-Lappen and Obbard (2015), Br^- enrichment reported by Hara et al. (2018), and a range of values (small to no depletion on average) observed by Frey et al. (2020).

While the direct role of blowing snow is uncertain, other lofted particles, such as sea salt aerosol (SSA), might act as a source of bromine to the atmosphere. In the absence of open ocean in the Arctic winter and spring, sources of SSA include sublimation of blowing snow (Yang et al., 2008; Huang and Jaeglé, 2017; Zhao et al., 2017; Giordano et al., 2018; Huang et al., 2018; Frey et al., 2020), and leads in sea ice (Nilsson et al., 2001; Leck et al., 2002; May et al., 2016; Kirpes et al., 2019). Enhanced aerosol extinction was found to correlate with increased BrO concentrations measured by MAX-DOAS (Frieß et al., 2011; Peterson et al., 2015; Simpson et al., 2017; Swanson et al., 2020), although Simpson et al. (2017) noted that high extinction was necessary but not sufficient to maintain BrO aloft. Peterson et al. (2017) reported aircraft measurements of a lofted BrO plume maintained by bromine recycling on supermicron aerosol particles. In situ measurements by Hara et al. (2002) showed Br^- depletion in coarse mode SSA (>2 μm), and Br^- enhancement in the fine mode. Recent in situ measurements from Antarctica provide further evidence about the role of SSA in bromine release. Legrand et al. (2016) observed significant Br^- depletion in supermicron SSA in the spring, and Br^- enhancement in submicron particles. Hara et al. (2018) found springtime SSA to be depleted in Br^- in all size bins. Using measurements at altitudes of 2 m and at 29 m above the surface, Frey et al. (2020) found that, while individual measurements showed some scatter, SSA at 29 m generally showed strong depletion in bromide, whereas SSA at 2 m usually showed strong enrichment. The authors concluded that surface snow, blowing snow and aerosols likely all participate in bromine recycling, and aerosols likely contribute a significant amount of bromine to the atmosphere.

Satellite measurements of tropospheric BrO appear to confirm the role of SSA in bromine release. Modeled BrO release from SSA has been found sufficient to explain measurements from the Global Ozone Monitoring Experiment (GOME) and GOME-2 satellite instruments (e.g., Yang et al., 2010; Theys et al., 2011), and Arctic cyclones with high surface winds have been linked to large BrO plumes seen in GOME-2 data (Begoin et al., 2010; Sihler et al., 2012; Blechschmidt et al., 2016; Zhao et al., 2016b). More recently, Choi et al. (2018) showed that tropospheric BrO columns from the Ozone Monitoring Instrument (OMI) correlated with modeled SSA emissions in the Arctic, while bromine explosion frequency showed little to no correlation with FYI area. However, as often noted in the literature, the detection of shallow boundary layer BrO events (typical for snowpack bromine release) is not straightforward for nadir-viewing satellite instruments (GOME, GOME-2, OMI), given the need to separate the tropospheric BrO column from the total column (e.g., Sihler et al., 2012). Visibility of BrO from space increases for distributed BrO events in a deeper mixing layer, which are often associated with bromine activation on aerosols. As a result of this discrepancy between the sensitivities of ground-based and satellite measurements, the relative importance of the snowpack and SSA to the bromine budget in the Arctic troposphere remains uncertain.

1.3 Motivation and Scientific Objectives

The UV-vis measurements collected by the GBS instruments in Eureka represent an important long-term dataset in the Arctic, where the harsh environment and logistical challenges restrict ground-based measurements to a few well-equipped stations. The ozone, NO_2, and BrO measurements can be used to address both stratospheric and tropospheric ozone depletion. These topics are the subject of Chapters 4, 5, and 6 in this thesis, and the motivations behind each project are described below.

1.3.1 Satellite Validation

Long-term satellite datasets are essential to monitoring changes in the stratosphere, since satellites provide measurements with greater spatial coverage than any ground-based network. However, to ensure that the satellite measurements are well characterized, ground-based validation is required throughout the lifetime of the satellite instruments. This task is particularly challenging for satellites in high-inclination orbits, since they collect a large portion of their data in the Arctic, where the coverage of ground-based instruments is sparse, and measurements are restricted to the sunlit part of the year. The Optical Spectrograph and InfraRed Imager System (OSIRIS) and the Atmospheric Chemistry Experiment (ACE) satellite instruments have been taking measurements in high-inclination orbits since 2001 and 2003, respectively. The ozone and NO_2 products from these instruments have been validated before (e.g., Brohede et al., 2007b; Degenstein et al., 2009;

Dupuy et al., 2009; Kerzenmacher et al., 2008; Sioris et al., 2017). However, there are no recent comparisons in the Arctic involving OSIRIS and both ACE instruments (the Fourier Transform Spectrometer, or FTS, and the Measurement of Aerosol Extinction in the Stratosphere and Troposphere Retrieved by Occultation, or MAESTRO). As the satellite data processing improves and new versions of the datasets are released, it is important to verify the consistency of ozone and NO_2 measurements at high latitudes. This task is especially important given that OSIRIS and ACE are currently the only satellite instruments measuring NO_2 profiles in the high Arctic.

To support validation efforts, and to facilitate additional springtime measurements, Eureka has been the site of the annual Canadian Arctic ACE/OSIRIS Validation Campaigns since 2004 (Kerzenmacher et al., 2005). Ozone and NO_2 measurements from PEARL have been used to validate the ACE and OSIRIS satellite instruments in a series of papers (Kerzenmacher et al., 2005; Sung et al., 2007; Fraser et al., 2008; Batchelor et al., 2010; Fu et al., 2011; Lindenmaier et al., 2011; Adams et al., 2012a; Griffin et al., 2017), and one aim of this thesis is to update the validation results with more recent datasets and new data versions. Specifically, this project aims to answer the following scientific questions:

- How consistent are the ozone and NO_2 columns retrieved from the aging OSIRIS, ACE-FTS, and ACE-MAESTRO satellite instruments when compared to each other, and to ground-based measurements? How do the results compare to previous validation efforts, and what are the reasons for any changes in the results?
- Is there any drift over time in the differences between the various satellite and ground-based instruments?
- Does the location of the polar vortex have a significant impact on springtime comparisons? Can these impacts be quantified using dynamical parameters derived from reanalysis data?
- Can the validation results be improved by implementing a cloud screening algorithm for the ground-based DOAS instruments?

Addressing these questions is important in order to maintain confidence in the satellite data products, which are widely used. Identification of drifts and biases (or lack thereof) leads to improved data products and better scientific results. The validation results provide a useful consistency check for the ground-based datasets as well, and inform studies utilizing these measurements.

1.3.2 Stratospheric Ozone Depletion

A historically important (and still relevant) motivation for the ground-based measurements is the assessment of stratospheric ozone depletion in the Arctic. While CFCs in the stratosphere are declining and ozone levels are expected to return to 1980 levels by the mid-21st century (WMO, 2018), the large interannual variability of the polar vortex can still lead to significant ozone loss. These processes are not fully understood and difficult to predict, underscored by the unexpected magnitude of ozone depletion in 2011 (e.g., Manney et al., 2011b). In 2020, ozone depletion again reached similar levels, surpassing several records set in 2011 (Bernhard et al., 2020; Grooß and Müller, 2020; Inness et al., 2020; Lawrence et al., 2020; Manney et al., 2020; Wohltmann et al., 2020). Even with the gradual recovery of the ozone layer, it is possible that greater ozone depletion might yet occur (Manney et al., 2020).

Continuous, localized measurements from ground-based instruments provide an important piece of the puzzle to understand the processes underlying these extreme events. Eureka is in an excellent location to study ozone loss, as the vortex is often located overhead in the spring. Measurements inside the vortex in 2011 have been used in several studies to assess ozone depletion (Adams et al., 2012b; Lindenmaier et al., 2012; Adams et al., 2013; Pommereau et al., 2013). In 2020, the vortex was unusually strong and stable, and it was located above Eureka longer than in any previous year in the measurement record. This presents a unique opportunity to study both the destruction and recovery of ozone inside the vortex. The longevity of the vortex also aids in estimating ozone loss, as measurements after chemical ozone depletion ceased yield a better representation of overall chemical loss than measurements in early spring. This project aims to use long-term datasets of measured and modeled ozone (and related species) at Eureka to address the following scientific questions:

- How did trace gas concentrations evolve inside the polar vortex during the unusual spring in 2020? What were the key differences between ozone depletion in 2020 and 2011?

- What was the contribution of dynamical factors to the exceptionally low ozone columns measured in spring 2020? How did stratospheric dynamics contribute to the recovery of ozone inside the polar vortex?

- What is the agreement of modeled ozone and related trace gases with measurements at Eureka? Is this agreement consistent inside and outside the polar vortex?

- What are the estimates of chemical ozone loss when comparing measurements to modeled passive ozone? Can these estimates be generalized to assess overall ozone loss inside the vortex over Eureka?

Understanding the mechanisms behind these extreme events is important to accurately project the future of the ozone layer, especially in light of anthropogenic factors that compound the already considerable variability of Arctic ozone loss. There is uncertainty regarding how the rising concentrations of greenhouse gases will affect stratospheric ozone (Eyring et al., 2013), or how changing ozone concentrations will influence the global climate. In addition, emissions of ozone-depleting substances, either unregulated by (Hossaini et al., 2015), or in contravention of (Montzka et al., 2018; Rigby et al., 2019), the Montreal Protocol present a continued risk to the stratospheric ozone layer.

1.3.3 Tropospheric Bromine Activation

In the Arctic troposphere, the springtime halogen activation and corresponding ozone depletion events are not fully understood. While the snowpack and sea salt aerosols likely both release bromine, ground-based studies are inconclusive regarding the relative importance of each source (e.g., Custard et al., 2017; Frey et al., 2020). Satellite measurements support the major role of SSA in bromine activation (e.g., Choi et al., 2018), although this is in part due to the different sensitivities of ground-based and satellite instruments. The balance of different bromine sources is likely variable, and in part controlled by meteorological conditions. While case studies of specific bromine explosion events reveal valuable details about specific processes, attempts to disentangle the complex roles of meteorology and transport benefit from the use of long-term datasets. There are, however, few multi-year datasets of ground-based BrO measurements described in the literature.

The GBS measurements of BrO constitute one such dataset, which provides useful insights into the underlying processes of bromine activation. In addition, the elevation of the PEARL Ridge Lab (610 m) means that the instrument often measures above the boundary layer. This presents an interesting opportunity to examine BrO both in and above the boundary layer from a ground-based station. The discrepancy between satellite and ground-based sensitivities is likely smaller for such an elevated measurement site. This project aims to use the GBS BrO dataset, along with in situ measurements in Eureka, to better understand the role of local meteorology in bromine activation, as well as the relative contributions of the snowpack and SSA. The goals are summarized by the following science questions:

- How do wind speed and atmospheric stability influence bromine activation? What is the role of vertical mixing and topography in determining BrO values observed from an elevated measurement site?

- What is the relative importance of the snowpack and aerosols in bromine release? Can the effects of transport and local sources be separated using measurements at Eureka?
- Is the snowpack on first-year sea ice the only source of snowpack-related bromine? Does the snowpack on the multi-year ice areas near Eureka contribute to the observed BrO values?
- What are the likely sources of springtime aerosol in Eureka? Can the importance of aerosol particles for bromine activation be categorized based on size distribution and chemical composition?

Addressing these questions is important to assess the current and future impacts of tropospheric halogen chemistry. Our understanding of bromine vertical distribution over mountainous terrain is limited, and bromine above the boundary layer could influence free tropospheric ozone, which is a greenhouse gas. In addition, bromine explosions lead to the deposition of gaseous elemental mercury, with potentially harmful impacts on the Arctic ecosystem (Schroeder et al., 1998; Steffen et al., 2008; Cole and Steffen, 2010; Berg et al., 2013). A more complete understanding of these topics is also necessary to evaluate the impacts of climate change. Total sea ice cover is decreasing in the Arctic, accompanied by an increased fraction of first-year sea ice coverage (Kwok, 2018). Changing precipitation patterns might alter the springtime snow cover, both on sea ice and on land. The effect of these changes on bromine explosions and the Arctic environment are not yet understood.

1.3.4 Urban NO_2 Pollution

In addition to its previously described roles in the polar atmosphere, near-surface ozone is toxic in high concentrations. This is of particular importance at mid-latitudes, where ozone is a common secondary pollutant, created from the reactions of nitrogen oxides, carbon monoxide, and volatile organic compounds. Ozone concentrations are typically monitored by in situ instruments, as remote sensing of tropospheric ozone is challenging. On the other hand, MAX-DOAS instruments are well suited to measure tropospheric NO_2, an ozone precursor and itself a pollutant. The Pandora instruments, distributed worldwide, regularly perform MAX-DOAS measurements, and a major aim of the PGN is long-term air quality monitoring via measurements of NO_2 (and other species). Currently, however, there are no PGN data products that utilize the MAX-DOAS measurements for air quality monitoring. Tropospheric partial columns (Spinei et al., 2014) and surface concentrations (Zhao et al., 2019b) have been retrieved from Pandora measurements, but none of these approaches use the MAX-DOAS dataset. Furthermore, NO_2 profiles are not readily available for Pandora instruments.

Alongside the Pandora spectrometer in Eureka, ECCC operates several Pandora instruments in and around Toronto (Zhao et al., 2016a, 2020b). The project presented in Chapter 7 of this thesis aims to use measurements from two of these instruments (in Downsview, Toronto, at 43.78°N, 79.47°W) to retrieve NO_2 profiles and answer the following science questions:

- Do Pandora MAX-DOAS measurements have sufficient sensitivity to retrieve profiles of tropospheric NO_2? How do results from parametric and optimal estimation retrieval methods compare?
- How consistent are the retrieved partial columns when compared to the standard Pandora NO_2 total columns? What is the relationship between the retrieved surface NO_2 concentrations and those measured by in-situ measurements in Toronto?
- What are the patterns of temporal variability in the retrieved NO_2 dataset? What are the patterns in the vertical distribution of NO_2?
- What was the effect of the 2020 COVID-19 lockdown on NO_2 columns and surface concentrations in Toronto?

This project is largely focused on the creation and characterization of a Pandora NO_2 profile dataset. Profiles and surface concentrations are arguably the most useful quantities for air quality monitoring, and utilizing the MAX-DOAS measurements is a necessary step to harness the full measurement capabilities of the Pandora instruments. Given the large volume of data, two retrieval algorithms (Frieß et al., 2011; Beirle et al., 2019) are used. The retrieval results are compared to each other, and to standard NO_2 products (total columns and in situ measurements), to evaluate which algorithm provides a better balance of quality and efficiency. The lockdowns related to the COVID-19 pandemic in 2020 present an interesting case study for this NO_2 dataset. Early results show that NO_2 columns decreased drastically in Toronto (e.g., Griffin et al., 2020) and in other cities globally (e.g., Bauwens et al., 2020). The NO_2 profiles and surface concentrations retrieved from Pandora measurements provide an excellent dataset to investigate these reductions in detail.

1.4 Thesis Outline and Scientific Contributions

This thesis has eight chapters. Chapters 2 and 3 provide additional background information, and Chapters 4 to 7 represent the main scientific body of the thesis. A brief outline of each chapter is given below.

The first part of Chapter 2 describes the UT-GBS and PEARL-GBS instruments, for which I have been responsible since 2016. To set up and maintain the instruments, I have travelled to Eureka five times, and to Cabauw in the Netherlands once. During each campaign, I performed the laboratory tests and resolution measurements, using guidelines developed by Matt Bassford, Elham Farahani, Annemarie Fraser, Cristen Adams, and Xiaoyi Zhao. The second part of Chapter 2 describes the data processing for the GBS instruments, from the basic DOAS analysis to the final results: total columns for ozone and NO_2, and tropospheric columns for aerosols and BrO.

Chapter 3 has two parts. The first part describes the measurement history of the UT-GBS and PEARL-GBS in Eureka. During the springtime Canadian Arctic ACE/OSIRIS Validation Campaigns, I was responsible for the reassembly (of the PEARL-GBS in 2016 and 2017), calibration, troubleshooting, and operation of the GBS instruments. I acquired the data for 2016-2019, and Ramina Alwarda and I made the measurements together in 2020. I have reprocessed the entire time series of the GBS instruments, and implemented the conversion of the GBS data to Hierarchical Data Format (HDF). These files replaced the previous dataset in the NDACC archive. The rest of Chapter 3 concerns the second Cabauw Intercomparison of Nitrogen Dioxide measuring Instruments (CINDI-2) campaign, held in September 2016. Xiaoyi Zhao and I spent several months working together to deploy the PEARL-GBS as a field instrument for the campaign. I was in charge of the hardware and logistical aspects, while Xiaoyi was responsible for upgrading the software to match campaign data acquisition protocols. We deployed the instrument together in August 2016. I took care of the instrument operation and the daily data submission, while Xiaoyi performed the first round of profile retrievals. In the following years, I have contributed PEARL-GBS results to three CINDI-2 publications (Donner et al., 2020; Kreher et al., 2020; Tirpitz et al., 2021), as discussed in the relevant sections of Chapter 3.

Chapter 4 presents validation results for the ACE and OSIRIS satellite instruments using ground-based datasets from Eureka. I found that the comparison results are consistent with previous validation efforts, and there are no significant drifts between the satellite and ground-based datasets. I also quantified the impact of both dynamical variability and clouds on subsets of the comparison results. The cloud filter for the UT-GBS ozone data was implemented by Xiaoyi Zhao. Satellite ozone and NO_2 data were provided by Chris Boone, Adam Bourassa, Doug Degenstein, Jim Drummond, Tom McElroy, Chris McLinden, Chris Sioris, and Jason Zou. The ground-based datasets were prepared and provided by Alistair Duff, Florence Goutail, Debora Griffin, Paul Jeffery, Erik Lutsch, Andrea Pazmino, and Kaley Walker. The dynamical parameters were provided by Gloria Manney and Luis Millán. This work has been published in the *Journal of Quantitative Spectroscopy and Radiative Transfer* (Bognar et al., 2019).

Chapter 5 uses the long-term datasets from Eureka (largely as described in Chapter 4) to assess the exceptional stratospheric ozone depletion observed in spring 2020. Record ozone minima were observed in the time series of all instruments, and ozonesonde profiles indicated unprecedented ozone loss in the lower stratosphere. Ground-based measurements (with data contributed by Ramina Alwarda, Vitali Fioletov, Florence Goutail, Beatriz Herrera, Andrea Pazmino, Kaley Walker, Tyler Wizenberg, and Xiaoyi Zhao) indicate that chlorine activation was ongoing until the end of March. PSCs were detected in lidar data as late as 20 March (data from Jim Drummond and Emily McCullough). I assessed the dynamical contributions to low ozone using dynamical parameters provided by Gloria Manney and Luis Millán. Chemical ozone loss was calculated using passive ozone from model simulations performed by Martyn Chipperfield, Sandip Dhomse, and Wuhu Feng. This work has been submitted to the *Journal of Geophysical Research: Atmospheres* special issue, "The Exceptional Arctic Stratospheric Polar Vortex in 2019/2020: Causes and Consequences" (Bognar et al., 2020a).

Chapter 6 examines four years of springtime BrO partial columns, retrieved from PEARL-GBS MAX-DOAS measurements, to understand the factors contributing to tropospheric BrO variability at Eureka. I implemented the profile retrievals for the 2016-2019 data, building on the case studies performed by Xiaoyi Zhao. The retrieval code was provided by Udo Frieß. I found that BrO events clearly differentiate by local wind direction, and each wind direction corresponds to distinct air mass histories. For air coming from the Arctic Ocean, sea ice contact correlates with BrO values. On the other hand, storms coming from the Western Arctic almost always generate BrO enhancements, and these show a much weaker relationship to sea ice contact. Surface ozone measurements at Eureka (courtesy of Audra McClure-Begley and Sara Morris) indicate that vertical mixing during these strong wind episodes generates enhanced BrO with little to no ozone depletion. The source of this storm-related BrO is likely SSA. In situ aerosol measurements (provided by Rachel Chang, Patrick Hayes, Samantha Tremblay, and Andy Vicente-Luis) show that the presence of coarse mode aerosols is a necessary and sufficient condition for observing BrO at Eureka. That aerosols are necessary was expected given the altitude of the measurement site, but the fact that high aerosol concentrations always correspond to increased BrO indicates that SSA likely play an active role in bromine release. This work has been published in the *Journal of Geophysical Research: Atmospheres* (Bognar et al., 2020b).

Chapter 7 presents the NO_2 profile dataset retrieved from Pandora MAX-DOAS measurements in Toronto. The Pandora data and in situ measurements used in this project were provided by Ramina Alwarda, Vitali Fioletov, and Xiaoyi Zhao. The profile retrieval algorithms were provided by Steffen Beirle and Udo Frieß. I found that retrieval results using parametric and optimal estimation retrieval algorithms agree well for partial columns, and show some discrepancies for surface concentrations. Using parametric retrieval results for the full time series (2018-2020), I found that partial columns agree well with the standard NO_2 total columns, while surface concentrations are only weakly correlated to in situ measurements. It appears that the COVID-19 lockdown led to a significant reduction of NO_2 concentrations, especially on weekdays. The most striking impact of the lockdown in the dataset is the drastic reduction of peak NO_2 abundances. This work will form the basis of a future publication, which will also utilize the profile dataset for the validation of satellite NO_2 products.

The last chapter (Chapter 8) presents the conclusions and includes suggestions for future work. Overall, the major contributions of this thesis include: the use of GBS measurements to validate the ACE and OSIRIS satellite instruments and assess the unprecedented stratospheric ozone depletion in spring 2020, the creation of a multi-year tropospheric BrO dataset to characterize bromine activation in Eureka, and the retrieval and validation of an NO_2 profile dataset for Pandora instruments in Toronto.

Chapter 2

Instrumentation and Data Processing

This chapter describes the UT-GBS and the PEARL-GBS instruments, as well as the measurement techniques and retrieval methodology used. The UT-GBS was first deployed in 1998 (1999 in Eureka), and the PEARL-GBS was assembled in 2006. Since those beginnings, the instruments, data processing, and the measurement techniques have continued to evolve. Each step of this process has been documented in previous PhD theses, by Farahani (2006), Fraser (2008), Adams (2012), and Zhao (2017). This chapter summarizes the technical history of the GBS instruments, with a focus on the 2016-2020 period. The chapter then discusses the measurement methodology and the retrieval techniques used to produce the final data products. The GBS results are used in the satellite validation and stratospheric ozone depletion studies (Chapters 4 and 5), as well as in the bromine activation study (Chapter 6). The GBSs have participated in several field campaigns over the years (four Middle Atmosphere Nitrogen TRend Assessment (MANTRA) and two CINDI campaigns). These campaigns, along with the measurement history of the GBS instruments, are described in Chapter 3.

2.1 GBS Spectrometers

The UT-GBS and the PEARL-GBS are UV-vis spectrometers that were first deployed in Eureka in 1999 and 2006, respectively. Both the UT-GBS and the PEARL-GBS started as zenith-sky instruments, and both were upgraded with solar trackers (i.e., suntrackers) to allow multiple viewing geometries (starting from 2015 and 2008, respectively). The instrument components and configurations have been updated over the years to improve data quality, as described in the following sections. When in Eureka, both instruments are located in the PEARL Ridge Lab. Indoors, the PEARL Ridge Lab is separated into individual laboratories, including the UV-vis Lab and the IR Lab, while suntracker systems are located on the Ridge Lab roof platform. The UT-GBS is currently located on the UV-vis Lab mezzanine (with the suntracker directly above), and the PEARL-GBS is located on the IR Lab mezzanine (with the suntracker on the Northwest corner of the roof platform). The location of the instruments has changed over the years, as dictated by the requirements of new measurement strategies.

The GBS instruments are grating spectrometers that use a diffraction grating to separate the wavelengths (λ) of light. For light incident at angle θ_i, the diffraction can be described as

$$sin(\theta_i) + sin(\theta_m) = Nm\lambda, \tag{2.1}$$

where θ_m is the diffraction angle, m is the diffraction order, and N is the grating density in grooves per mm (gr mm^{-1}). Assuming that the incident angle is constant, we can differentiate Equation 2.1 with respect to λ (where θ_m is a function of λ). The resolution of the grating is then given by

$$\Delta\lambda = \frac{\Delta\theta_m cos(\theta_m)}{Nm}. \tag{2.2}$$

Smaller $\Delta\lambda$ corresponds to higher resolution, which can be achieved by increasing the grating density, using higher orders of diffraction, or increasing the diffraction angle close to 90°.

2.1.1 The UT-GBS

The main component of the UT-GBS is a Triax-180 crossed Czerny-Turner triple-grating UV-vis spectrometer, built by Instruments S.A./Jobin Yvon/Horiba. Figure 2.1 shows the schematic of the Triax-180 spectrometer. Light enters through a slit, it is directed to the diffraction grating by the collimating mirror, and the focusing mirror directs the light onto the detector. A mechanical shutter can be inserted between the slit and the collimating mirror to improve the signal-to-noise ratio (SNR). The spectrometer has a focal length of 0.190 m (f-number[1] 3.9) and a 12×30 mm focal plane. Spectra are recorded using a thermoelectrically cooled charge-coupled device (CCD) detector. The three gratings in the instrument are mounted on a motorized turret, allowing selection of the grating, the wavelength range, and the resolution. The UT-GBS grating turret contains 400, 600, and 1800 gr mm^{-1} gratings. The 400 gr mm^{-1} grating was ruled using

---

[1] The ratio of the focal length to the diameter of the entrance pupil.

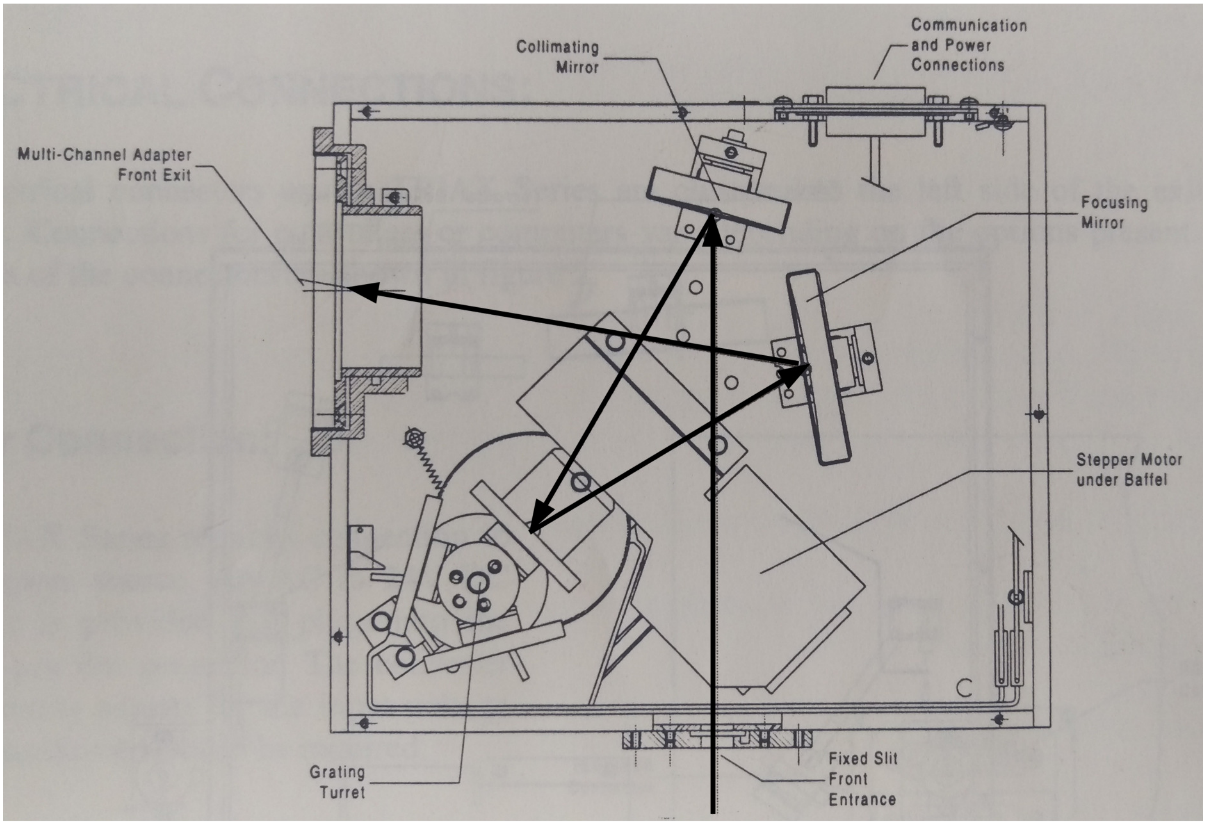

Figure 2.1: Top view diagram of the Triax-180 spectrometer. The path of light is indicated by the black arrows. Figure adapted from the Triax User Manual (Horiba, 2014).

diamond needles, while the higher density gratings are holographic, formed using the interference fringes of two laser beams. The properties of the gratings are described in detail by Farahani (2006), Fraser (2008), and Adams (2012).

The UT-GBS uses a fixed 0.1 mm entrance slit. Up to 2011, the instrument used an adjustable mechanical slit (set to 0.1 mm). The mechanical slit was removed in February 2012 since it occasionally jammed open, with significant impacts on resolution (Adams, 2012; Zhao, 2017). The UT-GBS can use mechanical shutters to synchronize the light entering the spectrometer to the exposure times of the CCD. Shutters were used for most measurements up to and including 2012. Due to increasing measurement volumes (and therefore increasing load on the shutters), the shutters were only used for the spring campaigns from 2013 to 2018. Since the shutters were not designed for long-term, continuous operation, shutter failures were common, often resulting in loss of measurements until the shutter could be replaced or removed. Furthermore, there is no clear evidence that using the shutters increased data quality, and so shutters were not used starting from 2019.

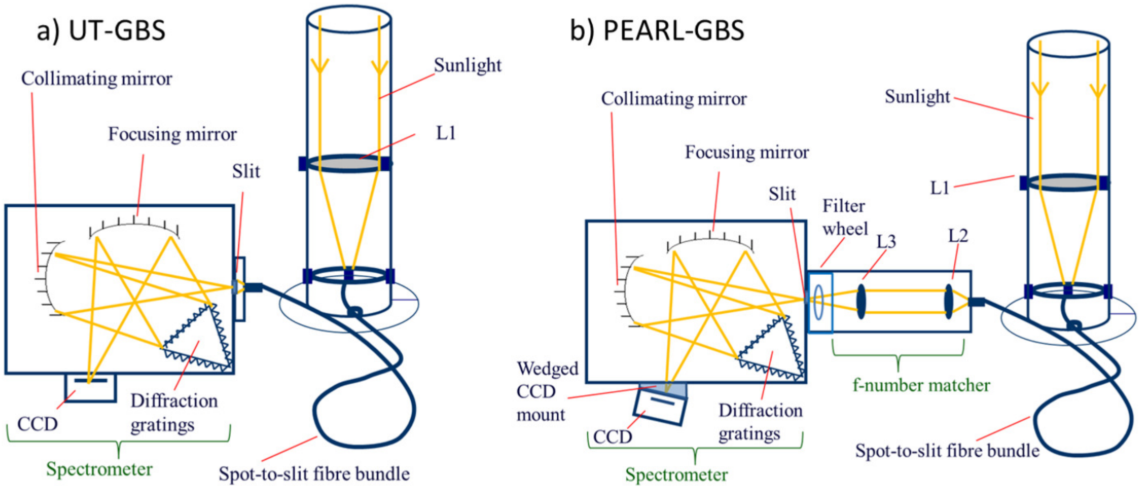

Figure 2.2: Schematics of the spectrometer and input optics for **a)** the UT-GBS, and **b)** the PEARL-GBS. Reproduced from Figure 2.1 of Zhao (2017).

The UT-GBS records spectra using a 2048×512 pixel back-illuminated CCD detector with a UV-enhanced coating. The physical size of the detector is 27.6×6.9 mm^2 and each pixel is 13.5×13.5 μm^2. The 2048 horizontal pixels correspond to wavelength information, and the 512 vertical pixels correspond to the height of the light incident on the slit. The detector is cooled to 201 K by a Peltier thermoelectric cooling system in order to minimize dark current. The UT-GBS has used three detectors since 1998 (Fraser, 2008). The original back-illuminated 2000×800 pixel CCD (cooled to 230 K) was replaced for the 2004 MANTRA campaign (see Chapter 3) with a loaner CCD, a front-illuminated 1024×128 pixel detector (liquid nitrogen cooled, 140 K). In 2005, the third CCD (described above) was installed, and it has been in use since. The high voltage power supply to the CCD controller unit was replaced after a failure in March 2019.

The input optics and their coupling to the spectrometer is shown in Figure 2.2a for the UT-GBS. The setup of the instrument has not been changed since March 2015, and the description here largely follows Zhao (2017). Light is focused on the spot end of a spot-to-slit fibre bundle by lens L1 (Fig. 2.2a, 40 mm diameter, f-number 4). The 10-m-long fibre bundle contains 37 silica fibres, and the slit end is coupled directly to the spectrometer entrance slit using an AFO-XY fibre mount. The long fibre bundle (coiled in several loops) depolarizes incoming light, which is important since DOAS instruments are sensitive to polarization (Platt and Stutz, 2008). The original setup (since 1998) utilized a liquid light guide (LLG) instead of a fibre bundle. To compensate for the low transmittance of the LLG, a different L1 (f-number 2.5) was used, and an f-number matcher was inserted between the LLG and the entrance slit. The purpose of the f-number matcher was to increase the f-number of L1 to match the spectrometer (f-number 3.9), and avoid loss of signal. The LLG was replaced with a 1-m fibre bundle in March 2011. Given the higher transmittance of the fibre bundle, the setup was simplified in February 2012 by removing the f-number matcher and replacing L1 with the lens currently in use. This modification also reduced optical aberrations in the UT-GBS measurements (Adams, 2012; Zhao, 2017). The current 10-m fibre bundle was installed in February 2013.

The UT-GBS operated in zenith-viewing geometry from 1998 to 2014, with the input optics in Figure 2.2 pointing straight up through a plexiglass window in one of the hatches in the UV-vis Lab. In March 2015, the UT-GBS was coupled to the UT-Suntracker unit #1, to allow MAX-DOAS measurements as well. The tracker setup is described in more detail in Section 2.1.4. At the same time in March 2015, the UT-GBS spectrometer was placed in a temperature-controlled box (GBS cooling unit #2). GBS cooling unit #2 consists of an aluminum box (constructed in 2002 by Cases Unlimited Inc.) with 1.27 cm of black foam insulation, two air conditioners (one with both heating and cooling capabilities), and a temperature monitor (Xytronix X-300). The UT-GBS spectrometer had no ambient temperature control in Eureka for 1999-2014.

Since 2015, the UT-GBS performs a combination of zenith-sky (all solar zenith angles, or SZA) and MAX-DOAS (SZA $< 84°$) measurements using the 600 gr mm^{-1} grating, focusing on stratospheric ozone and NO_2, as well as tropospheric NO_2 and oxygen collisional dimer (O_4). Spectra are recorded using in-house Labview software (as described by Adams, 2012; Zhao, 2017) on the Sundog2 laptop. More details on the measurement history and acquisition parameters are given in Chapter 3.

2.1.2 The PEARL-GBS

The overall design of PEARL-GBS is very similar to the UT-GBS. The PEARL-GBS is also build around a Triax-180 spectrometer, with a different set of gratings (300, 600, and 1200 gr mm^{-1}) on the grating turret. The PEARL-GBS uses an updated version of the UT-GBS CCD with enhanced broadband coating. The CCD is attached to the spectrometer using a 10° wedged CCD mount, in order to bring the detector normal axis in alignment with the spectrometer's main optical axis, and ensure uniform resolution across the detector (Adams, 2012; Zhao, 2017). The wedged mount was installed in February 2013. The CCD was repaired twice: first after a vacuum seal issue in 2010, and after a complete failure in April 2011. In March 2016, the CCD was exposed to temperatures around $-10°$C during a freezing event in the PEARL Ridge Lab. This caused the CCD bias to temporarily increase to 5-6 times the normal level, even while the CCD cooling appeared to function properly. The bias returned to normal levels after the cold snap, with no detectable changes in CCD performance.

The PEARL-GBS used mechanical shutters for most measurements in 2006-2012, and for springtime measurements for 2013-2016. During testing in summer 2016, the shutters began experiencing synchronization issues, likely due to a failure of the CCD shutter control module. For this reason, and given the instability of the shutters themselves (see Sect. 2.1.1), the PEARL-GBS measurements were performed without shutters starting from spring 2017. Unlike the UT-GBS, the PEARL-GBS has always used a fixed entrance slit. A 0.05 mm slit was used from 2006 to 2010, and the current 0.1 mm slit has been in place since 2011.

The PEARL-GBS input optics and the connection to the spectrometer are shown in Figure 2.2. Light is focused onto a spot end of a spot-to-slit fibre bundle by lens L1 (4 mm diameter, f-number 2.5). The 30-m-long fibre contains 37 silica fibres, and the slit end is coupled to the spectrometer via and f-number matcher and a filter wheel. The original setup utilized a LLG (2006-2009), and the LLG was replaced by a 1 m spot-to-slit fibre bundle in March 2010. The current 30-m fibre bundle was installed in October 2014. The f-number matcher contains two lenses: L2 collimates the light, and L3 focuses the light to the 3.9 f-number of the spectrometer (Adams, 2012). The filter wheel contains a set of fused silica neutral density filters with metallic coatings (transmittances of 25%, 1%, 0.1%, and 0.01%) (Zhao, 2017). These filters replaced the old set of reflective filters in October 2014, since the old filters resulted in poor data quality (Adams, 2012).

The PEARL-GBS was initially installed in the UV-vis Lab, and performed only zenith-sky measurements. In February 2008, UT-Suntracker unit #1 was installed above the input optics to allow direct-sun measurements. The PEARL-GBS was temporarily moved to the penthouse on the PEARL Ridge Lab roof for 2009. The filter wheel was used (with the old filters) for passive direct-sun measurements in 2008-2011. The filter wheel stepper motor, however, occasionally skipped steps, causing a drift in the filter positions over time. As a consequence, no direct-sun measurements have been performed since 2011. While the filter wheel stepper motor was replaced in March 2016, and the filter wheel is now more stable, direct-sun measurements were not added to the Eureka measurement schedule due to difficulties with active tracking (see Sect. 2.1.4).

In October 2014, a new suntracker unit (UT-Suntracker #2) was installed on the roof of the PEARL Ridge Lab to allow unobstructed line-of-sight for the MAX-DOAS measurements (Zhao, 2017). Since no roof hatches are available near the tracker location in the Northwest corner of the roof platform, the 30-m fibre bundle (described above) was necessary to bring the light from the suntracker to the spectrometer. To enable this setup, the PEARL-GBS was moved from the UV-vis lab to the IR Lab. The spectrometer was placed in the IR Lab crawl space to prevent overheating. Since all components of UT-Suntracker #2 are located outside (as opposed to inside a hatch, which is the case for UT-Suntracker #1), hardware failures happen occasionally. Both motor controllers for the suntracker motors had to be replaced in March 2017, and the elevation motor controller was replaced again in March 2020. The elevation motor was also replaced in March 2020.

In March 2017, the spectrometer was moved to the IR Lab mezzanine, and placed in a temperature-controlled box (GBS cooling unit #1). GBS cooling unit #1 consists of an aluminum box (constructed in 1998 by Cases Quantum Scientific) with 1.27 cm of black foam insulation, one air conditioner with both heating and cooling capabilities (Delta-T DI-02A, 2000 BTUH), and a temperature monitor (Xytronix X-300). Prior to this change, the PEARL-GBS spectrometer only had temperature control in 2013-2014, when it was housed in GBS cooling unit #2 (Zhao, 2017).

Since 2012, the PEARL-GBS focuses on zenith-sky (all SZA) and MAX-DOAS (SZA $< 86°$) measurements using the 1200 gr mm^{-1} grating. The target species include stratospheric NO_2, OClO, and BrO, as well as tropospheric BrO and O_4. Spectra are recorded using in-house Labview software (as described by Adams, 2012; Zhao, 2017) on the Moondog3 laptop. More details on the measurement history and acquisition parameters are given in Chapter 3.

2.1.3 Instrument Resolution

The laboratory testing procedures for the GBS instruments are described in detail by Adams (2012). The resolution and stray light tests, as well as dark current and bias characterization are performed every spring in Eureka. The testing procedures are also repeated every time the instruments are reassembled, the CCD is refocused, or the optical components are updated.

The resolution and sampling of the UT-GBS and the PEARL-GBS are shown in Tables 2.1 and 2.2, respectively. Instrument resolution can vary from year to year due to refocusing of the CCD, as well as the different CCDs, entrance slits, and optical fibres used. Furthermore, the resolution is not uniform across the CCD, with lower resolution at the detector edges compared to the detector centre. The list of emission lines included in the resolution tests also influences the results. The values in Tables 2.1 and 2.2 represent the range of resolution across the regions of the CCD that are typically used in the

Table 2.1: UT-GBS sampling and resolution from 1998 to 2020.

	Sampling (FWHM, pixels)			Resolution (nm)		
Grating (gr mm^{-1})	400	600	1800	400	600	1800
Original CCD: 1998-Eu2004[a]	7-20	6-20	7-16	0.8-5.4	0.5-2.3	0.2-0.8
Loaner CCD: MANTRA 2004[a]	3-19	3-18	3-12	"	"	"
New CCD: 2005-2009[b]	5-14	5.5-16	7-12	"	"	"
New CCD + input optics: 2010[c]	7-13	7.5-13	7.5-10.5	1.1-2.1	0.9-1.3	0.2-0.3
New CCD + input optics + new fibre: 2011[c]	"	"	"	0.9-1.4	0.6-2.0	"
New CCD + new input optics: 2012-2020[d]	6-13	7-13	7.5-12	0.5-1.9	0.4-1.8	0.1-0.4

[a] Values combined from Farahani (2006) and Fraser (2008).

[b] Values from Fraser (2008).

[c] Values from Adams (2012).

[d] Combined with 2012-2016 values from Zhao (2017). The resolution was 1.0-1.9, 0.8-1.5, and 0.2-0.4 nm (400, 600, and 1800 gr mm^{-1}) for 2016-2020.

retrievals. The grating(s) used for Eureka measurements in each year is shown in Tables 3.2 and 3.3.

It should be noted that since 2015, the PEARL-GBS test results are not necessarily representative of the actual resolution. This is because the lamp tests cannot be performed using the standard input optics, since the suntracker assembly (and therefore the end of the 30-m fibre bundle) is located outside on the roof. For testing, the 30-m fibre bundle is detached from the f-number matcher, and a 6-m fibre bundle (with a separate L1 lens) is attached. The slit ends of the fibre bundles are attached as accurately as possible, and so the real resolution is likely very close to the lamp test results.

2.1.4 Suntracker System

The UT-Suntracker was developed at the University of Toronto for UV-vis and infrared spectrometers from off the shelf components (Adams, 2012). The trackers consist of an aluminum frame, two custom-made UV-enhanced aluminum mirrors, and two DC motors. The mirrors are mounted at 45° angles, as shown in Figures 2.3 and 2.4. The first mirror is rotated by the elevation motor (Newport URS75BCC), and the entire mirror platform is rotated by the azimuth motor (Newport URS150BCC). The motors are controlled independently through two Newport SMC100CC motor controllers. Light passes through a hole in the center of the azimuth motor, and the input optics are placed in the path of the beam under the suntracker. UT-Suntracker #1 was assembled and tested in Toronto

Table 2.2: PEARL-GBS sampling and resolution from 2006 to 2020.

	Sampling (FWHM, pixels)			Resolution (nm)		
Grating (gr mm^{-1})	300	600	1200	300	600	1200
Original setup: 2006-2009[a]	5-14	4.5-16	7-12	1.0-3.0	0.5-2.5	0.2-1.8
New fibre: 2010[b]	4-6	3.5-5	4-4.5	0.9-1.3	0.4-0.6	0.17-0.19
New fibre + slit: 2011-2012[c]	7-15	7-15	7-12	1.4-3.0	0.7-1.5	0.3-0.5
New fibre + slit + wedged CCD mount: 2013-2020[d]	"	"	7-13	1.6-3.1	0.8-1.3	"

[a] Values combined from Farahani (2006) and Fraser (2008).

[b] Values from Adams (2012).

[c] Values from Zhao (2017).

[d] Combined with 2013-2016 values from Zhao (2017). Optimized for 1200 gr mm^{-1} grating in 2020 (∼0.35 nm resolution), resulting in worse resolution for 300 gr mm^{-1} grating (excluding 2020, max. resolution was 2.5 nm).

in 2006-2007, and it was installed in a hatch in the UV-vis lab at PEARL in February 2008. The suntracker was coupled to the PEARL-GBS for 2008-2014, and to the UT-GBS since March 2015. UT-Suntracker #2 was assembled for the CINDI campaign (Chapter 3), and it was installed on the roof of the PEARL Ridge Lab in October 2014.

The suntracker control software was developed at Dalhousie University by Franklin (2015). The suntrackers are capable of passive pointing, passive tracking (of the sun or moon), and active tracking (with the aid of a camera). For the GBS instruments, the tracker software (Trax6.5.6) runs on separate laptops with Linux systems, and communicates with Labview on the instrument laptops through Transmission Control Protocol (TCP) (Zhao, 2017).

Figure 2.3 shows the schematics of the UT-Suntracker #1 setup for the UT-GBS. The suntracker is located under an acrylic, UV-transparent double dome in one of the UV-vis Lab hatches. The communication to the tracker controllers and then to the motors is sent through serial cables, and the entire setup is located indoors. Figure 2.4 shows the schematics of the UT-Suntracker #2 setup for the PEARL-GBS. The suntracker and the controllers are identical to UT-Suntracker #1. The assembly, however, is located entirely on the roof of the PEARL Ridge Lab, with the controllers and input optics inside a box, and the suntracker and the dome on top of the box. The communication signal is sent to the motor controllers through an ethernet cable and a series of signal converters.

Active tracking for the PEARL-GBS was implemented in 2015 by Zhao (2017). For active tracking, a portion of the beam under the suntracker is redirected to a camera using pick-off mirrors. The PEARL-GBS setup uses a network camera (StarDot NetcamXL)

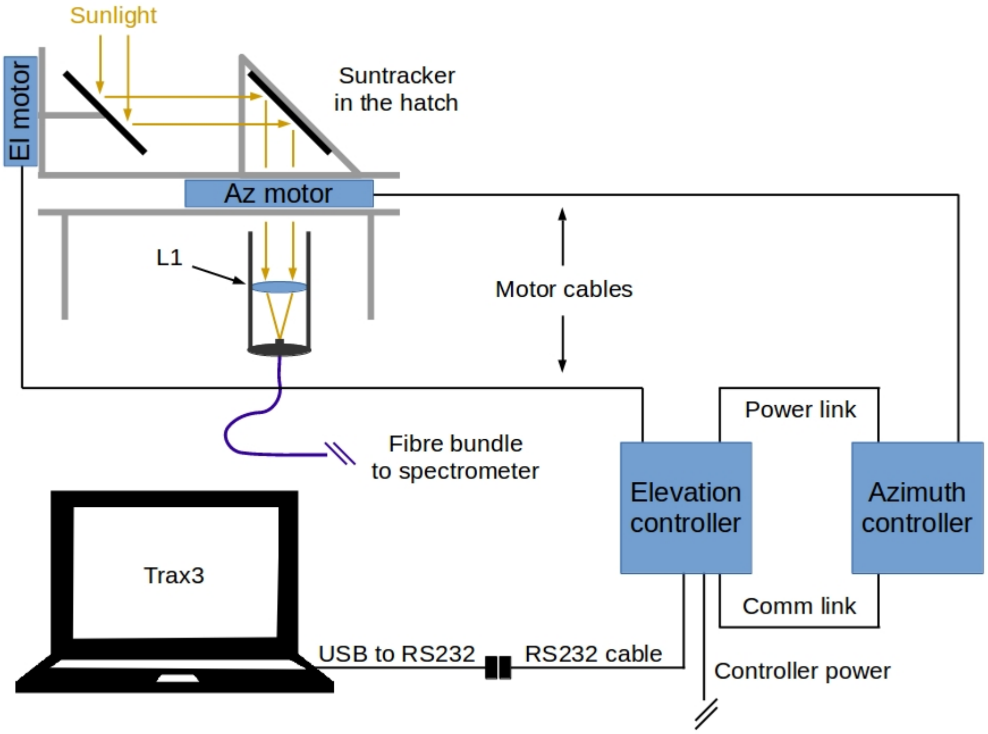

Figure 2.3: Schematic diagram of the UT-GBS suntracker setup (UT-Suntracker unit #1). Trax 3 is the laptop used to run the tracker software for the UT-GBS. The path of sunlight to the input optics is indicated by the yellow arrows, and the input optics (including lens L1) correspond to Figure 2.2a.

with a neutral density filter placed in front. The camera continuously takes images of the solar disk, and applies corrections to the tracker pointing (elevation and azimuth) to keep the sun centered in the camera field-of-view (FOV) (Franklin, 2015). No direct-sun measurements were performed in 2015 (failure of the filter wheel) and 2016 (failure of the camera). The camera was replaced and mounted on a new mount in 2017, but no direct-sun measurements were taken for several reasons. Active tracking requires a precise setup, since the tracker pointing is corrected to the position of the solar disk in the camera images. The setup of UT-Suntracker #2, however, is unstable. The tracker assembly experiences extreme temperature variations, leading to warping and distortion of the support structure to which the camera mount is attached. This would likely introduce pointing drifts and result in variable data quality, since precise pointing is essential for direct-sun measurements. In addition, the additional demand on the tracker motors and

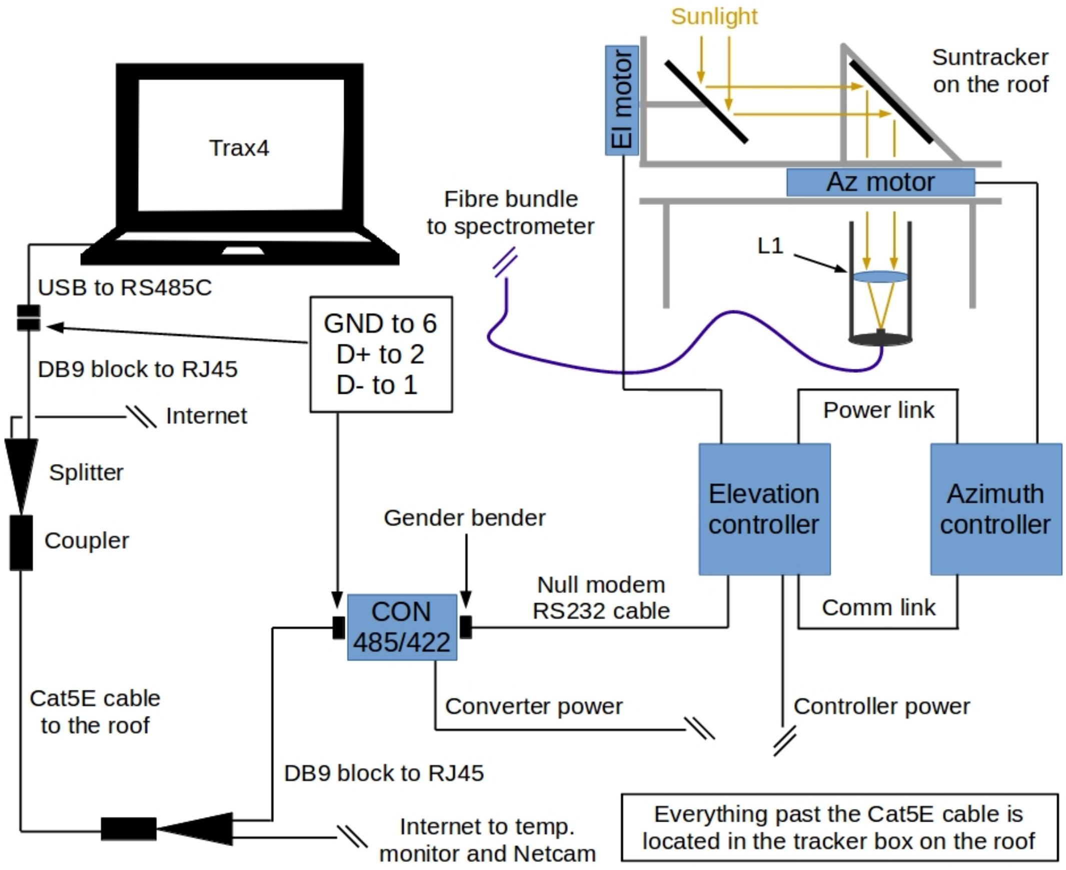

Figure 2.4: As Figure 2.3, for the PEARL-GBS suntracker setup (UT-Suntracker unit #2).

controllers would increase the likelihood of hardware failure, repair of which might present a significant challenge outside the spring campaign period. Given these limitations, and the fact that the PEARL-GBS suntracker was relocated specifically to improve MAX-DOAS viewing angles, it was decided that the PEARL-GBS should focus on zenith-sky and MAX-DOAS measurements only.

2.2 Measurement and Retrieval Methodology

2.2.1 Differential Optical Absorption Spectroscopy

DOAS is a well-established technique to study atmospheric composition using UV-vis spectrometers. Developed in the 1970s (Noxon, 1975; Perner and Platt, 1979; Platt et al., 1979), DOAS remains a popular technique for atmospheric measurements from both ground-based stations and from space. This section explains the DOAS technique, largely based on the description of Platt and Stutz (2008). The following sections then outline methods for extracting trace gas column or profile information from the DOAS results.

As solar radiation travels through the atmosphere, light is absorbed and scattered by atmospheric constituents. The scattering processes determine the path that light takes to a detector. Absorption of radiation depends on the amount of substance along the light path, and radiation in the atmosphere is attenuated according to the Beer-Lambert-Bouguer law (Perrin, 1948):

$$I(\lambda) = I_0(\lambda) \times \exp\big[-\sigma(\lambda)cL\big]. \tag{2.3}$$

Here, $I_0(\lambda)$ is the intensity of radiation at the source as a function of wavelength, and $I(\lambda)$ is the intensity that reaches the detector after travelling through a layer of thickness L. The absorber is present in the layer at a uniform concentration of c, and $\sigma(\lambda)$ is the wavelength-dependent absorption cross-section of the absorber. The term $\sigma(\lambda)cL$ represents the optical depth due to the absorber.

Equation 2.3 is appropriate for absorption ($\sigma(\lambda)$) that does not depend on variables along the light path (e.g., temperature and pressure). For such absorbers, $cL = u$, where u is the slant column density (SCD) of the absorber. In the atmosphere, multiple absorbers (trace gases) need to be considered, and detector effects have to be included as well. Equation 2.3 can then be written as

$$I(\lambda) = I_0(\lambda) \times A(\lambda) \times \exp\Big[-\sum_i \big(\sigma_i(\lambda)u_i\big) + \epsilon_R + \epsilon_M\Big], \tag{2.4}$$

where $\sigma_i(\lambda)$ and u_i are the absorption cross-section and SCD of the i^{th} trace gas, respectively, $A(\lambda)$ is the instrument function that represents wavelength-dependent instrument effects (e.g., grating and detector efficiencies), and ϵ_R and ϵ_M are the optical depths due to Rayleigh and Mie scattering, respectively.

Atmospheric measurements using ground-based absorption spectroscopy are difficult, since the true intensity ($I_0(\lambda)$) and the instrument function ($A(\lambda)$) are hard to determine. The DOAS approach avoids these problems by taking the ratio of two spectra, to cancel $I_0(\lambda)$ and the instrument function. In order to maximize the change in u_i, a spectrum with minimal SCD is selected as the reference spectrum (I_R). Taking the logarithm of the ratio of the measurement and the reference then gives

$$\ln\left(\frac{I(\lambda)}{I_R(\lambda)}\right) = -\sum_i \big(\sigma_i(\lambda)(u_i - u_{R,i})\big) + \Delta\epsilon_R + \Delta\epsilon_M. \tag{2.5}$$

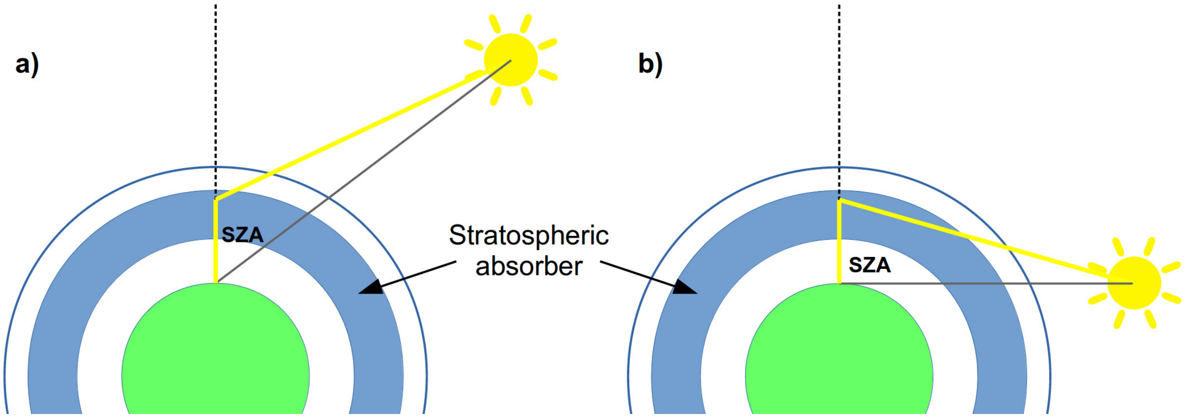

Figure 2.5: Zenith-sky viewing geometry for DOAS instruments at **a)** high sun and **b)** twilight. The stratospheric absorber is highlighted in blue.

In Equation 2.5, $u_i - u_{R,i}$ is the differential SCD (dSCD) of the i^{th} absorber, that is the amount of trace gas along the light path at the time of the measurement minus the amount in the reference spectrum. $\Delta\epsilon_R$ and $\Delta\epsilon_M$ are the differential optical depths due to Rayleigh and Mie scattering.

The key concept of DOAS is based on the fact that Rayleigh and Mie scattering vary slowly with wavelength, and the absorption cross-sections can also be separated into narrow $(\sigma_i'(\lambda))$ and broad $(\sigma_{0,i}(\lambda))$ features. The broad features represented by $\sigma_{0,i}(\lambda)$ vary slowly with wavelength, and can be grouped with the scattering terms. These slow-varying components can then be fitted with a low-order polynomial, and subtracted from Equation 2.5. The resulting equation,

$$\ln\left(\frac{I(\lambda)}{I_R(\lambda)}\right) - polynomial = -\sum_i \left(\sigma_i'(\lambda) \times dSCD_i\right), \tag{2.6}$$

then contains the rapidly varying components on the right-hand side (called the differential cross-section), and the left-hand side is called the differential optical depth. The dSCDs for each absorber can then be retrieved from Equation 2.6 using a combination laboratory-measured cross-sections of known absorbers.

The exact viewing geometry, and the selection of an appropriate reference spectrum, depend on the desired outcome. The simplest DOAS viewing geometry is zenith-scattered-light or ZSL-DOAS (Fig. 2.5), where the instrument is looking straight up at light scattered from the zenith. The path that light takes to the instrument is controlled by the SZA. This method is sensitive to trace gases in the stratosphere. Daily noontime spectra (taken at the smallest available SZA) are selected as references for Equation 2.5, and the

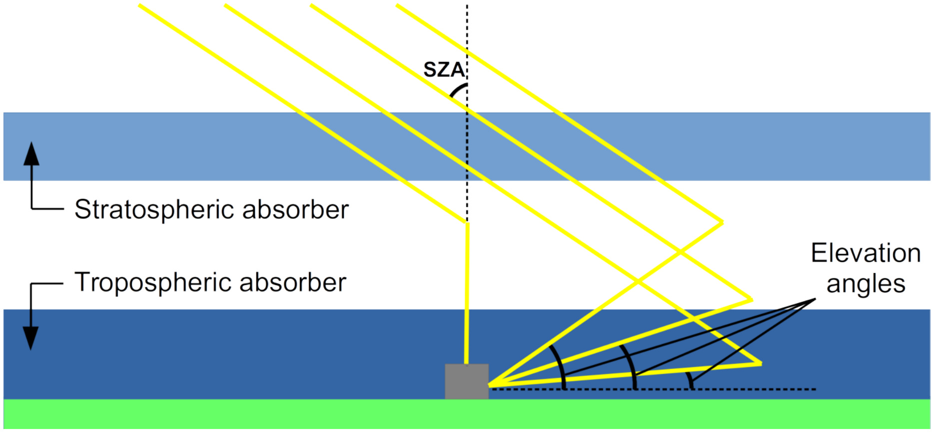

Figure 2.6: MAX-DOAS viewing geometry with simultaneous light paths for four elevation angles (including zenith-sky).

measurements of interest are twilight measurements. A high sun (small SZA) spectrum has the shortest stratospheric path length (Fig. 2.5a), while a twilight spectrum (large SZA) has the longest (Fig. 2.5b), maximizing the dSCD.

If tropospheric sensitivity is desirable, MAX-DOAS (Hönninger et al., 2004) is an ideal approach. Here, scattered light is measured as a function of the elevation angle (Fig. 2.6). As the elevation angle decreases, the tropospheric path length increases, giving rise to enhanced absorption by (and therefore increased sensitivity to) trace gases near the altitude of the instrument. Zenith-sky spectra from each elevation scan are used as the reference for the given scan. The stratospheric absorption is present in spectra at all elevation angles, and so it largely cancels in the dSCD retrieval. The temporal proximity of the spectra and the reference is essential for MAX-DOAS since both the stratospheric and tropospheric absorption change with the SZA.

2.2.2 dSCD Retrieval

For the GBS measurements, the dSCD retrieval is performed using QDOAS version 3.1 (Danckaert et al., 2017), a software package developed at the Belgian Institute for Space Aeronomy (BIRA-IASB). QDOAS uses a non-linear least squares fitting algorithm to separate the dSCDs of the individual absorbers. Alongside the trace gas cross-sections, a pseudo-cross-section is typically included to account for the Ring effect (Grainger and Ring, 1962). The Ring effect is the filling in of the lines of the solar spectrum during twilight due to rotational Raman scattering, and a correction can be calculated based on the rotational levels of the main components of the atmosphere (Chance and Spurr, 1997). The fit to the measured spectrum is typically performed in a restricted wavelength window, in order to maximize sensitivity to the trace gas of interest, and minimize interference from other species. The individual cross-sections are convolved to the resolution of the instrument, and a correction for the resulting I_0 effect is included (Aliwell et al., 2002). An offset might also be applied during the fit, to correct for stray light and dark current effects. Reference spectra are aligned by QDOAS to an atlas of solar lines (Kurucz, 1984). The shift and stretch of individual spectra with respect to the calibrated reference are fitted as well.

The fit parameters used in QDOAS for the ZSL-DOAS data products (ozone, NO_2-vis, and NO_2-UV) are shown in Table 2.3. Daily reference spectra were used in the dSCD retrieval. The fit settings for ozone and NO_2-vis (hereafter simply NO_2) follow the NDACC UV-vis WG recommendations, with the exception of the ozone fitting window. The right edge of the fitting window was changed from 550 nm to 545 nm for both GBSs in order to avoid irregularities near the CCD edge (see Adams, 2012). The NO_2 wavelength window is set to 425-490 nm. Cross-sections of ozone (Bogumil et al., 2003), NO_2 (Vandaele et al., 1998), O_4 (Greenblatt et al., 1990), and water vapour (Rothman et al., 2005) are included in the fits, alongside a Ring pseudo-cross-section (Chance and Spurr, 1997) and a 3rd order polynomial. The NO_2 fit includes 1st order offset correction, and no offset is fitted for ozone. The NO_2-UV retrievals follow the NO_2 settings as closely as possible, with the only differences being the fit window (350-380 nm for NO_2-UV), and the addition of BrO (Fleischmann et al., 2004) and OClO (Wahner et al., 1987) cross-sections in the fits.

In order to retrieve OClO and BrO dSCDs in the spring, the measured spectra are averaged to increase the SNR. Twilight spectra are averaged in 0.5° SZA bins, and the average of all spectra within 0.03° of the minimum daily SZA are used as a reference. The fit parameters used in QDOAS are the same as for NO_2-UV (shown in Table 2.3), with the exception of the fitting window for the BrO retrieval. The BrO fitting window was set to 345-359 nm (Zhao et al., 2016b). For the final data products, the OClO and BrO dSCDs are averaged between 89° and 91° SZA. As a result, these dSCDs are only retrieved in the spring, when 90° SZA is available (polar sunrise to mid-April). Detection limits for the OClO and BrO dSCDs were estimated as 3× the combined (in quadrature) mean DOAS fitting error and standard deviation of the 89-91° SZA dSCDs.

The ozone dSCD fits for both the UT-GBS and the PEARL-GBS measurements (when using the 600 gr mm^{-1} grating) were affected by systematic residuals prior to 2012 (see Appendix B of Adams, 2012). The 300 and 400 gr mm^{-1} UT-GBS measurements were not affected. In short, to correct for these residuals, the DOAS analysis was performed on noontime data on a clear day (summer 2007), with only a 3rd order polynomial.

Table 2.3: QDOAS fit parameters for the ZSL-DOAS measurements.

	Ozone	NO_2	NO_2-UV
Fitting window	450-545 nm	425-490 nm	350-380 nm
Cross-section			
Ozone	Bogumil et al. (2003) at 223 K	Bogumil et al. (2003) at 223 K	Bogumil et al. (2003) at 223 K
NO_2	Vandaele et al. (1998) at 220 K	Vandaele et al. (1998) at 220 K	Vandaele et al. (1998) at 220 K
O_4	Greenblatt et al. (1990) with corrected wavelengths	Greenblatt et al. (1990) with corrected wavelengths	Greenblatt et al. (1990) with corrected wavelengths
H_2O	HITRAN 2004 (Rothman et al., 2005)	HITRAN 2004 (Rothman et al., 2005)	–
BrO	–	–	Fleischmann et al. (2004) at 223 K
OClO	–	–	Wahner et al. (1987) at 203 K
Ring	Chance and Spurr (1997)	Chance and Spurr (1997)	Chance and Spurr (1997)
Systematic residuals	Adams (2012), see text	See text	–
Polynomial	3rd order	3rd order	3rd order
Offset correction	–	1st order	1st order
Shift and stretch	1st order	1st order	1st order

The residuals were then smoothed with a running average, and were included as cross-sections in the ozone dSCD fits. The magnitude of these "residual cross-sections" was much larger for the PEARL-GBS than for the UT-GBS. The PEARL-GBS dSCDs showed a correlation with the magnitude of the residuals, so the dSCD values were corrected with the slope of this correlation (Adams, 2012). No such correction was necessary for the UT-GBS data. The systematic residuals have been effectively eliminated for the UT-GBS after changes to the input optics in 2012. The residual cross sections were nevertheless included in the dSCD fits for the entire time series, to ensure consistency. The PEARL-GBS only took measurements with the 600 gr mm^{-1} grating for 2006-2010, and the residual cross-section was included for the full time series. In addition to the ozone retrievals, systematic residuals were noticed in the 600 gr mm^{-1} NO_2 fits for the

Table 2.4: QDOAS fit parameters for the MAX-DOAS measurements.

Fitting window	BrO: 337-361.9 nm O_4: 335-367 nm
Cross-section	
BrO	Fleischmann et al. (2004) at 223 K
O_4	Hermans et al. (2003)
Ozone	Bogumil et al. (2003) at 223 K
Ozone (orthogonal)	Bogumil et al. (2003) at 243 K
NO_2	Vandaele et al. (1998) at 220 K
OClO	Wahner et al. (1987) at 204 K
Ring	Chance and Spurr (1997)
Polynomial	4^{th} order
Offset correction	1^{st} order
Shift and stretch	1^{st} order

PEARL-GBS. To generate a residual cross-section, measurements from 1 July 2007 were analyzed using the methods outlined above. The residual cross-sections were included for the full time series of 600 gr mm^{-1} PEARL-GBS measurements. The NO_2 dSCDs showed no correlation with the magnitude of the residual cross-section, and so no correction was implemented.

In the UV lab, light from the overhead fluorescent lamps might find its way into the GBS input optics through reflections. Residual structures matching fluorescent lamp spectra have been found in the dSCD fits of both the UT-GBS and PEARL-GBS spectra (600 gr mm^{-1} only) when they were coupled to UT-Suntracker #1 in the UV lab. This extra signal (called "lamp signal") consists of broad emission across the entire visible wavelength range, with a narrow peak at 436 nm, and broad peaks at ~490 nm and ~545 nm. Systematic residuals due to the lamp signal are generally only discernible when signal levels are already low (SZA > 92°), and therefore do not interfere with the dSCD fits. On some days, however, the lamp signal is stronger, and leads to systematic residuals at lower SZA. This issue was of particular concern in spring 2017, when a large square diffuser was placed on top of the UT-GBS input optics. The edges of the diffuser extended past the diameter of the cover around the UT-GBS input optics, likely enhancing scattering of light from below onto the focusing lens. To correct for these systematic residuals, partial cross-sections for each feature were constructed from a nighttime (SZA > 100°) spectrum in spring 2017. Individual cross-sections were necessary as the relative intensity of the features was highly variable. The broad component of the lamp signal was not explicitly corrected for, as features that vary slowly with wavelength are removed using a polynomial as part of the DOAS fit. For the PEARL-GBS data, separate cross-sections were created from high-SZA measurements in September 2007. The partial cross-sections were included for all springtime UT-GBS fits for 2017 (both ozone and NO_2). In other years (2015-2020 for the UT-GBS, 2006-2010 for the PEARL-GBS), the cross sections were only included on individual days when the lamp signal was present in the residuals for SZA $< 92°$ (i.e. when the lights were left on in the UV lab).

The parameters for the MAX-DOAS products (BrO and O_4) are shown in Table 2.4. The zenith-sky measurements immediately before and after the current scan were interpolated to the time of each measurement, and used as a reference for the dSCD retrieval. The fitting windows (337-361.9 nm for BrO, 335-367 nm for O_4) were selected based on Appendix A of Zhao (2017). The same cross-sections of BrO (Fleischmann et al., 2004), O_4 (Hermans et al., 2003), ozone at 223 and 243 K (Bogumil et al., 2003), NO_2 (Vandaele et al., 1998), and OClO (Wahner et al., 1987) were included for both fitting windows.

2.2.3 Vertical Column Densities

From ZSL-DOAS measurements, the vertical column density (VCD) of a trace gas can be determined. The SCD is related to the VCD by the air mass factor (AMF) such that VCD = SCD/AMF. The AMF represents the optical path enhancement along the slant path. The dSCD (Eqn. 2.5) of a trace gas is defined as $\mathrm{SCD}-\mathrm{SCD_R}$, where $\mathrm{SCD_R}$ is the reference column density (RCD), the amount of trace gas in the reference spectrum. Combining these relationships gives the following expression:

$$\mathrm{VCD(SZA)} = \frac{\mathrm{dSCD(SZA)} + \mathrm{RCD}}{\mathrm{AMF(SZA)}} \tag{2.7}$$

where all quantities (save the RCD) are necessarily the functions of the solar zenith angle.

In order to solve for the VCD, the RCD needs to be determined first. To obtain the RCD, we can rearrange Equation 2.7 to give

$$\mathrm{dSCD(SZA)} = \mathrm{AMF(SZA)} \times \mathrm{VCD(SZA)} - \mathrm{RCD}. \tag{2.8}$$

We can then apply the so-called Langley plot method: the dSCDs are plotted against the AMFs. In the Langley plot, the slope represents the VCD, and the y-intercept is the RCD. A more accurate estimate of the RCD, however, can be obtained by calculating the average of the RCDs from the two twilights each day, since the same daily reference spectrum is used for both twilights. VCDs as a function of SZA can then be obtained by substituting the averaged RCD into Equation 2.7. The final VCD value is calculated as the average of VCD(SZA) over a limited SZA range around SZA = 90°.

The AMFs used in the GBS retrievals are provided by the NDACC UV-vis WG in the form of look-up tables (LUTs)[2]. The AMFs were calculated using the UVSPEC/DISORT radiative transfer model (RTM) (Mayer and Kylling, 2005). The ozone AMFs (see Hendrick et al., 2011) are based on the Total Ozone Mapping Spectrometer (TOMS) version 8 ozone and temperature profile climatology (Bhartia et al., 2004) in the 0-60 km altitude range, and on the AFGL standard atmosphere above 60 km. The NO_2 AMFs were generated using the harmonic stratospheric NO_2 profile climatology of Lambert et al. (1999, 2000) between 20 and 60 km, and SAOZ balloon observations between 12 and 17 km. As a result, the NO_2 AMFs represent 12-60 km, and the resulting VCDs are in fact stratospheric partial columns. The ozone and NO_2 AMFs are provided in 10° latitude bands, as a function of SZA, wavelength, surface albedo, station altitude, and day of the year. The surface albedo climatology of Koelemeijer et al. (2003) is used to obtain realistic albedo values. VCDs are not retrieved from the OClO and BrO dSCDs.

To calculate the final VCD value, VCD results from the GBS measurements are averaged over the 86-91° SZA range. The average is weighted using the dSCD fitting error divided by the AMF. The daily SZA coverage in Eureka is highly dependent on the season, due to the latitude of the measurement site. As Eureka emerges from the polar night, only high SZA are available, and so VCDs near the start of the measurement period are calculated using an extended SZA range (up to 92°). Conversely, in the summer, twilight measurements are not available. To extend the measurements into the polar day, the highest available 5° SZA range is used for the VCD retrievals. The wavelengths used for the AMF LUTs are the approximate centres of the fitting windows for each trace gas: 505 nm for ozone, 457 nm for NO_2, and 365 nm for NO_2-UV. The ozone LUTs require ozone column as input to interpolate the AMFs accurately. For this purpose, the GBS ozone retrievals use Eureka ozonesonde total columns, interpolated to the time of the measurements.

The uncertainties of the final VCD values are calculated following Adams (2012), as shown in Table 2.5. The total error calculations are unchanged, with the exception of the multiplication factor for the AMF uncertainty for ozone. The number (0.04 in Adams, 2012) has been updated (to 0.0364) to match the original source (Hendrick et al., 2011). In addition, the distribution of uncertainties as random or systematic was updated based

---

[2] `http://ndacc-uvvis-wg.aeronomie.be/tools.php`

Table 2.5: The budget of systematic and random uncertainties for the ZSL-DOAS ozone and NO_2 VCDs. Each uncertainty source is estimated for a given twilight by multiplying the relevant parameter from the DOAS retrieval by the listed multiplication factors. After Table 4.8 of Adams (2012), with the uncertainties grouped following Table 4 of Hendrick et al. (2011).

Source of uncertainty	Multiply by	Multiplication factor	
		Ozone	NO_2
Systematic uncertainty			
Absolute cross-section	SCD	0.031	0.05
Cross-section T-dependence	SCD	–	0.08
RCD baseline uncertainty	–	10^{17} molec cm^{-2}	2×10^{15} molec cm^{-2}
RCD variation	$\lvert RCD_{am} - RCD_{pm}\rvert$	0.5	0.5
Systematic residual	residual dSCD	10^{17} molec cm^{-2}	–
Random uncertainty			
Instrument uncertainty	SCD	0.01	0.01
Line filling by Raman scat.	SCD	0.01	0.05
QDOAS fitting errors	dSCD error	3	3
AMF uncertainty	AMF	0.0364	0.05
VCD variation*	–	–	–

* The 1-sigma standard deviation of VCD(SZA) over the given twilight was added to the random uncertainty in quadrature.

on Table 4 of Hendrick et al. (2011).

In order to remove low-quality data, both the dSCDs and the VCDs are filtered. The dSCDs are filtered according to the root-mean-square (RMS) of the residuals. For ozone and NO_2, RMS thresholds of 0.002 for SZA $< 90°$ and 0.003 for SZA $> 90°$ are applied. For NO_2-UV, the RMS threshold is 0.002 for SZA $< 87°$ and 0.003 for SZA $> 87°$ (Adams, 2012). The results of the VCD retrieval are filtered according to the parameters listed in Table 2.6. To ensure fit quality in the Langley plots, VCDs are only accepted if there are at least eight measurements in the selected SZA range, and the range itself spans at least 2°. Langley fits with R^2 less than 0.9 for ozone and 0.6 for NO_2 were also filtered out.

In addition, NO_2 measurements were only accepted if both morning and evening twilights were available, in order to avoid biased RCD values caused by the diurnal variation of NO_2 in the spring. For ozone, when one twilight was missing, the RCD variation (and therefore the systematic uncertainty) could not be calculated. In those cases, when the other twilight passed all other error filters, the systematic error was interpolated from the nearest two valid measurements.

Table 2.6: VCD filters used in the GBS retrievals. The NO_2 and NO_2-UV filters are identical.

Parameter	Ozone filter	NO_2 filter
Total uncertainty	<60 DU	$<2\times10^{15}$ molec cm^{-2} or <200%
Langley plot R^2	≥0.9 (0.8 for 2003-4)	≥0.6
Data points in Langley plot	≥8	≥8
Min. accepted SZA range	2°	2°

2.2.4 Tropospheric Profiles

Like ZSL-DOAS measurements, MAX-DOAS data can be converted to vertical information. As the viewing elevation angle decreases, the mean scattering height decreases, and the pathlengths in the surface layer (or the layer the instrument is located in) increase (Fig. 2.6). Scattering in the troposphere, however, is complex, and cannot be simplified to a single-scattering problem as in the case of ZSL-DOAS. Especially for small elevation angles, multiple-scattering calculations are necessary to accurately characterize the path sunlight takes to the instrument. Furthermore, the presence of aerosols and larger airborne particles (e.g., blowing snow) in the surface layers can significantly alter tropospheric light paths. Therefore, to covert MAX-DOAS dSCDs to vertical profiles, detailed RTM simulations are necessary.

There are two main approaches to MAX-DOAS profile retrievals. The first family of algorithms retrieve profiles on a full vertical grid (usually 50-200 m layer thickness) using the optimal estimation method (OEM) (Rodgers, 2000) and online RTM calculations. The second method uses a small number of parameters (usually two to four) to describe the profile shape. These so-called parametric algorithms can use pre-calculated LUTs, and are much faster than OEM algorithms. OEM methods, on the other hand, provide better error analysis, and characterize the vertical resolution and information content of the profile. OEM results are strongly influenced by the choice of a priori information, whereas parametric approaches are less dependent on prior knowledge of the atmospheric state. A detailed overview and comparison of the most popular MAX-DOAS profiling algorithms is given in Frieß et al. (2019) and Tirpitz et al. (2021).

The aim of any remote sensing retrieval is to estimate the atmospheric state ($\boldsymbol{x}$, number density profiles in this thesis) from the measurement vector ($\boldsymbol{y}$, dSCDs). The two are related by the forward model (F, typically a RTM), which represents the underlying physics of the measurement:

$$\boldsymbol{y} = F(\boldsymbol{x}, \boldsymbol{b}) + \boldsymbol{\epsilon}. \tag{2.9}$$

Here, $\boldsymbol{b}$ represents additional model parameters (e.g., temperature and pressure) which are not retrieved, and $\boldsymbol{\epsilon}$ is the measurement error. OEM algorithms use a Bayesian approach, and introduce the a priori state vector ($\boldsymbol{x}_a$) and its corresponding covariance matrix ($\mathbf{S}_a$) (Rodgers, 2000). The vector $\boldsymbol{x}_a$ represents the best knowledge of the atmospheric state before the measurements were made. The maximum a posteriori (MAP) estimate ($\hat{\boldsymbol{x}}$) can then be obtained by minimizing the following cost function:

$$\chi^2 = [\boldsymbol{y} - F(\boldsymbol{x}, \boldsymbol{b})]^T \, \mathbf{S}_\epsilon^{-1} \, [\boldsymbol{y} - F(\boldsymbol{x}, \boldsymbol{b})] + (\boldsymbol{x} - \boldsymbol{x}_a)^T \, \mathbf{S}_a^{-1} \, (\boldsymbol{x} - \boldsymbol{x}_a), \tag{2.10}$$

where $\mathbf{S}_\epsilon$ is the measurement covariance matrix, and the forward model is assumed to be exact. Equation 2.10 evaluates the agreement between the measured and modeled dSCDs, taking into account uncertainties of both the measurements and the a priori information.

The sensitivity of the retrieved state ($\hat{\boldsymbol{x}}$) to the true atmospheric state ($\boldsymbol{x}$) is quantified by the averaging kernel matrix, $\mathbf{A} = \partial\hat{\boldsymbol{x}}/\partial\boldsymbol{x}$. Each row of the averaging kernel represents the sensitivity of the retrieved number densities in that layer to the values in all other layers. Neglecting the retrieval error, the retrieved profile can be expressed with the averaging kernel as

$$\hat{\boldsymbol{x}} = \mathbf{A}\boldsymbol{x} + (\mathbf{I} - \mathbf{A})\boldsymbol{x}_a. \tag{2.11}$$

In the ideal case, $\mathbf{A}$ is an identity matrix ($\mathbf{I}$), and the retrieved state corresponds exactly to $\boldsymbol{x}$. In practice, the rows of $\mathbf{A}$ are peaked functions, with half-widths that are a measure of the vertical resolution of the retrieval (Rodgers, 2000). $\mathbf{A}$ then smoothes the true profile, and $\hat{\boldsymbol{x}}$ tends to be biased towards the a priori, especially in altitude regions where sensitivity to the true atmospheric state is low. The trace of the averaging kernel gives the degrees of freedom for signal (DOFS), which represents the number of independent pieces of information obtained in the retrieval.

The method for minimizing the cost function (Eqn. 2.10) depends on the linearity of the problem (Rodgers, 2000). For linear (or near-linear and therefore linearizeable) problems, Equation 2.9 can be expressed as

$$\boldsymbol{y} = \mathbf{K}\boldsymbol{x} + \boldsymbol{\epsilon}, \tag{2.12}$$

where $\mathbf{K} = \partial F(\boldsymbol{x}, \boldsymbol{b})/\partial\boldsymbol{x}$ is the weighting function or Jacobian matrix. In this case, the minimum of the cost function can be calculated analytically, and so $\hat{\boldsymbol{x}}$ has an exact solution. For moderately non-linear problems, $\mathbf{K}$ depends on the atmospheric state, and so an iterative approach is necessary to minimize the cost function. Retrieval algorithms generally use the Gauss-Newton method or the Levenberg-Marquardt algorithm to find the zero of the gradient of the cost function. The need to recalculate $\mathbf{K}$ for each iteration is in part responsible for the time-consuming nature of OEM retrieval algorithms.

In OEM methods, a priori information is necessary since the atmospheric state vector is poorly constrained by the measurements. Parametric retrievals avoid this problem by representing the atmospheric state with just a few parameters, such that $\boldsymbol{x} = \boldsymbol{x}(\boldsymbol{p})$. Instead of a full altitude grid, the parameters might describe the total column, the profile shape, and the layer thickness, for example. The cost function for parametric retrievals might then be written as

$$\chi^2 = [\boldsymbol{y} - F(\boldsymbol{x}(\boldsymbol{p}), \boldsymbol{b})]^T \, \mathbf{S}_\epsilon^{-1} \, [\boldsymbol{y} - F(\boldsymbol{x}(\boldsymbol{p}), \boldsymbol{b})]. \tag{2.13}$$

Parametric algorithms do not require an a priori trace gas profile, but prior information about the atmosphere (i.e., some components of $\boldsymbol{b}$) is still required. The small number of parameters enables the use of pre-calculated LUTs (instead of online RTM calculations), significantly increasing the speed of the retrieval process. On the other hand, the forward model can be highly non-linear in the parameters, and so ensemble methods are often better suited to minimize the cost function (e.g., Beirle et al., 2019).

Regardless of the retrieval method, MAX-DOAS retrievals of trace gases generally use a two-step approach (suggested by Sinreich et al., 2005). First, the aerosol extinction profiles and corresponding aerosol optical depths (AODs) are retrieved from O_4 dSCDs. Since O_4 has a well-known and nearly constant vertical profile, changes in the O_4 dSCDs can be used to derive information on the atmospheric aerosol profile (Wagner et al., 2004; Frieß et al., 2006). In the second step, the retrieved extinction profiles are used as a forward model parameter for the trace gas profile retrieval.

The OEM algorithm used here is the University of Heidelberg remote sensing group profile retrieval code (HeiPro) (Frieß et al., 2011; Yilmaz, 2012). HeiPro uses the MAP method based on the Levenberg-Marquardt algorithm. The RTM SCIATRAN (version 2.2) (Rozanov et al., 2005) serves as the forward model. HeiPro is used in Chapters 3 and 7 for tropospheric aerosol and NO_2 retrievals, and in Chapter 6 for tropospheric aerosol and BrO retrievals. Details about the parameters and a priori conditions used for each study are provided in the relevant chapters.

The parametric retrieval algorithm used here is the Mainz profile algorithm (MAPA) (Beirle et al., 2019). MAPA uses three parameters to describe the vertical profile: the integrated column, the layer height, and a shape parameter. Parameters are determined using a Monte Carlo (MC) approach, where the parameter space is covered by random numbers, and the parameters that best match the measurements are selected. This method improves the limited error characterization of parametric approaches (compared to OEM) by providing distributions instead of single matches for each parameter. Pre-calculated LUTs from the RTM McArtim (Deutschmann et al., 2011) serve as the forward model. The LUT nodes include a list of elevation angles, SZA, and relative azimuth angles, as well as a range of values for each parameter. MAPA is used for tropospheric aerosol and NO_2 retrievals in Chapter 7, and more details about the retrieval setup can be found there.

Chapter 3

Field Campaigns

This chapter describes the measurement history of the UT-GBS and the PEARL-GBS. Both instruments have participated in several field campaigns in the Arctic and elsewhere, and the locations and measurement dates for each of these campaigns are summarized in Table 3.1. The UT-GBS was assembled in 1998 as a travelling instrument, and its first measurements were taken during the MANTRA campaign in Vanscoy, Saskatchewan, in August of the same year. The instrument participated in the three following MANTRA campaigns as well (in 2000, 2002, and 2004). Starting in 1999, the UT-GBS was deployed at Eureka each spring, first as an independent instrument, then as part of the Stratospheric indicators of Climate Change campaigns (the 2002 edition of which was held in Resolute Bay, Nunavut), and since 2004, as part of the Canadian Arctic ACE/OSIRIS Validation Campaigns. In 2009, the UT-GBS participated in the CINDI campaign in Cabauw, Netherlands, as described in detail by Adams (2012). In between campaigns, the instrument took measurements at the University of Toronto Atmospheric Observatory (TAO). Since the CINDI campaign, the UT-GBS has been installed at Eureka, taking measurements during the sunlit part of the year. The PEARL-GBS was installed as a permanent instrument in the PEARL Ridge Lab in 2006. The Eureka measurements of both instruments are discussed in Section 3.1. In 2016, the PEARL-GBS participated in the CINDI-2 campaign in Cabauw, Netherlands, as described in detail in Section 3.2.

3.1 Eureka Campaigns and GBS Reprocessing

Since 2004, springtime measurements in Eureka are coordinated as part of the Canadian Arctic ACE/OSIRIS Validation Campaigns (Kerzenmacher et al., 2005). These campaigns are sponsored by the Canadian Space Agency, and aim to validate measurements from the ACE instruments on board the Canadian SCISAT-1 satellite, and the OSIRIS

Table 3.1: Measurement history of the GBS instruments, updated from Zhao (2017).

Campaign	Location	UT-GBS	PEARL-GBS
MANTRA	Vanscoy, Saskatchewan (52°N, 107°W)	19-26 Aug 1998[a,b,c]	–
		18-26 Aug 2000[d]	
		20 Aug - 3 Sept 2002[d]	
		3 Aug - 15 Sept 2004[e,f,g]	
Stratospheric indicators of Climate Change	Resolute Bay, Nunavut (75°N, 95°W)	15 Mar - 15 Apr 2002	–
Stratospheric indicators of Climate Change (spring 2001, 2003), Canadian Arctic ACE/OSIRIS Validation Campaigns (2004 to present), and CANDAC/PAHA (year-round, 2006 to present)	Eureka, Nunavut (80°N, 86°W)	22 Mar - 11 Apr 1999[h,i,j,u]	
		24 Feb - 29 Mar 2000[d,j,u]	
		(28 Feb - 23 Mar 2001[d])	
		1-17 Mar 2003[d,j,k,s,u]	
		24 Feb - 13 Apr 2004[e,j,k,l,m,s,u]	
		25 Feb - 30 Mar 2005[e,j,k,m,s,u]	
		23 Feb - 31 Mar 2006[e,j,k,m,s,u]	17 Aug - 17 Oct 2006[e,j,n,s]
		23 Feb - 12 May 2007[e,j,k,n,s,u]	23 Feb - 18 Oct 2007[e,j,k,n,s,u]
		27 Feb - 16 Oct 2008[j,k,s,u]	23 Feb - 17 Oct 2008[j,k,o,s,u]
		23 Feb - 31 Mar 2009[j,k,s,u]	7 Mar - 18 Oct 2009[j,k,s,u]
		28 Feb - 17 Oct 2010[j,k,r,s,u]	13 Apr - 13 Oct 2010[j,k,s,u]
		23 Feb - 18 Oct 2011[j,k,p,r,s,u]	16 Mar - 3 Apr 2011[j,k,p,q,s,u]
		23 Feb - 11 May 2012[r,s,u]	3 Mar - 22 Apr 2012[s,u]
		1 Mar - 17 Oct 2013[r,s,u]	25 Feb - 10 Oct 2013[s,u]
		4 Mar - 18 Oct 2014[r,s,u]	23 Feb - 13 Oct 2014[s,u]
		25 Feb - 18 Oct 2015[r,s,u]	2 Mar - 10 Oct 2015[s,u]
		23 Feb - 17 Oct 2016[r,s,u]	6 Mar - 8 May 2016[s,t,u]
		22 Feb - 17 Oct 2017[r,s,u]	4 Mar - 17 Oct 2017[s,t,u]
		24 Feb - 18 Oct 2018[u]	28 Feb - 17 Oct 2018[t,u]
		23 Feb - 18 Oct 2019[u]	26 Feb - 15 Oct 2019[t,u]
		23 Feb - 17 Oct 2020[u]	6 Mar - 26 Sept 2020[u]
Toronto Atmospheric Observatory	Toronto, Ontario (44°N, 79°W)	19 Dec 2001 - 11 Feb 2002	
		12 Dec 2002 - 3 Feb 2003	
		29 Jul - 28 Aug 2003	
		7 Jan - 3 Feb 2004	
		2 May - 14 Dec 2005	
		18 Apr - 31 Dec 2006[e]	
		27 Jun - 25 Dec 2007	
		8 Jan - 14 Jan 2008	
		10 Dec 2013 - 10 Jan 2014	16 Dec 2016 - 13 Jan 2017
CINDI/NDACC Certification	Cabauw, Netherlands (52°N, 56°E)	13 Jun - 17 Jul 2009[1,2,3]	–
CINDI-2	Cabauw, Netherlands (52°N, 56°E)	–	31 Aug - 29 Sept 2016[4,5,6]

[a]Bassford et al. (2001) [b]Bassford et al. (2005) [c]Melo et al. (2005)
[d]Farahani (2006) [e]Fraser (2008) [f]Fraser et al. (2007a) [g]Fraser et al. (2007b)
[h]Bassford et al. (2000) [i]Melo et al. (2004) [j]Adams et al. (2012b) [k]Adams et al. (2012a)
[l]Kerzenmacher et al. (2005) [m]Fraser et al. (2008) [n]Fraser et al. (2009) [o]Adams et al. (2010)
[p]Adams et al. (2013) [q]Zhao et al. (2016b) [r]Zhao et al. (2019a) [s]Bognar et al. (2019)
[t]Bognar et al. (2020b) [u]Bognar et al. (2020a) [1]Roscoe et al. (2010) [2]Piters et al. (2012)
[3]Pinardi et al. (2013) [4]Kreher et al. (2020) [5]Donner et al. (2020) [6]Tirpitz et al. (2021)

instrument on the Swedish Odin satellite. The intensive phase of the campaigns typically takes place from late February to mid-March, with pre-campaign and extended phases providing coverage from mid-February into April. The UT-GBS and the PEARL-GBS participate every spring, and the instruments typically continue measurements throughout the sunlit part of the year.

The measurement dates in Eureka for both the UT-GBS and the PEARL-GBS are listed in Table 3.1. These dates reflect the periods for which useful VCD results could be obtained. The instruments typically start collecting spectra before the listed start dates (from 10-15 February), and measurements continue past the end dates (until 20-25 October for year-round measurements). These measurements, however, are not useful for VCD retrievals due to the high SZA values that cover less than 2° of the desired 86-91° SZA range. Measurement dates for the other locations in Table 3.1 follow the references listed, and are unchanged from Adams (2012) and Zhao (2017).

The measurement modes and gratings used by the UT-GBS and PEARL-GBS for Eureka measurements are shown in Tables 3.2 and 3.3, respectively. Each individual measurement is comprised of the average of 2-300 spectra, depending on light conditions. The exposure time (5-13 ms to 30 s) is determined before each measurement to optimize the signal level, and the maximum exposure time for one measurement is set to 100 s. Both instruments perform only ZSL-DOAS measurements during twilight. Below SZAs of 84° for the UT-GBS and 86° for the PEARL-GBS, the instruments currently perform MAX-DOAS measurements. Zenith measurements are part of each MAX-DOAS scan, but their frequency is reduced given the list of other elevation angles in the sequence. The UT-GBS uses elevation angles of 5°, 8°, 10°, 15°, 30°, and 90° in each MAX-DOAS scan. The PEARL-GBS sequence varied over the years, depending on the location of the suntracker. For 2010, elevation angles of 1°, 2°, 4°, 10°, 15°, 30°, and 90° were used. For 2011-2014, the elevation angles were as for the current UT-GBS sequence (with the smallest elevation angle changed to 6° in 2011). Since the installation of UT-Suntracker unit #2 in October 2014, the PEARL-GBS uses elevation angles of -1°, 0°, 1°, 2°, 5°, 10°, 15°, 30°, and 90° (with the 2° angle missing in 2015).

The VCD time series (ozone, NO_2 and NO_2-UV) for both instruments was reprocessed for this thesis, using the dSCD and VCD retrieval settings described in Chapter 2. The main change compared to the previous reprocessing (Adams, 2012) was the use of the updated NDACC UV-vis WG recommendations for NO_2, with the expanded 425-490 nm fitting window (instead of 425-450 nm) and the updated NO_2 AMF LUTs. The distribution of the VCD uncertainties was also changed, as described in Chapter 2. The dSCD retrievals were performed in a newer version of QDOAS, with an improved wavelength

Table 3.2: Summary of UT-GBS springtime measurements at Eureka.

Year	Grating (gr mm^{-1})	Spectral quality	Processing issues
Zenith sky measurements only			
1999	400	Fair, mechanical slit (MS) 0.1 mm	Extended RMS filter used
2000	600, 1800	Good, MS 0.1 mm	1800 gr mm^{-1} data not used
2001	600	Poor: slit jammed open (4-5 nm resolution) MS $>$ 0.2 mm	Data not used
2003	400, 600	Fair: acquisition software error (reduced signal) MS 0.1 mm	Two spectra averaged prior to analysis, extended RMS filter used
2004	400	Fair: acquisition software error (reduced signal) MS 0.1 mm	Two spectra averaged prior to analysis, extended RMS filter used
2005	600	Good, MS 0.1 mm	–
2006	600	Good, MS 0.1 mm	–
2007	600	Good, MS 0.1 mm	–
2008	600, 1800	Good, MS 0.1 mm	–
2009	600, 1800	Good, MS 0.1 mm	–
2010	600, 1800	Poor: slit jammed open (slightly reduced signal and resolution) MS 0.1 mm	–
2011	600	Good, with improved resolution, MS 0.1 mm	–
2012	600	Good, F# matcher and MS removed, fixed slit (FS) 0.1 mm	Summer/fall data not used
2013	600	Good, FS 0.1 mm	–
2014	600	Good, FS 0.1 mm	–
Zenith sky and MAX-DOAS			
2015	600	Good, FS 0.1 mm	Summer data not used, lamp signal present
2016	600	Good, FS 0.1 mm	Summer data not used, lamp signal present
2017	600	Good, FS 0.1 mm	Strong lamp signal present
2018	600	Good, FS 0.1 mm	Lamp signal present
2019	600	Good, FS 0.1 mm	Lamp signal present
2020	600	Good, FS 0.1 mm	Lamp signal present

Table 3.3: Summary of PEARL-GBS springtime measurements at Eureka.

Year	Grating (gr mm^{-1})	Spectral quality	Processing issues
Zenith sky measurements only			
2006	600	Good, fixed slit (FS) 0.05 mm	–
2007	600, 1200	Good, FS 0.05 mm	Five spectra averaged for UV, lamp signal present
Zenith sky and direct sun			
2008	600, 1200	Good, FS 0.05 mm	Five spectra averaged for UV, lamp signal present
2009	600, 1200	Good, FS 0.05 mm	–
Zenith sky, direct sun, and MAX-DOAS			
2010	600, 1200	Good, with improved resolution, FS 0.05 mm	Five spectra averaged for UV MAX-DOAS in spring/summer only
2011	1200	Good, FS 0.1 mm	–
Zenith sky and MAX-DOAS			
2012	1200	Good, FS 0.1 mm	Summer/fall data not used
2013	1200	Good, FS 0.1 mm	Summer data not used
2014	1200	Good, FS 0.1 mm	MAX-DOAS in spring/summer only
2015	1200	Good, FS 0.1 mm	–
2016	1200	Good, FS 0.1 mm	–
2017	1200	Good, FS 0.1 mm	MAX-DOAS in March only
2018	1200	Good, FS 0.1 mm	–
2019	1200	Good, FS 0.1 mm	–
2020	1200	Good, FS 0.1 mm	–

calibration algorithm and an updated input format. In addition to the reprocessing, a rapid delivery (RD) VCD retrieval was also implemented, in order to improve the availability of GBS data. The RD VCDs differ from the consolidated product only in the case of ozone, since ozonesonde columns (used as input for the AMF LUTs) are not available in time for rapid delivery. The RD ozone retrieval uses a two-step approach, where AMF LUT inputs are fixed at 300 DU in the first step, and the VCDs from the first step are used as AMF LUT inputs for the final VCDs.

All VCDs were converted to HDF files compliant with the Generic Earth Observation Metadata Standard, as recommended by NDACC. Each HDF file contains the VCDs and the corresponding random and systematic uncertainties, as well as partial columns and

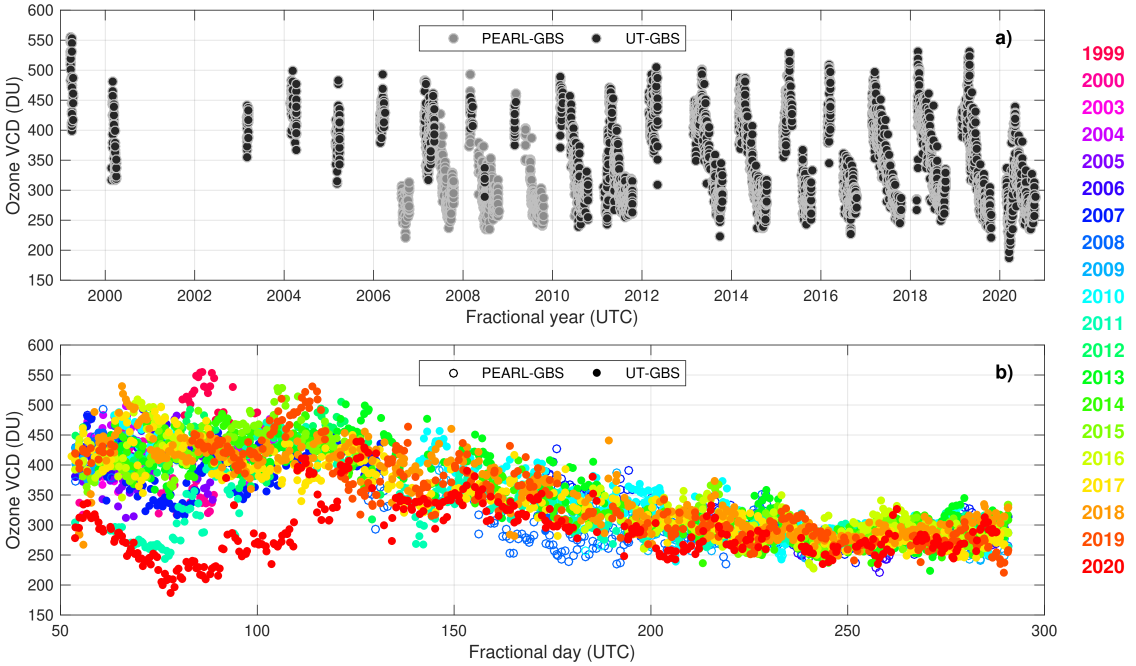

Figure 3.1: **a)** Time series and **b)** year-to-year variability of ozone VCDs (corresponding to individual twilights) from the UT-GBS and the PEARL-GBS.

averaging kernels retrieved from LUTs developed at BIRA-IASB. The files also contain ancillary profiles from radiosondes and ozonesondes, when those data are available. The set of yearly HDF files was submitted to NDACC as version 3 data, replacing the partial version 1 archive (Zhao, 2017). Version 1 contained a coding error where the lower confidence bound of the RCD was used in the VCD calculations, instead of the actual RCD value given by the Langley plots. Version 3 was assigned to the now consolidated data in order to distinguish from the RD product, which is marked as version 2. RD data (processed within 30 days of the measurement dates) are submitted through NDACC to the Copernicus Atmosphere Monitoring Service (CAMS).

Notable data processing or data quality issues for each year of Eureka measurements are shown in Tables 3.2 and 3.3 for the UT-GBS and PEARL-GBS, respectively. Dates of useful measurements for each year are indicated in Table 3.1. Notes in Tables 3.2 and 3.3 indicate if the actual measurement period (for ZSL-DOAS and/or MAX-DOAS) was significantly different from the dates of useful measurements.

The UT-GBS data quality was not ideal in 1999, and so the dSCDs were filtered using an extended RMS filter of 0.004 for SZA $< 90°$ and 0.006 for SZA $> 90°$ (Adams, 2012), double the standard RMS limits described in Chapter 2. The same extended filter was necessary in 2003 and 2004, since due to a software error, only one spectrum was

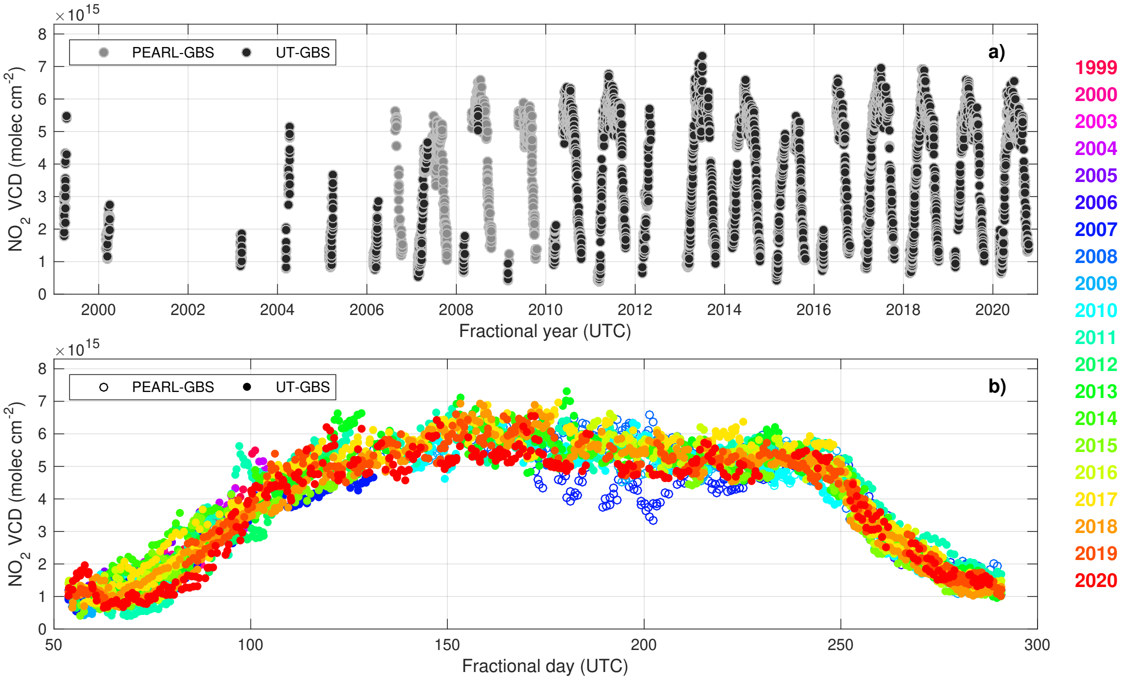

Figure 3.2: Same as Figure 3.1, for NO_2 VCDs.

included in the average for each measurement (Fraser et al., 2007a). For 2003 and 2004, pairs of spectra were averaged before the dSCD retrieval. For the aforementioned three years, both the 400 and 600 gr mm^{-1} gratings were used, and data from the two gratings was treated as a single dataset for the VCD retrieval. For 2000, data quality using the 600 gr mm^{-1} grating was good, and data from the 1800 gr mm^{-1} grating was not used. In 2001, the mechanical slit jammed open, leading to significantly reduced resolution (Adams, 2012). 2001 data were therefore excluded from the UT-GBS dataset. There were no data quality issues for 2005-2009 and 2011. In 2010, the mechanical slit jammed open again, but the resolution did not degrade drastically, and no corrective action was required for the retrievals. The UT-GBS collected UV spectra during most of 2008 and 2009, and during part of spring 2010. For part of 2012, there was no operator coverage at PEARL. In the summer, the UT-GBS CCD experienced severe overheating issues that compromised data coverage and quality. As a result, measurements past day 133 in 2012 were excluded from the UT-GBS dataset.

Starting from 2013, the UT-GBS CCD gain settings were adjusted in the summer in order to reduce signal levels and avoid saturation. The available gain settings are 1.7× (default), 2.0×, 4.0×, 6.7×, 13.3×, and 26.7×, in order of decreasing sensitivity. The settings are related to the number of electrons required for the CCD to register one count, and the 1.7× setting corresponds to one electron per count. The 4.0× gain setting does not significantly impact data quality, while noise levels increase for the 6.7× gain setting, and the 13.3× gain setting compromises data quality. The 4.0× gain setting was used in 2013 (days 138-279), 2014 (days 128-294), 2015 (days 64-127), 2016 (past day 183), 2017 (past day 145), 2018 (days 129-227), 2019 (past day 83), and 2020 (past day 71). The 13.3× gain setting was used for days 128-211 in 2015 and for days 83-182 in 2016, and these dates were excluded from the VCD dataset. The 6.7× gain setting was used past day 212 in 2015. The lamp signal (discussed in Chapter 2) was present at varying intensities in springtime spectra since 2015, as noted in Table 3.2.

The PEARL-GBS started measurements using the 600 gr mm^{-1} grating in 2006 (Table 3.3). Visible measurements were made in the second half of each year for 2007-2010, with no data quality issues. Since 2011, the PEARL-GBS takes UV measurements using the 1200 gr mm^{-1} grating. For the twilight UV measurements, five spectra were averaged prior to analysis in 2007, 2008, and 2010, in order to improve the SNR. As for the UT-GBS, measurements in the summer of 2012 were sparse and of low quality, and these data (past day 114) were excluded from the PEARL-GBS dataset. The PEARL-GBS CCD has three gain settings, 'high sensitivity' (default), 'best dynamic range', and 'high light'. The 'best dynamic range' setting adjusts the CCD gain based on exposure, and is not suitable for DOAS applications. This setting was used for part of 2013, and the measurements (days 110-205) were excluded from the data analysis. There were no significant data quality issues in 2014-2020. Occasional malfunctions of UT-Suntracker unit #2 (Chapter 2) mean that the MAX-DOAS time series does not necessarily cover the same period as the ZSL-DOAS measurements, as indicated in Table 3.3.

The top panels in figures 3.1 and 3.2 show the ozone and NO_2 VCD time series from both the UT-GBS and the PEARL-GBS. The combined dataset spans 22 years, and contains 20 years' of measurements, mostly from the UT-GBS. The bottom panels in each figure show the year-to-year variability of ozone and NO_2. Ozone columns generally show a springtime maximum, with decreasing values throughout the sunlit part of the year. Significant scatter is observed during the spring, due to variability introduced by the polar vortex. NO_2 columns are typically small in the spring and fall, and reach their maxima in the summer. Apart from springtime variability, the NO_2 VCDs show large scatter in the summer, mainly due to noise introduced by the small AMF variation between noon and high-SZA measurements (which results in small dSCDs) during the polar day. Figure 3.3 shows the time series and year-to-year variability of the NO_2-UV measurements (mostly PEARL-GBS data). NO_2-UV closely follows the NO_2 time series. More of the data is filtered during the summer months, due to the higher noise levels in

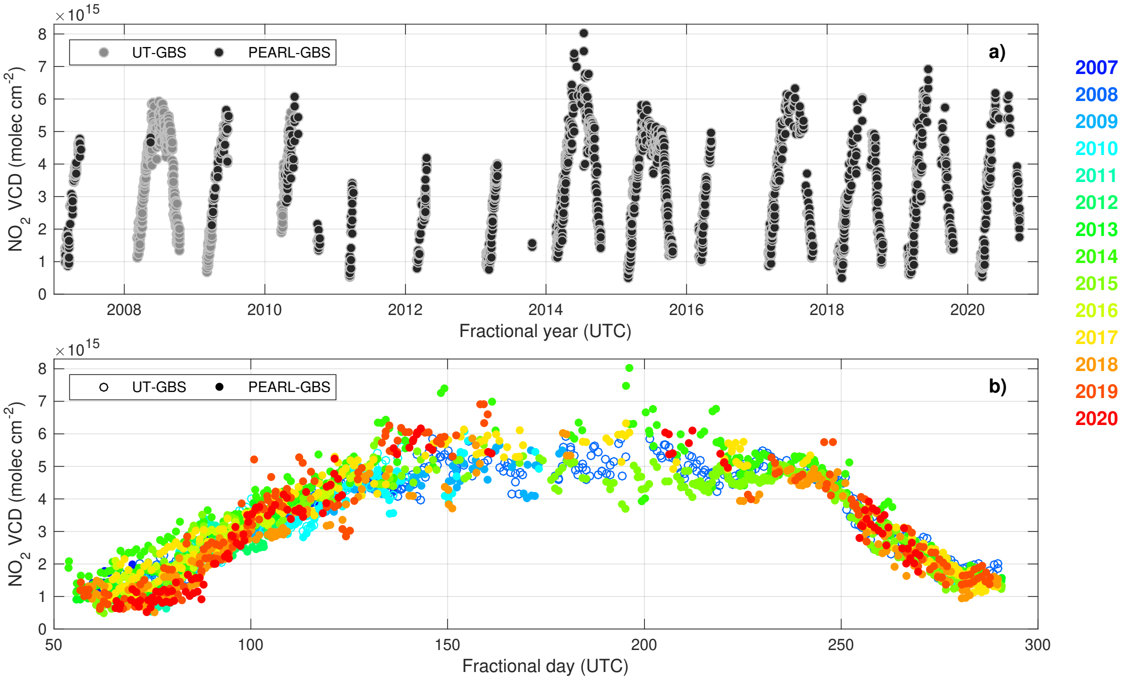

Figure 3.3: Same as Figure 3.1, for NO_2-UV VCDs.

the UV measurements.

Since the UT-GBS and the PEARL-GBS are similar instruments with complementary data coverage, the reprocessed VCD datasets have been merged to create unified ozone, NO_2, and NO_2-UV time series (similar to Adams, 2012). All three datasets agree within 2%, although there is only limited overlap between the two instruments. Twilight data were averaged when both instruments had measurements. These merged datasets (referred to as the GBS dataset for the visible products and as the GBS-UV dataset for NO_2-UV) were used to validate ozone and NO_2 measurements from satellite instruments (Chapter 4), and to assess the exceptional stratospheric ozone depletion in spring 2020 (Chapter 5).

3.2 CINDI-2 Campaign (2016)

The CINDI-2 campaign, organized by the Royal Netherlands Meteorological Institute (KNMI), took place in Cabauw, Netherlands, from 25 August to 7 October, 2016[1], and

---

[1] The site opened for instrument setup and testing on 25 August, the main campaign period covered 12-28 September, and measurements were optionally extended to 7 October.

the PEARL-GBS participated[2]. CINDI-2 followed the first CINDI campaign held in 2009 (Roscoe et al., 2010), in which the UT-GBS took part (Adams, 2012). The general goal of CINDI-2 was to intercompare the new generation of ground-based remote-sensing and in situ air quality instruments, while implementing lessons learned during CINDI. Specifically, the campaign sought to support the creation of high-quality ground-based datasets for use in trend analysis and satellite data validation (Kreher et al., 2020). Results from CINDI-2 were used to initialize the Fiducial Reference Measurements for Ground-Based DOAS Air-Quality Observations (FRM4DOAS) network of MAX-DOAS instruments. The validation aspect is especially important for new and upcoming UV-vis satellite instruments, including the Copernicus Sentinel 5 Precursor satellite (launched in October 2017) and the future Copernicus Sentinel 4 and 5 missions. In the following, the general description of the campaign is based on Hendrick et al. (2016) and Kreher et al. (2020). Details about the PEARL-GBS participation are also included in Zhao (2017).

CINDI-2 was held at the Cabauw Experimental Site for Atmospheric Research (CESAR; 52°N, 5°E; 0.7 m below sea level). CESAR is a rural site with few local pollution sources, but several large cities (Utrecht, Rotterdam, The Hague, and Amsterdam) are located within 60 km. As a result, the site regularly experiences pollution episodes. The supporting instrumentation at the CESAR facility include the 200 m meteorological tower, a Raman lidar, ceilometers, and sun photometers. For the campaign, additional measurements were made by in situ NO_2, ozone and aerosol instruments, as well as NO_2 and ozone sondes and a NO_2 lidar. The interpretation of the results was aided by mobile instruments (DOAS and in situ) that collected measurements in the vicinity of the main campaign site (Hendrick et al., 2016). A total of 36 DOAS instruments participated in the campaign, performing mainly ZSL-DOAS, MAX-DOAS, and direct-sun measurements. The list of instruments included a long-path DOAS (LP-DOAS) system, an imaging DOAS instrument, and a Cavity-Enhanced DOAS instrument. The layout of the measurement site, with the location of the main instruments, is shown in Figure 3.4a.

The participating instruments were categorized by their pointing capabilities as one-dimensional (1D) and two-dimensional (2D) MAX-DOAS instruments. The 1D instruments were mounted on top of a row of containers to allow unobstructed line-of-sight along the main azimuth viewing angle of 287°, and 2D instruments were mounted on a second level of containers to enable full azimuthal scans. Most 2D instruments, including the PEARL-GBS, performed a combination of MAX-DOAS scans and direct-sun measurements, according to the campaign data acquisition protocol (Hendrick et al., 2016). In

---

[2] The PEARL-GBS was assembled and tested on site during 1-7 September, and the instrument was disassembled on 29 September.

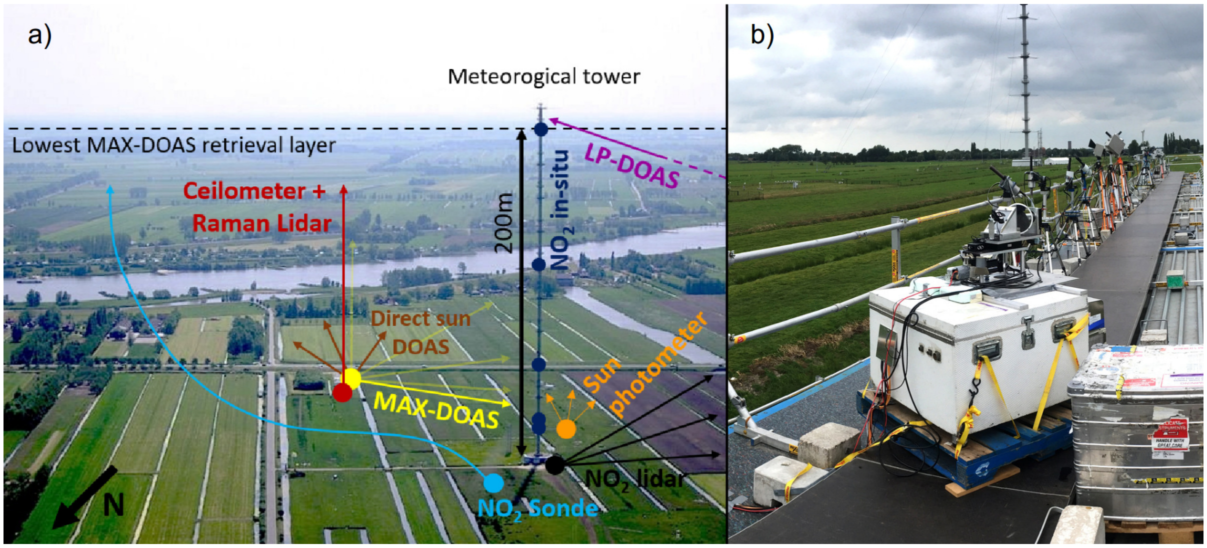

Figure 3.4: **a)** Placement and viewing directions of the instruments at the CESAR, and **b)** a closeup of the MAX-DOAS instruments, with the PEARL-GBS in the foreground. Panel **a)** adapted from Tirpitz et al. (2021).

each hour from 6:00 UTC to 16:45 UTC, the 2D instruments performed one full elevation scan of nine elevation angles at the reference azimuth of 287°, and then a full azimuthal scan (at azimuth angles of 355°, 45°, 95°, 135°, 195°, and 245°) with four elevation angles for each azimuth. Almucantar scans and direct-sun measurements were each performed twice during the one-hour measurement blocks. Additional zenith-sky measurements and a horizon scan were integrated into the measurement sequence at noon, and zenith-sky measurements were taken before 6:00 UTC and after 16:45 UTC. The data acquisition protocol specified start times and total integration times for each individual measurement, in order to ensure that the same air masses would be measured by all instruments with good synchronization. Table 3.4 shows the main target species for the intercomparison. The main species of interest were NO_2, O_4 (and aerosols), ozone, and formaldehyde (HCHO). Measurements were performed in both the UV and visible wavelength ranges, as listed in Table 3.4.

In Eureka, PEARL-GBS is installed indoors as a lab instrument (as opposed to a field instrument). To prepare for outdoor deployment during the CINDI-2 campaign, GBS cooling unit #1 (weatherproof; previously used for the MANTRA campaigns) was refurbished and fitted with a new air conditioner (Chapter 2). The aluminum box includes a UV-transparent window, and a UT-Suntracker was mounted directly above the window to allow multiple viewing geometries during the campaign. The spectrometer and input optics (as shown in Figure 2.2b), as well as the camera for active tracking and the suntracker motor controllers, were installed inside the aluminum box. In order to protect the UT-Suntracker from the elements, a plexiglass cover was constructed to cover the suntracker during the night (or on rainy days). The cover was removed each day for the scheduled MAX-DOAS and direct-sun measurements. A 90° FOV web camera was mounted on the suntracker to capture images of sky conditions. The final setup of the PEARL-GBS (inside GBS cooling unit #1 with the suntracker mounted on top) is shown in Figure 3.4b.

The PEARL-GBS took measurements in the visible wavelength range (using the 600 gr mm^{-1} grating) for the entire campaign. While the grating turret would allow alternating UV and visible measurements, the turret positions are not exactly repeatable. Alternating turrets, therefore, would have introduced significant variability in the wavelength calibration of the measured spectra. The PEARL-GBS measurements were frequently saturated during the testing phase, in part due to the high core count of the fibre bundle used. To reduce signal levels, a diffuser was placed on top of the input optics, and the 1% transmission neutral density filter was used for all ZSL-DOAS and MAX-DOAS measurements throughout the entire campaign. The filter for direct sun measurements was selected automatically based on signal level.

The 2D MAX-DOAS acquisition sequence and its implementation for the PEARL-GBS are described in detail by Zhao (2017). In general, the PEARL-GBS measurements accurately followed the prescribed sequence, with only slight adjustments. For direct-sun measurements, two acquisitions were performed instead of one, with the first one as a test measurement to select the optimal neutral density filter for the second measurement. For the almucantar scans, only 11 of the 15 azimuth angles were included in order to fit the scan into the required 5 minute window. In terms of the timing of the measurements, the PEARL-GBS performed well, and followed the acquisition schedule with an error margin of a few seconds (Fig. 2b of Kreher et al., 2020).

The following sections describe the elevation calibration of the instruments (including the PEARL-GBS), as well as the performance of the PEARL-GBS in both the slant column and profile intercomparisons.

3.2.1 Elevation Calibration

Participating instruments employed a variety of elevation calibration methods during CINDI-2, as described in detail by Donner et al. (2020). This section summarizes the results from Donner et al. (2020) that use PEARL-GBS measurements. In addition to the synchronization and colocation of the measurements, pointing accuracy is a key issue for MAX-DOAS comparisons and retrievals, given the sensitivity of MAX-DOAS to trace

Table 3.4: Data products included in the CINDI-2 semi-blind intercomparison (Kreher et al., 2020). The PEARL-GBS measured in the visible range only.

Data product	Wavelength range (nm)
NO_2*	425-490
NO_2-small*	411-445
NO_2-UV	338-370
O_4*	425-490
O_4-UV	338-370
HCHO	336.5-359
O_3*	450-520
O_3-UV	320-340

*Measured by the PEARL-GBS.

gases near the instrument altitude. As an example, for elevation angles near 0°, a pointing error of 1° might lead to a change of more than 20% in the retrieved NO_2 dSCDs (Donner et al., 2020). During CINDI-2, individual groups used near-lamp measurements, white stripe scans, or solar measurements to establish the pointing accuracy of instruments. Calibration methods, however, vary significantly from instrument to instrument. The PEARL-GBS suntracker is usually calibrated by levelling the tracker base and the input optics using a precision bubble level. The optical axis is assumed to be perfectly aligned with the hardware components.

In order to consistently calibrate a large number of instruments in the field, an optional far-lamp calibration exercise was performed on the nights of 8, 10, 13, and 19 September (Donner et al., 2020). A xenon lamp was placed along the main MAX-DOAS azimuth angle of 287° at a distance of around 1280 m from the measurement site. Participating instruments then performed high-resolution elevation scans aimed at the light source, and pointing offsets between instruments were identified based on the differences in the apparent position of the light source in the scans. Donner et al. (2020) calculated the expected elevation of the xenon lamp to be -0.19° for the 2D MAX-DOAS instruments on the upper row of containers. To derive the lamp elevation from the measurements, intensities at 365, 405, 436 and 546 nm were examined as a function of elevation angle.

The PEARL-GBS performed full 2D scans of the light source on 10 September, at a 0.05° vertical resolution (elevation angles) and a 0.5° horizontal resolution (azimuth angles). An example of the results is shown in Figure 3.5a, alongside data from the three other instruments that performed similar scans. The smoothness of the intensity distributions is variable across the instruments, which can largely be explained by the different fibre configurations of the instruments. Smoother results are obtained with spot fibre entrances (as for the PEARL-GBS), and sharper intensity changes result from ring fibre configurations. While apparent positions vary, the sizes of the lamp images are similar for all four instruments. To accurately determine the lamp elevation, Donner et al. (2020) used two methods. First, intensities along a single azimuth (black dotted lines in Fig. 3.5a) were fitted with a Gaussian function. The results, along with the centres of the Gaussians, are shown in Figure 3.5b. For the second approach, intensities for each elevation angle were integrated across all azimuth angles, and the results were fitted with a Gaussian, as shown in Figure 3.5c. The two methods return similar values for the individual instruments, but the spread between instruments is significant, as discussed below.

Other instruments that participated in the calibration exercise either performed cross-scans (one azimuth and one elevation scan) or simple 1D scans of the xenon lamp. The mean lamp elevation angles from all instruments (Fig. 14 of Donner et al., 2020) show a spread of 0.9°, with the values centered around the expected elevation. Some of the spread in the results is due to the different height of the instruments. For example, some instruments were mounted on tall tripods, while the PEARL-GBS suntracker was mounted lower, on the cooling unit (Fig. 3.4b). Nevertheless, most of the spread is due to the different elevation calibrations of the instruments. The PEARL-GBS measured a mean lamp elevation of -0.3° (close to the expected value of -0.19°), with good consistency across multiple lamp measurements on 10 and 19 September[3].

While the lamp measurements are a good measure of pointing accuracy for individual nights, they are less useful for monitoring the stability of the instruments. In addition, only 12 of the 36 instruments participated in the xenon lamp exercise. To address these concerns, horizon scans were integrated into the campaign data acquisitions sequence for the MAX-DOAS instruments. Unlike methods that require an active light source, horizon scans can be performed during daytime, and one scan was recorded by each instrument near noon. The horizon scans measured the change of intensity when scanning from -5° to 5° (steps of 0.2° from -2° to 2°, 1° otherwise) along the main azimuth angle of 287°. The position of the horizon can be calculated by fitting an error function (Gaussian integral) of the form

$$S = A\left[\operatorname{erf}\left(\frac{x - x_0}{B}\right) + 1\right] + C(x - x_0) + D \tag{3.1}$$

to the measured intensities as a function of elevation angle x (Donner et al., 2020; Kreher et al., 2020). In Equation 3.1, A, B, C, and D are fitting parameters, and x_0 is the centre

---

[3] Based on initial results from 10 September, a correction factor of -0.2° was applied in the suntracker software for the main campaign phase. The 10 September lamp scan elevations were corrected by this value to reflect the actual elevation angles measured during the main campaign phase.

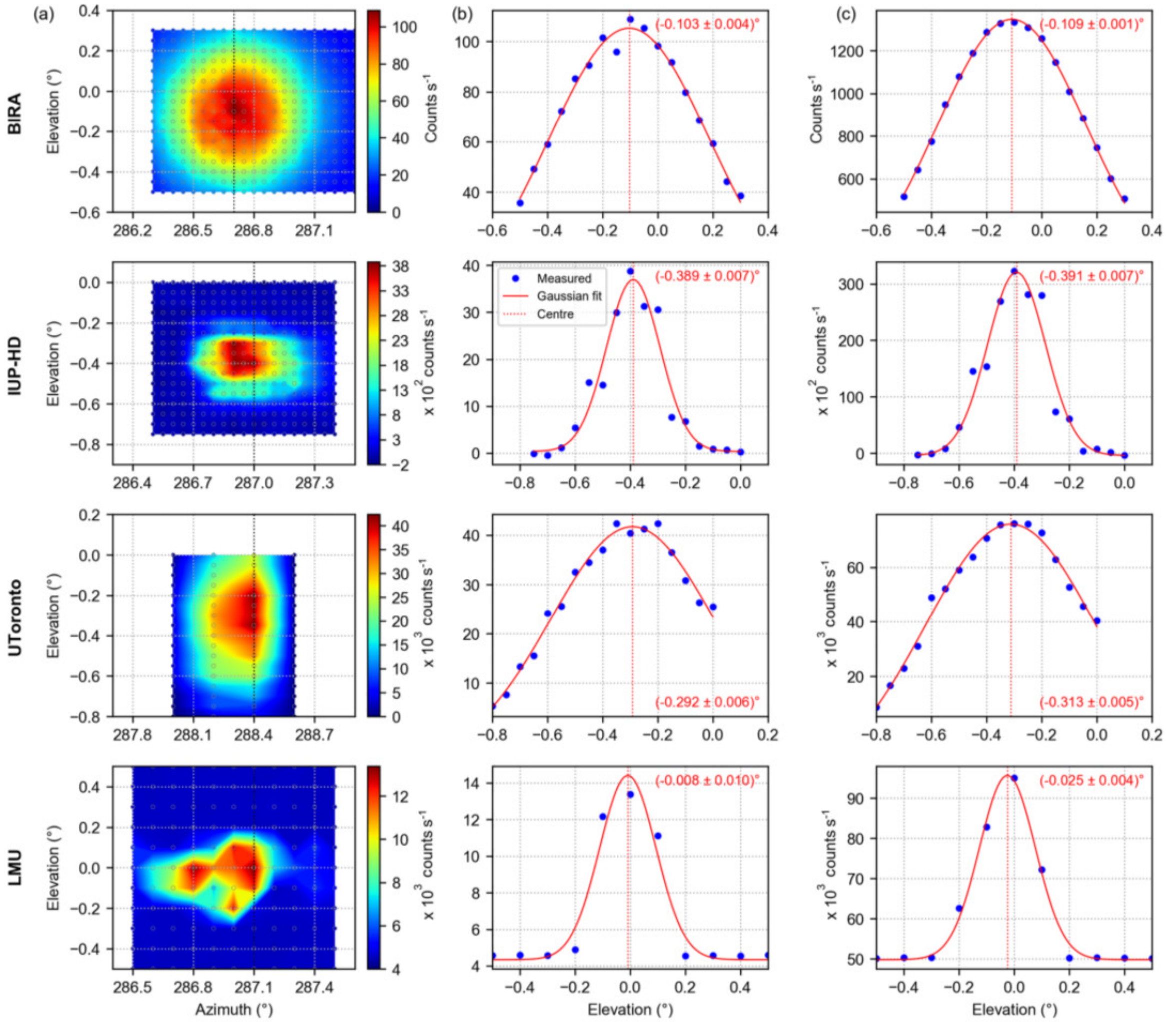

Figure 3.5: **a)** 2D intensity distributions of the xenon lamp measured by the PEARL-GBS (labelled ‘UToronto’) and other participating instruments. Panels **b)** and **c)** show transects along the dashed lines in **a)** and the azimuthal sum of the intensities at each elevation, respectively. Gaussian fits and their centres are indicated as well. Reproduced from Figure 11 of Donner et al. (2020).

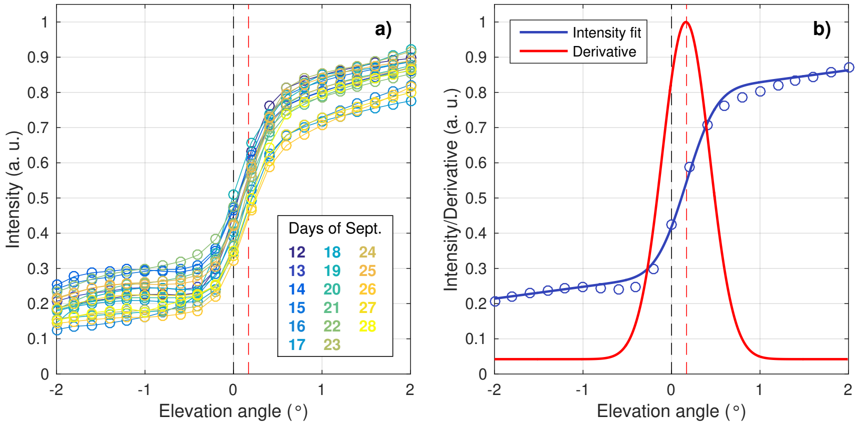

Figure 3.6: **a)** Noontime horizon scans from the PEARL-GBS during the main CINDI-2 campaign phase (12-28 September). The intensities were calculated for 440±1 nm, and each curve was normalized to their corresponding maximum. **b)** Example of the error function fit for 13 September. The numerical derivative of the fit function is also shown. The red dashed line in each figure indicates the expected horizon elevation of 0.17°.

of the curve. The value of x_0 then indicates the elevation of the horizon. The expected position of the horizon was assumed to be the at the transition of tree tops to the open sky for CINDI-2. While the apparent position of the horizon might vary as a function of cloud cover or the presence of fog, scans on clear days with high visibility provide a good measure of the pointing accuracy and pointing stability of the instruments.

Figure 3.6a shows the daily horizon scans performed by the PEARL-GBS for 12-28 September. The normalized intensity (at 440±1 nm) is variable, but the transition from low intensity (ground/trees) to high intensity (sky) is clear and consistent. An example of the horizon elevation fit using Equation 3.1 is shown in Figure 3.6b. The centre of the curve (the horizon elevation) is illustrated by the derivative of the fit function. The derivative can also be used to estimate the FOV of the instruments. Using the full width at half maximum of the derivative, the mean (median) PEARL-GBS FOV was estimated to be 0.70° (0.65°). The mean (median) horizon elevation across the 12-28 September period was 0.19° (0.19°). This is in very good agreement with the horizon elevation of 0.17° calculated for the 2D MAX-DOAS instruments by Donner et al. (2020). The PEARL-GBS pointing was consistent throughout the campaign, as shown in Figure 17 of Donner et al. (2020), and Figure 5 of Kreher et al. (2020). This is in agreement with the consistent lamp elevations measured during the far-lamp exercises on 10 and 19 September. Figure 3.7 highlights the good performance of the PEARL-GBS relative to the other instruments that performed horizon scans. The median horizon elevation for the

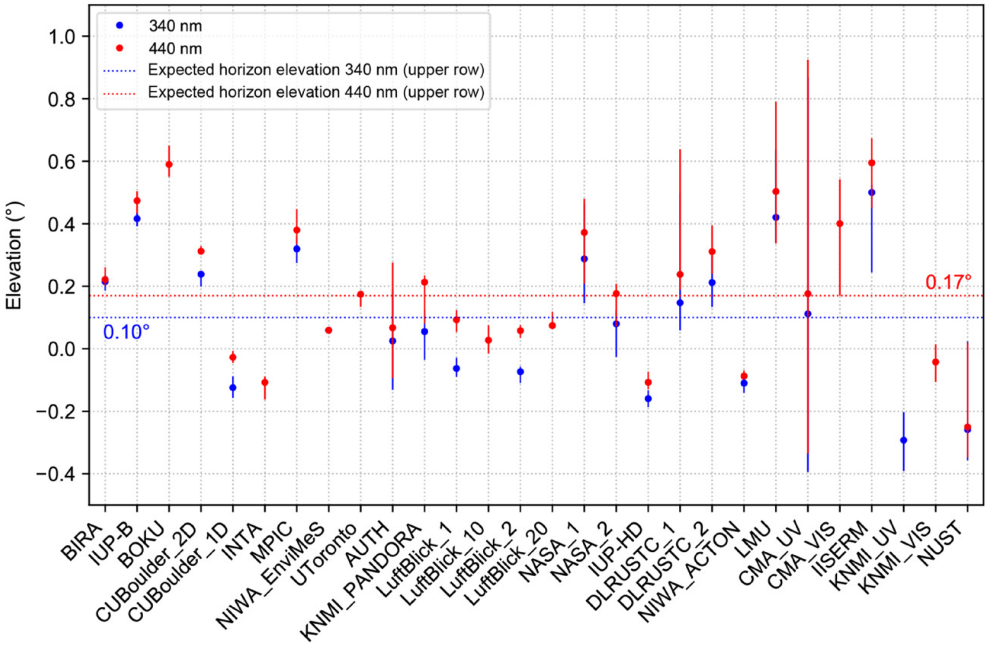

Figure 3.7: Median horizon elevations for all CINDI-2 instruments that performed horizon scans. The lines show the 25th and 75th percentiles. The 'UToronto' label corresponds to the PEARL-GBS. The expected elevation of the horizon varies with wavelength, likely due to a surface albedo effect. Reproduced from Figure 15 of Donner et al. (2020).

PEARL-GBS was among the closest to the expected value, and the variability (indicated by the horizontal lines) was minimal. The scatter among the instruments is around 0.9, in agreement with the results from the xenon lamp measurements (for a smaller set of instruments).

Donner et al. (2020) found that the measured lamp elevations and the results of the horizon scans are in good agreement. The offset between the two elevations was around 0.2 to 0.6° across all the instruments, and 0.49° for the PEARL-GBS. The expected offset is 0.36°, which is in agreement with the PEARL-GBS value, given that Donner et al. (2020) estimated an uncertainty of ±0.05° for the far-lamp measurements and ±0.25° for the horizon scans. The uncertainty is higher for the horizon elevations since the visible horizon (treetops for CINDI-2) is variable, and the exact elevation depends on the azimuth viewing angles of the instruments. Overall, the discrepancy between the elevation calibration of individual instruments (0.9°) was larger than the estimated uncertainties in the calibration methods. Pointing differences close to a degree can significantly impact low elevation angle measurements. This result indicates that regardless of the good synchronization of measurements during CINDI-2, dSCD comparisons might still show significant differences purely due to discrepancies in measurement geometry.

3.2.2 Slant Column Intercomparisons

The formal CINDI-2 semi-blind intercomparison exercise took place from 12 to 28 September. The results of the intercomparison are presented by Kreher et al. (2020), and are summarized here with a focus on the PEARL-GBS. For each data product listed in Table 3.4, the retrieval settings and parameters were specified according to Appendix A of Kreher et al. (2020). Daily reference spectra (the mean of zenith-sky measurements between 11:30:00 and 11:41:00 UTC) were used to retrieve both the ZSL-DOAS and MAX-DOAS dSCDs. Since the choice of processing software was not specified, the PEARL-GBS data analysis was performed using the usual software and methods described in Chapter 2. The PEARL-GBS measured in the visible range during CINDI-2, and so the retrieved products were NO_2, O_4, NO_2 in the small wavelength range (NO_2-small), and ozone. The dSCDs for each day were processed and submitted by the morning of the next day, and the anonymized results were shown and discussed during the daily meetings in the afternoon. The final data products used in the intercomparison paper were submitted approximately three weeks after the end of CINDI-2.

The weather during the semi-blind phase was exceptionally favorable for comparisons given the location and the season. The first four days (12-15 Sept.) were mainly sunny with high temperatures (>30 °C). The following week (16-22 Sept.) was mainly cloudy, and the last six days (23-28 Sept.) were characterized by clear skies and occasional broken clouds. While fog occurred occasionally in the mornings, there was only a single day (25 Sept.) when rain fell during the measurement period. MAX-DOAS NO_2 and O_4 dSCDs were highly variable during the campaign, while ozone dSCDs were dominated by stratospheric ozone, as expected (Kreher et al., 2020). The PEARL-GBS data coverage was nearly complete during the campaign, with data missing only on the afternoons of 25 and 26 September (rain and CCD connectivity issues, respectively).

To evaluate the agreement between the different instruments, all dSCDs were compared to a reference dataset, constructed from the median of selected instruments. The analysis was based on a linear least-squares regression method weighted by reported dSCD uncertainties. Kreher et al. (2020) found that for MAX-DOAS NO_2 and O_4, the RMS values from the linear regression are an order of magnitude larger than the dSCD retrieval errors. This indicates that despite the good synchronization, trace gas variability and possibly aerosol or cloud features limit the reproducibility of the measurements. The way the instruments smooth atmospheric variability (depending on FOV and integration time) would then dominate the random uncertainty budget. Differences in elevation calibration, as discussed in the previous section, also play an important role in the comparisons. Other than for MAX-DOAS measurements, regression RMS values were much

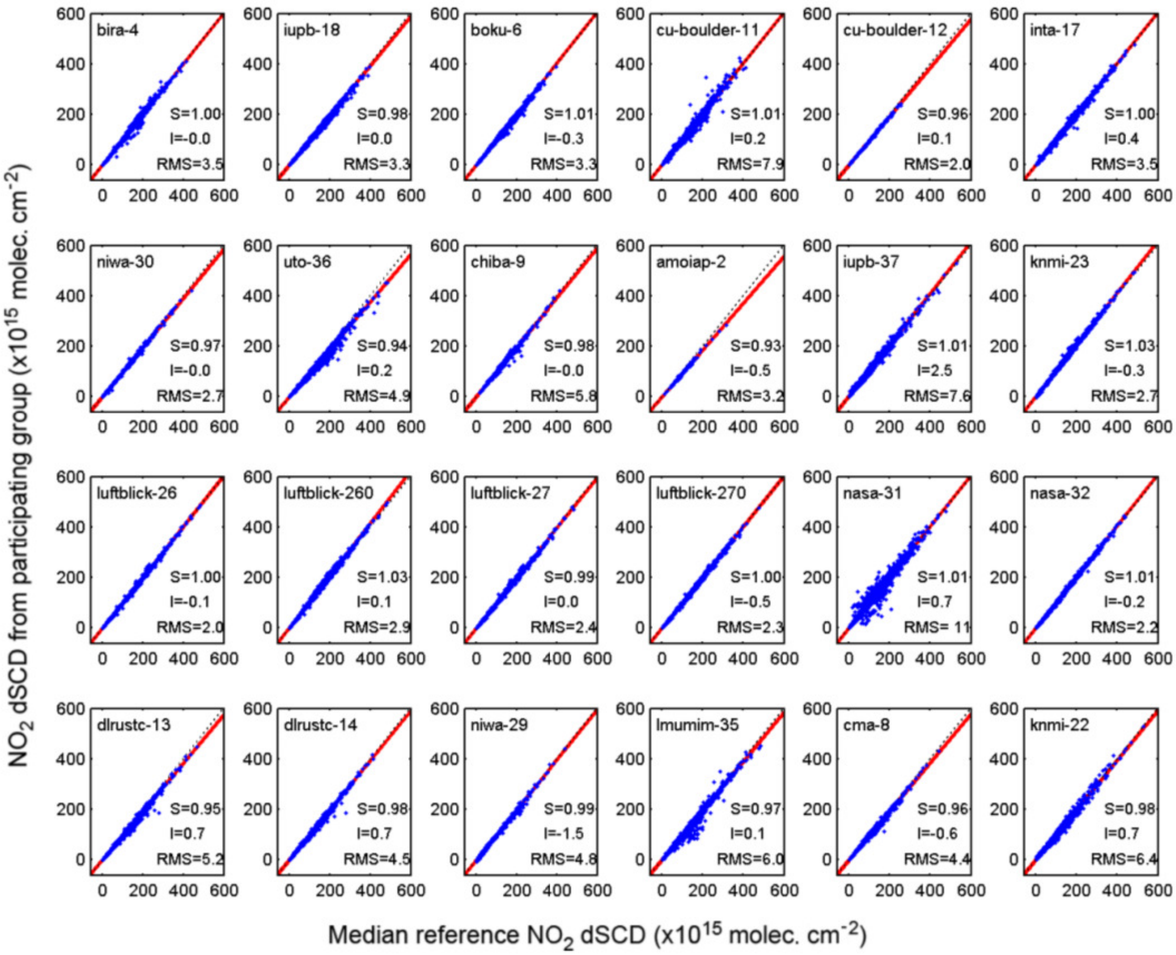

Figure 3.8: Regression analysis for MAX-DOAS NO$_2$ dSCDs against the median dataset for the entire semi-blind period, including all elevation and azimuth angles. The 'uto-36' label corresponds to the PEARL-GBS. The 1-to-1 line (dotted line) and the linear regression (red line), as well as the slope (S), intercept (I) and RMS of the regression, are indicated on each plot. Reproduced from Figure 10 of Kreher et al. (2020).

larger than fit uncertainties for zenith-sky ozone as well.

As an example of the regression analysis, the results for MAX-DOAS NO$_2$ are shown in Figure 3.8. Similar plots for all products are shown in the supplement of Kreher et al. (2020). The MAX-DOAS plots include measurements from all azimuth and elevation angles, while for zenith-sky measurements, dSCDs were compared for SZA between 75 and 95°. The fit results from the linear regression quantify the mean systematic bias (slope), the offset (intercept), and the measurement noise (RMS) when compared to the reference dataset. Figure 3.8 shows very good correlation for MAX-DOAS NO$_2$ among the different instruments. Results for the PEARL-GBS show good intercept and average RMS values, with a slight bias (slope of 0.94). The correlations for NO$_2$-small and ozone

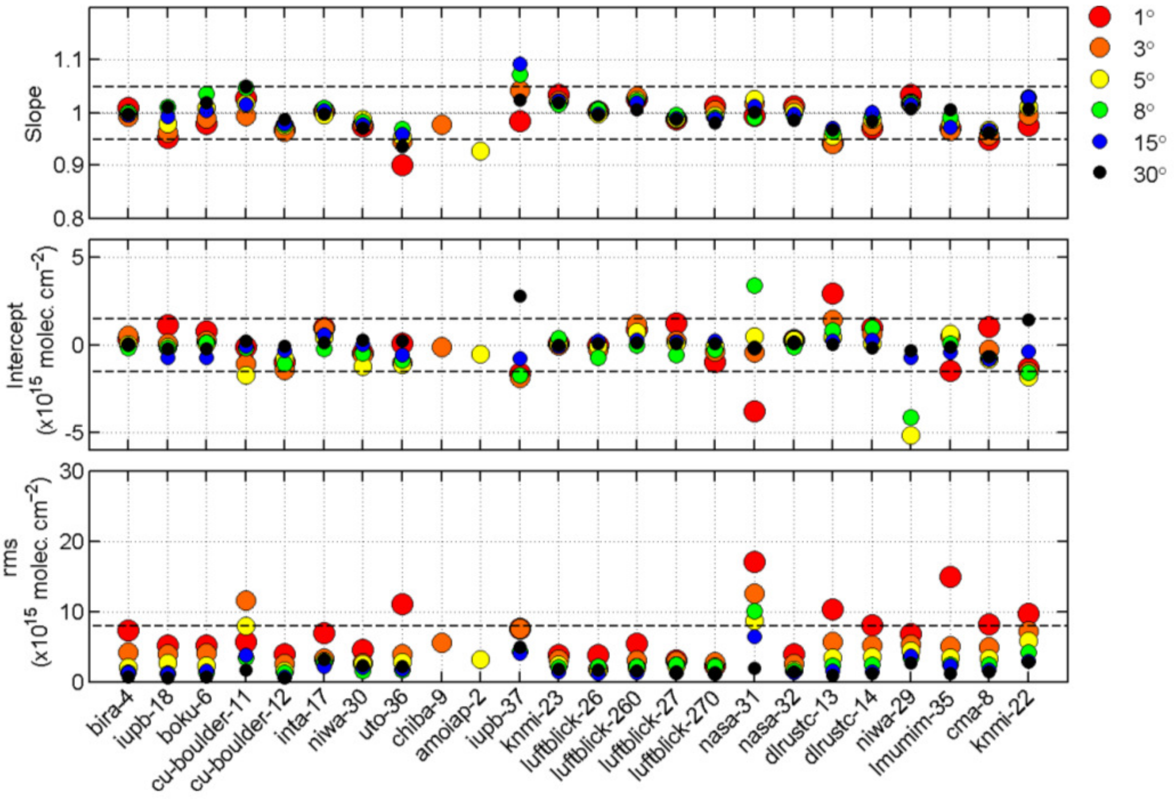

Figure 3.9: Summary of the slopes, intercepts, and RMS values for the NO_2 linear regression (shown in Fig. 3.8) for individual elevation angles. The 'uto-36' label corresponds to the PEARL-GBS. The dashed lines represent the limits for quantifying outliers. Reproduced from Figure 17 of Kreher et al. (2020).

are similarly tight, and the PEARL-GBS results show the same tendencies as for NO_2. For O_4, the correlations are overall noisier than for any of the other products, and the PEARL-GBS data show no bias when compared to the reference dataset. For zenith-sky data, PEARL-GBS NO_2 and NO_2-small follow the tight correlation seen for all instruments, while PEARL-GBS ozone shows a tight correlation with a slight bias (slope of 0.95) (supplement of Kreher et al., 2020).

The dependence of the MAX-DOAS comparison results on elevation angles is evident from Figure 3.9, which shows the linear regression parameters from Figure 3.8 for individual elevation angles. The dashed lines in Figure 3.9 indicate the performance criteria selected to assess instrument performance. The criteria were adapted from previous NDACC campaigns (for NO_2, NO_2-small, and ozone), or derived from the distribution of each parameter (for O_4). The PEARL-GBS NO_2 data perform well, with little variation as a function of elevation angle. The exception are the 1° dSCDs, which show high RMS and a significant slope. Other elevation angles generally fulfill the performance criteria for all parameters. PEARL-GBS NO_2-small dSCDs show a very similar relationship to the reference dataset. For O_4, the 1° measurements are no longer outliers, but overall spread for elevation angles is slightly larger than for NO_2. The regression parameters for ozone dSCDs show little dependence on elevation angle, in line with the other participating instruments.

Kreher et al. (2020) summarized the performance of each instrument using the assessment matrix shown in Figure 3.10. Instruments are grouped by type, with the PEARL-GBS in the custom-built category. The color coding in Figure 3.10 indicates how well each instrument met the performance criteria for each product. Only about one third of the participating instruments met all the criteria for the MAX-DOAS products. The PEARL-GBS was close to meeting all criteria, as only one criterion (the slope of the linear regression) was not satisfied for the ozone and NO_2 products. In the case of the two NO_2 products, this is in part due to the larger slope for the 1° dSCDs. The zenith-sky results show better agreement overall, with more than half of the participating instruments meeting all performance criteria. The PEARL-GBS once again was close to meeting all criteria, with only the slope of the ozone regression outside the expected range.

It should be noted that the PEARL-GBS was not measuring under ideal conditions during CINDI-2. As discussed above, unusually high signal levels during the day necessitated the use of both a diffuser and a neutral density filter, the latter of which are not used for measurements in Eureka. As a result, the SNR for the measured spectra was lower than usual, especially during twilights. In order to conform to the data acquisition schedule, total integration times were also shorter than normal, with fewer spectra included in the average for individual measurements. In addition, dew often accumulated on the plexiglass suntracker cover in the mornings, potentially affecting the quality of morning zenith-sky measurements. Possible errors in the QDOAS processing might have also contributed to the large slopes for the NO_2 products, as central reprocessing of measured spectra showed improved results for the PEARL-GBS (and improved results overall) (Van Roozendael, 2018). The less than ideal conditions contributed to increased RMS values in the dSCD fits, as shown by the second set of numbers in each rectangle in Figure 3.10. While still meeting the performance criteria, the PEARL-GBS fit RMS shows some of the highest values for all products, contrary to what might be expected for the low-noise, cooled CCD used by the instrument. Consequently, the RMS values for the linear regression with respect to the reference dataset (first set of numbers in Fig. 3.10) are also on the higher end for the PEARL-GBS dSCDs.

Overall, the PEARL-GBS performed well in the semi-blind intercomparison exercise. The instrument followed the data acquisition sequence accurately, and displayed

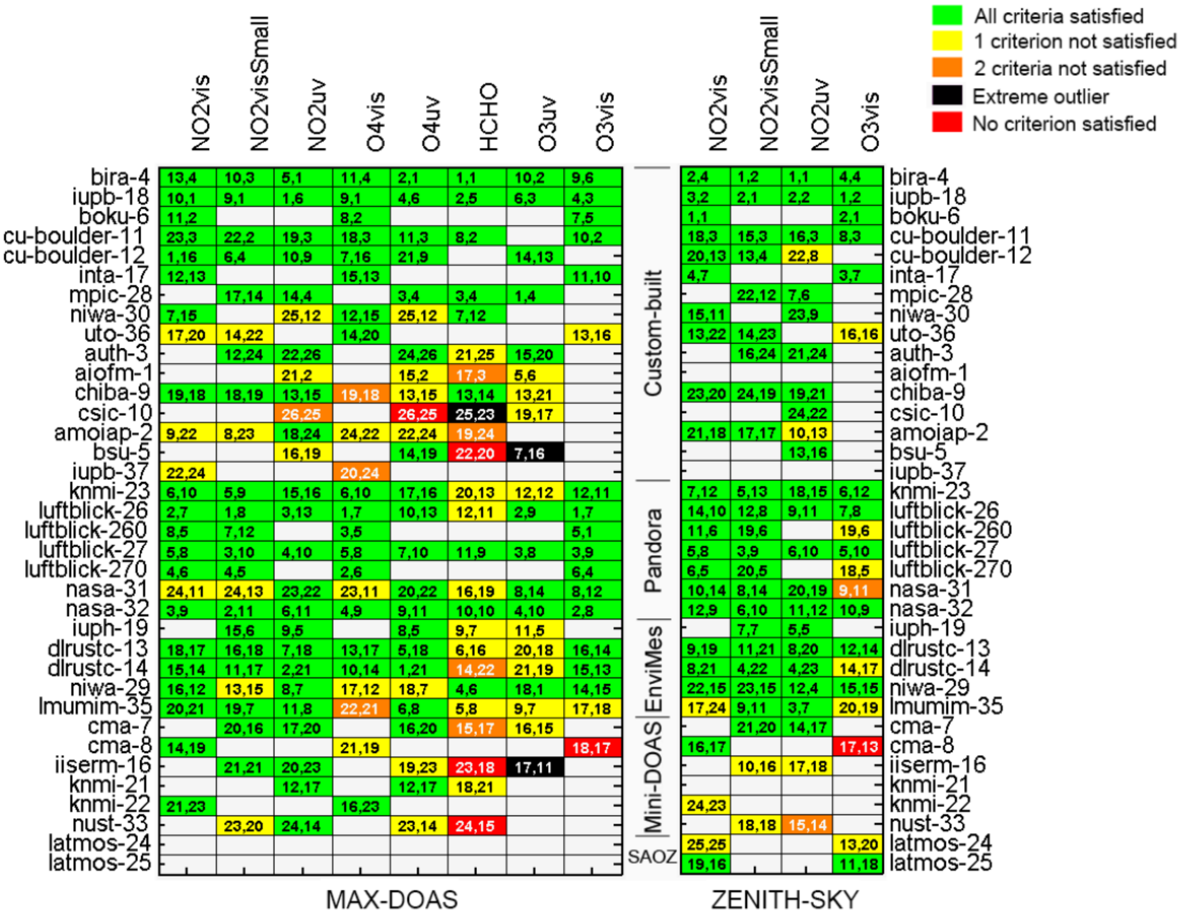

🟩 All criteria satisfied
🟨 1 criterion not satisfied
🟧 2 criteria not satisfied
⬛ Extreme outlier
🟥 No criterion satisfied

		MAX-DOAS								ZENITH-SKY			
		NO2vis	NO2visSmall	NO2uv	O4vis	O4uv	HCHO	O3uv	O3vis	NO2vis	NO2visSmall	NO2uv	O3vis
Custom-built	bira-4	🟩 13,4	🟩 10,3	🟩 5,1	🟩 11,4	🟩 2,1	🟩 1,1	🟩 10,2	🟩 9,6	🟩 2,4	🟩 1,2	🟩 1,1	🟩 4,4
	iupb-18	🟩 10,1	🟩 9,1	🟩 1,6	🟩 9,1	🟩 4,6	🟩 2,5	🟩 6,3	🟩 4,3	🟩 3,2	🟩 2,1	🟩 2,2	🟩 1,2
	boku-6	🟩 11,2			🟩 8,2				🟩 7,5	🟩 1,1			🟩 2,1
	cu-boulder-11	🟩 23,3	🟩 22,2	🟩 19,3	🟩 18,3	🟩 11,3	🟩 8,2		🟩 10,2	🟩 18,3	🟩 15,3	🟩 16,3	🟩 8,3
	cu-boulder-12	🟩 1,16	🟩 6,4	🟩 10,9	🟩 7,16	🟩 21,9		🟩 14,13		🟩 20,13	🟩 13,4	🟨 22,8	
	inta-17	🟩 12,13			🟩 15,13				🟩 11,10	🟩 4,7			🟩 3,7
	mpic-28		🟩 17,14	🟩 14,4		🟩 3,4	🟩 3,4	🟩 1,4			🟩 22,12	🟩 7,6	
	niwa-30	🟩 7,15		🟨 25,12	🟩 12,15	🟨 25,12	🟩 7,12			🟩 15,11		🟩 23,9	
	uto-36	🟨 17,20	🟨 14,22		🟩 14,20				🟨 13,16	🟩 13,22	🟩 14,23		🟨 16,16
	auth-3		🟩 12,24	🟩 22,26		🟩 24,26	🟨 21,25	🟩 15,20			🟩 16,24	🟩 21,24	
	aiofm-1			🟨 21,2		🟨 15,2	🟧 17,3	🟨 5,6					
	chiba-9	🟩 19,18	🟩 18,19	🟩 13,15	🟧 19,18	🟨 13,15	🟩 13,14	🟨 13,21		🟩 23,20	🟩 24,19	🟩 19,21	
	csic-10			🟧 26,25		🟥 26,25	⬛ 25,23	🟨 19,17				🟩 24,22	
	amoiap-2	🟨 9,22	🟨 8,23	🟩 18,24	🟨 24,22	🟨 22,24	🟧 19,24			🟩 21,18	🟩 17,17	🟨 10,13	
	bsu-5			🟨 16,19		🟩 14,19	🟥 22,20	⬛ 7,16				🟩 13,16	
	iupb-37	🟨 22,24			🟧 20,24								
Pandora	knmi-23	🟩 6,10	🟩 5,9	🟩 15,16	🟩 6,10	🟩 17,16	🟨 20,13	🟨 12,12	🟩 12,11	🟩 7,12	🟩 5,13	🟩 18,15	🟩 6,12
	luftblick-26	🟩 2,7	🟩 1,8	🟩 3,13	🟩 1,7	🟩 10,13	🟨 12,11	🟩 2,9	🟩 1,7	🟩 14,10	🟩 12,8	🟩 9,11	🟩 7,8
	luftblick-260	🟩 8,5	🟩 7,12		🟩 3,5				🟩 5,1	🟩 11,6	🟩 19,6		🟨 19,6
	luftblick-27	🟩 5,8	🟩 3,10	🟩 4,10	🟩 5,8	🟩 7,10	🟩 11,9	🟩 3,8	🟩 3,9	🟩 5,8	🟩 3,9	🟩 6,10	🟩 5,10
	luftblick-270	🟩 4,6	🟩 4,5		🟩 2,6				🟩 6,4	🟩 6,5	🟩 20,5		🟨 18,5
	nasa-31	🟨 24,11	🟨 24,13	🟩 23,22	🟨 23,11	🟩 20,22	🟨 16,19	🟩 8,14	🟩 8,12	🟩 10,14	🟩 8,14	🟩 20,19	🟧 9,11
	nasa-32	🟩 3,9	🟩 2,11	🟩 6,11	🟩 4,9	🟩 9,11	🟩 10,10	🟩 4,10	🟩 2,8	🟩 12,9	🟩 6,10	🟩 11,12	🟩 10,9
EnviMes	iuph-19		🟩 15,6	🟩 9,5		🟩 8,5	🟨 9,7	🟨 11,5			🟩 7,7	🟩 5,5	
	dlrustc-13	🟩 18,17	🟩 16,18	🟩 7,18	🟩 13,17	🟩 5,18	🟨 6,16	🟨 20,18	🟩 16,14	🟩 9,19	🟩 11,21	🟩 8,20	🟩 12,14
	dlrustc-14	🟩 15,14	🟩 11,17	🟩 2,21	🟩 10,14	🟩 1,21	🟧 14,22	🟨 21,19	🟩 15,13	🟩 8,21	🟩 4,22	🟩 4,23	🟨 14,17
	niwa-29	🟩 16,12	🟨 13,15	🟩 8,7	🟨 17,12	🟨 18,7	🟩 4,6	🟩 18,1	🟩 14,15	🟩 22,15	🟩 23,15	🟩 12,4	🟩 15,15
	lmumim-35	🟩 20,21	🟩 19,7	🟩 11,8	🟧 22,21	🟩 6,8	🟨 5,8	🟨 9,7	🟨 17,18	🟨 17,24	🟩 9,11	🟩 3,7	🟨 20,19
Mini-DOAS	cma-7		🟩 20,16	🟩 17,20		🟩 16,20	🟧 15,17	🟨 16,15			🟩 21,20	🟩 14,17	
	cma-8	🟩 14,19			🟨 21,19				🟥 18,17	🟩 16,17			🟥 17,13
	iiserm-16		🟩 21,21	🟩 20,23		🟨 19,23	🟥 23,18	⬛ 17,11			🟨 10,16	🟨 17,18	
	knmi-21			🟩 12,17		🟩 12,17	🟨 18,21						
	knmi-22	🟩 21,23			🟩 16,23					🟨 24,23			
	nust-33		🟨 23,20	🟩 24,14		🟨 23,14	🟥 24,15				🟨 18,18	🟧 15,14	
SAOZ	latmos-24									🟨 25,25			🟨 13,20
	latmos-25									🟩 19,16			🟩 11,18

Figure 3.10: Assessment of all 36 instruments and all MAX-DOAS and ZSL-DOAS data products for the CINDI-2 semi-blind intercomparison. Colors indicate the number of comparison criteria fulfilled, and white indicates lack of data. The numbers in the boxes rank the instruments in terms of increasing regression RMS (first value) and RMS from the initial dSCD retrieval (second value). The 'uto-36' label corresponds to the PEARL-GBS. Figure reproduced from Kreher et al. (2020).

remarkable pointing stability throughout the campaign. The challenges notwithstanding, the delivered data products met most of the performance criteria established by Kreher et al. (2020).

3.2.3 Aerosol and NO_2 Profile Intercomparisons

Since the main benefit of MAX-DOAS measurements is the profile information contained in the dSCDs, a profiling task force was established as part of the CINDI-2 campaign. There are numerous retrieval algorithms currently employed in the MAX-DOAS community, but no comprehensive intercomparison of these algorithms has been performed to date. The main aim of the profiling task force was to fill this gap by evaluating the degree of consistency between various algorithms using uniform settings and datasets. The first results of this exercise were presented by Frieß et al. (2019), who compared results from eight retrieval algorithms using synthetic spectra. As the next step, retrieval results from 15 participating groups and nine different algorithms (using measurements from CINDI-2) were analyzed by Tirpitz et al. (2021). This section summarizes the results of Tirpitz et al. (2021), with a focus on the contributions from the PEARL-GBS and the University of Toronto (hereafter UTOR) group.

In order to investigate the differences between the algorithms, each group used the same dSCDs for the profile retrievals. This common dataset was the same reference dSCD dataset that was used as the baseline for the semi-blind intercomparisons (Kreher et al., 2020). Results from each group using data from the individual instruments were also included, but these datasets were not the main focus of Tirpitz et al. (2021). Profiles of aerosol extinction and NO_2 were retrieved from dSCDs in both the UV and visible ranges, using RTM wavelengths of 360 and 477 nm for aerosols, and 360 and 460 nm for NO_2. HCHO profiles (at 343 nm) were also retrieved, while results from the NO_2-small window were not used (see Table 3.4 for the list of dSCD products). To ensure that the largest number of groups could participate, only dSCDs along the main viewing azimuth angle of 287° were used in this study. Profiles were retrieved for the entire semi-blind phase, 12-28 September (ten full elevation scans per day).

Profiles of extinction and NO_2 were retrieved from the PEARL-GBS and the reference dSCD datasets using HeiPro (Chapter 2). Only the species in the visible range were retrieved from the PEARL-GBS dataset, while most species were retrieved using the reference dataset. Profiles were not retrieved from HCHO data, and HCHO results from other groups are not discussed here. The UTOR results, alongside results from the Institute of Environmental Physics, University of Heidelberg (hereafter IUPHD) group, were the only datasets retrieved using HeiPro. These results were compared to five other OEM algorithms (results from ten groups), two parametric algorithms (results from two groups), and one analytical algorithm (results from one group).

To reduce possible sources of discrepancies, the main retrieval settings and inputs were fixed for each group. Vertical profiles of pressure, temperature, and ozone (one profile each for the entire period) were averaged from 2013-2015 ozonesonde measurements. Profiles were retrieved on a fixed altitude grid (0-4 km, 200 m vertical resolution), with the instrument altitude set to 0 m. For the aerosol retrievals, the single scattering albedo was set to 0.92 and the asymmetry factor to 0.68. The surface albedo was set to 0.06 for all retrievals. The a priori profiles for the OEM algorithms were specified as exponentially-decreasing profiles with a scale height of 1 km, with a corresponding AOD and NO_2

VCD of 0.18 and 9×10^{15} molec cm^{-2}, respectively. These profiles correspond to a surface extinction of 0.1837 km^{-1} and a surface NO_2 concentration of 9.18×10^{10} molec cm^{-3}. The a priori covariance matrices were constructed using a variance of 50% and a correlation length of 200 m. The retrievals were performed following the two-step approach described in Chapter 2.

Tirpitz et al. (2021) compared the retrieval results to the median of all results using a linear least-squares regression method and root-mean-square deviation (*RMSD*), both weighted by the reciprocal of the quadratic sum of the uncertainties on the datapoints. The results were also compared to independent datasets, including AOD from sun photometers, extinction profiles from ceilometers, NO_2 profiles from sondes and an NO_2 lidar, NO_2 tropospheric VCDs from direct-sun DOAS measurements, and NO_2 surface concentrations (0-200 m) from LP-DOAS and in situ measurements. The arrangement of the instruments on the measurement site is shown in Figure 3.4a. For comparisons of OEM results to independent profiles (e.g., sonde data), the profiles were smoothed with the retrieval averaging kernels according to Equation 2.11. Cloud conditions were retrieved from two MAX-DOAS instruments following Wagner et al. (2014) and Wang et al. (2015), and the conditions were categorized as either ‘clear-sky’ or ‘presence of clouds’.

Tirpitz et al. (2021) found that the vertical sensitivity for all species is limited to the lowest 1.5 km of the atmosphere. For the OEM retrievals, DOFS are generally between 2 and 3 for both aerosols and NO_2. DOFS are significantly higher (by 0.6-0.7) for the species in the visible range than for the UV species for both aerosols and NO_2, likely due to the shorter pathlengths in the UV. Clouds, on the other hand, only have a small negative impact on DOFS, with differences of $\sim$0.1 for all species and wavelengths. Based on the average standard deviation (ASDev) of all profiles across all retrieval layers, the profiles show good agreement in clear conditions. There is more variability among the species in the visible range compared to the UV, with ASDev values increasing by 90% and 50% for aerosols and NO_2, respectively. Clouds have a large impact on the aerosol results, with ASDev values increasing by factors of 3 and 4 for the UV and visible retrievals, respectively, for profiles flagged as cloudy. NO_2 results, on the other hand, are only marginally affected by clouds.

Figure 3.11 shows the summary of the comparison results for HCHO and NO_2 VCDs. The VCDs are compared to both the median of all the retrieved VCDs, as well as to tropospheric columns from direct-sun measurements. *RMSD* values for NO_2 and NO_2-UV with respect to the median are overall smaller than the reported retrieval uncertainties, indicating good agreement between the different algorithms. *RMSD* values for the direct-

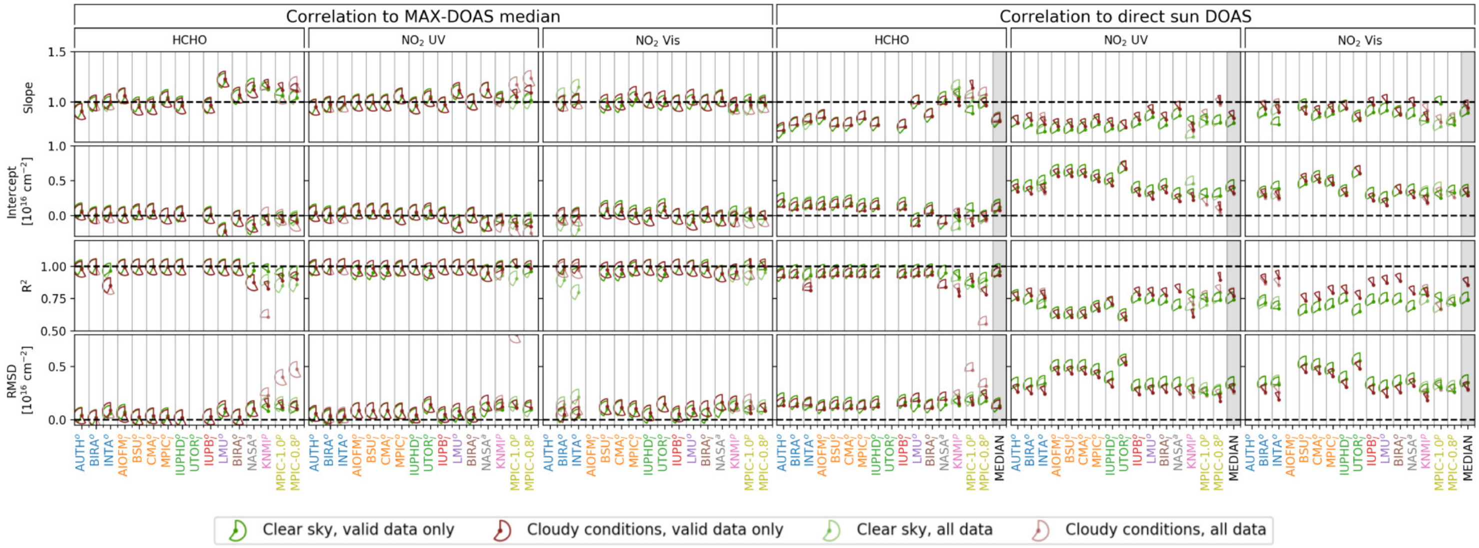

Figure 3.11: Correlation statistics for trace gas VCDs. The three columns on the left show the agreement among the participating groups, while the three columns on the right show the agreement with direct-sun DOAS measurements. Green and red symbols represent cloud-free and cloudy conditions, respectively. The pies indicate the fraction of the total number of profiles (170) that contributed to the respective value. For groups that implemented additional quality flags, light symbols represent the unflagged dataset. Reproduced from Figure 17 of Tirpitz et al. (2021).

sun comparisons, on the other hand, are on average three times larger than retrieval uncertainties. These comparisons show R^2 values of $\sim$0.75 (compared to $\sim$1 for the median), and retrieved VCDs generally underestimate direct-sun tropospheric columns, with slopes and intercepts that are significantly different from 1 and 0, respectively. HeiPro results from UTOR and IUPHD are generally similar, but the IUPHD results compare better to direct-sun measurements. Results for the AOD comparisons (see Fig. 14 in Tirpitz et al., 2021) show that unlike for NO$_2$, $RMSD$ values are on the order of the reported uncertainties even for comparisons to the median. $RMSD$ values are several times larger than retrieval uncertainties for the sun photometer comparisons. While agreement between the algorithms is consistent regardless of cloud cover, sun photometer comparisons are significantly worse in the presence of clouds (although sun photometer data are limited in cloudy conditions). While the differences between UTOR and IUPHD are not large when both are compared to the median of the retrieved AODs, the comparisons to sun photometer data indicate that IUPHD results perform better in clear conditions, and worse in cloudy conditions, than the UTOR results.

As is the case for HeiPro, Tirpitz et al. (2021) noted that some variability is apparent between most groups that use the same retrieval algorithm. This indicates the importance

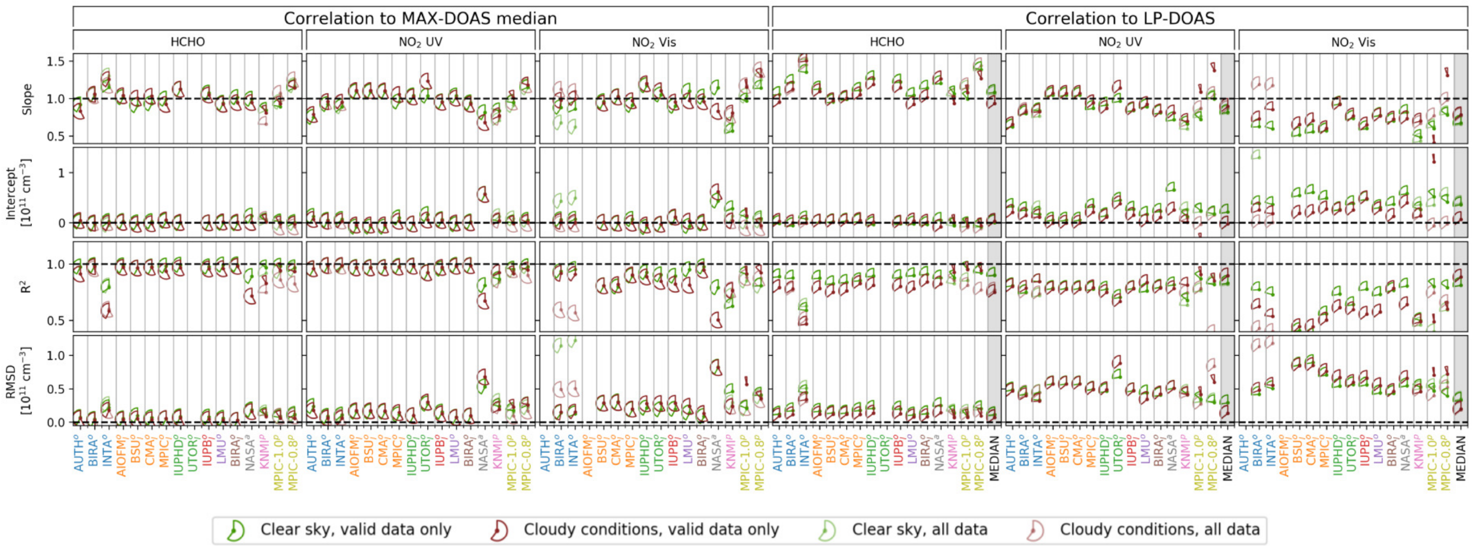

Figure 3.12: Same as Figure 3.11, for trace gas surface concentrations (0-200 m) and comparisons to LP-DOAS measurements. Reproduced from Figure 20 of Tirpitz et al. (2021).

of the retrieval settings that were not prescribed. For the HeiPro results, most of the differences were traced to the number of iteration steps used in the optimization scheme for the aerosol retrievals (5 for UTOR, 20 for IUPHD)[4]. Changing the number of iterations to match the IUPHD settings increases the UTOR AODs by 13% and 21% in the UV and visible ranges, respectively (5% and 13% when excluding 16-18 September, the days most affected by clouds). NO_2 VCDs (which use the extinction profiles as a priori) increase by 1.6% and 3.8% for the UV and visible retrievals, respectively. With these changes, the UTOR and IUPHD results show better agreement.

The trace gas surface concentrations (concentration in the bottom retrieval layer, 0-200 m) were compared to the median surface concentrations and the LP-DOAS measurements. Instead of measuring scattered light, the LP-DOAS instrument uses an active light source to illuminate retroreflectors and measures the reflected light (see e.g., Pöhler et al., 2010; Merten et al., 2011; Nasse et al., 2019). The fixed light path results in accurate trace gas concentrations averaged over the line-of-sight, and the elevation of the retroreflector (207 m on the CESAR meteorological tower, Fig. 3.4a) means that the LP-DOAS measurements are the most appropriate base of comparison for the surface concentrations retrieved from the MAX-DOAS measurements. The summary of the comparison results is shown in Figure 3.12. *RMSD* values NO_2 and NO_2-UV are smaller than

---

[4] Differences with minor impacts included the use of fixed weighting functions and a stratospheric aerosol climatology by the IUPHD group.

the reported uncertainties for comparisons to the median, while *RMSD* values are a factor of three and two larger (NO_2 and NO_2-UV, respectively) for the LP-DOAS comparisons. For both the median and LP-DOAS comparisons, the UV results show better agreement than visible results. This is likely the reflection of greater horizontal variability of NO_2 over the larger viewing distances in the visible range. In part for similar reasons, R^2 values with respect to the LP-DOAS data are as low as 0.5 in some cases for NO_2 in the visible range. HeiPro results are similar for the UTOR and IUPHD groups for NO_2, while NO_2-UV results show more variability for both the median and LP-DOAS comparisons. This is largely the result of the number of iterations used for the aerosol retrieval, as discussed above. Matching the number of iterations leads to a 10% decrease and a 15% increase in the UV and visible surface concentrations, respectively, bringing the UTOR and IUPHD results into better agreement.

The differences in the HeiPro results as a function of wavelength range are apparent in Figure 3.13 as well, which shows the correlation of UV and visible VCDs and surface concentrations. While the IUPHD surface concentrations show very good correlation, the UTOR results show a significant slope. This bias is largely eliminated if the number of iterations in the aerosol retrieval are the same between the two groups. The disagreement between the UV and visible surface concentrations is not unusual, however, as results from most groups show a similar correlation. This is in agreement with the better correlation between NO_2-UV and LP-DOAS shown in Figure 3.12. VCDs, on the other hand, generally agree well between the UV and visible results, with only a slight slope that is similar for most groups and retrieval algorithms. Unlike surface concentrations, the agreement for UTOR and IUPHD is very similar for VCDs.

Overall, Tirpitz et al. (2021) concluded that while the profiling algorithms generally retrieve the same features, comparisons to the median yield *RMSD* values on the order of, or greater than, the uncertainties reported by the algorithms. HeiPro performed well in the comparisons, and differences between the UTOR and IUPHD results were found to mainly be caused by the different number of iteration steps in the aerosol retrieval. These results indicate that the choice of retrieval algorithm, and even the choice of minor RTM and algorithm settings, might significantly impact the profile results. Considering retrieval results using the participants' measured dSCDs, the consistency between the results decreased (*RMSD* values increased), in line with the dSCD differences identified by Kreher et al. (2020). Tirpitz et al. (2021), however, noted that the comparisons to supporting observations showed a smaller increase in average *RMSD*, and comparison results even improved for some products (UV AODs and NO_2-UV VCDs). This means that even through the scatter between participants increased when the measured dSCDs

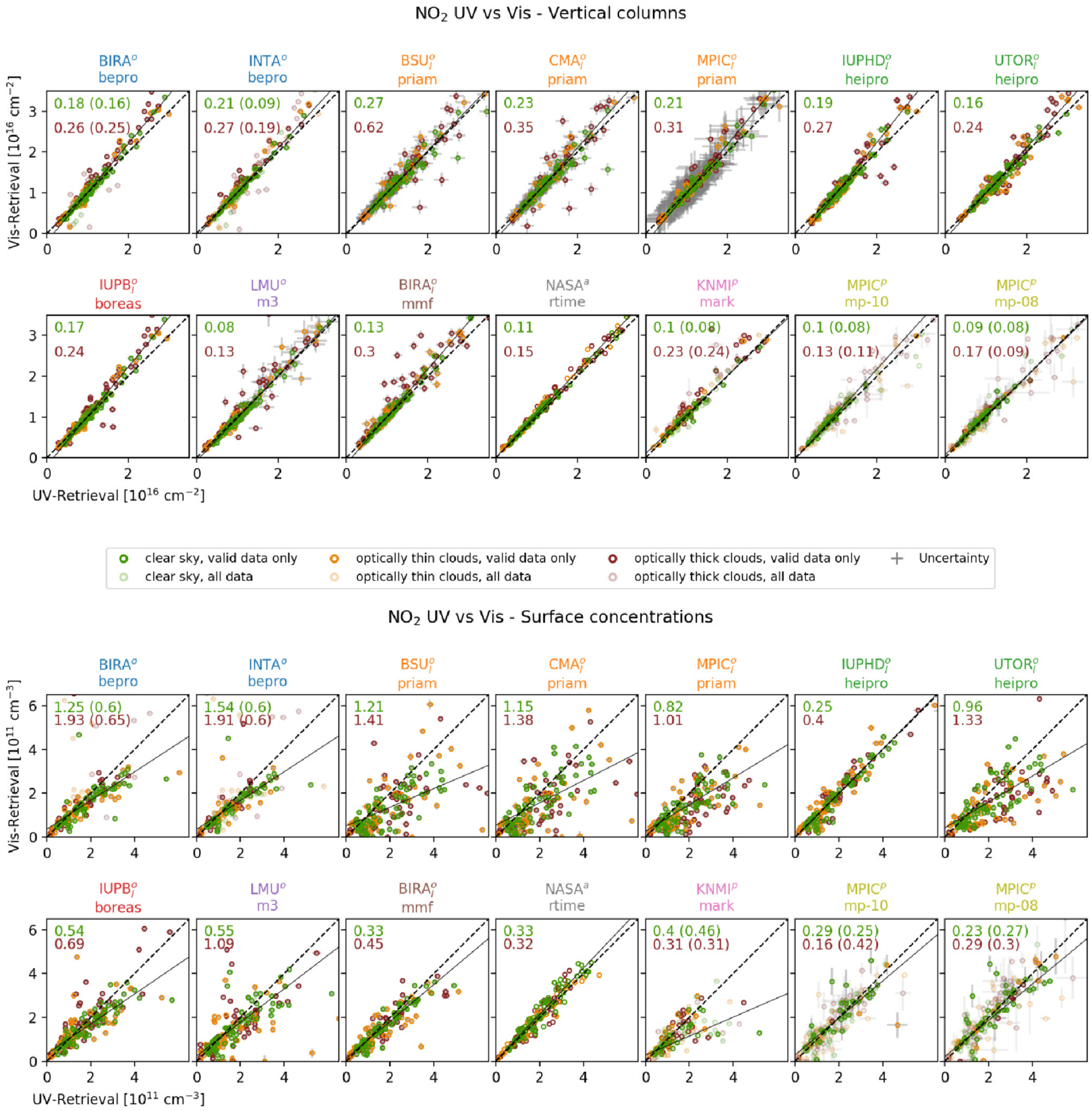

Figure 3.13: Correlation of retrieved NO_2 VCDs (top) and surface concentrations (bottom) in the UV and visible spectral ranges. Marker colors indicate cloud conditions and data validity. The numbers correspond to the error-weighted *RMSD* values for clear (green) and cloudy (red) conditions. Adapted from Figures 21 and 22 of Tirpitz et al. (2021).

were used, the average quality of the dSCDs was maintained.

3.3 Summary

This chapter described the measurement history of the GBS instruments in Eureka, and the participation of the PEARL-GBS in CINDI-2. The GBS dataset now includes 20 years of measurements (five spring periods and 15 full years) in Eureka. The full time series of the ozone, NO_2, and NO_2-UV VCDs were reprocessed with consistent retrieval settings, and the results were submitted to the NDACC archive in HDF format. A rapid delivery retrieval was also implemented, and data are regularly submitted to CAMS in HDF format.

The PEARL-GBS was successfully deployed as a 2D MAX-DOAS instrument for the CINDI-2 campaign in September 2016. The PEARL-GBS participated in an elevation calibration exercise, and the pointing stability of the instrument was excellent (Donner et al., 2020). The retrieved dSCDs of O_4, NO_2, and ozone were found to agree well with other instruments, and the PEARL-GBS met most of the campaign performance criteria (Kreher et al., 2020). Profiles of extinction and NO_2, retrieved both from the measurements and a median dSCD dataset, were consistent with other instruments and with supporting datasets (Tirpitz et al., 2021).

Chapter 4

Validation of ACE and OSIRIS Ozone and NO_2 Measurements

This chapter presents long-term intercomparisons (2003-2017) between ozone and NO_2 measured by the OSIRIS and ACE satellite instruments, and by ground-based instruments at PEARL. Comparisons of ozone partial columns show good agreement between OSIRIS and ACE-FTS data (1.2%), while ACE-MAESTRO ozone shows a negative bias when compared to the other two datasets (6.7% and 5.9%, respectively). Satellite-plus-sonde ozone total columns agree with the ground-based datasets with mean relative differences of 0.5-12.0%. For NO_2, partial columns from ACE-FTS and OSIRIS agree with ground-based partial columns with mean relative differences of 0.7-33.2%. Dynamical coincidence criteria improved the ACE to ground-based FTIR ozone comparisons, while little to no improvements were seen for other instruments, and for NO_2. A ±1° latitude criterion improved the spring and fall NO_2 comparisons. There are no apparent systematic changes in the observed differences between the satellite and the ground-based instruments over time, indicating that the OSIRIS and ACE instruments continue to perform well. The study described in this chapter has been published in the *Journal of Quantitative Spectroscopy and Radiative Transfer* (Bognar et al., 2019).

4.1 Instruments and Data Processing

This work utilizes ozone, NO_2, and NO_2-UV measurements made at Eureka by the UT-GBS and the PEARL-GBS (merged into the GBS and GBS-UV datasets), as well as ozone and NO_2 from SAOZ ZSL-DOAS instruments. In addition, measurements from two FTIR instruments, one Brewer spectrophotometer (#69), and ozonesondes are included. The datasets used in this study, along with the corresponding abbreviations and temporal

Table 4.1: Data products used in this study. The abbreviations listed are used in all subsequent figures and tables. The measurement periods are separated as spring only (S), spring and fall (S/F) and year-round (Y).

Data product	Abbreviation	Ozone	NO_2
GBS	GV	S: 2003–2005 Y: Aug. 2006–2017	S: 2003–2005 Y: Aug. 2006–2017
GBS-UV	GU	—	S: 2007, 2009–2013, 2016 Y: 2008, 2014, 2015, 2017
SAOZ	SA	S: 2005–2010, 2012–2014 S/F: 2011, 2015–2017	S: 2005–2010, 2012–2014 S/F: 2011, 2015–2017
Bruker FTIR	BK	Y: Aug. 2006–2017	Y: Aug. 2006–2017
PARIS-IR	PA	S: 2006–2017	—
Brewer	BW	Y: 2004–2017	—
OSIRIS*	OS	Y: 2003–2017	Y: 2003–2017
ACE-FTS v3.5/3.6	AF	S/F: 2004–2017	S/F: 2004–2017
ACE-MAESTRO v3.13	AM	S/F: 2004–2017	—

* Data versions are v5.10 for ozone and v6.0 for NO_2.

coverage, are listed in Table 4.1. Uncertainties, as reported in the datasets, are given in Table 4.2.

4.1.1 Ground-based Instruments

The SAOZ instruments (Pommereau and Goutail, 1988) form a global network that measures stratospheric trace gases using ZSL-DOAS. SAOZ instruments were deployed at the PEARL Ridge Lab in 2005-2017 as part of the Canadian Arctic ACE/OSIRIS Validation Campaigns. SAOZ-15 took springtime measurements in 2005-2009, while SAOZ-7 was installed in 2010 and took year-round measurements in 2011 and 2015-2017 with springtime data in the intervening years. For 2005-2007 and 2010, the instruments recorded spectra from inside the lab through a UV-transparent window. For 2008-2009 and since 2011, SAOZ was located in a box on the roof of the PEARL Ridge Lab.

The SAOZ instruments are UV-visible spectrometers with a fixed grating that allows measurements in the 270-620 nm region. Spectra are recorded with an uncooled 1024-pixel linear photodiode array detector. The resolution is approximately 1 nm across the detector, and the instruments have a FOV of 20°. SAOZ-15 and SAOZ-7 are identical instruments and show excellent agreement, therefore measurements from the two instruments are treated as a single dataset. Details of the data analysis are described in Section 4.1.1.1. While SAOZ instruments are NDACC certified, the Eureka instruments are not part of the NDACC network. The SAOZ V3 dataset was used in this study, and changes compared to the V2 dataset are described in Section 4.1.1.1.

The Bruker FTIR was installed in the PEARL Ridge Lab in 2006 (Batchelor et al., 2009). Solar absorption spectra are recorded using either a mercury cadmium telluride (HgCdTe) or an indium antimonide (InSb) detector (both liquid-nitrogen-cooled), and a potassium bromide (KBr) beamsplitter. Seven narrow-band interference filters are used to cover a range of 600-4300 cm^{-1}. Measurements take approximately 4-8 minutes, consist of two to four co-added spectra, and have a resolution of 0.0035 cm^{-1}. No apodization is applied to the measurements. The Bruker FTIR is part of NDACC, and retrieved ozone profiles are submitted to the NDACC database, while the NO_2 retrievals are currently a research product. The retrieval details for both ozone and NO_2 can be found in Section 4.1.1.2.

The Portable Atmospheric Research Interferometric Spectrometer for the InfraRed (PARIS-IR) took measurements at the PEARL Ridge Lab in 2004-2017 as part of the Canadian Arctic ACE/OSIRIS Validation Campaigns. Measurements are only included for the 2006-2017 period, as the instrument has been operated in a consistent fashion since the 2006 campaign. PARIS-IR has a design similar to that of the ACE Fourier Transform Spectrometer (ACE-FTS) (Fu et al., 2007). Solar absorption spectra are recorded using liquid-nitrogen-cooled HgCdTe and InSb detectors, and a zinc selenide (ZnSe) beamsplitter. The measurements are recorded in the 750-4400 cm^{-1} range, at a 0.02 cm^{-1} resolution and without the use of narrow-band filters. Measurements are recorded approximately every 7 minutes and consist of 20 co-added spectra. No apodization is applied to the measurements. The details of the ozone retrieval can be found in Section 4.1.1.2.

Brewer instruments use a holographic grating with a slit mask to measure the intensity of direct sunlight at six wavelengths in the UV range (Kerr, 2002). The first two wavelengths are used for internal calibration and SO_2 retrievals, respectively. Ozone total columns are calculated using relative intensities at the four remaining wavelengths (310.1, 313.5, 316.8, and 320 nm), with slight changes to the analysis to account for the high latitude of the measurement site (Adams et al., 2012a). Several Brewer instruments were deployed in Eureka over the 2003-2017 period. In this study, only Brewer #69 (a MKV single monochromator) is included, since this instrument measured hourly ozone for 2004-2017. During this time, Brewer #69 was located on the roof of the EWS building. Brewer ozone columns are calculated from an average of five successive measurements. Table 4.2 shows the mean of the reported standard deviations in the filtered Brewer #69 dataset. This value (0.4%) is similar to the random uncertainty of 0.5% estimated for Brewer measurements by (Zhao et al., 2020a).

Electrochemical concentration cell (ECC) ozonesondes are launched by ECCC from

Table 4.2: Reported uncertainty budgets for each of the datasets used in this study. Square brackets denote partial columns. For the list of abbreviations, see Table 4.1.

Instruments	Ozone		NO_2	
	DU	%	molec cm^{-2}	%
GV	22.7	6.6	$[5.9\times10^{14}]$	[19.0]
GU	—		$[6.5\times10^{14}]$	[22.8]
SA	23.4	5.9	$[2.8\times10^{14}]$	[13.6]
BK	21.8	5.6	$[2.3\times10^{14}]$	[7.5]
PA	21.9	4.9	—	
BW	1.3*	0.4*	—	
OS	[1.8]*	[0.6]*	$[4.5\times10^{13}]^{*,1}$	$[1.7]^{*,1}$
AF	[1.1]*	[0.4]*	$[1.8\times10^{13}]$*	[1.1]*
AM	$[2.1]^{*,2}$	$[0.7]^{*,2}$	—	

* Random uncertainties only.

[1] Based on estimate of uniform 1×10^8 molec cm^{-2} uncertainty for each profile.

[2] Calculated using only the uncertainty values less than 10% to exclude profiles where the error calculation failed.

the EWS on a weekly basis (Tarasick et al., 2016). During the intensive phase of the Canadian Arctic ACE/OSIRIS Validation Campaigns (2004-2017, typically early March), ozonesondes were launched daily, weather permitting. In this study, ozonesondes were used in the ZSL-DOAS retrievals (Sect. 4.1.1.1), to extend satellite partial columns of ozone to the surface (Sect. 4.2.2), and to initialize the photochemical box model used for NO_2 diurnal scaling (Sect. 4.2.2).

4.1.1.1 Differences Between the GBS and SAOZ Retrievals

The GBS and SAOZ instruments use the DOAS technique (Platt and Stutz, 2008) to retrieve ozone and NO_2 columns from zenith-scattered sunlight. The GBS and SAOZ analyses were performed independently, with slight differences in the retrieval settings. The GBS dSCDs were retrieved with daily reference spectra, while the SAOZ retrievals used a fixed reference spectrum for each year. For ozone, SAOZ retrievals used the 450-550 nm window recommended by the NDACC UV-vis WG (Hendrick et al., 2011), while the GBS instruments used 450-545 nm to avoid irregularities near the CCD edge. For NO_2, the GBS datasets used the recommended 425-490 nm window, while the SAOZ retrievals used an extended, range, 410-530 nm. The GBS-UV dataset used the 350-380 nm window. The NO_2-UV data are not a standard NDACC product, but the retrievals followed the NO_2-vis recommendations as closely as possible.

For the GBS instruments, daily RCDs were calculated from the average of the RCDs for each twilight using the Langley plot method. For SAOZ, a fixed RCD was calculated for each year, since yearly references were used in the DOAS analysis. For both instruments, single VCD values for each twilight were calculated as the mean of the individual vertical columns in the 86-91° SZA range, weighted by the DOAS fitting error, divided by the AMF. Both the GBS and SAOZ retrievals use the AMF LUTs provided by NDACC (Hendrick et al., 2011). The ozone AMF calculations require the input of daily ozone data. The GBS retrievals used total columns interpolated from ozonesonde data, while the SAOZ analysis used measured SCDs. The NO_2 AMF LUTs, compiled separately for sunrise and sunset conditions, do not require prior vertical column information. The NO_2 concentration below 12 km and above 60 km in the LUTs is set to zero, and so the ZSL-DOAS NO_2 VCDs in this study are 12-60 km partial columns.

ZSL-DOAS measurements are particularly challenging in the high Arctic. The ideal SZA window of 86-91° is not available for much of the sunlit part of the year, and the maximum SZA at the summer solstice is just over 76°. The SAOZ VCDs are only retrieved in the spring and fall, when the 86-91° window is available. In order to extend the measurements into the polar day, the GBS retrievals use the highest available 5° SZA window in the summer. Around the summer solstice, however, the maximum AMFs for both ozone and NO_2 are only about one fourth of the AMFs at 90° SZA. In addition, the range in AMFs for SZAs of 71-76° is smaller than 1, while the AMF range is greater than 10 for the NDACC recommended SZA window. This leads to larger uncertainties in the summertime VCD retrievals. Spring and fall present their own unique challenges. The lack of high-sun spectra to use as daily references negatively impacts the quality of the GBS dSCDs, and small NO_2 concentrations lead to very large uncertainties in the GBS RCD calculations. To investigate the differences between satellite minus GBS and satellite minus SAOZ intercomparisons, ozone and NO_2 VCDs were retrieved from the original SAOZ dSCDs using the GBS VCD retrieval code. This retrieval extended the SAOZ data to include year-round measurements in 2011 and 2015-2017. This dataset (hereafter $\text{SAOZ}_{\text{allyear}}$) used the same settings as the SAOZ retrieval, with the exception of the SZA range. Similar to the GBS retrievals, the highest available 5° SZA window was used to obtain summer data.

The mean total uncertainty for the 2003-2017 GBS ozone dataset was calculated to be 6.6%, which is larger than the 5.9% reported for NDACC ozone columns (Hendrick et al., 2011). The larger value, however, is consistent with the challenges of high-latitude measurements outlined above. The GBS NO_2-vis and NO_2-UV datasets have mean total uncertainties of 19.0% and 22.8%, respectively. To ensure the consistency of the daily RCD and uncertainty calculations, GBS VCDs were only computed if both twilights had measurements. The SAOZ dataset contains only the errors from the DOAS fitting procedure. The total uncertainty of SAOZ ozone was estimated to be 5.9% (Hendrick et al., 2011). SAOZ NO_2 measurements have an estimated precision of 1.5×10^{14} molec cm^{-2} and accuracy of 10%. Combined in quadrature, this yields a 13.6% total uncertainty for the SAOZ NO_2 measurements used in this study.

The SAOZ V3 dataset used here is different from the V2 data used in previous validation studies. For ozone, the changes are limited to new reference spectra (and therefore reprocessed dSCDs and new RCD values) for 2008-2010. For NO_2, the changes are more substantial. The V2 dataset was processed using a single set of AMFs representative of Arctic summer evenings, and the retrievals produced total columns. The V3 retrievals use the NDACC AMF LUTs, and produce 12-60 km partial columns. The same wavelength range (410-530 nm) was used for both NO_2 retrievals.

4.1.1.2 FTIR Measurements

The Bruker FTIR and the PARIS-IR employ a similar technique to retrieve vertical volume mixing ratio (VMR) profiles from measured solar-absorption spectra. VMR profiles are retrieved using the SFIT4 version 0.9.4.4 retrieval algorithm, which, as with the previous SFIT2 retrieval algorithm, is based upon the methods of Pougatchev et al. (1996). SFIT4 uses an optimal estimation method that iteratively adjusts the retrieved VMR to best fit the measured spectra (Rodgers, 2000). The trace gas a priori profiles required by SFIT4 are provided by the mean of a 40-year (1980-2020) run of the Whole Atmosphere Community Climate Model (Eyring et al., 2007), while daily pressure and temperature profiles used in the retrieval are provided by the U.S. National Centers for Environmental Prediction (NCEP) and interpolated to the geolocation of PEARL. Spectroscopic line lists are from HITRAN 2008 (Rothman et al., 2009) as recommended by the NDACC Infrared Working Group (IRWG).

The ozone retrievals for both instruments use a single microwindow, spanning 1000.0 to 1004.5 cm^{-1} (Griffin et al., 2017), which also contains the interfering species H_2O, CO_2, and the ozone isotopologues O_3^{668} and O_3^{686}. Profiles are simultaneously retrieved for H_2O and CO_2 from the Bruker FTIR spectra, whereas for PARIS-IR spectra H_2O and the ozone isotopologues are retrieved as profiles. Profiles of the remaining species, O_3^{668} and O_3^{686} for the Bruker FTIR and CO_2 for PARIS-IR, are scaled from their a priori values. Retrievals are performed on a 29-layer grid, from 0.61 to 100 km, for PARIS-IR, and on a 47-layer grid, from 0.61 to 120 km, for the Bruker FTIR.

The a priori covariance matrix for the Bruker FTIR ozone retrievals is formed from diagonal values of 5% from the surface (0.61 km) to approximately 45 km. Above 45 km, the diagonal values are scaled to 4.2% to reduce oscillations in the retrieved profiles.

Off-diagonal elements are formed from an exponential inter-layer correlation, with a correlation width of 2 km, applied from the surface to the top of the atmosphere at 120 km. The a priori covariance matrices of the interfering species H_2O and CO_2 are formed with diagonal elements of 20% for all altitudes with no inter-layer correlation. These a priori covariance matrices provided optimal DOFS while minimizing unphysical oscillations in the retrievals. The mean DOFS for ozone is approximately 5, with minimum values near 4 and maximum values near 6.

The a priori covariance matrix for PARIS-IR is constructed from diagonal values of 7% for all altitudes, with no inter-layer correlation. The a priori covariance matrices of the interfering species H_2O, O_3^{668} and O_3^{686} are formed with diagonal elements of 20% for all altitudes again with no inter-layer correlation. The mean DOFS for ozone is approximately 3, with minimum values of approximately 1 and maximum values around 4.5.

The Bruker FTIR NO_2 retrievals use five microwindows centered on 2914.65, 2918.23, 2919.53, 2922.58, and 2924.84 cm^{-1}. The interfering species are CH_4, CH_3D, H_2O, ozone and OCS. CH_4 and CH_3D are retrieved as profiles, whereas H_2O, ozone, and OCS are scaled from their a priori values. The retrievals are performed on the same 47-level grid as for ozone. The a priori covariance matrix for the NO_2 retrieval is formed from diagonal values of 40% for all altitudes, and an exponential inter-layer correlation (with a correlation width of 4 km) for the off-diagonal elements. The a priori covariance matrices of the interfering species CH_4 and CH_3D are formed with diagonal elements of 25% for all altitude levels, with no inter-layer correlation. The mean DOFS for the NO_2 retrieval is 1.2, with minimum values near 0.8 and maximum values around 1.6. The DOFS show strong seasonality, with spring and fall values between 1.2 and 1.6, and summertime values of 1-1.2.

A full error analysis was performed following Rodgers (2000), which includes the forward model parameter error and the measurement noise error. Adding these in quadrature, the mean uncertainty for the entire ozone time series from 2006-2017 is 5.6% of the retrieved total column for the Bruker 125HR and 4.9% for PARIS-IR. These values are similar to mean uncertainties of other FTIR ozone retrievals from the NDACC IRWG. The mean uncertainty for 2006-2017 is 7.5% for the Bruker FTIR NO_2 retrievals. The smoothing error was not included in the mean uncertainty calculations (von Clarmann, 2014).

The retrievals were quality controlled using the RMS values of the residual and the DOFS. An RMS:DOFS ratio of 1.0 was used in the Bruker FTIR ozone retrieval, while the PARIS-IR retrieval used a value of 6.0, and the Bruker FTIR NO_2 retrieval used a value of

1.5. Profiles with RMS:DOFS ratios higher than the aforementioned limits were excluded to eliminate poor spectral fits and maintain adequate retrieved information. Additionally, several outliers were omitted from the datasets based on a qualitative analysis of the fitted spectra.

4.1.2 Satellite Instruments

The Odin satellite, carrying the OSIRIS instrument (Murtagh et al., 2002; Llewellyn et al., 2004), was launched in February 2001. OSIRIS measures limb-radiance profiles at a 1-2 km resolution, and measurements near PEARL are available throughout the sunlit part of the year. The optical spectrograph in OSIRIS is a UV-visible grating spectrometer that measures scattered sunlight from 280 to 800 nm with 1 nm resolution. Spectra are recorded on a 1353 × 286 pixel CCD detector.

The ozone profiles in the version 5.10 dataset (Bourassa et al., 2018) used in this study are retrieved using the SaskMART algorithm. SaskMART (Degenstein et al., 2009) is a multiplicative algebraic reconstruction technique (MART) that uses information from the UV and visible ozone absorption bands. The SASKTRAN RTM (Zawada et al., 2015) is used as the forward model in the retrievals. The v5.10 dataset corrects a pointing bias drift, apparent in the preceding version from 2012 onward. The retrieval algorithm is unchanged compared to previous versions. The NO_2 retrievals use a different approach. A modified DOAS algorithm is used to retrieve SCDs, which are converted to profiles using MART and the SASKTRAN model. The OSIRIS version 6.0 NO_2 (Sioris et al., 2017) is used in this study. The v6.0 dataset is substantially different from the previous operational product (v3.0) which used optimal estimation and a different forward model.

ACE (Bernath et al., 2005), on board the SCISAT satellite, consists of two main instruments: ACE-FTS and ACE-MAESTRO. Launched in August 2003, SCISAT takes solar occultation measurements. The instruments collect data near PEARL during sunset from late February to mid-March, and during sunrise from late September to mid-October.

The ACE-FTS is a high-resolution (0.02 cm^{-1}) infrared Fourier transform spectrometer that measures in the 750-4400 cm^{-1} range. Interferograms are recorded on two photovoltaic detectors (InSb and HgCdTe). The first step in the retrieval is the determination of pressure and temperature profiles based on a detailed CO_2 analysis. The VMR profiles are then retrieved using a global nonlinear least squares fitting algorithm (Boone et al., 2005). The ACE-FTS data version 3.5/3.6 (Boone et al., 2013) is included in this study. The v3.5 and v3.6 data use identical algorithms in different computing environments.

The current processing differs from the previous version (v3.0) only in the low-altitude pressure and temperature inputs from October 2011 onward.

The ACE-MAESTRO is a UV-visible-near-IR double spectrograph with a resolution of 1-2 nm. The two channels cover 280-550 nm and 500-1030 nm, and spectra are recorded on 2014-pixel linear photodiode array detectors. Profiles are retrieved using a two-step approach where SCDs are retrieved using a modified DOAS procedure, and vertical profiles are derived using a nonlinear Chahine relaxation inversion (McElroy et al., 2007). The retrievals use ACE-FTS temperature and pressure profiles. The ACE-MAESTRO version 3.13 ozone product is used in this study. The v3.13 retrieval improves the reference spectrum and error calculations of the preceding version (v3.12/3.12.1). The v3.13 dataset does not include NO_2, since it is retrieved from the UV spectrometer, and the UV channel has been experiencing gradual degradation since the launch. UV data are not considered useful past October 2010[1]. ACE-MAESTRO NO_2 was excluded from this study due to the low coincidence count of the available data in the v3.12.1 dataset.

4.2 Comparison Methodology

The validation metrics used to assess the similarity of the datasets, as well as the methods for selecting coincident measurements, are described in Section 4.2.1. The procedures for extending ozone profiles using ozonesonde data, and for scaling NO_2 columns using a photochemical model are described in Section 4.2.2. The methodology used to assess the long-term consistency of the satellite datasets is described in Section 4.2.3. Throughout this chapter, the convention is that ‘spring’ and ‘fall’ are defined as the periods when the sun crosses the horizon daily (i.e. 90° SZA is available). These periods, from day 53 to day 105 (23 February to 14/15 April) and from day 240 to day 291 (27/28 August to 17/18 October), include all ACE measurements, and all ZSL-DOAS measurements with the ideal 86-91° SZA range. The remainder of the sunlit part of the year is referred to as summer.

4.2.1 Comparison Metrics and Coincidence Criteria

To evaluate systematic differences between the datasets, mean absolute and relative differences were used. The mean absolute difference between a set of coincident measurements

---

[1] ACE-MAESTRO Level 2 Version 3.13 Data Description and File Formats, `https://databace.scisat.ca/level2/mae_v3.13/ACE-MAESTRO-V3.13-Data.pdf`. Accessed 2018/09/28.

x and y is given by

$$\Delta_{abs} = \frac{1}{N}\sum_{i=1}^{N}(x_i - y_i), \tag{4.1}$$

where N is the number of coincident measurements. The mean relative difference, defined with respect to the average of the measurement pairs, is given by

$$\Delta_{rel} = \frac{1}{N}\sum_{i=1}^{N}\frac{(x_i - y_i)}{(x_i + y_i)/2} \times 100\%. \tag{4.2}$$

The standard errors ($\sigma/\sqrt{N}$, where σ is the standard deviation of the differences) were also calculated for the mean absolute and relative differences. The standard error is the reported error throughout this paper. In addition, to quantify the statistical spread of the absolute differences, the *RMSD* is used:

$$RMSD = \sqrt{\frac{1}{N}\sum_{i=1}^{N}(x_i - y_i)^2}. \tag{4.3}$$

Unlike the standard deviation of the differences, *RMSD* captures the bias between the datasets as well. If there is no bias between the datasets, then $RMSD = \sigma$. For satellite to ground-based comparisons, the sign convention is such that x is the satellite dataset and y is the ground-based dataset.

The statistical dependency of the datasets was evaluated using Pearson's correlation coefficient (R). In correlation plots, the linear relationship between the datasets was characterized using the ordinary least squares (OLS) method, and the reduced major-axis (RMA) method (York et al., 2004). The RMA solution is equivalent to minimizing the sum of squares of the perpendicular distances between the points and the fitted line. Since the RMA solution is symmetrical, it doesn't require the assignment of one dataset as the independent variable. Measurement uncertainties were not included in the linear fits, since some of the datasets include random errors only, while some of the datasets do not provide uncertainty values for individual measurements, only an estimate of the overall uncertainty.

Since pairwise comparison metrics are sensitive to uncertainties in both datasets, triple colocation analysis (TCA) is also used. TCA is commonly used in global validation studies (Stoffelen, 1998; Toohey and Strong, 2007; Loew and Schlenz, 2011; McColl et al., 2014; Su et al., 2014; Gruber et al., 2016; Kinzel et al., 2016; Loew et al., 2017) to estimate uncertainties in the individual datasets. By adding a third coincident dataset, TCA allows an estimate of the root-mean-square error (*RMSE*) and correlation with respect to the unknown truth for each dataset. The *RMSE* is the square root of the random error variance, and is given by

$$RMSE(x) = \sqrt{\sigma_x^2 - \frac{\sigma_{xy}\sigma_{xz}}{\sigma_{yz}}}, \tag{4.4}$$

for one dataset, using the three coincident datasets x, y and z. $\sigma_{xy}, \sigma_{xz}, \sigma_{yz}$ are the covariances of the datasets, and σ_x^2 is the variance of the measurements in question. The correlation with respect to the unknown truth is defined as

$$R^t = \sqrt{\frac{\sigma_{xy}\sigma_{xz}}{\sigma_x^2\sigma_{yz}}}. \tag{4.5}$$

The *RMSE* and R^t are analogous to the *RMSD* and R values from pairwise comparisons, however while *RMSD* and R are sensitive to uncertainties in both datasets, *RMSE* and R^t are only sensitive to uncertainties in dataset x.

All comparison metrics (pairwise or triple colocation) used in this study are affected by colocation mismatch, that is differences between the spatiotemporal sampling of the inhomogeneous ozone and NO_2 distributions by different instruments. Ozone colocation errors have been estimated by Verhoelst et al. (2015). They used GOME-2 and NDACC ozone measurements, combined with modeled observations, to quantify the error budgets of satellite to ground-based intercomparisons for a host of ground-based stations (67°N to 75°S). They found that colocation errors dominate the error budgets, and can account for differences of 10% or more at high-latitude stations. Using similar methods, colocation errors between OSIRIS and ACE-FTS ozone can also be estimated. For the coincidence criteria used in this study (12 h and 500 km), and including the Arctic (poleward of 60°N) only, the mean relative difference between OSIRIS and ACE-FTS 10-55 km partial columns is expected to be 6.4-6.9%[2]. Colocation errors for satellite to ground-based comparisons are expected to be similar, while for NO_2, the values are expected to be larger due to the high latitudinal gradient and diurnal variation.

The contribution of colocation error to the *RMSE* values varies depending on the combination of instruments, due to differences in viewing geometries and measurement techniques. In order to limit the effect of colocation error, the calculated *RMSE* values are specific to instrument pairs, and only the sum of the *RMSE* values is reported for each pair. This way, satellite datasets are not penalized when grouped with two ground-based instruments, and vice versa. *RMSE* values for the individual instruments were calculated as the average *RMSE* from all triplets that included both instruments in the pair. For

---

[2] P. Sheese, personal communication.

Table 4.3: Sum of the averaged *RMSE* values for all possible instrument pairs that involve at least one satellite instrument. The values were calculated using TCA, as described in Section 4.2.1. The uncertainty values are the standard errors on the averaged *RMSE* values, combined in quadrature. The number of triplets considered in the average (i.e. the number of third instruments), as well as the total number of triple coincidences (N_{tot}) are indicated for each pair. Instrument abbreviations are given in Table 4.1.

Instr. Pair	Ozone Sum of *RMSE* (DU)	Triplets	N_{tot}	Instr. Pair	NO_2 Sum of *RMSE* (x10^{14} molec cm^{-2})	Triplets	N_{tot}
OS, AF	25.8 ± 2.8	5	4047		—		
OS, AM	35.2 ± 1.4	5	3550		—		
AF, AM	21.2 ± 1.7	5	5229		—		
OS, GV	36.1 ± 2.1	6	23303	OS, GV	5.7 ± 0.5	3	1918
OS, SA	32.2 ± 3.0	6	9687	OS, GU	5.6 ± 0.3	3	1749
OS, BK	36.0 ± 4.5	6	23309	OS, SA	5.5 ± 0.4	3	1204
OS, PA	42.2 ± 3.4	6	17268	OS, BK	4.7 ± 0.3	3	2597
OS, BW	27.2 ± 2.1	4	33372	AF, GV	3.3 ± 0.4	3	887
AF, GV	38.4 ± 4.5	5	2874	AF, GU	3.5 ± 0.4	3	656
AF, SA	33.3 ± 5.5	5	3169	AF, SA	3.7 ± 0.3	3	925
AF, BK	41.1 ± 5.2	5	5943	AF, BK	3.7 ± 0.1	3	482
AF, PA	41.5 ± 5.7	5	12252		—		
AM, GV	46.5 ± 3.3	5	2439		—		
AM, SA	40.0 ± 4.7	5	2669		—		
AM, BK	46.9 ± 5.2	5	5277		—		
AM, PA	50.7 ± 4.4	5	10950		—		

example, using ACE-FTS and GBS ozone, the triplets with SAOZ, Bruker FTIR, PARIS-IR, ACE-MAESTRO, and OSIRIS data were considered, the *RMSE* values (five for both ACE-FTS and GBS) were averaged, and then added to get the final value shown in Table 4.3. This process was repeated for all instrument pairs considered in this study. The final *RMSE* values provide an upper limit on the expected spread between data from various instrument pairs. R^t values for each instrument were calculated in a similar fashion, except those values were not added in the final step.

Temporal coincidence criteria were selected based on the measurement methods of the instruments. For twilight-measuring instruments (ACE-FTS, ACE-MAESTRO, and the ZSL-DOAS instruments), comparisons were restricted to the same twilight. In addition, comparisons between ACE-FTS and ACE-MAESTRO were restricted to the same occultation. For all other instrument pairs, coincidences were generated by pairing measurements from both datasets to the nearest measurement in the other dataset, within a ±12 hour time window. For triple colocation, these coincidence criteria were applied simultaneously to all three pairs within the group.

For spatial coincidences, satellite measurements within 500 km of the PEARL Ridge Lab were considered. The approximate location of the air masses sampled by each instrument is shown in Figure 2 of Adams et al. (2012a). The primary reason for using a 500 km radius was to reduce the impact of the spring and fall latitudinal NO_2 gradient on the comparison results. These impacts are assessed in Section 4.5.1. Comparison results for a 1000 km radius around PEARL show that for NO_2, mean differences change significantly and the correlation coefficients decrease, when compared to the 500 km results. Figure 5 of Adams et al. (2012a) shows modeled ratios of NO_2 partial columns at various latitudes for SZA = 90°, as a function of day of the year. Ratios of partial columns at 78°N over 82°N (typical difference for coincidences within 500 km) could be as high as 7 in early spring and late fall, while latitude differences typical for a 1000 km radius correspond to ratios of 20-25 during the same periods. Ozone comparisons show only small differences when the radius is increased to 1000 km. Using the 500 km radius ensures that the results are directly comparable to Adams et al. (2012a), who also used this radius around PEARL to compare datasets from the instruments included in this study.

4.2.2 Partial Columns

ACE-FTS and ACE-MAESTRO VMR profiles were converted to number density using ACE-FTS pressure and temperature profiles. The OSIRIS profiles are reported as number densities. For the integration to partial columns, profiles were accepted only if all levels in the selected altitude range had valid values. While negative VMR values for ACE-FTS and ACE-MAESTRO were accepted as valid data, none of the profiles considered in the comparisons include negative values within (or immediately outside) the ozone or NO_2 partial column ranges.

For comparisons between satellite instruments, ozone partial columns from 14 to 52 km were calculated, in order to maximize the number of available profiles from all three satellite instruments. For comparison to ground-based instruments, the satellite partial columns were extended down to the altitude of the given instrument (610 m for the PEARL Ridge Lab and 10 m for the EWS; a difference of 1-2 DU) using ozonesonde profiles. This approach is similar to the methods of Adams et al. (2012a) and Fraser et al. (2008). Sonde profiles were interpolated to the satellite measurement time, and the resulting profiles were smoothed between 12-16 km with a moving average to avoid discontinuities in the joint profile. Excluding the smoothing step results in a mean change of only 0.3% in the satellite total columns. Ozone above 52 km was neglected, since it accounts for less than 0.2% (<1 DU) of the total ozone column according to the NDACC ozone climatology (Hendrick et al., 2011) for Eureka.

For NO_2 partial columns, an altitude range of 12-40 km was chosen. The lower altitude limit was determined by the ZSL-DOAS retrievals, since the standardized NDACC AMFs only include NO_2 above 12 km. The upper value was set to 40 km to ensure that the results are comparable to Adams et al. (2012a). No correction was applied to extend the columns above 40 km, since NO_2 above that altitude accounts for less than 2% of the total column, which is much smaller than the measurement uncertainties for the ground-based instruments. For OSIRIS, the upper altitude limit was reduced to 32 km, since most profiles only extended to that altitude. For comparison to ground-based instruments, OSIRIS NO_2 partial columns were scaled to 40 km using NDACC LUT profiles calculated using the time, geolocation, and mean wavelength of the OSIRIS measurements.

Diurnal variation of NO_2 must be considered when comparing measurements taken at different times of the day. In the spring and fall, NO_2 increases during the day due to release from night-time reservoirs. During the polar day (mid-April to late-August), NO_2 decreases at noon due to photolysis to NO. To account for the diurnal variation, NO_2 partial columns were scaled to local noon (e.g. Lindenmaier et al., 2011; Adams et al., 2012a) using a photochemical box model (McLinden et al., 2000; Brohede et al., 2007a). The model was initialized for 80°N using the NDACC surface albedo climatology and ozonesonde profiles of ozone and temperature interpolated to local noon for each day. For a detailed discussion of the scaling procedure, see Adams et al. (2012a).

Diurnal variation of NO_2 also leads to errors in individual measurements through the so-called diurnal effect (Fish et al., 1995; Newchurch et al., 1996; Hendrick et al., 2006; McLinden et al., 2006). The diurnal effect occurs mainly because sunlight passes through a range of SZA before reaching the instruments, and NO_2 is at different stages of its diurnal cycle for different SZA. For ACE-FTS, NO_2 profiles below 25 km can increase by up to 50% as a result of the diurnal effect (Kerzenmacher et al., 2008). For OSIRIS, these errors are less relevant since only measurements with SZA greater than 85° are expected to change due to the diurnal effect (McLinden et al., 2006; Brohede et al., 2007b), and the v6.0 dataset used here contains no such measurements near PEARL. The ZSL-DOAS instruments likely underestimate NO_2, since the SZA at 30 km along the estimated line-of-sight is $\sim$3° smaller ($\sim$2° for UV) than the SZA at the instrument location for the standard 86-91° SZA window. Bruker FTIR measurements are affected in the early spring, when SZA in the 30 km layer can be up to 5° smaller than the SZA at the ground. The discrepancy for the Bruker FTIR, however, quickly decreases in the spring as the sun climbs higher in the sky. In addition to the diurnal effect, the diurnal variation of

NO_2 also leads to strong latitudinal gradients in the spring and fall. NO_2 concentrations are smaller at higher latitudes, due to the decreasing number of daylight hours with increasing latitude. The impact of the diurnal effect and the latitudinal gradient on the comparison results is examined in Section 4.5.1. For satellite to ground-based comparisons as a function of SZA, the SZA at the location of the ground-based instrument (and at the time of the ground-based measurement) was used.

Satellite profiles were not smoothed in this study, for reasons detailed below. The OSIRIS, ACE-FTS and ACE-MAESTRO satellite instruments measure at a higher vertical resolution than the ground-based instruments considered here. To account for this difference, the satellite profiles might be smoothed with the ground-based averaging kernels according to the method of Rodgers and Connor (2003). Smoothing the satellite profiles for comparisons with the Bruker FTIR and the PARIS-IR is straightforward, and is routinely implemented in validation studies (e.g. Dupuy et al., 2009; Batchelor et al., 2010; Griffin et al., 2017). However, given the good sensitivity of the FTIR instruments to most of the ozone and NO_2 columns (Batchelor et al., 2009; Lindenmaier et al., 2011), smoothing is expected to have a small impact on ozone and NO_2 comparisons.

The Brewer and ZSL-DOAS retrievals, on the other hand, do not provide averaging kernels or use a priori ozone profiles. To address this problem, approximate ZSL-DOAS averaging kernels were developed at BIRA-IASB in the form of LUTs. The averaging kernel calculations are based on the methods of Eskes and Boersma (2003). In the current iteration, however, the averaging kernels are calculated for 90° SZA only. This limits their use to spring and fall for PEARL data. Furthermore, most of the changes in the smoothed profiles can be attributed to the systematic differences between the unsmoothed satellite profiles and the climatology used as a priori in the smoothing process.

Considering only the profiles coincident with ground-based measurements, satellite-plus-sonde ozone columns change, on average, by less than 0.2% and 1.4% when smoothed with the Bruker FTIR and PARIS-IR averaging kernels, respectively. The magnitude of the change is similar for all satellite datasets. Smoothing with the ZSL-DOAS averaging kernels changes the spring and fall ozone columns by less than 1%. Satellite NO_2 partial columns change by less than 2% when smoothed with the Bruker FTIR averaging kernels. The change is less than 2.5% when smoothed with the ZSL-DOAS averaging kernels for the visible range, while smoothing with the UV averaging kernels leads to changes of 3-4%. All of the changes are small compared to the level of agreement between, and the combined error budgets of, the satellite minus ground-based instrument pairs for both ozone and NO_2.

Given the potential problems with the ZSL-DOAS averaging kernels, and the lack of

Brewer averaging kernels, no smoothing was performed for the satellite to ground-based comparisons, in order to treat all datasets in a consistent manner.

4.2.3 Time Series Analysis

Given the long data record for all instruments included in this study (see Table 4.1), the decadal stability of the satellite data products can be assessed. For each instrument pair, the daily mean relative differences were calculated, and a linear fit with respect to time was used to obtain an estimate of the drift between the two instruments (e.g. Adams et al., 2014; Hubert et al., 2016). The linear regression was performed using a bi-square weighted robust fitting method (Holland and Welsch, 1977). Robust methods are preferable over OLS methods, since the former are less sensitive to outliers and data gaps. The uncertainties given by the robust fit were verified using bootstrap resampling (Efron and Tibshirani, 1986), and the two uncertainty calculations were found to be in very good agreement.

The uncertainties reported for the drift values (σ) were calculated using a correction for the autocorrelation of the noise, (Weatherhead et al., 1998; Adams et al., 2014) such that

$$\sigma = 2\sigma_{fit} \times \sqrt{\frac{1+\phi}{1-\phi}}, \tag{4.6}$$

where σ_{fit} is the uncertainty from the robust fit, and ϕ is the lag-1 autocorrelation of the noise. The residual daily mean relative differences are assumed to represent the distribution of noise in the data (Gardiner et al., 2008). The values of σ yield a more conservative estimate of the uncertainty as compared to the fit uncertainties. Potential seasonality in the relative difference time series was not taken into account explicitly, due to the limitations of OLS fitting methods for sparsely sampled time series, and the large scatter (relative to the potential seasonality) in the relative difference datasets. To assess the feasibility of drift detection for each dataset, the number of years (n^*) required to detect a real drift of a given magnitude in the data was also calculated, as given by Weatherhead et al. (1998):

$$n^* = \left(\frac{3.3\sigma_N}{\mid \omega \mid} \sqrt{\frac{1+\phi}{1-\phi}} \right)^{2/3}. \tag{4.7}$$

The factor of 3.3 returns n^* for the given drift value (ω) with 90% certainty, and σ_N is the standard deviation of the noise. The statistical significance of the drift value for each dataset was assessed using both the error on the drift (σ) and the number of years (n*)

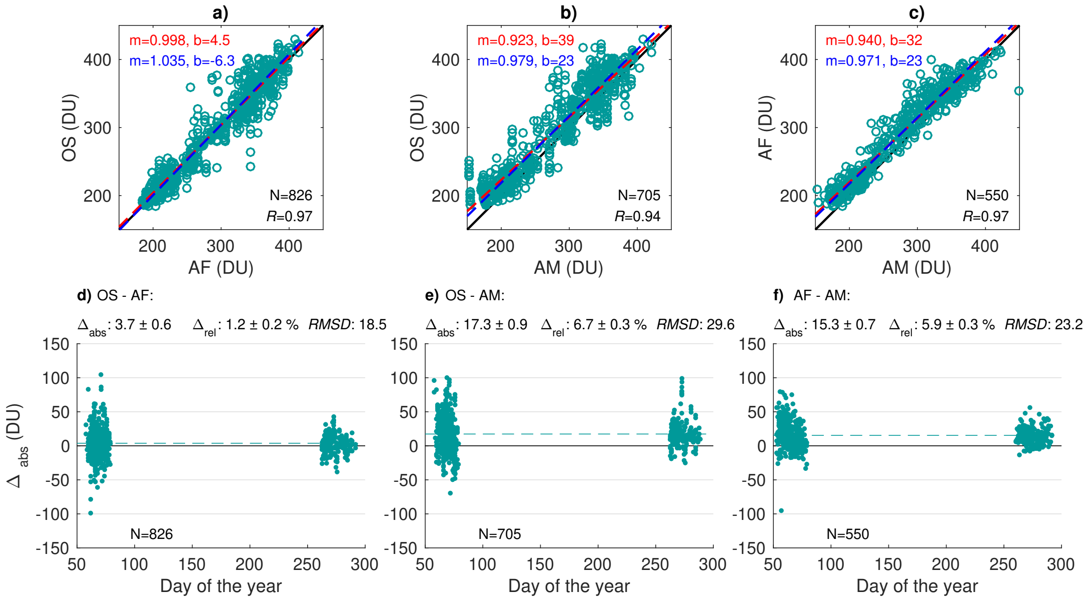

Figure 4.1: **a)** to **c)** Correlation plots and **d)** to **f)** seasonal absolute differences between OSIRIS, ACE-FTS, and ACE-MAESTRO 14-52 km ozone partial columns. The correlation plots include best fit lines using the OLS (red dashed line) and RMA (blue dashed line) methods, as well as the one-to-one line (black). The slope, intercept, number of coincidences, and correlation coefficient are given as m, b, N, and *R*, respectively. In the difference plots, the dashed lines show the mean absolute difference. The errors shown for the mean differences and the *RMSD* values are the standard error. Abbreviations and measurement periods are given in Table 4.1.

required to detect the drift with 90% certainty.

In addition to the drift values for each satellite minus ground-based time series, the mean drift for each satellite data product was calculated using a variance-weighted mean (Hubert et al., 2016). Weights of σ_i^{-2} were used, where σ_i is the uncertainty of the drift value for the i^{th} instrument pair in the average. The uncertainty on the mean drift is given by $(\sum \sigma_i^{-2})^{-1/2}$.

4.3 Ozone Results

4.3.1 Satellite Versus Satellite Partial Columns

Results of the comparisons between OSIRIS, ACE-FTS and ACE-MAESTRO 14-52 km ozone partial columns are shown in Figure 4.1. The three datasets show good correlation, with correlation coefficients of 0.94 or greater (Fig. 4.1a-c). The slopes of the linear fits are close to 1, and the OLS and RMA methods agree well. The RMA fit is perhaps a better

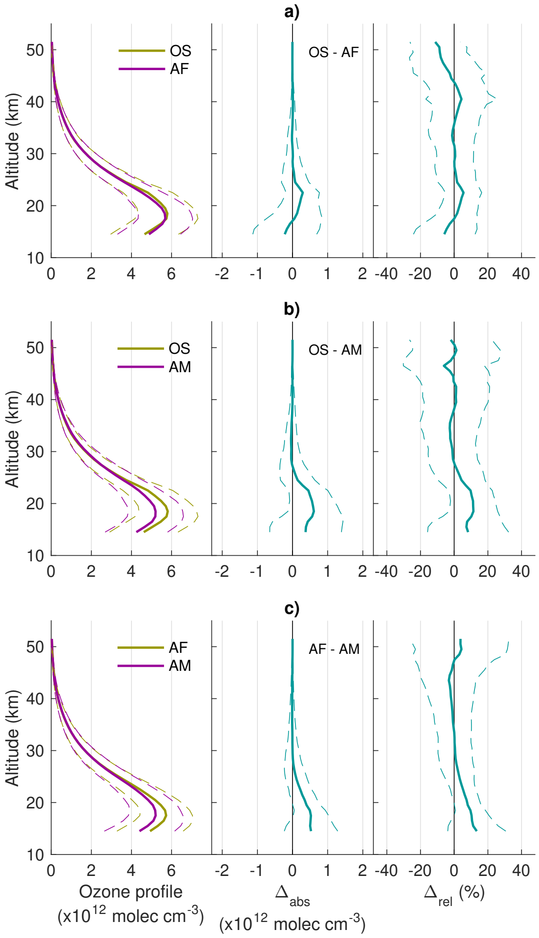

Figure 4.2: Mean ozone number density profiles and mean differences for all coincidences between OSIRIS, ACE-FTS and ACE-MAESTRO. The left panels show the mean profiles, with one standard deviation limits indicated by the dashed lines. The middle and right panels show the absolute and relative differences, respectively, at each altitude level.

reference in this case, since none of the satellite datasets could be considered the reference dataset for the OLS fit. Correlation coefficients with the unknown truth (R^t from TCA) are 0.97 or greater for all three satellite instruments. Absolute differences between the satellite datasets are shown in Figure 4.1d-f. OSIRIS and ACE-FTS show a mean relative difference of 1.2%. ACE-MAESTRO is systematically lower than OSIRIS and ACE-FTS, by 6.7% and 5.9%, respectively. The spread of the absolute differences (indicated by the *RMSD* value) is lowest for the OSIRIS minus ACE-FTS comparison, at 18.5 DU. *RMSD* values for ACE-MAESTRO are higher, 29.6 DU and 23.2 DU, when compared to OSIRIS and ACE-FTS, respectively. The *RMSD* values for the OSIRIS comparisons are within the maximum range expected from the *RMSE* calculations using TCA (Table 4.3), while the *RMSD* between the ACE instruments is outside the maximum expected range. The estimated values of the drift are 1.3 ± 2.4 % decade^{-1} for OSIRIS minus ACE-FTS, -2.1 ± 3.8 % decade^{-1} for OSIRIS minus ACE-MAESTRO, and -2.1 ± 3.3 % decade^{-1} for ACE-FTS minus ACE-MAESTRO. None of these values are statistically significant, indicating that there are no systematic changes between satellite datasets over time.

Previous versions of the ozone products from the three satellite instruments have been compared before. Fraser et al. (2008) compared ACE-FTS v2.2 and ACE-MAESTRO v1.2 partial columns between 15 and 40 km in a 500 km radius around PEARL for 2004-2006, and found mean relative differences of 5.5% to 22.5%. The 2003-2017 mean of 5.9% found in this study falls within this range. Dupuy et al. (2009) compared OSIRIS v2.1, ACE-FTS v2.2, and ACE-MAESTRO v1.2 profiles on a global scale for 2004-2006. They found that ACE-MAESTRO agreed with OSIRIS to ±7% in the 18-59 km range, while ACE-FTS was on average 6% larger than OSIRIS between 9 and 45 km, and progressively larger (up to 44%) between 45 and 60 km. This is opposite to the findings of this study, where ACE-FTS and ACE-MAESTRO partial columns are both smaller than OSIRIS partial columns. The discrepancy is likely due to the fact that coincidences in this study are limited to the Arctic, while Dupuy et al. (2009) covered all latitudes. This conclusion is also supported by Adams et al. (2012a), who compared OSIRIS v5.0x, ACE-FTS v3.0, and ACE-MAESTRO v1.2 partial columns for 14-52 km (same altitude range as in this study) near PEARL for 2004-2010. Mean relative differences between OSIRIS and ACE-FTS were reported to be 1.2%, identical to the value found in this study. Comparisons involving ACE-MAESTRO partial columns show an approximate doubling of the relative differences, from 2.8% (Adams et al., 2012a) to 6.7% and 5.9%. Given that the OSIRIS minus ACE-FTS comparison remained unchanged, this difference is likely due to changes in the more recent ACE-MAESTRO v3.13 dataset. The relative differences show the same doubling for the 2004-2010 period (used by Adams et al. (2012a)), indicating that the issue is related to the v3.13 processing. Adams et al. (2012a) also reported slopes significantly less than 1 for OSIRIS minus ACE-MAESTRO and ACE-FTS minus ACE-MAESTRO comparisons, with y-intercepts similar to those shown in red in Figure 4.1b and c.

To further investigate this apparent low bias in ACE-MAESTRO data, 14-52 km ozone number density profiles were also compared for all three satellite instruments. The mean profiles and standard deviations for all coincidences are shown in Figure 4.2. ACE-MAESTRO underestimates the peak ozone concentrations compared to both OSIRIS (Fig. 4.2b) and ACE-FTS (Fig. 4.2c), by more than 10%. OSIRIS and ACE-FTS profiles agree well (Fig. 4.2a), with only a small difference in the altitude of the peak ozone

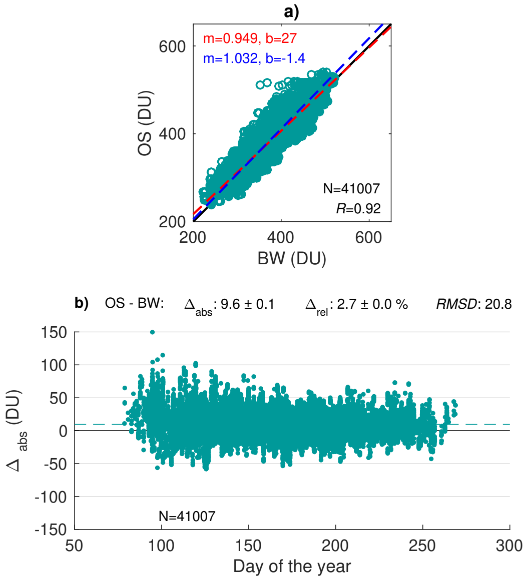

Figure 4.3: Same as Figure 4.1, with OSIRIS-plus-sonde surface-52 km ozone columns and Brewer total columns.

concentrations. The agreement above 25 km is good for all instrument pairs. ACE-FTS number densities are larger than OSIRIS above 45 km, consistent with Dupuy et al. (2009).

4.3.2 Satellite Versus Ground-based Partial Columns

Correlation plots of the satellite-plus-sonde ozone columns (surface-52 km) and the ground-based datasets are shown in Figures 4.3 and 4.5. Comparisons with the Brewer ozone data (Fig. 4.3) are only shown for OSIRIS, since there are too few (less than 15) Brewer measurements in early spring and late fall for meaningful comparisons with ACE. The instrument pairs have correlation coefficients of 0.86-0.95 for OSIRIS, 0.90-0.96 for ACE-FTS, and 0.87-0.94 for ACE-MAESTRO. The ZSL-DOAS instruments show better correlation with the ACE instruments than the direct-sun measurements, while OSIRIS shows high correlation coefficients for all instruments except PARIS-IR. R^t values from TCA are 0.94-0.97 for OSIRIS, 0.94-0.96 for ACE-FTS, and 0.92-0.94 for ACE-MAESTRO. R^t for the ground-based instruments ranges from 0.92 to 0.98. The seasonal evolution of the absolute differences between the instrument pairs, as well as the mean absolute and relative differences and *RMSD* values for each pair are shown in Figure 4.6. Most instrument pairs (with the exception of OSIRIS minus Brewer, ACE minus Bruker FTIR, and ACE-MAESTRO minus PARIS-IR) agree within the combined retrieval un-

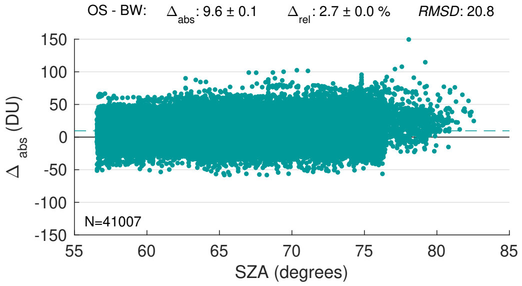

Figure 4.4: Same as Figure 4.3b, with seasonal absolute differences between OSIRIS-plus-sonde surface-52 km ozone columns and Brewer total columns, as a function of the SZA corresponding to each Brewer measurement.

certainties (absolute and relative) indicated in Table 4.2. Note that the error estimates for the satellite data and for the Brewer measurements include random errors only.

The comparison of OSIRIS-plus-sonde ozone columns to Brewer data shows a mean relative difference of 2.7%, with the largest differences observed in the spring (Fig. 4.3). The vast majority of the coincidences, however, occur in the summer, and so the larger springtime differences contribute minimally to the mean. The relative differences (not shown) are distributed evenly throughout the year. The *RMSD* value of 20.8 DU is within the expected range from the *RMSE* calculations shown in Table 4.3. OSIRIS-plus-sonde ozone columns show no SZA-dependent differences when compared to Brewer data (Fig. 4.4). Brewer measurements only extend above 76° SZA for a few years, so the distribution of the differences for those angles is not well sampled. Removing Brewer measurements with SZA $>$ 76° does not affect the comparison results.

OSIRIS and ACE-FTS satellite-plus-sonde columns are consistently larger than the GBS ozone columns, by 4.4% and 2.6%, respectively. The absolute differences are most pronounced for the higher ozone values in early spring. OSIRIS and ACE-FTS show better agreement with the SAOZ dataset across the range of ozone column values, with mean relative differences of 2.3% and -0.5%, respectively. ACE-MAESTRO ozone is systematically lower than OSIRIS and ACE-FTS, and therefore agrees better with GBS (-1.2%) than SAOZ (-4.4%). The offset between the GBS and SAOZ intercomparisons is similar for both ACE instruments. The largest absolute differences (as well as relative differences, not shown) for each satellite minus ZSL-DOAS instrument pair are observed in the early spring (Fig. 4.6a, c, and e). The *RMSD* values for the satellite minus ZSL-DOAS comparisons are all within the maximum expected range shown in Table 4.3. Comparisons to the GBS dataset consistently result in higher *RMSD* (30.4, 33.9, and 36.5 DU for OSIRIS, ACE-FTS, and ACE-MAESTRO) than comparisons to SAOZ (26.7, 24.4, and 35.5 DU,

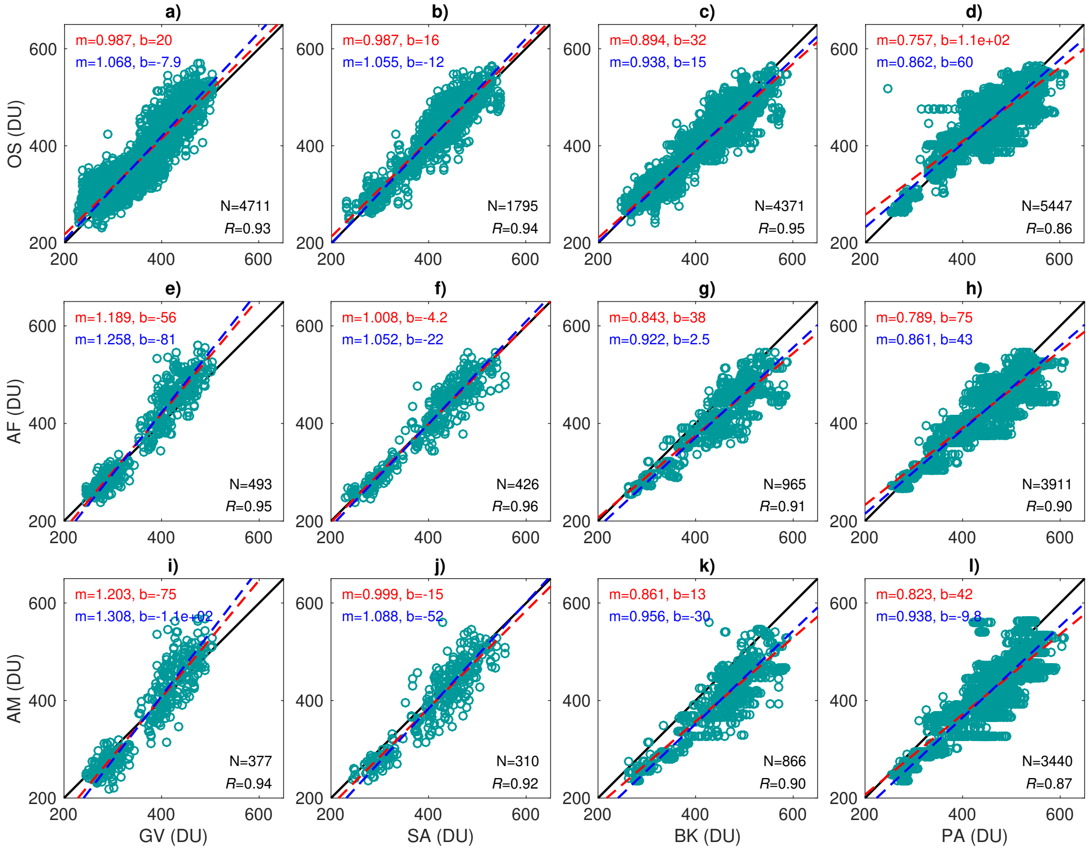

Figure 4.5: Correlation plots for satellite-plus-sonde surface-52 km ozone columns (y-axes) against the ground-based total columns (x-axes). The plots include best fit lines using the OLS (red dashed line) and RMA (blue dashed line) methods, as well as the one-to-one line (black). The slope, intercept, number of coincidences, and correlation coefficient are given as m, b, N, and R, respectively. Abbreviations and measurement periods are given in Table 4.1.

respectively). This difference is smallest for ACE-MAESTRO, and the highest *RMSD* values are also seen in the ACE-MAESTRO comparisons. The satellite-plus-sonde minus ZSL-DOAS ozone differences (Fig. 4.7a, c, and e) show no obvious SZA dependence. Most datapoints cluster around 88.5°, the mean SZA of the ideal twilight ZSL-DOAS measurements. The large scatter in these comparisons reflects the large differences observed in the spring.

All three satellite-plus-sonde ozone datasets are systematically lower than the Bruker FTIR (Fig. 4.6b, d, and f). This difference (absolute and relative) is also most pronounced in the spring, resulting in large mean relative differences for ACE-FTS and ACE-MAESTRO comparisons, -7.5% and -12.0%, respectively. In the case of OSIRIS, the agreement is -2.1%, and it remains better than 3% in all seasons. The satellite-plus-

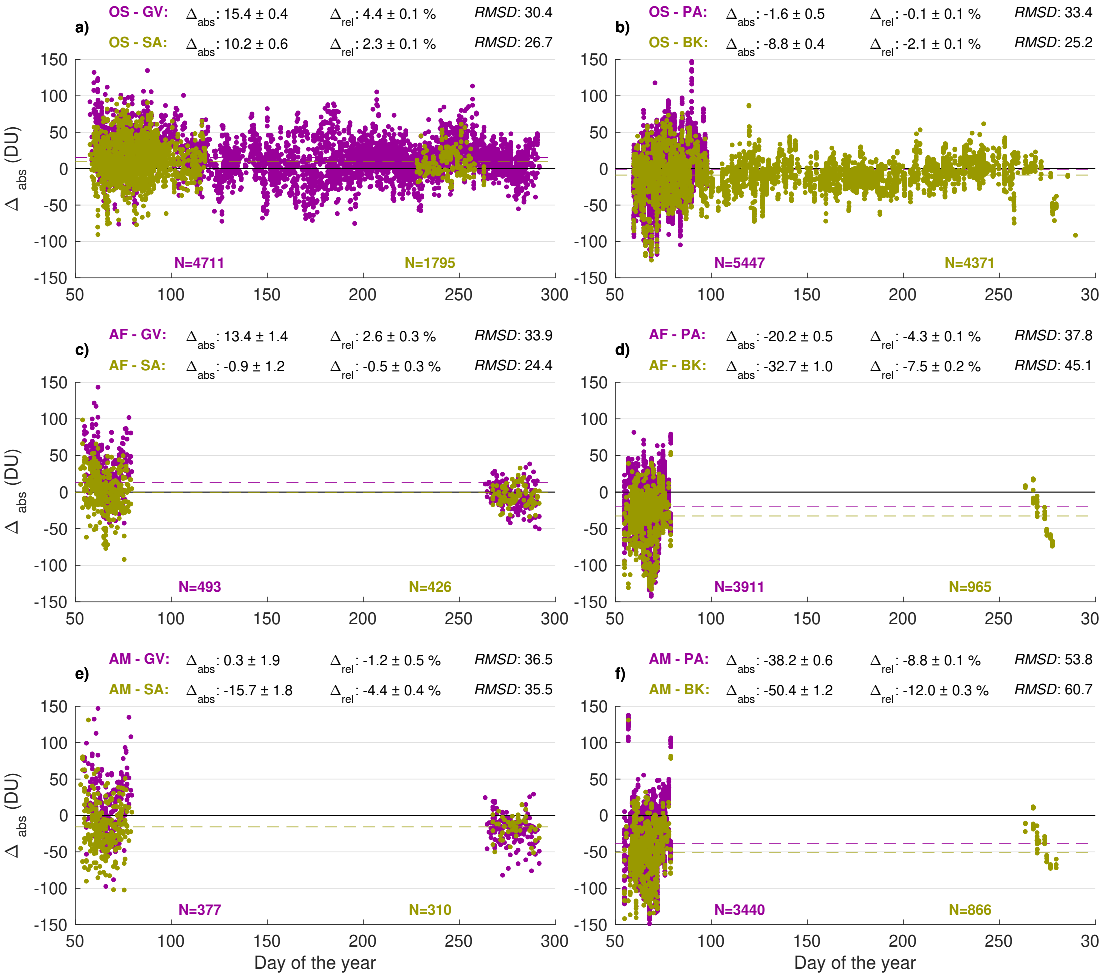

Figure 4.6: Seasonal absolute differences between satellite-plus-sonde surface-52 km ozone columns and the ground-based datasets. The dashed lines represent the mean absolute differences. The errors shown for the mean differences and the *RMSD* values are the standard error. Abbreviations and measurement periods are given in Table 4.1.

sonde columns show better agreement with the PARIS-IR, resulting in mean relative differences of -4.3% for ACE-FTS, -8.8% for ACE-MAESTRO, and -0.1% for OSIRIS. The OSIRIS minus Bruker FTIR differences (Fig. 4.7b) are largely independent of SZA when the sun is high, while for SZA $> 80°$ the differences increase due to atmospheric variability in the springtime. The OSIRIS minus PARIS-IR comparisons show the same pattern, with slightly more scatter in the absolute differences. The ACE instruments show large scatter when compared to the Bruker FTIR and PARIS-IR ozone columns (Fig. 4.7d and e), with the largest negative outliers concentrated around SZA $\gtrsim 84°$.

Comparisons of 14-52 km satellite partial columns to Bruker FTIR and PARIS-IR partial columns show small changes in relative differences (compared to surface-52 km

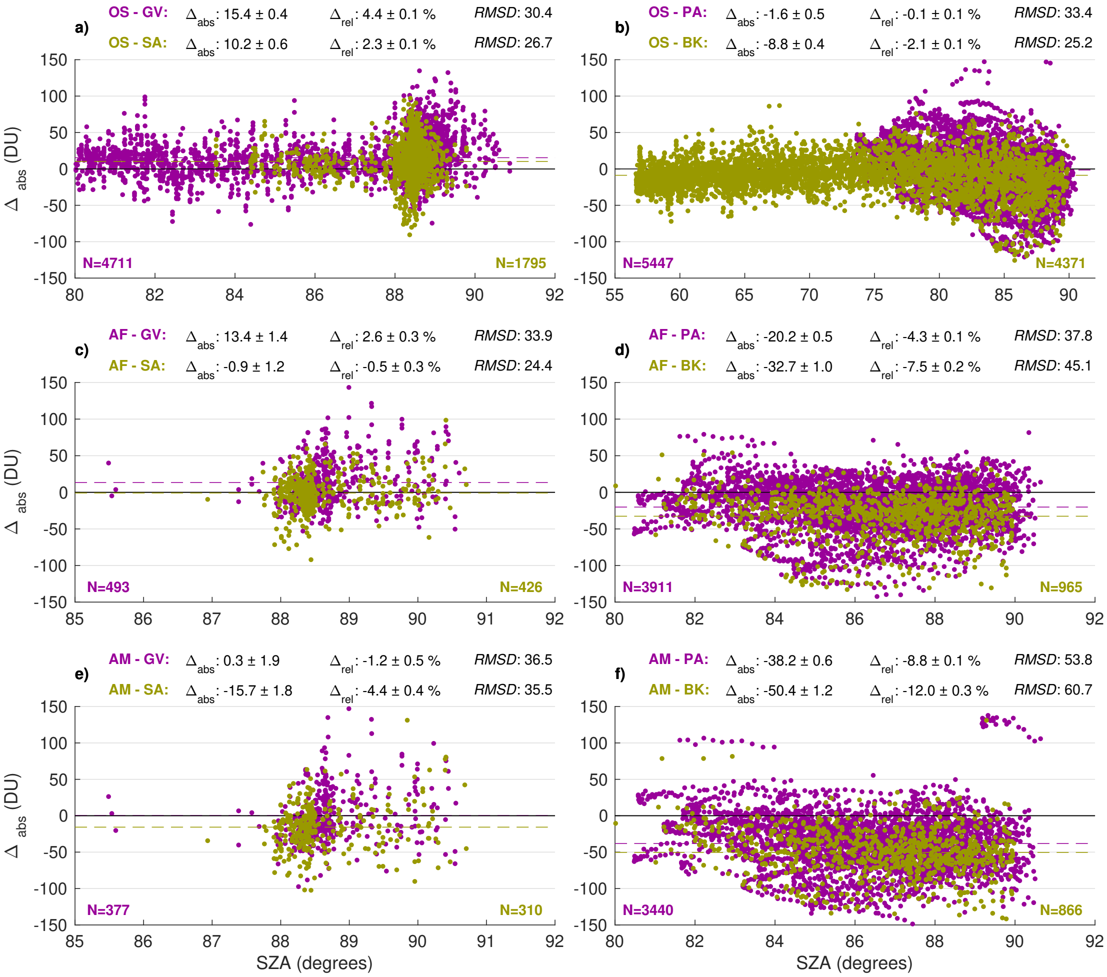

Figure 4.7: Same as Figure 4.6, with the SZA of the ground-based measurements on the x-axis instead of day of the year. Note that the SZA limits are different for each subplot.

satellite-plus-sonde columns) for the Bruker FTIR, to -2.3%, -7.3%, and -13.4% for OSIRIS, ACE-FTS and ACE-MAESTRO. These changes are significant within standard error for ACE-MAESTRO only. PARIS-IR differences show larger (and significant) changes, to 1.5%, -0.4%, and -6.1%, respectively. Results using PARIS-IR partial columns, however, need to be interpreted with caution, since the retrieval is optimized for total columns, and has lower DOFS than the Bruker FTIR retrieval.

The *RMSD* values (using surface-52 km satellite-plus-sonde ozone columns) are 25.2, 45.1, and 60.7 DU for OSIRIS, ACE-FTS, and ACE-MAESTRO, when compared to the Bruker FTIR. The values are 33.3, 37.8, and 53.8 DU, respectively, when compared to PARIS-IR. For the Bruker FTIR, only the OSIRIS comparison falls in the expected range from the *RMSE* values (Table 4.3), while PARIS-IR satisfies the *RMSE* condition for

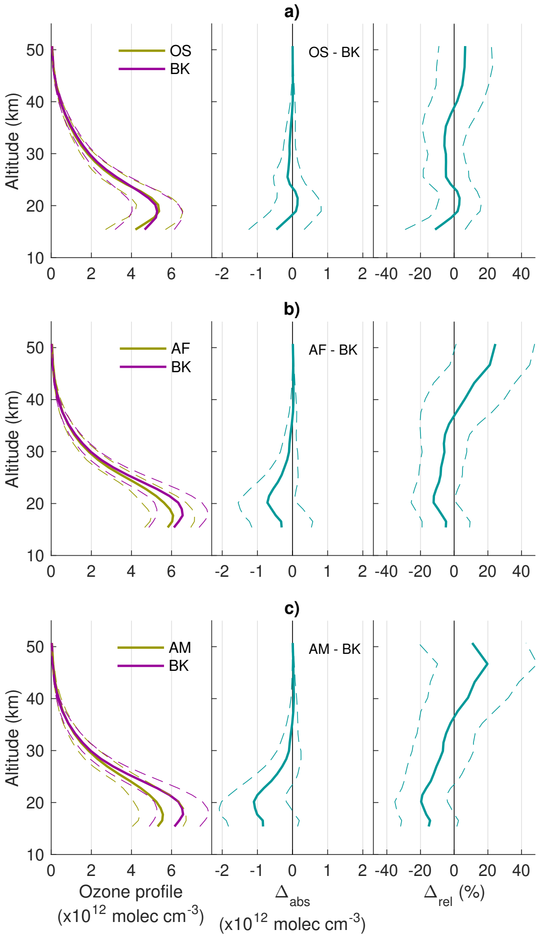

Figure 4.8: Same as Figure 4.2, with satellite profiles against Bruker FTIR profiles.

OSIRIS and ACE-FTS.

Comparisons of 14-52 km ozone profiles from the Bruker FTIR and the satellite instruments (linearly interpolated to the Bruker FTIR retrieval grid) are shown in Figure 4.8. PARIS-IR profiles were not used due to the comparatively low DOFS of the PARIS-IR retrievals. OSIRIS profiles show good agreement with the Bruker FTIR profiles; the mean values are within 5% for all but the lowermost three layers. ACE-FTS and ACE-MAESTRO show patterns similar to each other, with the ACE-MAESTRO differences shifted due to the systematic differences discussed in Section 4.3.1. The ACE-FTS and ACE-MAESTRO profiles below 40 km are smaller than the Bruker FTIR values by as much as 12% and 20%, respectively, while relative differences above 40 km are of similar magnitude but with opposite sign. The large differences in the ACE minus Bruker FTIR column intercomparisons are the result of the large differences in the measured peak ozone concentrations. When only early spring data are considered for OSIRIS, the relative differences show a pattern similar to the ACE instruments, but with less of a difference below 40 km. The high-altitude differences may be related to the fast-decreasing vertical resolution of the Bruker FTIR above 30 km. To test if the discrepancies are due to the different vertical resolutions of the satellite instruments and the Bruker FTIR, the profile comparisons were repeated using satellite profiles smoothed with the Bruker FTIR averaging kernels. The new comparisons (not shown) are similar to the unsmoothed results, indicating that smoothing does not have a large impact on the mean profile comparisons. The springtime measurements are likely affected by the location of the polar vortex; this is examined in Section 4.5.1.

4.3.2.1 Comparison to Previous Validation Studies

The ZSL-DOAS instruments at Eureka have been used in several satellite validation studies. Fraser et al. (2008) compared ACE-FTS v2.2 and ACE-MAESTRO v1.2 15-40 km ozone partial columns (extended with ozonesonde data) to 2004-2006 GBS and SAOZ columns. The GBS and SAOZ ozone was retrieved using identical settings in that study. When comparing ACE-FTS to ZSL-DOAS data, they found mean relative differences of 3.2% to 6.3% for GBS ozone, and 0.1% to 4.3% for SAOZ. These values are comparable to the 2.6% and -0.5% found in this study. For ACE-MAESTRO, Fraser et al. (2008) found differences of -19.4% to -1.2% for GBS and -12.9% to -1.9% for SAOZ. The present values of -1.2% and -4.4% are within the range estimated by Fraser et al. (2008). Adams et al. (2012a) compared OSIRIS v5.0x, ACE-FTS v3.0 and ACE-MAESTRO v1.2 ozone columns with GBS and SAOZ V2 measurements for 2003-2011 using methodology similar to the methods in this paper. For OSIRIS, they found differences of 5.7% and 7.3% with respect to GBS and SAOZ data, which are larger than the 4.4% and 2.3% reported in this study. Since the present study also uses the OSIRIS v5.x data, the reduction in the differences with respect to the GBS measurements is largely due to the longer data record, while the SAOZ intercomparisons were improved by the new SAOZ V3 dataset as well (Sect. 4.1.1.1; V3 ozone is significantly larger than V2 data for 2008-2010). Adams et al. (2012a) reported ACE-FTS relative differences of 6.5% and 4.8% for GBS and SAOZ, which are also larger than the 2.6% and -0.5% found in this study. In addition to the reasons mentioned before, this improvement is largely due to the addition of more fall ACE-FTS data, which generally agrees better with the ZSL-DOAS datasets (Fig. 4.6c). ACE-MAESTRO relative differences changed from 5.0% and 1.6% (Adams et al., 2012a) to -1.2% and -4.4% for GBS and SAOZ, respectively, reflecting the apparent negative bias in the new ACE-MAESTRO dataset.

Bruker FTIR ozone was first compared to ACE-FTS v2.2 measurements by Batchelor et al. (2010). They compared 6-43 km partial columns to ACE-FTS partial columns smoothed by the Bruker FTIR averaging kernels, and found a mean relative difference of -5.6% for 2007-2008. This is comparable to the -7.5% relative difference reported in this study. Batchelor et al. (2010) found that the location of the polar vortex had a significant impact on the comparison results. Implementing stricter coincidence criteria based on line-of-sight scaled potential vorticity (sPV) and temperature values improved the relative differences to -0.4%. The impact of the vortex position in the results of this study is further discussed in Section 4.5.1. Using the stricter coincidence criteria of Batchelor et al. (2010), Griffin et al. (2017) compared smoothed ACE-FTS v3.5 ozone partial columns to Bruker FTIR partial columns in the 9-48.5 km range. They found mean relative differences of -3.6% for 2007-2013, smaller than the value found in this study. PARIS-IR ozone has only been compared to ACE-FTS previously. Fu et al. (2011) compared 2006 measurements to smoothed ACE-FTS v2.2 data in the 9.5-84.5 km range, and found a mean relative difference of -5.2%, while Griffin et al. (2017) found -3.5%. Both these values are similar to the -4.3% reported here.

Adams et al. (2012a) compared Bruker FTIR total columns to OSIRIS v5.0x, ACE-FTS v3.0 and ACE-MAESTRO v1.2 satellite-plus-sonde columns using methods similar to the ones applied here, and found mean relative differences of 0.1%, -4.7%, and -6.1%, respectively. These values are smaller than the values of -2.1%, -7.5%, and -12.0% found in this study. Most of the differences can be explained by year-to-year variability introduced by the polar vortex in the spring (see Sect. 4.5.1), and by the shift in the ACE-MAESTRO data. Adams et al. (2012a) also compared Brewer ozone total columns to OSIRIS-plus-sonde columns, and found a mean relative difference of 2.8%, very close to the 2.7% in this study. The two values agree within their combined standard errors. The comparison results for satellite and ground-based ozone columns from this study and from relevant publications are summarized in Figure 4.16a.

4.3.2.2 Decadal Stability

Drift values and corresponding uncertainties for each of the relative difference time series are shown in Table 4.4. OSIRIS-plus-sonde ozone columns show a statistically significant drift of 2.7 ± 1.3 % decade^{-1} only when compared to the Brewer measurements. The mean drift also becomes significant as a result. The number of years required to detect a real drift of 2.7 % decade^{-1} (see Sect. 4.2.3), however, is $n^* = 23$, while the OSIRIS to Brewer comparisons span only 14 years. In addition, OSIRIS shows no significant drift when compared to any other ground-based dataset, and so it cannot be said with confidence that the drift between OSIRIS-plus-sonde ozone columns and Brewer measurements is

Table 4.4: Drift values and corresponding uncertainties for the satellite minus ground-based daily mean relative difference time series, as described in Section 4.2.3. The variance-weighted mean value is also indicated for each satellite data product. Drifts that are significant based on the uncertainty alone are highlighted in bold. Whether these drifts are meaningful, or the results of evolving comparison statistics, is discussed in Sections 4.3.2.2 (for ozone) and 4.4.1.2 (for NO_2). None of the drifts are significant based on the number of years (n*) required to detect a real drift in the datasets. Instrument abbreviations are given in Table 4.1.

Satellite Instrument	Ground-based Instrument	Ozone drift (% decade^{-1}) Pairwise	Mean	NO_2 drift (% decade^{-1}) Pairwise	Mean
OS	GV	-0.9 ± 3.1	**1.2 ± 0.9**	-2.9 ± 9.5	-5.1 ± 5.7
	GU	—		-1.2 ± 13.7	
	SA	-1.5 ± 2.7		-4.0 ± 13.8	
	BK	0.4 ± 2.2		**-10.4 ± 10.3**	
	PA	-2.3 ± 5.1		—	
	BW	**2.7 ± 1.3**		—	
AF	GV	-5.0 ± 5.1	**-3.3 ± 2.4**	7.4 ± 12.8	**8.3 ± 7.7**
	GU	—		5.3 ± 18.5	
	SA	-2.5 ± 4.2		12.8 ± 13.3	
	BK	-4.6 ± 4.9		3.6 ± 21.4	
	PA	-1.1 ± 5.5		—	
AM	GV	-2.3 ± 7.7	-0.9 ± 3.3	—	—
	SA	-0.2 ± 7.3		—	
	BK	-4.1 ± 6.8		—	
	PA	1.2 ± 5.3		—	

real. Hubert et al. (2016) found significant drifts in the differences between OSIRIS ozone data and ozonesonde and lidar measurements. These issues, however, were related to a pointing bias, and were corrected in the v5.10 dataset (Bourassa et al., 2018) (see Sect. 4.1.2).

ACE-FTS-plus-sonde ozone columns show no statistically significant drift when compared to any of the ground-based instruments, and the n^* values indicate that none of the time series are long enough to say with confidence that the drifts returned by the linear regression are real. When the mean across all instrument pairs is considered, the drift becomes significant, since the combined uncertainty is reduced. This apparent negative drift is expected, given the better agreement of fall ACE-FTS data with ZSL-DOAS measurements, and the fact that most fall coincidences occur after 2013 (see Sect. 4.3.2.1). The mean drift is not significant when fall ZSL-DOAS data are excluded, or when the spring and fall data are fitted separately. The lack of drift in ACE-FTS data is consistent with the results of Hubert et al. (2016).

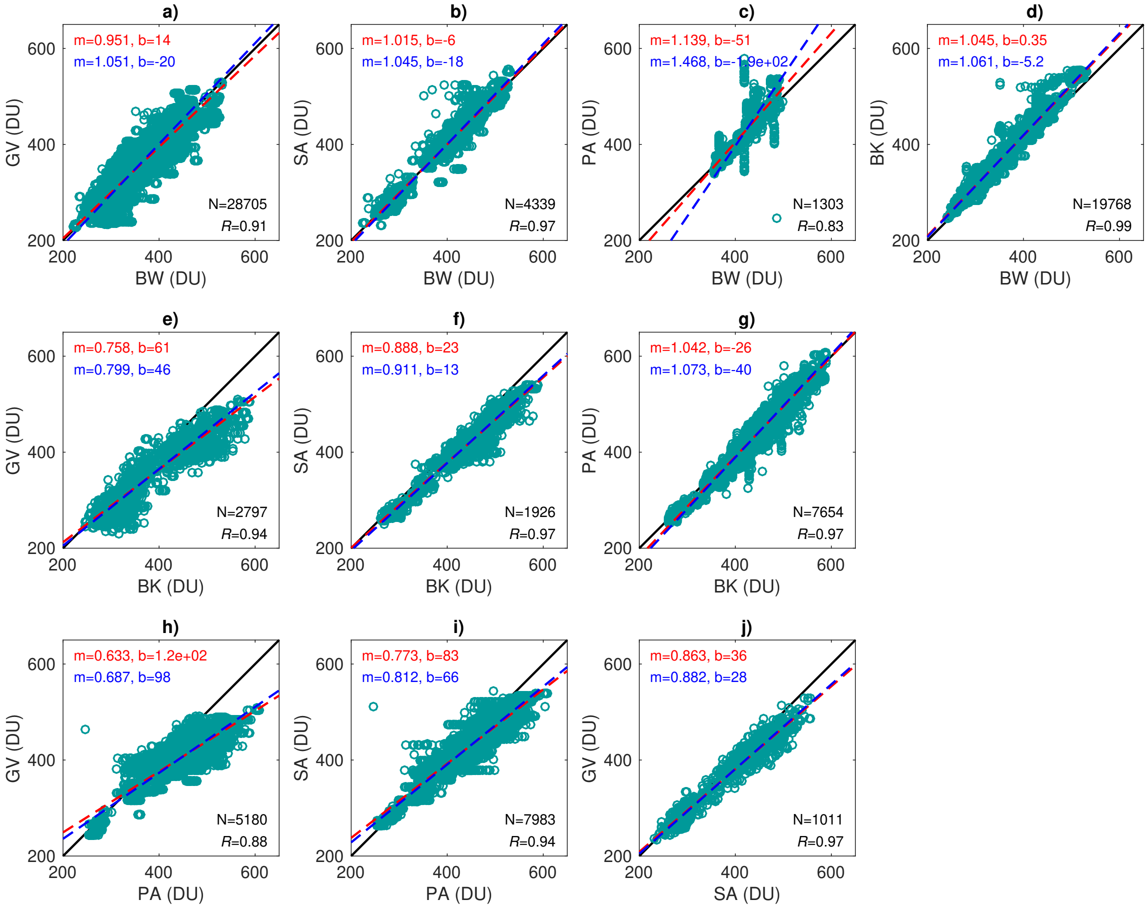

Figure 4.9: Same as Figure 4.5, with ozone total columns from the ground-based instruments.

There is no significant drift between ACE-MAESTRO-plus-sonde ozone columns and the individual ground-based instruments, and the mean drift is also zero within the uncertainty, in agreement with Hubert et al. (2016). All of the n^* values are larger than the number of years available in each relative difference time series. The uncertainties on the drift values are larger than for the ACE-FTS data, reflecting the larger scatter seen in the comparison results (Fig. 4.6). The lack of drift in the ACE-MAESTRO data lends further credibility to the conclusion that the observed low bias (Sect. 4.3.1) is related to the v3.13 reprocessing, and not to changes in the dataset over time.

4.3.3 Ground-based Versus Ground-based Partial Columns

Understanding the relationship of the ground-based datasets with each other is important for interpreting the results of the satellite vs. ground-based instrument comparisons.

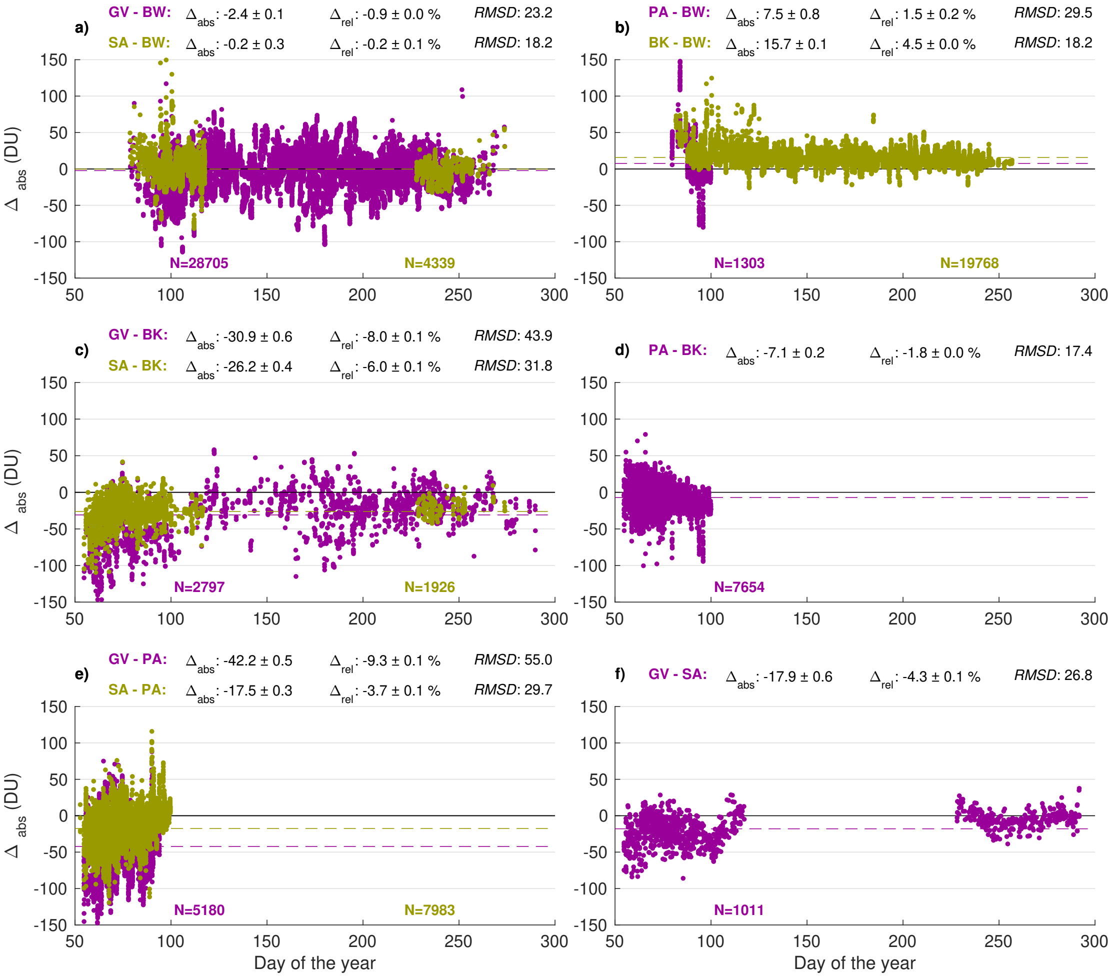

Figure 4.10: Same as Figure 4.6, with ozone total columns from the ground-based instruments.

Results for the ground-based ozone comparisons are summarised below. The coincidence criteria and comparison metrics were the same as detailed in Section 4.2. Ozone total columns from the GBS, SAOZ, Bruker FTIR, PARIS-IR and Brewer instruments show good correlation (Fig. 4.9), with correlation coefficients of 0.83 or greater. The lowest value is found for the PARIS-IR minus Brewer comparison, since the two instruments have limited temporal overlap.

The seasonal differences between the ground-based instruments are shown in Figure 4.10. The ZSL-DOAS instruments correlate very well ($R = 0.97$), but the GBS ozone is systematically smaller than SAOZ, with a mean relative difference of -4.3%. The largest absolute differences occur in the spring. Comparing GBS to SAOZ$_{\text{allyear}}$ ozone (Sect. 4.1.1.1), the mean relative difference is reduced to -3.2%, due to better agreement in the summer. It should be noted that the FOV of SAOZ instruments (~20°) is much larger than that of the GBS instruments (~1°), which might affect measurements when ozone more is variable (i.e. during the spring). The mean difference of -4.3% is comparable to Fraser et al. (2008) and Adams et al. (2012a), who found values of -6.9% to -3.7% (2005-2006), and -3.2% (2005-2011), respectively. Both GBS and SAOZ compare well to Brewer ozone columns, with mean relative differences of -0.9% and -0.2%, respectively, indicating that outside early spring, ZSL-DOAS retrievals are consistent between GBS and SAOZ. These values also agree well with the results of Adams et al. (2012a), who found mean relative differences of -1.4% and 0.4% for GBS and SAOZ total columns, respectively.

The Bruker FTIR and PARIS-IR measure more ozone than the GBS, SAOZ, and Brewer instruments. The mean relative differences for the Bruker FTIR are 8.0%, 6.0%, and 4.5%, respectively, while the PARIS-IR differences are 9.3%, 3.7%, and 1.5%, respectively. The absolute differences are the largest in the early spring, and the overestimation by Bruker FTIR is present consistently during the entire year. These results for the Bruker FTIR are comparable to the values of 6.9%, 9.2%, and 2.6% from Adams et al. (2012a). The Bruker FTIR minus Brewer relative differences agree well with Schneider et al. (2008), who also found a 4.5% difference between the datasets at a subtropical site. Schneider et al. (2008) attributed the differences to discrepancies in the UV and infrared spectroscopic parameters. The Bruker FTIR total columns show good agreement with PARIS-IR data, with a mean difference of -1.8%. This is consistent with Batchelor et al. (2010) who found -1.2%, and Griffin et al. (2017) who found -0.3%.

4.4 NO_2 Results

Satellite NO_2 measurements were only compared to the ground-based datasets. The comparison of OSIRIS and ACE-FTS NO_2 was excluded due to the limited number (38) and seasonal distribution (late September in a few years only) of coincident measurements. The results of the satellite minus ground-based intercomparisons are discussed below. Unlike for ozone, NO_2 profiles from the Bruker FTIR were not compared to the satellite profiles, since the mean degrees of freedom for signal for the Bruker FTIR 12-40 km partial columns is 1.2 on average.

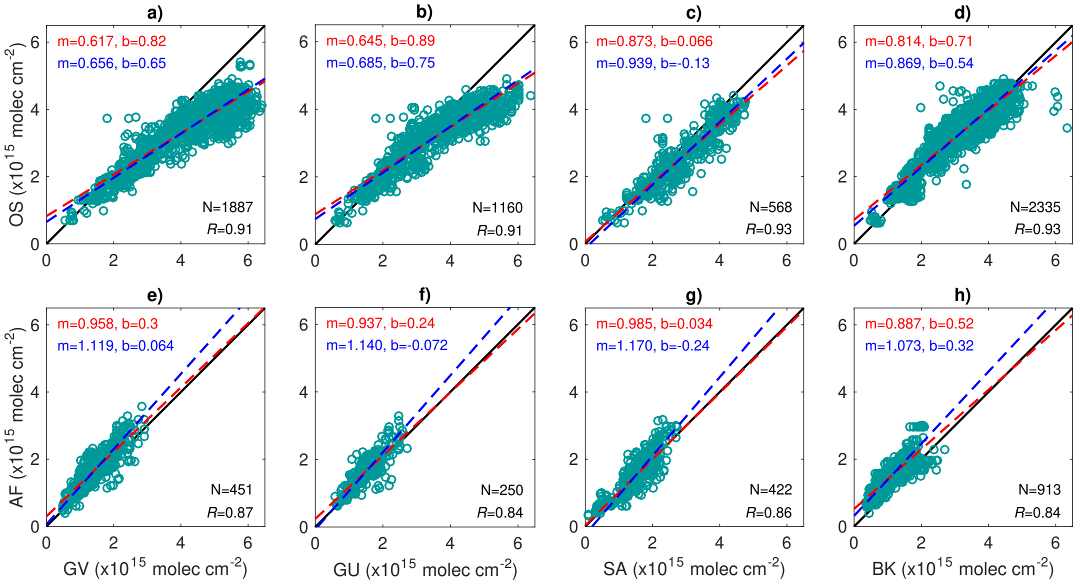

Figure 4.11: Same as Figure 4.5, with 12-40 km NO_2 satellite partial columns against ground-based partial columns.

4.4.1 Satellite Versus Ground-based Partial Columns

Correlation plots of the satellite and ground-based 12-40 km NO_2 partial columns are shown in Figure 4.11. Correlation coefficients for OSIRIS are in the 0.91-0.93 range. The values are slightly smaller for ACE-FTS, between 0.84-0.87. One reason for this might be that ACE-FTS only measures in the spring and fall, and so only a smaller range of NO_2 partial column values is available to constrain the linear relationship. R^t coefficients from TCA are 0.94-0.96 for OSIRIS and 0.88-0.92 for ACE-FTS, while the ground-based datasets have R^t values in the 0.88-0.97 range. The absolute differences between the instrument pairs throughout the year are shown in Figure 4.12, alongside the mean absolute and relative differences and *RMSD* values. Most instrument pairs (with the exception of OSIRIS minus GBS and ACE-FTS minus Bruker FTIR) agree within the combined retrieval uncertainties (absolute and relative) indicated in Table 4.2.

OSIRIS NO_2 shows a similar relationship to the GBS and GBS-UV products (Fig. 4.12a), where there is good agreement in the spring, OSIRIS partial columns are much smaller than the ground-based data in the summer, and this difference is reduced in the fall. The relative differences (not shown) and the differences as a function of SZA (Fig. 4.13a) follow the same pattern. The mean relative differences are -19.9% and -8.1% with respect to GBS and GBS-UV, respectively. Since the GBS dataset is longer and has

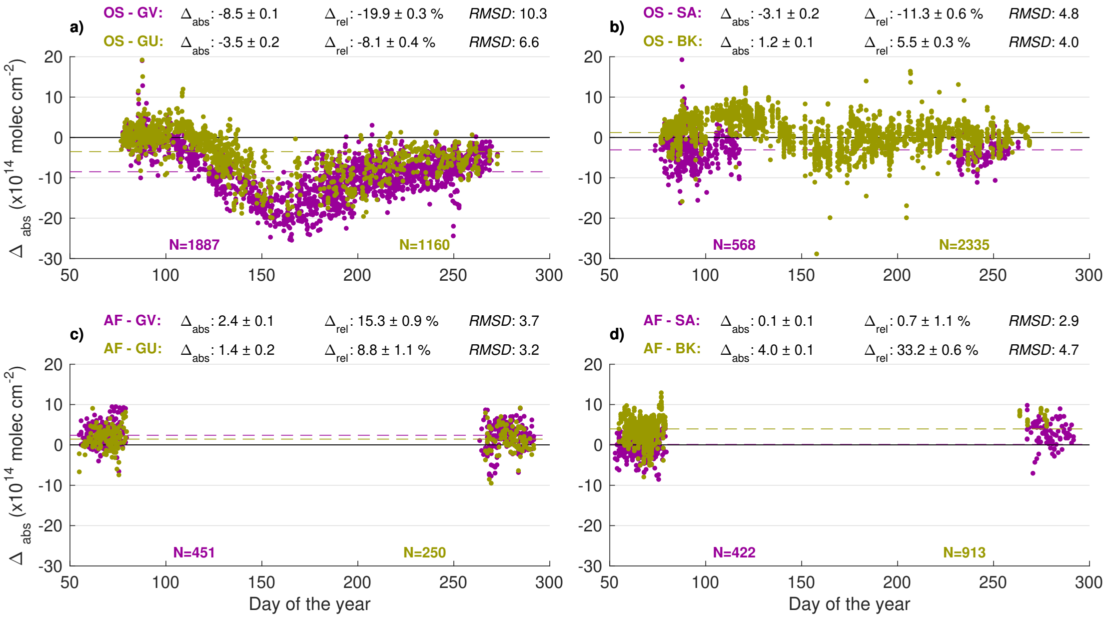

Figure 4.12: Same as Figure 4.6, with 12-40 km NO_2 satellite partial columns against ground-based partial columns.

more summer data, the mean differences are heavily weighted by the large differences in the summer. OSIRIS NO_2 is also smaller than SAOZ, with a relative difference of -11.3% (Fig. 4.12b), and similar absolute differences in the spring and fall. The relative differences (not shown) are larger in the spring for the SAOZ comparisons. The *RMSD*s for the GBS datasets (10.3-6.6×10^{14} molec cm^{-2}) are larger than the maximum expected spread from the *RMSE* calculations (Table 4.3), likely due to the large summertime differences. The *RMSD* for SAOZ is smaller (4.8×10^{14} molec cm^{-2}), and within the expected range. The SAOZ$_{\text{allyear}}$ dataset (Sect. 4.1.1.1) provides four years of summer data to further evaluate the differences between OSIRIS and ground-based ZSL-DOAS instruments. The OSIRIS minus SAOZ$_{\text{allyear}}$ NO_2 comparison (not shown) results in a mean relative difference of -10.5%, and the differences follow the same pattern described for the GBS instruments. The large summertime OSIRIS minus ZSL-DOAS differences suggest the presence of systematic errors in the datasets or in the scaling factors from the photochemical box model (Adams et al., 2012a). The differences in viewing geometries, combined with the challenges of ZSL-DOAS retrievals in the summer (Sect. 4.1.1.1) likely contribute to the seasonal pattern as well.

OSIRIS NO_2 partial columns are larger than Bruker FTIR measurements by a mean difference of 5.5%. The seasonal pattern in the absolute differences (Fig. 4.12b) and relative differences (not shown) is somewhat similar to the ZSL-DOAS datasets, although the

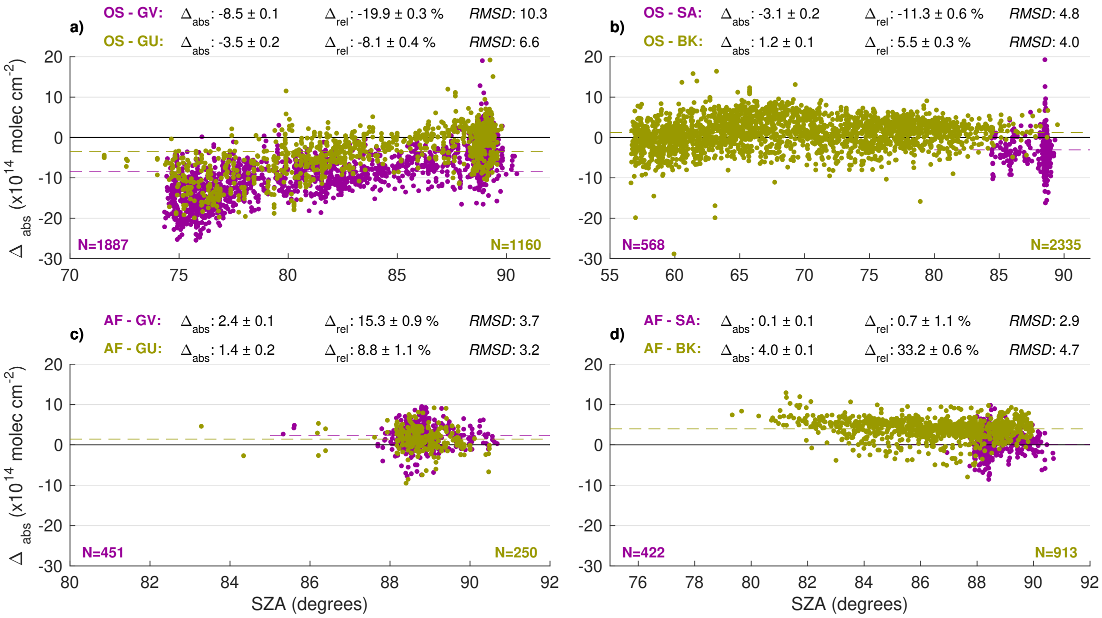

Figure 4.13: Same as Figure 4.12, with 12-40 km NO_2 satellite partial columns against ground-based partial columns, with the SZA of the ground-based measurements on the x-axis instead of day of the year. Note that the SZA limits are different for each subplot.

summertime negative shift in the absolute differences is less pronounced. Overall, OSIRIS shows better agreement with Bruker FTIR than with the ZSL-DOAS instruments. This is reflected in the *RMSD* (4.0×10^{14} molec cm^{-2}), which is the smallest among the four OSIRIS comparisons. OSIRIS NO_2 partial columns show no obvious dependence on SZA when compared to the Bruker FTIR data (Fig. 4.13b).

The ACE-FTS NO_2 partial columns are systematically larger than the GBS and GBS-UV datasets, with mean differences of 15.3% and 8.8%, respectively (Fig. 4.12c). The SAOZ data, on the other hand, agree well with ACE-FTS, with a mean difference of only 0.7% (Fig. 4.12d). The level of agreement is similar in spring and fall for the GBS datasets, while SAOZ appears to measure less NO_2 in the fall compared to ACE-FTS. The ACE-FTS NO_2 partial columns are also smaller than the Bruker FTIR, by 33.2% on average. The majority of coincidences occur in the spring, due to the limited number of Bruker FTIR measurements in the fall. The *RMSD* for the GBS and GBS-UV datasets (3.7-3.2×10^{14} molec cm^{-2}) are comparable, but the GBS value falls outside the range indicated in Table 4.3. The ACE-FTS minus SAOZ comparison shows the smallest spread (2.9×10^{14} molec cm^{-2}, within the expected range), while the Bruker FTIR shows the largest (4.7×10^{14} molec cm^{-2}, outside the expected range). The ACE-FTS NO_2 partial columns show no SZA dependence when compared to the ZSL-DOAS instruments (Fig. 4.13c and d), as most datapoints cluster around 88.5°, the mean SZA of the ideal twilight ZSL-DOAS measurements. ACE-FTS comparisons to the Bruker FTIR are largely independent of SZA, with the exception of the few low-SZA measurements (Fig. 4.13d).

4.4.1.1 Comparison to Previous Validation Studies

Fraser et al. (2008) compared ACE-FTS v2.2 22-40 km NO_2 partial columns to 2004-2006 GBS and SAOZ columns. They found mean relative differences of -10.7% to -19.7% for GBS, and -11.9% to -13.6% for SAOZ. These values are opposite of the findings in this study, but direct comparisons are difficult due to the different partial column range and the fact that Fraser et al. (2008) calculated total columns (instead of the 12-60 km range used here) for the ground-based instruments. More direct comparison is possible to the results of Adams et al. (2012a), who used settings similar to the ones in this study for the GBS datasets. They calculated 17-40 km partial columns for the satellite intercomparisons, using the OSIRIS v3.0 and ACE-FTS v2.2 datasets. For OSIRIS, they found mean relative differences of -7.8% and -3.3% for GBS and GBS-UV. The differences with respect to the GBS datasets are much larger (-19.9% and -8.1%) in this study. This is primarily the result of the different seasonal distribution of the OSIRIS v6.0 NO_2 measurements. Near PEARL, there are fewer OSIRIS measurement in the spring and fall, when the agreement with the ground-based partial columns is better. Adams et al. (2012a) also found a seasonal variation in the absolute differences similar to what is shown in Figure 4.12a. For ACE-FTS, they found relative differences of 15.2% and 13.6% using GBS and GBS-UV data, similar to the 15.3 % and 8.8% found in this study. The larger change in the GBS-UV comparison is likely due to the low number of coincidences (38) in Adams et al. (2012a). Using SAOZ V2 data, they found mean relative differences of 10.2% for OSIRIS and 12.7% for ACE-FTS, which are substantially different from the values of -11.3% and 0.7% found in this study. However, changes in the SAOZ NO_2 AMF calculations (Sect. 4.1.1.1) likely account for most of these differences. The significant changes in the SAOZ dataset are evident in the ground-based intercomparisons as well (Sect. 4.4.1).

The Bruker FTIR NO_2 has only been used in one previous validation study. Using a previous version of the retrievals, Adams et al. (2012a) compared 17-40 km OSIRIS partial columns to Bruker FTIR partial columns. They found a mean relative difference of 12.2% for 2006-2011, and the differences showed a seasonal pattern similar to the OSIRIS minus ZSL-DOAS comparisons. The mean OSIRIS minus Bruker FTIR difference is smaller in this study (5.5%), and the seasonal variation is less pronounced, since the updated Bruker

FTIR NO_2 shows better agreement with OSIRIS for low NO_2 concentrations in the spring and fall. ACE-FTS NO_2 measurements have not previously been compared to the Bruker FTIR at Eureka, since Adams et al. (2012a) excluded Bruker FTIR measurements with SZA $> 80°$. The satellite to ground-based NO_2 partial column comparison results, and the changes compared to previous publications, are summarised in Figure 4.16b.

4.4.1.2 Decadal Stability

Drift values and corresponding uncertainties for each of the relative difference time series are shown in Table 4.4. There is no statistically significant drift between OSIRIS NO_2 partial columns and most ground-based instruments, except for a marginally significant drift of -10.4 ± 10.3 % decade^{-1} when compared to the Bruker FTIR dataset. The mean drift for OSIRIS NO_2 partial columns is not statistically significant. The drift with respect to the Bruker FTIR dataset is related to the fact that springtime coincidences show large positive differences (but also large scatter), and the majority of springtime coincidences occur prior to 2012. This leads to a negative drift in the springtime comparisons. None of the other instruments show a significant drift for spring data only, and the OSIRIS minus Bruker FTIR drift is not significant when spring data are excluded. In addition, the number of years required to detect a drift of -10.4 % decade^{-1} in the OSIRIS minus Bruker FTIR dataset is $n^* = 20$, and there are only 12 years of coincident measurements available.

ACE-FTS NO_2 partial columns show no statistically significant drift when compared to any of the ground-based datasets. The mean drift, however, is statistically significant. Similar to the ozone comparisons, this apparent positive drift is expected, since ACE-FTS minus SAOZ differences are larger in the fall than in the spring (see Sect. 4.4.1), and fall coincidences only occur in 2015-2017. The mean drift is not significant when fall SAOZ data are excluded, or when the spring and fall data are fitted separately. In addition, n* values for each of the individual drifts are larger than the number of years available in the relative difference time series.

4.4.2 Ground-based Versus Ground-based Partial Columns

The GBS, GBS-UV, SAOZ, and Bruker FTIR NO_2 data show correlation coefficients of 0.92 or greater, as shown in Figure 4.14. The seasonal differences between the partial columns (12-60 km for the DOAS instruments and 12-40 km for the Bruker FTIR) are shown in Figure 4.15. The GBS-UV NO_2 is on average 3.6% lower than the GBS product. This agreement is reasonable, given the shorter pathlengths corresponding to UV

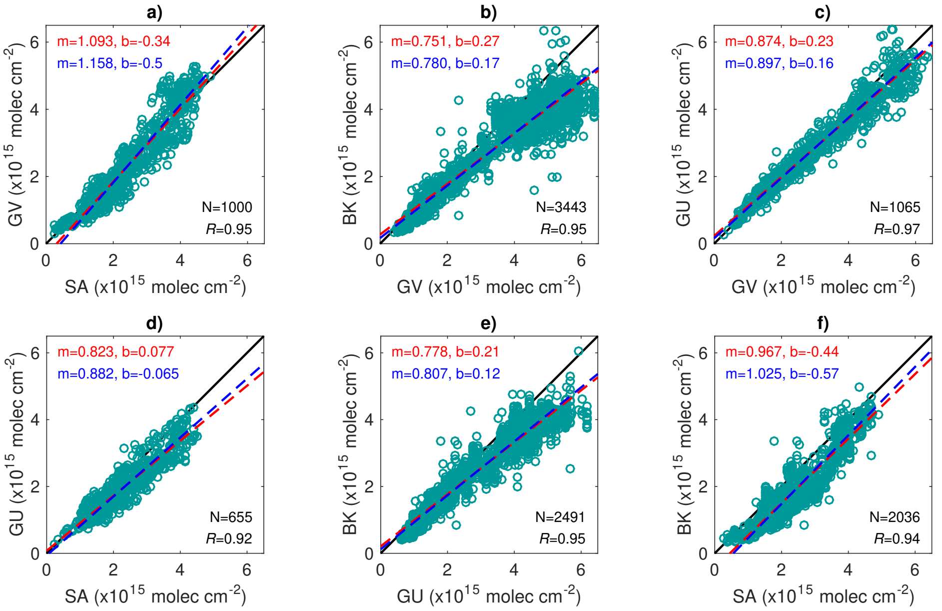

Figure 4.14: Same as Figure 4.5, with 12-60 km NO_2 partial columns (12-40 km for the Bruker FTIR) from the ground-based instruments.

measurements. The GBS and GBS-UV measurements are both smaller than SAOZ, with mean relative differences of -9.2% and -15.8%, respectively. The absolute differences are largest in the spring for both instrument pairs. The differences between SAOZ and the GBS datasets improve when the $\text{SAOZ}_{\text{allyear}}$ data are considered. GBS minus $\text{SAOZ}_{\text{allyear}}$ relative differences change sign in the summer, leading to a large improvement in the mean, to -1.1%. GBS-UV partial columns are consistently smaller than $\text{SAOZ}_{\text{allyear}}$, with a mean relative difference of -11.6%. The results for the GBS minus SAOZ comparisons are comparable to Fraser et al. (2008), who found values of -2.2% to -12.2% for 2005-2006, using 22-40 km partial columns and identical software for the GBS and SAOZ retrievals. Adams et al. (2012a) found mean differences of 3.8% and -6.4% for GBS and GBS-UV compared to SAOZ using 17-40 km partial columns. The large difference compared to the results of this study is likely due to the changes in the SAOZ NO_2 dataset (see Sect. 4.1.1.1).

The Bruker FTIR NO_2 partial columns are smaller than all the ZSL-DOAS datasets, with mean relative differences of -18.3%, -16.5%, and -30.7% with respect to GBS, GBS-UV, and SAOZ. The absolute differences peak in the summer, when NO_2 concentrations are at a maximum. The relative differences don't show any obvious seasonal variation. The smaller Bruker FTIR partial columns are consistent with the results of Adams et al. (2012a), who found mean relative differences of -16.3%, -19.2%, and -12.0% for GBS,

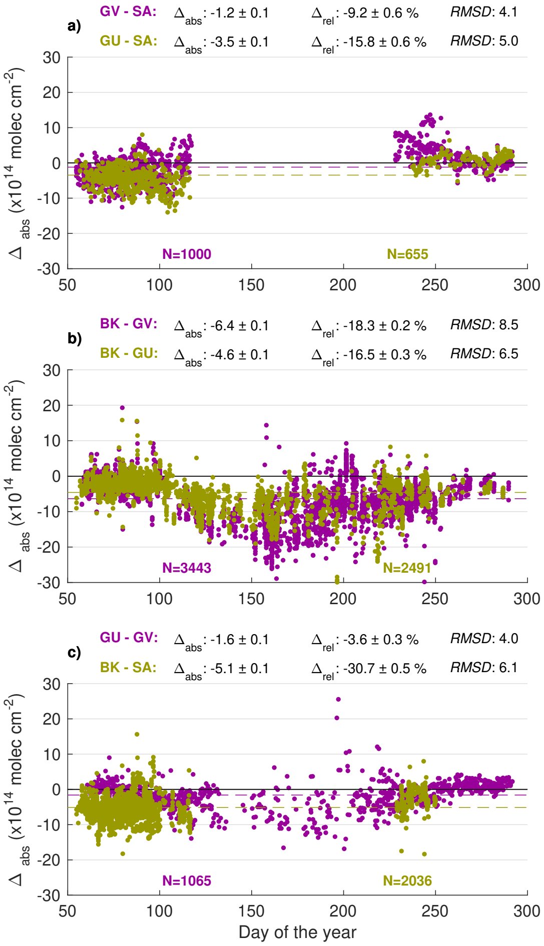

Figure 4.15: Same as Figure 4.6, with 12-60 km NO_2 partial columns (12-40 km for the Bruker FTIR) from the ground-based instruments.

GBS-UV, and SAOZ, using a different version of the Bruker FTIR NO_2 retrievals. Part of the reason for the smaller Bruker FTIR measurements is the choice of partial column altitude range. When the upper limit of the partial columns is extended to 60 km to match the ZSL-DOAS retrievals, the mean relative differences improve to -10.6%, -8.5%, and -20.7% for GBS, GBS-UV and SAOZ. The 12-40 km Bruker FTIR partial columns were used for the ground-based comparisons in order to keep the results consistent with the satellite comparisons.

4.5 The Impact of Atmospheric Conditions

4.5.1 Springtime Coincidence Criteria

Many of the instrument comparisons in this study show the poorest agreement during the spring, when the polar vortex might be located over or near Eureka. The vortex isolates airmasses in the stratosphere, and so measurements on either side of the vortex boundary might be spatially close, but have substantially different trace gas concentrations. To examine the effect of the polar vortex on the springtime comparisons, derived meteorological products (DMPs) (Manney et al., 2007) were used. DMPs were calculated from the second Modern-Era Retrospective analysis for Research and Applications (MERRA-2), an atmospheric reanalysis that uses the Goddard Earth Observing System Model Version 5.12.4 reanalysis system (GEOS-5) (Gelaro et al., 2017; GMAO, 2015). DMPs, such as sPV (Dunkerton and Delisi, 1986; Manney et al., 1994) and temperature, were calculated along the line-of-sight of the ACE-FTS, ACE-MAESTRO, GBS, SAOZ, Bruker FTIR and PARIS-IR instruments, and at the coordinates of the 25 km tangent point for OSIRIS measurements, using the Jet and Tropopause Products for Analysis and Characterization (JETPAC) package (Manney et al., 2011a, 2017).

The line-of-sight calculations for the ZSL-DOAS instruments are described by Adams et al. (2012a). Coincident measurements were kept only if the temperature differences between measurements at selected layers were less than 10 K, and measurements were either both inside (sPV $> 1.6\times10^{-4}$ s^{-1}) or both outside (sPV $< 1.2\times10^{-4}$ s^{-1}) the polar vortex at each layer. The time period selected for the comparisons with dynamical coincidence criteria was spring (up to day 105), as defined in Section 4.2.1. This period includes all the springtime ACE measurements, and most of the days when the lower stratosphere might be inside the polar vortex (as indicated by the DMP calculations).

For ozone, altitude levels of 14, 18, 20, and 22 km were selected, to coincide with the location of the peak ozone concentrations in the lower stratosphere. Adams et al. (2012a) used similar altitude levels (in pressure coordinates), excluding 22 km, while Batchelor et al. (2010) and Griffin et al. (2017) used the same levels with the addition of 24, 26, 30, 36, and 46 km. Imposing dynamical coincidence criteria throughout the entire stratosphere drastically reduced comparison statistics due to the 500 km distance limit used in this study. With the additional coincidence criteria, and using surface-52 km ozone columns, the ACE minus Bruker FTIR and ACE minus PARIS-IR comparisons showed large improvements. For the Bruker FTIR, ACE-FTS relative differences improved from -7.4 ± 0.2% to -3.9 ± 0.4%, while ACE-MAESTRO comparisons improved from -12.0 ± 0.3% to -7.3 ± 0.6%. For the PARIS-IR, the changes were -4.3 ± 0.1%

to -2.0 ± 0.3%, and -8.8 ± 0.1% to -4.5 ± 0.5%, respectively. Comparisons of ACE-FTS and ACE-MAESTRO measurements to ZSL-DOAS data did not improve with the additional coincidence criteria. OSIRIS comparisons to the ZSL-DOAS measurements showed modest improvements, from 6.7 ± 0.2% to 5.9 ± 0.2% for GBS and 2.3 ± 0.2% to 1.8 ± 0.2% for SAOZ. OSIRIS minus Bruker FTIR and PARIS-IR comparisons did not change significantly with the inclusion of the dynamical coincidence criteria.

The comparison results with the stricter coincidence criteria are similar to the findings of Adams et al. (2012a). They also saw the largest improvement for ACE-FTS minus Bruker FTIR (-5.0% to -3.1%), with modest or no improvements for the other instrument pairs. The good agreement of the ACE-FTS to Bruker FTIR comparisons using the dynamical coincidence criteria (-3.1 ± 0.8% (Adams et al., 2012a), -3.6 ± 0.6% (Griffin et al., 2017), and -3.9 ± 0.4% here) indicates that year-to-year variability in the location and strength of the polar vortex has a significant impact on the observed differences, and that the underlying agreement between ACE-FTS and Bruker FTIR is stable over time. There are no significant drifts in any of the relative difference time series filtered by the dynamical coincidence criteria.

While the location of the polar vortex influences the comparison results, removing these impacts is challenging for scattered light measurements such as OSIRIS and the ZSL-DOAS instruments. Precise line-of-sight calculations are not possible for these instruments due to the multiple paths taken by scattered sunlight before reaching the detectors. The dynamical coincidence criteria for OSIRIS are weakened due to the lack of line-of-sight information. In addition, ZSL-DOAS measurements are integrated over a much longer time than solar measurements. Springtime vertical columns are calculated using 2-4 hours of measurements, corresponding to a 30-60° change in solar azimuth. Using the estimated line-of-sight for the mean measurement time only (Adams et al., 2012a) may reduce the utility of the stricter coincidence criteria. Modest to no improvements in comparisons involving scattered light instruments are thus likely partially due to the cruder line-of-sight estimates used.

To investigate the impact of the polar vortex on 12-40 km NO_2 partial column comparisons, altitude levels of 24, 26, and 30 km were selected, since the peak NO_2 concentrations occur at higher altitudes than for ozone. The dynamical coincidence criteria, however, did not improve the comparison results, with the exception of the OSIRIS minus SAOZ relative differences (-12.2 ± 0.9% to -7.6 ± 1.1%). The small impact of the dynamical coincidence criteria for NO_2 is likely due to the large uncertainties in the measurements and the diurnal scaling, as well as the variability of NO_2, such as the latitudinal gradient and the diurnal effect (Kerzenmacher et al., 2008; Adams et al., 2012a).

To assess the impact of the latitudinal gradient on NO_2 comparisons, a ±1° latitude coincidence criterion was implemented using the 25 km tangent height of the OSIRIS measurements, the 30 km tangent height of the ACE-FTS measurements, and the corresponding 25 or 30 km point along the line-of-sight of the ground-based instruments. Since the latitudinal gradient is present during both spring and fall, measurements from both seasons (as defined in Section 4.2.1) were included. Ratios of modeled NO_2 partial columns at twilight for 79°N over 81°N (after Fig. 5 of Adams et al. (2012a)) are only as high as 2.5, compared to ratios of 7 for latitude differences typical for coincidences within a 500 km radius. The latitude filter improved the relative and absolute differences for six of the eight instrument pairs, although these improvements are only significant within standard error for the ACE-FTS minus GBS-UV comparison (8.8 ± 1.1% to 2.2 ± 2.6%). The remaining two comparisons (ACE-FTS to SAOZ and Bruker FTIR) resulted in inconclusive changes, where only the absolute or relative differences improved (none significant within standard error). The small changes using the ±1° latitude coincidence criterion indicate that using the 500 km radius to select coincidences is adequate even when NO_2 has a strong latitudinal gradient. If a 1000 km radius is used, the ±1° criterion significantly changes the results for six out of the eight instrument pairs, indicating that the larger radius would lead to systematic issues in the spring and fall NO_2 comparisons.

To estimate the impact of the diurnal effect, a new set of diurnal scaling factors was calculated for the ground-based instruments, using the SZA of the 30 km point along the line-of-sight instead of the time of the measurements. As expected, the scaled NO_2 partial columns increased, by 6-7% for the ZSL-DOAS instruments, and by 4% for the Bruker FTIR. The corresponding shift in the satellite minus ground-based differences results in better agreement for all the pairs where the satellite instrument overestimated the ground-based measurements, and the differences increased for pairs where the satellite instrument was already underestimating NO_2 compared to the ground-based data (see Fig. 4.12). These results indicate that the variability of NO_2 has a significant impact on comparisons at high latitudes.

4.5.2 Cloud-filtered ZSL-DOAS Ozone Dataset

Clouds are a large factor of uncertainty in ZSL-DOAS measurements, and they are not taken into account in the NDACC ozone AMF calculations. Hendrick et al. (2011) estimated that this omission accounts for a 3.3% uncertainty in the ozone columns. Cloudy AMFs are systematically larger than AMFs in clear conditions, mainly due to multiple scattering in the cloud layer. Existing cloud-screening algorithms for (mainly off-axis) DOAS instruments (Gielen et al., 2014; Wagner et al., 2014; Wang et al., 2015; Wagner et al., 2016) are based on the color index (CI) at various wavelength pairs. These algorithms, however, require small SZA measurements that are not available at high latitudes.

To assess the impact of clouds on ZSL-DOAS ozone measurements at Eureka, a cloud screening algorithm was developed for the UT-GBS and SAOZ datasets by Zhao et al. (2019a). Cloudy spectra were filtered out using calibrated CI and thresholds based on RTM simulations prior to the VCD retrieval. This method, however, still requires SZA values smaller than 85° for the individual measurements, and so has limited impact on the spring and fall measurements when only the UT-GBS daily reference spectra might be filtered. To extend the range of the filter, the temporal smoothness of the CI and the O_4 dSCDs was also taken into account, since they should vary smoothly in the absence of rapidly varying clouds. The cloud-filtered ZSL-DOAS datasets were retrieved using the GBS retrieval code, with the exception of the use of fixed RCDs for SAOZ. Zhao et al. (2019a) found that for 2010-2017 data, there is a 1-5% difference between cloudy and clear ZSL-DOAS measurements. Cloudy measurements show a positive bias, consistent with the enhanced AMFs in cloudy conditions.

Using the same 2010-2017 subset of GBS and SAOZ measurements as in Zhao et al. (2019a), the effects of clouds on the satellite minus ZSL-DOAS intercomparisons can be examined. The ACE-FTS and ACE-MAESTRO comparisons show only insignificant changes. This is consistent with the limited applicability of the cloud-filter algorithm in the spring and fall. When compared to OSIRIS data, the mean relative differences increased for both GBS and SAOZ, although the change is only significant within standard error for the former. Since the GBS dataset has more summer data than SAOZ, the effect of the cloud filter is expected to be larger. OSIRIS minus GBS differences changed from 3.2 ± 0.1% to 4.4 ± 0.2%, while correlation coefficients improved from 0.92 to 0.95. This is consistent with Zhao et al. (2019a), who found that the cloud filter changes the GBS minus Brewer differences from 0.05 ± 0.25% to -1.84 ± 0.71%.

These results suggest that clouds play an important role in satellite comparisons to ZSL-DOAS instruments at high latitudes. While the impact of clouds on spring and fall measurements is difficult to quantify, it is likely that ZSL-DOAS measurements have a positive bias during those periods as well. Since direct-sun measurements (e.g. the Bruker FTIR and Brewer measurements) have a natural clear-sky bias, comparison results across multiple datasets have to be interpreted with care.

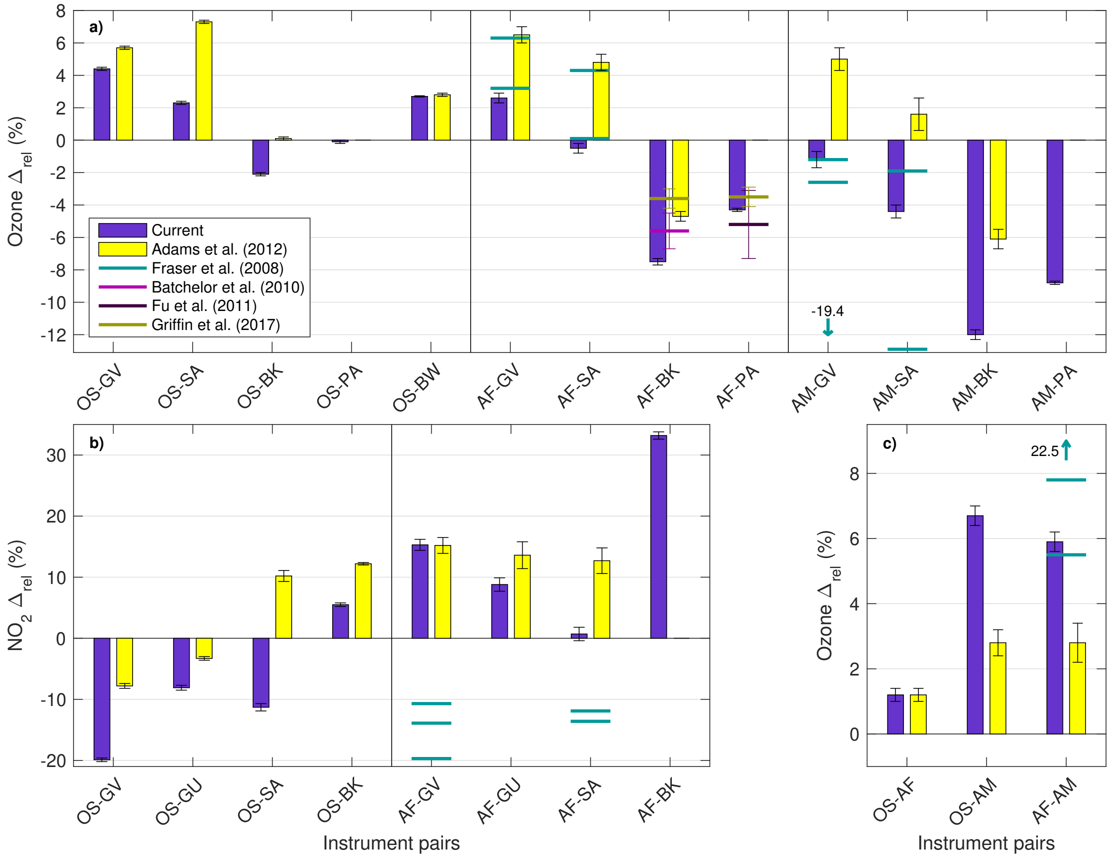

Figure 4.16: Mean relative differences between **a)** satellite-plus-sonde surface-52 km ozone columns and ground-based total columns, **b)** 12-40 km satellite NO_2 partial columns and ground-based partial columns, and **c)** 14-52 km satellite ozone columns. Bars show the results from this study, as well as the results from Adams et al. (2012a) (2003-2011). Additional lines indicate results from Fraser et al. (2008) (individual yearly values, 2004, 2005, and 2006 for GBS, 2005 and 2006 for SAOZ; note that for AF-GV, values are 6.3% for both 2005 and 2006), Batchelor et al. (2010) (2007-2008), Fu et al. (2011) (2006), and Griffin et al. (2017) (2006-2013). Error bars indicate standard error, where available. Abbreviations are given in Table 4.1.

4.6 Summary

This chapter presented comparisons of OSIRIS and ACE ozone and NO_2 measurements to ground-based measurements at Eureka. Satellite partial columns of ozone (14-52 km) were extended to the surface using ozonesonde data, while the 12-40 km NO_2 partial columns were compared directly to ground-based partial columns. All NO_2 measurements were scaled to local noon using a photochemical model to account for the diurnal variation of NO_2. Drifts between the various datasets were calculated using robust linear regression of the daily mean relative differences. To inform the validation results, the ground-based datasets were also compared to each other. Measurements of both ozone and NO_2 show reasonable agreement, with well-documented differences that are likely due to the varied measurement geometries and spectroscopic parameters of the ground-based datasets.

Ozone partial columns from the three satellite instruments show reasonable agreement. OSIRIS and ACE-FTS agree to within 1.2%, while ACE-MAESTRO ozone shows a 6.7% and 5.9% low bias when compared to OSIRIS and ACE-FTS, respectively. Profile comparisons show that relative to the OSIRIS and ACE-FTS, ACE-MAESTRO underestimates the peak ozone concentrations within 500 km of PEARL. This bias was not apparent in previous ACE-MAESTRO data versions (Adams et al., 2012a). The lack of drift between any of the satellite datasets indicates that the ACE-MAESTRO bias is related to changes in the v3.13 processing, and not to changes in the dataset over time. Satellite-plus-sonde ozone columns were compared to five ground-based datatsets. OSIRIS ozone columns agree with ground-based total columns with a maximum mean relative difference of 4.4%. The agreement is better than 7.5% for ACE-FTS ozone, while ACE-MAESTRO columns show a maximum relative difference of 12%, reflecting the low bias indicated by the satellite comparisons. The largest differences were observed for the ACE minus Bruker FTIR and PARIS-IR comparisons (the agreement is better than 4.4% for all other instrument pairs). Comparisons of satellite-plus-sonde ozone with a cloud-filtered ZSL-DOAS dataset indicate that the underlying agreements are likely different due to a positive bias in the ZSL-DOAS measurements in cloudy conditions.

Springtime ozone comparisons are affected by the polar vortex. This additional atmospheric variability is most significant for the ACE minus Bruker FTIR and PARIS-IR comparisons, since most of those coincidences (all for PARIS-IR) occur during the spring. Using stricter dynamical coincidence citeria in the spring, ACE minus Bruker FTIR and PARIS-IR comparisons improved by 2.3-4.7%. Results for the other instrument pairs showed modest to no improvements, likely due to the lack of precise line-of-sight information for the scattered-light measurements. This indicates that the polar vortex introduces significant uncertainty in the springtime comparisons, and accounting for these effects requires precise knowledge of the measurement light path.

Satellite NO_2 partial columns were compared to four ground-based datasets. OSIRIS partial columns agree with ground-based partial columns to within 19.9%, and the differences show significant seasonal variation, with the largest negative values in the summer. ACE-FTS partial columns show a maximum mean relative difference of 33.2%, that improves to better than 15.3% when excluding the Bruker FTIR comparison. Dynamical coincidence criteria did not improve the comparison results, likely due to the large uncertainties in the NO_2 measurements. Implementing a ±1° latitude coincidence criterion modestly improved spring and fall comparison results for most instrument pairs, suggesting that while the latitudinal gradient of NO_2 has a significant impact on validation exercises, a 500 km radius for coincidences is adequate for comparisons of NO_2 measurements.

None of the satellite-plus-sonde ozone columns or satellite NO_2 partial columns show a significant drift when compared to the ground-based datasets. While some of the calculated drifts are significant based on the linear regression only, most of these values were found to be related to the changing seasonal distribution of the coincidences, coupled with seasonal effects in the relative difference time series. None of the time series are long enough for confident detection of drifts of the magnitude given by the linear regression. The results in this study are generally consistent with previous validation results, as summarized in Figure 4.16. The lack of significant drift in any of the comparison time series indicates that OSIRIS, ACE-FTS and ACE-MAESTRO continue to provide reliable measurements of ozone and NO_2 in the Arctic.

Chapter 5

Unprecedented Ozone Depletion in Spring 2020

This chapter utilizes the long-term datasets from Eureka to assess the exceptional stratospheric ozone depletion in the spring of 2020. Measurements show that total column ozone in 2020 was at an all-time low in the 20-year dataset, 22 to 102 DU below previous records set in 2011. Ozone minima (<200 DU), enhanced OClO and BrO slant columns, and unusually low HCl, $ClONO_2$, and HNO_3 columns were observed in March. Polar stratospheric clouds were present as late as 20 March, and ozonesondes show unprecedented depletion in the March and April ozone profiles (to <0.2 ppmv). While both chemical and dynamical factors lead to reduced ozone when the vortex is cold, the contribution of chemical depletion was exceptional in spring 2020 when compared to typical Arctic winters. The mean chemical ozone loss over Eureka was estimated to be 111-126 DU (27-31%) using April measurements and passive ozone from the SLIMCAT chemical transport model. While absolute ozone loss was generally smaller in 2020 than in 2011, percentage ozone loss was greater in 2020. This chapter is based on a manuscript submitted to the *Journal of Geophysical Research: Atmospheres* (Bognar et al., 2020a).

5.1 Methods and Datasets

This work includes ozone, NO_2, BrO, and OClO measurements made at Eureka by the UT-GBS and the PEARL-GBS (merged into one GBS dataset). In addition, this work uses ozone and NO_2 measurements from the SAOZ instruments, ozone measurements from Brewer #69 and the Pandora instrument (#144), as well as measurements of ozone and relevant trace gases from the Bruker FTIR. The data products used, along with the corresponding temporal coverage and relative uncertainties, are listed in Table 5.1. Only

Table 5.1: Trace gas measurements used in this study, with mean relative uncertainties for each data product. Measurements up to 5 May in each year are included in the averages. The ozone and NO_2 products from the DOAS instruments (GBS, SAOZ) are total columns and 12-60 km partial columns, respectively. The BrO and OClO products are dSCDs, while data products from the Bruker FTIR, Brewer and Pandora instruments are direct-sun total columns.

Instrument	Availability	Data products and mean uncertainty (%)							
		O_3	NO_2	BrO	OClO	HCl	$ClONO_2$	HNO_3	HF
GBS	1999–2020	6.3	20.2	26.0[a]	24.2[a]	–	–	–	–
SAOZ	2005–2020	5.9[b]	13.9[b]	–	–	–	–	–	–
Bruker FTIR	2007–2020	5.4	8.4	–	–	2.1	12.0	19.7	3.5
Brewer #69	2001–2020	0.5[c]	–	–	–	–	–	–	–
Pandora	2019–2020	0.4[c]	–	–	–	–	–	–	–

[a] UV dSCDs (2007–2020), only including data over the detection limit.
[b] Estimates, see text.
[c] Random uncertainty only, see text.

springtime measurements (up to 5 May of each year) were used in this study. The SAOZ, Bruker FTIR (ozone and NO_2), and Brewer datasets are described in Chapter 4, and additional datasets used here are described below.

The Bruker FTIR retrievals of HCl, $ClONO_2$, HNO_3, and HF follow the recommendations of the NDACC IRWG. A full error analysis for all species was performed following Rodgers (2000), and the mean uncertainties for the retrieved total columns of HCl, $ClONO_2$, HNO_3, and HF are 2.1%, 12.0%, 19.7%, and 3.5%, respectively (up to 5 May, Table 5.1). Ozone and NO_2 have mean uncertainties of 5.4% and 8.4%, respectively, for the measurements used here. The averaging kernels indicate that for each trace gas, the retrievals have good sensitivity to the lower stratosphere (Batchelor et al., 2009; Lindenmaier et al., 2012), with mean DOFS of 3.3, 1.3, 2.7, 1.1, 2.7, and 2.8 for ozone, NO_2, HCl, $ClONO_2$, HNO_3, and HF, respectively. Results for all species were filtered using an RMS:DOFS filter, and retrievals with negative VMRs were rejected. One exception was HCl, where negative VMRs were accepted in order to increase the number of valid measurements in low-HCl conditions (2011 and 2020). Negative VMRs rarely occur in retrievals for the other species.

A Pandora spectrometer (#144) has been deployed at the PEARL Ridge Lab since February 2019. The Pandora instruments (Herman et al., 2009; Tzortziou et al., 2012) use a temperature-stabilized grating spectrometer and a CCD detector (see Chapter 7 for more details). While Pandora #144 utilizes a combination of viewing geometries (including direct-sun, direct-moon, zenith-sky, and multi-axis), only the direct-sun ozone measurements are used here. The direct-sun spectra are analyzed using the total optical absorption spectroscopy (TOAS) technique (Cede, 2019), and ozone is retrieved in the 310-330 nm range. The Pandora standard ozone column data products have a temperature dependence (Herman et al., 2015), i.e., 0.25 % K^{-1} when compared to Brewer data (Zhao et al., 2016a). This temperature dependence introduces a 1 to 3% seasonal bias between the Pandora and the Brewer standard data products (Zhao et al., 2020a). Thus, the Pandora ozone data are corrected by an empirical method with the ozone-weighted effective temperature (Zhao et al., 2016a). The random uncertainty of Pandora ozone measurements was estimated to be 0.4% by Zhao et al. (2016a).

In addition to observations of trace gases, instruments at Eureka provide measurements of a variety of atmospheric variables. The CANDAC Rayleigh-Mie-Raman Lidar (CRL) is a ground-based zenith-pointing lidar located at the Zero-altitude PEARL auxiliary laboratory (0PAL), within the EWS. The CRL transmits 532 nm and 355 nm light generated by separate, but co-aligned, Nd:YAG lasers. A 1 m telescope and eight photomultiplier tubes capture backscattered light at seven wavelengths: Rayleigh elastic channels (532 nm, 532 nm with depolarization, and 355 nm), Raman channels for molecular nitrogen (387 and 607 nm) and for water vapour (408 nm), and Rotational Raman channels (528 and 531 nm). A complete description of the original configuration of the CRL is available in Nott et al. (2012), and an updated description of the depolarization system is given in McCullough et al. (2017). The CRL focuses on tropospheric cloud and aerosol measurements at high temporal and vertical resolution (1 minute × 7.5 meter; see McCullough et al., 2019). Binning the data (e.g., 30 minute × 150 meter) allows the CRL to also provide data products well into the stratosphere. The two elastic backscatter channels (532 nm and 355 nm) can be used to detect PSCs.

Ozonesondes are launched on a weekly basis from the EWS (Tarasick et al., 2016). In addition to providing information for the estimation of ozone loss, ozonesondes were used in this study for the ZSL-DOAS retrievals, and to initialize the photochemical box model used for NO_2 diurnal scaling (see Chapter 4). Radiosondes are launched twice daily, weather permitting, from the EWS. Radiosonde temperature profiles were used to verify candidate PSC cases identified by CRL (Sect. 5.2). PSCs were identified based on the temperature regimes consistent with PSC formation: regions above the first tropopause with temperatures less than the threshold temperature for Type I PSC formation (T_{NAT} = 195 K). The first tropopause was identified as the lowest altitude at which the lapse rate was less than 2 K km^{-1}, and for which the average lapse rate over the following 2 km also did not exceed 2 K km^{-1} (WMO, 1957).

To investigate ozone loss inside the vortex, output from the TOMCAT/SLIMCAT (hereafter SLIMCAT) three-dimensional offline chemical transport model (CTM) (Chipperfield, 2006; Dhomse et al., 2013; Chipperfield et al., 2015; Dhomse et al., 2019) is used here. The model is forced by reanalysis fields from the European Centre for Medium-Range Weather Forecasts (ECMWF) Reanalysis 5$^{\text{th}}$ Generation (ERA5) product (Hersbach et al., 2018, 2020), and the chemistry component is performed separately for each time-step. SLIMCAT includes both active ozone, for which the full chemistry and dynamics are considered, and passive ozone, which is dynamical tracer with no chemistry. Passive ozone is set equal to active ozone on 1 December of each year. Passive ozone can be used to estimate chemical ozone loss as the difference between passive and active (or measured) ozone (e.g., Feng et al., 2007; Singleton et al., 2005, 2007; Adams et al., 2012b; Lindenmaier et al., 2012; Dhomse et al., 2013). This study uses 6-hourly model output for 2000-2020, interpolated to the geolocation of Eureka. Column values were calculated from trace gas VMR profiles using modeled pressure and temperature profiles.

To select measurements inside the polar vortex, MERRA-2 DMPs were used (Manney et al., 2007, see Chapter 4). Values of sPV and temperature were calculated along the line-of-sight of the ground-based instruments (for each individual measurement time), and vertically for SLIMCAT columns and radiosondes, using the JETPAC package (Manney et al., 2011a). For the purposes of this study, the inner edge of the vortex was defined as sPV = 1.6×10^{-4} s^{-1}, and the outer edge as sPV = 1.2×10^{-4} s^{-1} (Manney et al., 2007). To filter out measurements that potentially sample through the vortex edge, sPV criteria were tested at 16, 18, and 20 km (the altitude range of maximum ozone concentrations) along the line-of-sight of each instrument. Measurements were considered to be inside (outside) the vortex if the sPV at all three altitudes was greater (less) than the inner (outer) vortex edge threshold. Measurements not matching these criteria were assumed to be on the vortex edge and were excluded from the analysis.

5.2 The Spring 2020 Measurements in Context

The polar vortex was located above or near Eureka for much of spring 2020. All instruments sampled continuously inside the vortex from 25 February through 31 March. Before that, the earliest SAOZ measurements (20-22 February) were inside the vortex, and the ZSL-DOAS instruments sampled through the vortex edge on 23-24 February. In April and May, the vortex location was more variable. The instruments measured inside the vortex for 9-18 and 27-30 April, mostly through the vortex edge for 1-7 and 19-26 April, and on the edge or outside the vortex from 1 May on. The exceptional longevity of the vortex (Lawrence et al., 2020) is evidenced by the fact that 30 April is the latest in-vortex mea-

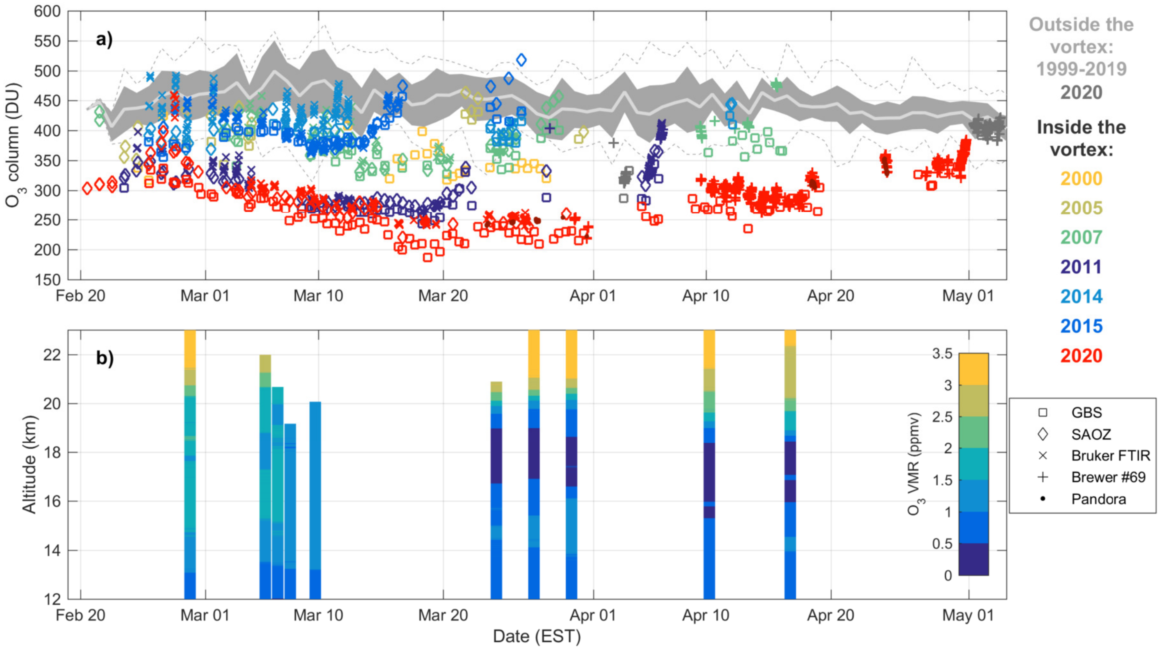

Figure 5.1: **a)** Measurements of total column ozone (DU) from the GBS, SAOZ, Bruker FTIR, Brewer, and Pandora instruments. Measurements outside the vortex in the time series of all instruments (up to 2019) are represented by the gray shaded area (daily mean and standard deviation) and the gray dashed lines (daily minima and maxima). The colored datapoints represent measurements inside the vortex, in years when the vortex was located above Eureka for a substantial part of the measurement period. In addition, 2020 measurements outside the vortex are plotted separately in dark gray. **b)** Ozone mixing ratio profiles (ppmv) from 2020 ozonesonde measurements. Only sondes that reached altitudes above 18 km are shown.

surement (by two weeks) in the 20-year dataset presented here. It should be noted that the number of in-vortex measurements depends on the location of the vortex, and also on the measurement coverage of the individual instruments. Direct-sun measurements require clear conditions, and unfavorable weather can significantly reduce measurement coverage, especially for the early spring (high SZA). ZSL-DOAS instruments, on the other hand, measure in cloudy conditions as well, but provide data for twilights only. Measurements in 2020 faced additional challenges as a result of the COVID-19 pandemic. The Bruker FTIR and SAOZ measurements ended on 26 and 30 March, respectively, due to lack of on-site support. GBS measurements, however, continued for the rest of the spring, and Brewer #69 measurements (which typically start in late March) provided direct-sun data for the rest of the spring. Pandora direct-sun measurements are limited to a few days in spring 2020, due in part to the lack of on-site support.

5.2.1 Record Low Ozone Measurements

Figure 5.1a shows measurements of ozone columns inside and outside the vortex for the full time series of all instruments. The 2020 measurements are exceptional, both considering the duration of in-vortex measurements, and the record low ozone columns. Ozone values inside the vortex show a clear decline through March, and all instruments recorded the all-time lowest values in their respective time series in the second half of March 2020. The GBS time series has the best coverage in spring 2020, and the lowest ozone values appear in this dataset, with ozone columns near or below 200 DU (minimum of 187 DU) for 16-19 March. SAOZ measurements show a minimum (221 DU) on March 16, although SAOZ has no measurements for 17-19 March. Bruker FTIR ozone columns were in the 240-250 DU range for 16-19 March, while the minimum value (240 DU) was reached on 26 March. The GBS and SAOZ instruments also measured column values between 210 and 250 DU in late March. The Brewer and Pandora datasets start on 30 and 23 March, respectively, and the minimum values (218 DU and 222 DU, respectively) were measured on 31 March for both instruments. The scatter between the various instruments is expected, and the GBSs generally measure the least ozone among the various instruments (Chapter 4). The GBS and Brewer time series continue (with good coverage) through April and early May, and show the gradual increase of ozone inside the vortex. The vortex was still strong (and ozone columns inside were still below background levels) by the end of April.

The decline of ozone columns inside the vortex in early March was similar to that in 2011, the only previous year with comparable ozone columns in the dataset. Minimum values in 2020, however, were much lower than those observed in 2011. In 2011, GBS, SAOZ, and Bruker FTIR measurements all reached their minima on 18 March. In March 2020, minimum ozone columns measured by the same instruments were lower than the 2011 minima by 56, 43, and 22 DU, respectively. Minimum ozone in the Brewer dataset was 102 DU lower in 2020 than in 2011, although Brewer #69 generally has few measurements inside the vortex. While the vortex moved away from Eureka in late March of 2011, there is no indication that ozone columns reached minima similar to 2020. Other years when the vortex spent a significant amount of time above Eureka do not show ozone columns comparable to 2011 and 2020 (nearest minima are 93-143 DU higher than the lowest 2020 values). Ozone supply, however, is variable from year to year (e.g., Tegtmeier et al., 2008), and a cold stratosphere generally corresponds to reduced ozone columns even without chemical depletion. Part of the record low column ozone in 2020 is likely related to dynamics, and this is examined further in Section 5.3.

Figure 5.1b shows ozone profiles measured by ozonesondes in spring 2020. The gradual depletion of ozone in the 16-20 km altitude range is apparent by early March, and the same altitude range shows exceptionally low mixing ratios in late March and April. Mixing ratios were consistently below 0.5 ppmv in a wide altitude range (with minima below 0.2 ppmv), indicating near-complete depletion of ozone. Such low values are unprecedented in the Arctic: even in 2011, mixing ratios did not drop below 0.5 ppmv (e.g., Solomon et al., 2014). Ozonesonde profiles from other Arctic sites paint a consistent picture of ozone depletion that is unprecedented in the Arctic, and is more similar to Antarctic winters than any previously observed Arctic winter (Wohltmann et al., 2020). The altitude of the depleted layer likely explains some of the differences between the column measurements in Figure 5.1a. Estimated scattering heights for ZSL-DOAS instruments are below 16 km (Adams et al., 2012a). As a result, path lengths in the 16-20 km altitude range are several times longer for ZSL-DOAS instruments than for direct-sun measurements. The increased sensitivity to the region of depleted ozone likely contributes to the lower ozone columns measured by the ZSL-DOAS instruments.

5.2.2 Other Trace Gases and PSCs

Figure 5.2 shows complementary measurements from the GBSs and Bruker FTIR, along with temperatures from DMPs and radiosondes. BrO and OClO dSCDs retrieved from GBS measurements (Fig. 5.2a and b) were significantly above background levels in 2020. This indicates ongoing chlorine activation from the earliest measurements (5 March) to late March, with occasional enhancements in early April. BrO and OClO enhancements in 2011 were similar to 2020, although the 2011 time series is much shorter. There are no other years in the data record with persistent enhancements of both BrO and OClO. The highest BrO dSCDs were recorded in 2015, but these correspond to smaller OClO enhancements (and much higher ozone columns) than either 2011 or 2020.

Extremely low values of chlorine reservoirs HCl and $ClONO_2$ in the Bruker FTIR dataset (Fig. 5.2c and d) are consistent with the elevated OClO values in the GBS data, and indicate chlorine activation and heterogeneous chemistry on PSCs. HCl column values were consistently very low in March, with the exception of a few measurements in late February. $ClONO_2$ measurements follow the same pattern, with an additional minor peak mid-March. Both HCl and $ClONO_2$ columns increase from 20 March to the end of the Bruker FTIR measurement period (26 March). This increase corresponds to a gradual decrease in the OClO dSCDs, consistent with conversion of active chlorine back into its reservoir species. These observations are generally consistent with satellite measurements of HCl and $ClONO_2$ presented by Manney et al. (2020). 2011 data tell a similar story,

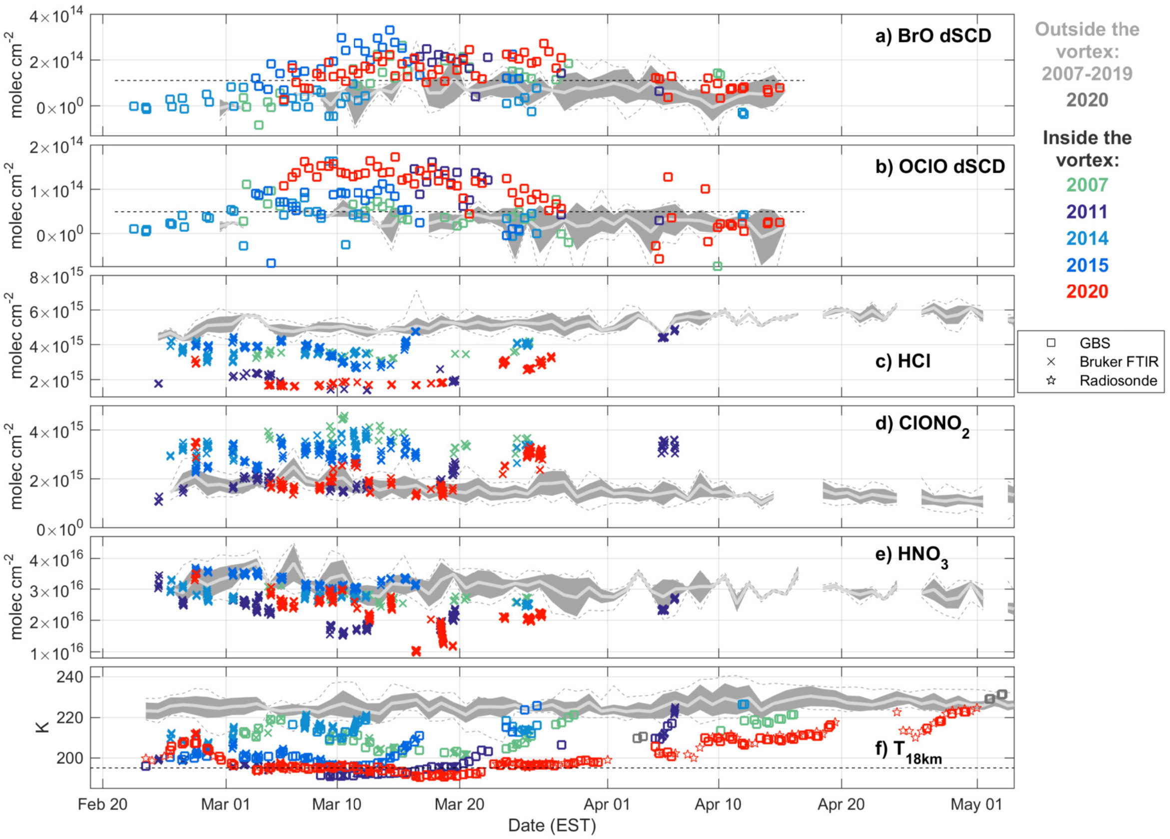

Figure 5.2: Twilight measurements of **a)** BrO and **b)** OClO dSCDs from the GBS dataset. The approximate detection limits ($1.10{\times}10^{14}$ and $4.87{\times}10^{13}$ molec cm^{-2}, respectively) are indicated by the dashed lines. Measurements of **c)** HCl, **d)** $ClONO_2$, and **e)** HNO_3 columns from the Bruker FTIR. **f)** Temperature at the 18 km level along the line of sight of the Bruker FTIR and GBS instruments, as well as T_{18km} from 2020 radiosonde measurements. The dashed line indicates T_{NAT} (195 K). Plot colors and shading as in Fig. 5.1a.

with low HCl and $ClONO_2$ column values into March, and increasing values in late March and April. HCl values dropped slightly lower in 2011 than in 2020, whereas for $ClONO_2$, the all-time minima were measured in 2020. $ClONO_2$ recovery started later in 2020, likely due in part to the slow increase of NO_2 concentrations (Fig. 5.4). In the rest of the measurement record, HCl and $ClONO_2$ show a marked decrease only in 2015, consistent with moderate enhancements of OClO.

While low HCl and $ClONO_2$ columns point to the presence of PSCs, HNO_3 (the main component of Type I PSCs) was not exceptionally low in the early spring of 2020 (Fig. 5.2e). HNO_3 remained close to typical background values until the second half of March. On 16-19 March, however, HNO_3 columns dropped to the lowest values by far in the

Bruker FTIR data record. Lower stratospheric temperatures from radiosondes and along the line-of-sights of the GBS and Bruker FTIR measurements (Fig. 5.2f) show that the same mid-March period saw the lowest temperatures in 2020. T_{18km} was well below T_{NAT}, creating prime conditions for PSC formation. $ClONO_2$ values reached their minimum in this cold period, but there was no discernible increase in the OClO dSCDs. Ozone columns also reached their minima on 16-19 March. CRL data indicate the presence of PSCs over Eureka during 16-20 March. Figure 5.3 shows the 532 nm attenuated backscatter coefficient from the CRL for the 0-20 km altitude range. The features between 12 and 16 km that are narrow in their altitude extent are most likely PSCs. These are particularly visible on 17 March at 14 km and 16 km, again on 18 March at 15 km, and present on 16 and 18 March at 13 km through 16 km. These features return signals brighter than the surrounding molecular background by a factor of approximately 2.5. In early March, temperatures hovered near (but generally above) T_{NAT}, consistent with the higher HNO_3 values observed by the Bruker FTIR. Accordingly, there are no PSC candidates detected in March CRL data before 16 March. Coincident high OClO values and low HCl and $ClONO_2$ columns indicate that PSCs were likely present elsewhere in the vortex (as shown by DeLand et al., 2020, for example), and the discrepancies are likely explained by the different time-scales for vortex mixing (~5-7 days) and chlorine deactivation (weeks) (e.g., Adams et al., 2012b). It should be noted that the vertical distribution of HNO_3 was different in 2011 and 2020, and HNO_3 values were anomalously high before PSC formation started in 2019/2020 (Manney et al., 2020).

From mid-March into April, the 2020 vortex was the coldest among any year with measurements inside the vortex. Temperatures remained near T_{NAT} until the end of March, and only reached background values by the end of April. This slow warming correlates with the slow increase of ozone inside the vortex, as examined further in Section 5.3. While the vortex temperatures hovered around T_{NAT} for the entire month of March, the first observations in 2020 reveal higher temperatures in late February. This increase corresponds to peaks in the HCl, $ClONO_2$ and HNO_3 data. DMPs show that these measurements were taken near the vortex edge. The potential impact of mixing through the vortex edge manifests as an increase of the ozone and NO_2 columns (Figs. 5.1 and 5.4), as well as an increase in SLIMCAT passive ozone in the vortex (Sect. 5.4). Temperatures followed a different pattern in 2011. The lowest temperatures were observed around 10 March, T_{18km} increased gradually to early April, and then increased rapidly as the vortex moved away from Eureka. Accordingly, HNO_3 measurements in mid-March were much lower in 2011 than in 2020. Chlorine reservoirs and OClO, on the other hand, show similar behavior in both years, indicating the role of mixing in the vortex. Temperatures in

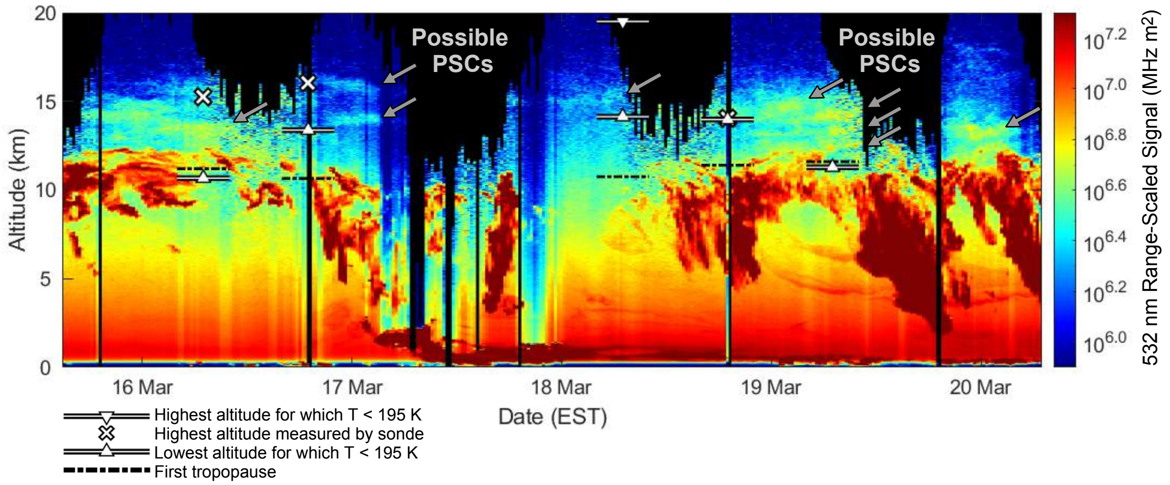

Figure 5.3: 532 nm range-scaled signal from the CRL for 16-20 March, during a period of PSC activity. Possible PSCs are particularly clear on 17 March as distinct features (∼0.5 km vertical extent) at 14 and 16 km, which are brighter than surrounding areas by a factor of approximately 2.5. Other regions showing possible PSCs are visible on 16-20 March, above 12 km. As per radiosonde temperature profiles, the PSC regions are all above the first tropopause (dot-dashed black lines; see text), and also have temperatures below T_{NAT} (195 K, lines with upward triangles). Black areas indicate low signal-to-noise ratios, generally due to the high solar background during daytime, and occasionally due to attenuation of the laser beam by tropospheric features below 12 km.

2015 were also quite low, hovering near T_{NAT} in March. The cold conditions did not last, however, and T_{18km} increased rapidly after 12 March.

NO_2 columns from the ZSL-DOAS instruments and the Bruker FTIR are shown in Figure 5.4a. To account for the diurnal variation of NO_2, partial columns were scaled to local noon using a photochemical box model (McLinden et al., 2000; Brohede et al., 2007a). For more details on the scaling procedure, see Chapter 4 and Adams et al. (2012a). Aside from the peak in late February discussed above, NO_2 columns were generally low in 2020. Unlike other trace gases, NO_2 measurements did not reach record lows in early spring: in-vortex NO_2 in 2011 was consistently below 2020 values. The 2020 measurements are consistent with the higher HNO_3 column values measured by the Bruker FTIR (Fig. 5.2e). The mean diurnal increase of NO_2, on the other hand, was at its all-time minimum in both the GBS and SAOZ datasets in 2020 (Fig. 5.4b, no diurnal scaling). As a result, the usual seasonal recovery of NO_2 concentrations in the vortex proceeded much more slowly than in any other year in the measurement record, and NO_2 column values remained unseasonably low into late March. The diurnal increase of NO_2 only returned to background values in late March, coincident with the increase of $ClONO_2$ values (Fig. 5.2d). A minor (and temporary) NO_2 increase after 10 March corresponds

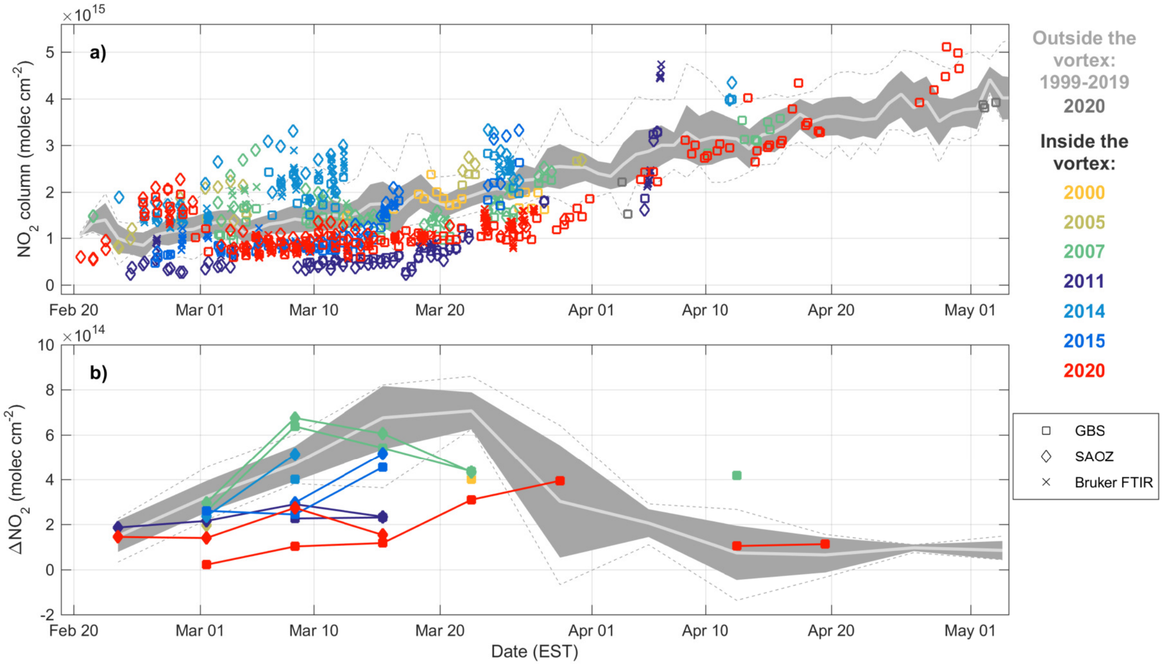

Figure 5.4: **a)** Measurements of NO_2 partial columns from the GBS and SAOZ instruments, and NO_2 total columns from the Bruker FTIR. The columns have been scaled to local noon. **b)** Weekly mean diurnal variability (evening minus morning) of NO_2 in the GBS and SAOZ measurements (without scaling). Mean values were calculated only if at least three daily values were available. Plot colors and shading as in Fig. 5.1a.

to the $ClONO_2$ peak discussed earlier, and it is likely related to mixing and transport, as opposed to local chemistry. In 2011, NO_2 columns were consistently lower than in 2020, but the diurnal increase was slightly above 2020 values. NO_2 concentrations recovered rapidly during the 2011 vortex breakup (Adams et al., 2013), while the increase was more gradual in 2020. The only other year with consistently low in-vortex NO_2 was 2015, but NO_2 values increased rapidly in mid-March, following similar trends in temperature and other trace gases. In other years, NO_2 in the vortex was generally above background levels.

Overall, every instrument used in this study measured record low ozone column values in spring 2020. The GBS, SAOZ, and Bruker FTIR instruments all measured the smallest (or close to the smallest) ozone columns (187-240 DU) in their respective time series on 16-19 March, well below 2011 minima. The same late March period also saw very low values of chlorine reservoirs HCl and $ClONO_2$, alongside temperatures below T_{NAT}, and an extraordinary drop in HNO_3 concentrations. These observations indicate the presence of PSCs (confirmed by CRL observations), and, combined with elevated OClO and BrO dSCDs, point to significant chemical ozone depletion. Ozonesonde profiles later in March (and well into April) showed unprecedented depletion of ozone in the 16-20 km altitude range, with mixing ratios below 0.2 ppmv. While the vortex was cold throughout the spring, T_{18km} was consistently above T_{NAT} in the early spring, and again past 21 March. Columns of HCl, $ClONO_2$, and NO_2 largely recovered by late March, and OClO dSCDs decreased below the detection limit. This indicates that chemical ozone loss inside the vortex likely stopped by the end of March (perhaps slightly later than in 2011). The vortex above Eureka appeared less denitrified in 2020 than in 2011, consistent with higher HNO_3 columns in 2020. Ozone columns in 2020 remained well below seasonal averages until the end of April. Dynamical and chemical contributions to these record low ozone columns are discussed in the following sections.

5.3 The Impact of Dynamics

5.3.1 Correlations of Ozone and Temperature

Accurate assessment of chemical ozone depletion in the Arctic is hindered by the fact that dynamical and chemical contributions to low ozone columns are difficult to separate. Approximately half of the variability in springtime ozone is due to interannual differences in ozone replenishment from above (Chipperfield and Jones, 1999; Tegtmeier et al., 2008). Since this replenishment is due to diabatic descent, resupply of ozone is generally smaller in cold winters, when diabatic descent is weaker. Mixing through the vortex edge also contributes to ozone variability, and less mixing in cold winters contributes to reduced ozone columns, especially in March (Salby and Callaghan, 2007). These factors (among others, see e.g., supplementary information of Manney et al., 2011b, and references therein) result in a good correlation between ozone and lower stratospheric temperature inside the vortex. On the other hand, since PSC formation is temperature-dependent, chemical ozone depletion also leads to a good correlation between ozone and temperature (e.g., Tilmes et al., 2006; Rex et al., 2006). The exact correlation, however, will depend on the balance of contributing factors, and so the relationship between ozone and temperature might be different depending on the relative importance of chemistry and dynamics.

Figure 5.5 shows the relationship of in-vortex ozone columns and T_{18km} for the GBS, SAOZ, Bruker FTIR, and Brewer datasets. The black dots and black dashed lines show the correlation for what might be considered ‘typical’ springtime conditions. These years (including early measurements in 2011 and 2020) all experienced a similar balance of chemical depletion and dynamical factors. The R^2 values are similarly high for all

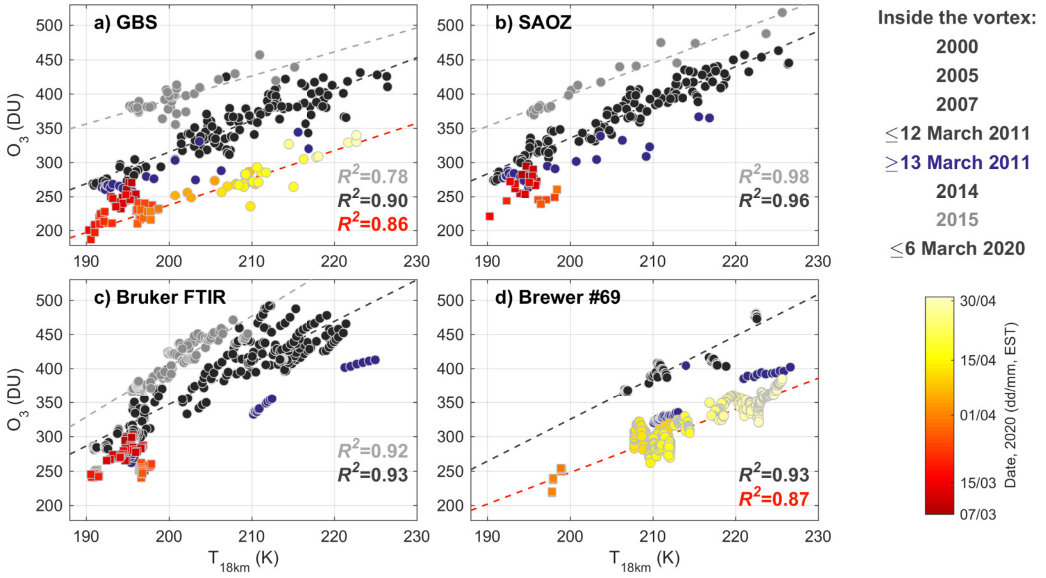

Figure 5.5: Ozone columns inside the vortex as a function of T_{18km} for **a)** the GBS, **b)** SAOZ, **c)** Bruker FTIR, and **d)** Brewer. In-vortex measurements for 'typical' years (alongside measurements from early spring 2011 and 2020) are shown in black, with a corresponding linear fit and R^2 value. In-vortex measurements for 2015 (and the corresponding linear fits and R^2 values) are plotted in gray. Measurements that start to deviate from the typical correlation (black dashed line) are plotted in blue for 2011, and with a color scale representing dates for 2020. For 2020, squares and dots correspond to March and April data, respectively. The red dashed lines show the linear fit for April 2020.

datasets, and the slopes vary only slightly, in accordance with the differences between ozone columns from each instrument. Even the limited number of points for the Brewer follow this correlation. Measurements from 2015 follow a different correlation, indicated by the gray dots and gray dashed lines in Figure 5.5. The slopes are approximately parallel to the correlation for typical years discussed above, but with a significant positive offset. R^2 values are also high, but with more variability between the instruments. As shown in Figures 5.1a and 5.2f, 2015 was a relatively cold year with anomalously high ozone. The reasons for this are examined in detail by Manney et al. (2015). A minor warming in January 2015 led to unusually strong descent and high ozone values, with minimal chemical ozone destruction. It is then reasonable that the correlation of ozone and temperature would be different from typical years, since the contribution of chemical depletion was largely absent in 2015, tipping the balance towards the dynamical factors.

Measurements in spring 2020 are another special case. While measurements up to 6 March still keep to the correlation for typical years, data for the rest of March clearly follow a different trajectory. This is shown by the color scale squares in Figure 5.5. March ozone columns decrease more rapidly than expected for temperatures near and below T_{NAT}, and this behavior is consistent across all instruments that have data in March. This indicates that chemistry was much more dominant than usual. Once chemical depletion stops in late March, ozone columns start increasing with temperature, but following a trajectory that is different from the correlation for typical years. The exceptionally long-lived vortex presents an opportunity to observe this recovery. The trajectory of ozone columns in April (color scale dots and red dashed lines in Fig. 5.5a and d) follows a line approximately parallel to the typical correlation, but with a significant negative offset. This offset (calculated at $T_{18km} = 210$ K) is 84 DU and 93 DU for the GBS and Brewer datasets, respectively, and might be interpreted as the approximate amount of additional chemical ozone destruction in 2020 compared to more typical Arctic winters. While adding late March data to the linear fits results in a very similar correlation, only April data were included, for consistency with the ozone loss estimates discussed in Section 5.4.

2011 ozone measurements follow a trajectory similar to 2020 (see also Adams et al., 2012b). Ozone columns start to clearly deviate from the typical correlation from 13 March onward. The few late-season measurements in 2011 correspond to the rapid increase of ozone on 4-6 April (Fig. 5.1a), and follow a trajectory with a negative ozone offset on the correlation plots. While direct comparisons are difficult given that the instruments mostly measured outside the vortex after 23 March 2011, the ozone offset in Figure 5.5a and 5.5d is generally larger in 2020 than in 2011. These offsets highlight that chemical ozone destruction in both 2011 and 2020 was exceptional in the context of the data record presented here.

5.3.2 HF Scaling

Measurements of HF from the Bruker FTIR can be used as another dynamical tracer. Since HF is long-lived and chemically unreactive, it can be used as a tracer of vertical motion (Mankin et al., 1990; Toon et al., 1992). HF columns increase when the air column is descending with replenishment at the top with air from neighbouring columns. As a result, HF columns are generally larger in the vortex than outside the vortex.

HF displays a significant increasing trend in the Arctic stratosphere (e.g., Griffin et al., 2017), likely due to an increase in its source gases. To estimate the HF trend for the Bruker FTIR, yearly springtime averages of HF columns were calculated outside the vortex (after Griffin et al., 2017), using the vortex criteria described in Section

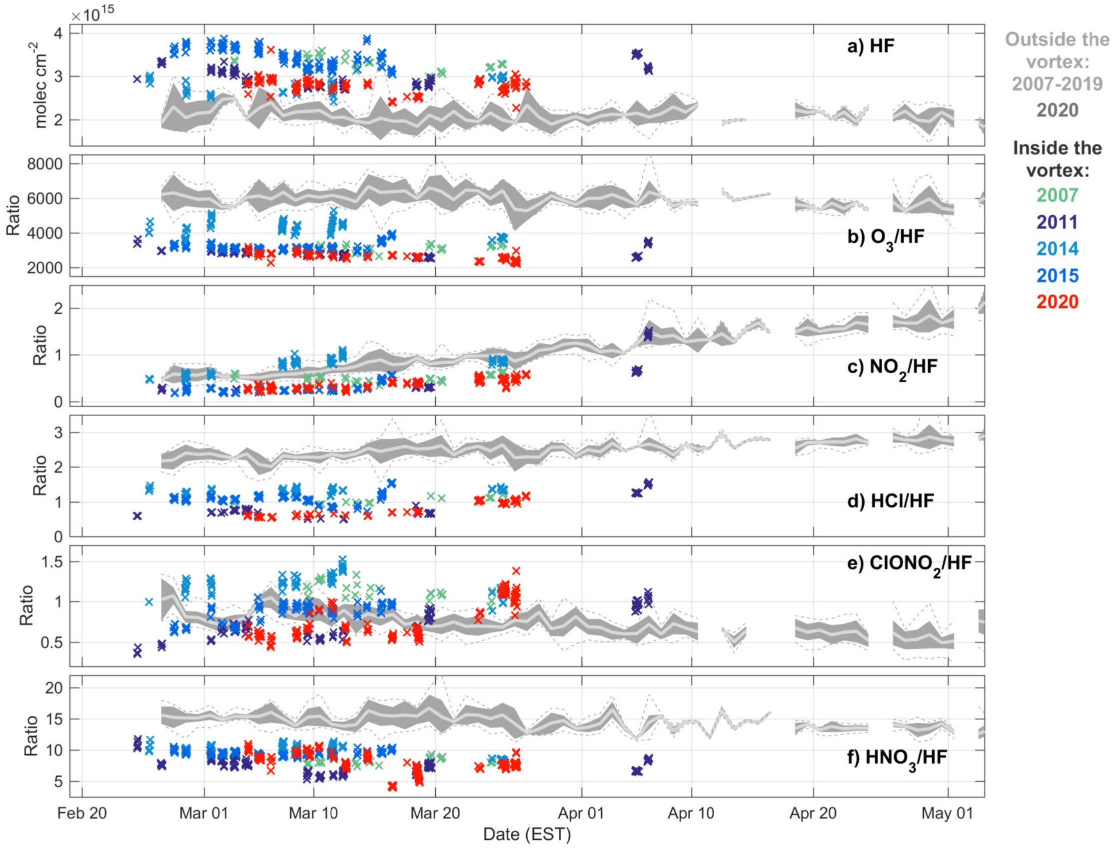

Figure 5.6: **a)** Measurements of HF columns from the Bruker FTIR. Measurements of **b)** ozone, **c)** NO_2, **d)** HCl, **e)** $ClONO_2$, and **f)** HNO_3, normalized by the HF columns. NO_2 columns were scaled to local noon prior to normalization. Measurements outside the vortex (up to 2019) are represented by the gray shaded area (daily mean and standard deviation) and the gray dashed lines (daily minima and maxima). The colored datapoints represent measurements inside the vortex, in years when the vortex was located above Eureka for a substantial part of the measurement period.

5.1. The yearly springtime averages were then fitted using a robust fitting method, as described in Chapter 4. The line of best fit indicates a statistically significant increase of $4.3 \pm 2.6 \times 10^{13}$ molec cm^{-2} yr^{-1} (2.1 ± 1.2 % yr^{-1} relative to 2007) in the yearly mean HF columns for 2007-2019 (no out-of-vortex measurements in 2020). This value is smaller than the 3.8 ± 1.4 % yr^{-1} value reported by Griffin et al. (2017) using PARIS-IR data, although that study considered a shorter time period in the spring. To correct for this trend, the line of best fit (yearly values) was subtracted from all HF data, using 2007 as the baseline. The trend-corrected HF columns are shown in Figure 5.6a. Considering in-vortex measurements only, the smallest HF columns were measured in 2011, 2014, and 2020, and the largest columns were measured in 2015. This indicates unusually strong descent in 2015, consistent with Manney et al. (2015). Uncorrected HF columns for 2020 are much higher than those in 2011, but this increase is almost entirely due to the long-term trend, as the trend-corrected HF columns are similar for 2011 and 2020.

To remove some of the dynamical effects from the Bruker FTIR dataset, measurements of ozone, NO_2, HCl, $ClONO_2$, and HNO_3 were normalized with the nearest trend-corrected HF measurement (within a ±2 hour time window) (after Lindenmaier et al., 2012, but with trend-corrected HF columns). The results are shown in Figure 5.6b-f. Since column values of HF and other trace gases would change in unison if the main driver was dynamics, it is assumed that any decrease in the HF ratios is largely the result of chemistry. It should be noted that the trend correction changes the HF columns, but does not substantially impact the year-to-year variability of the HF ratios described below.

The 2020 time series of HF-normalized HCl and $ClONO_2$ (Fig. 5.6d and e) show the same evolution as the columns in Figure 5.2c and d, with consistently low values in March, and increasing column values past 20 March. The 2011 ratios are also similar to the column values, indicating that the extremely low columns of HCl and $ClONO_2$ in both years were primarily due to heterogeneous chemistry, and not variability of transport. The evolution of HF-normalized HNO_3 (Fig. 5.6f) follows the same patterns as seen in Figure 5.2e, but the differences between individual years are smaller. The large drop in HNO_3 concentrations on 16-19 March 2020 is still apparent in the HF-normalized time series, confirming that HNO_3 was taken up on PSC particles. HF-normalized NO_2 columns (Fig. 5.6c) show that when accounting for dynamical differences, NO_2 levels were similarly low in 2020 and 2011. The slow increase of NO_2 columns in 2020 is apparent in the HF-normalized time series, in agreement with Figure 5.4b.

Compared to Figure 5.1a, the HF-normalized ozone time series (Fig. 5.6a) tells a very similar story. HF-normalized ozone was smaller in 2020 than in any previous year, with the minimum values recorded on 26 March (consistent with the Bruker FTIR ozone minima). Differences between 2020 and other years are reduced in the HF-normalized time series, as expected since transport generally plays a significant role in maintaining higher ozone concentrations inside the vortex. The trend-corrected HF columns indicate that vertical motion was likely similar in 2011 and 2020. The fact that HF-normalized ozone still reached all-time minima in 2020 further highlights the role of chemical ozone depletion.

5.4 Measured and Modeled Ozone

The narrow altitude region of depleted ozone seen in the ozonesonde profiles (Fig. 5.1b), the sharp deviations from the typical relationship of ozone and temperature (Fig. 5.5), and record low HF-normalized ozone (Fig. 5.6b) all indicate that chemical ozone loss played a large role in spring 2020. Since the instruments used here do not measure during the winter (polar night), there are no in-vortex measurements from periods with no chemical ozone depletion, and therefore ozone loss cannot be estimated from the measurements alone. In order to quantify chemical ozone loss, the passive tracer method is used here. Absolute ozone loss is calculated by subtracting measured ozone from SLIMCAT passive ozone, and relative ozone loss is calculated as absolute loss over passive ozone. It should be noted that empirical ozone loss estimates have large uncertainties, and passive subtraction could potentially overestimate ozone loss (Griffin et al., 2019a, and references therein). Part of the uncertainty in the passive tracer loss estimates depends on how well the model represents the atmosphere. The agreement of SLIMCAT results with measurements is examined in the next section.

5.4.1 SLIMCAT Comparisons

To compare trace gas columns from SLIMCAT to measured column values, the 6-hourly SLIMCAT output was linearly interpolated to the individual measurement times. For the comparisons, the mean absolute difference was calculated as

$$\Delta_{abs} = \frac{1}{N}\sum_{i=1}^{N}(MODEL_i - MEAS_i), \tag{5.1}$$

and the mean relative differences were calculated as

$$\Delta_{rel} = \frac{1}{N}\sum_{i=1}^{N}\frac{(MODEL_i - MEAS_i)}{MEAS_i} \times 100\%, \tag{5.2}$$

where $MEAS_i$ and $MODEL_i$ are the individual measurements and corresponding SLIMCAT values, respectively. The reported uncertainty in the figures and in the text is the standard deviation of the differences. Differences were calculated separately for measurements inside and outside the vortex, using the vortex criteria for the measurements, as described in Section 5.1. Since the instruments generally look south from Eureka, most measurements that sample inside the vortex correspond to times when the vertical profile directly over Eureka is also inside the vortex. For the ozone loss estimates in 2011

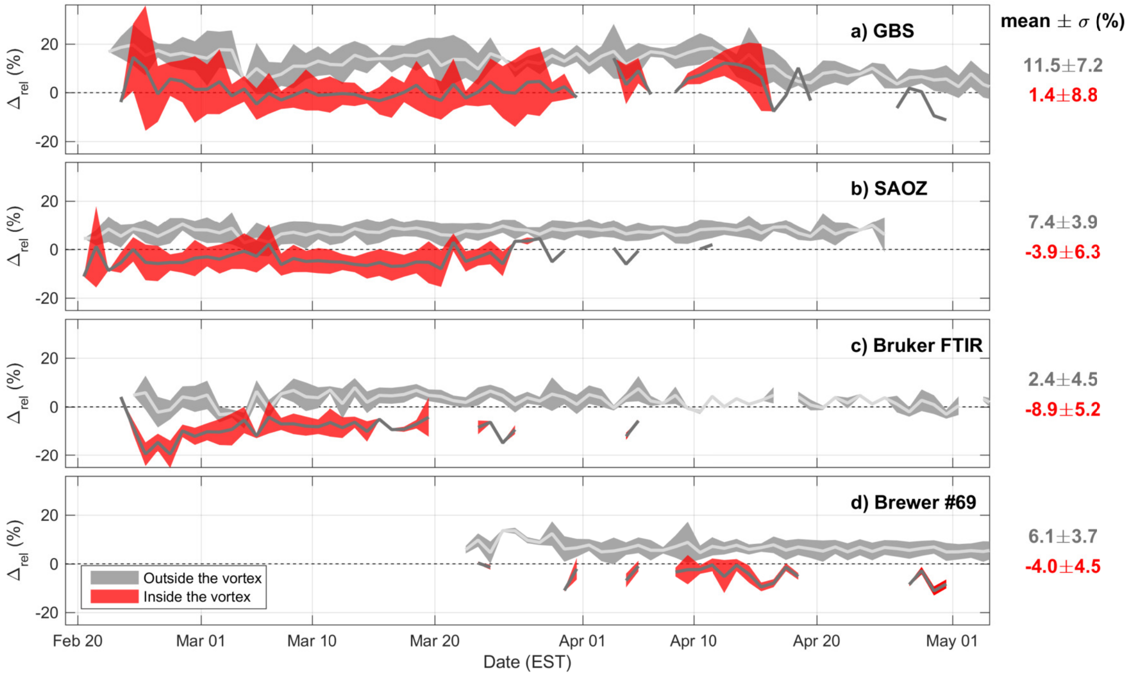

Figure 5.7: Relative differences between SLIMCAT active ozone and measurements of ozone from **a)** GBS, **b)** SAOZ, **c)** Bruker FTIR and **d)** Brewer instruments, for all years with available data. The solid lines and shaded areas show daily mean and corresponding standard deviation from all available years. Measurements inside the vortex are shown by the red shading, while out-of-vortex measurements are shown in gray. Standard deviations are only plotted if more than two measurements are available for the given day. The overall mean absolute differences (and corresponding standard deviations) are indicated on the right for measurements inside and outside the vortex.

and 2020, vortex criteria were tested explicitly for SLIMCAT columns as well. In the following, comparisons of SLIMCAT ozone, HCl, $ClONO_2$, and HNO_3 to GBS, SAOZ, Bruker FTIR and Brewer measurements are shown, using all measurements from each instrument. SLIMCAT simulates the other trace gases of interest (OClO, BrO and NO_2) as well, but comparison of these results is not straightforward given the large diurnal variation of each trace gas, and the coarse temporal resolution (6 hours) of the SLIMCAT output.

Figure 5.7 shows the relative differences between SLIMCAT active ozone and measured ozone as a function of time of year and vortex location. SLIMCAT generally agrees well with (and slightly underestimates) measurements inside the vortex. The mean relative differences are 1.4%, -3.9%, -8.9%, and -4.0% for the GBS, SAOZ, Bruker FTIR and Brewer data, respectively. The changes in the mean relative differences are consistent with the agreement between the various instruments (Chapter 4). The SLIMCAT

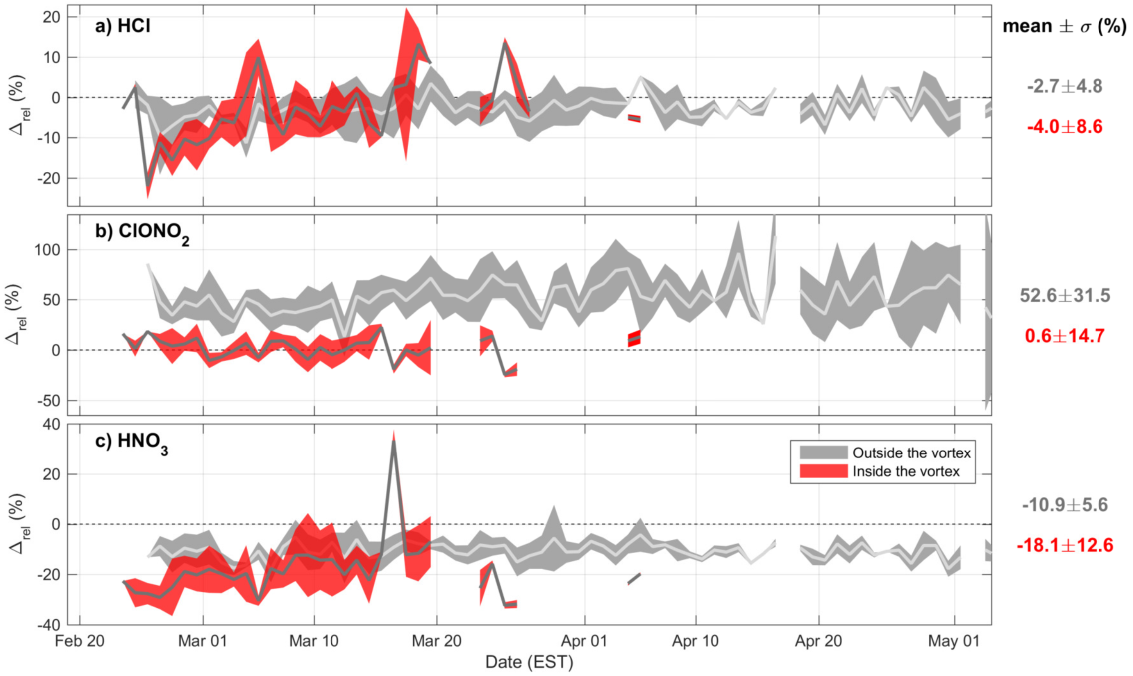

Figure 5.8: Same as Figure 5.7, with SLIMCAT vs Bruker FTIR relative differences for **a)** HCl, **b)** $ClONO_2$, and **c)** HNO_3. Note that the y-axis limits are different for each trace gas.

results show the largest deviations when compared to Bruker FTIR measurements in late February. This peak is in large part the consequence of differences in spatial sampling. The SLIMCAT columns correspond to vertical profiles above Eureka, while the Bruker FTIR measurements have ground footprints of hundreds of km in the early spring due to large SZA. The largest deviations between SLIMCAT and the Bruker FTIR occur for SZA $> 87°$, which is expected given that the Bruker FTIR line-of-sight reaches 16 km altitude (the approximate lower boundary of the peak ozone concentrations) on average 150 km away from Eureka for such large SZA. Excluding measurements with SZA $> 87°$ reduces the late February differences, and so the mean relative differences improve to -8.2 ± 3.9%. Comparisons to the GBS and SAOZ datasets do not show significant seasonal differences, likely due to longer stratospheric pathlengths for the ZSL-DOAS measurements. Brewer measurements inside the vortex are mostly restricted to 2020, and so the mean differences should be interpreted with caution.

SLIMCAT active ozone outside the vortex generally overestimates the measurements. A consistent offset of 10-11% (40-45 DU) is apparent between inside and outside comparisons across all instruments. Comparisons to MLS data indicate that this difference is already present at the start of the winter[1]. The difference is likely related to model dynamics, and not to the springtime ozone depletion chemistry.

Figure 5.8 shows the relative differences between SLIMCAT HCl, $ClONO_2$, and HNO_3 and Bruker FTIR measurements, as a function of time of year and vortex location. HCl comparisons show similarly good agreement inside and outside the vortex, but with a significant early-season slope in the in-vortex differences. This is largely the result of the sampling issues discussed above. Excluding Bruker FTIR measurements with $SZA > 87°$, the comparisons inside the vortex improve to -1.8% (from -4.0% when including all measurements). Measurement SZA does not have a significant impact on comparisons outside the vortex, likely because of the more uniform HCl background (Fig. 5.2c). $ClONO_2$ comparisons indicate very good agreement inside the vortex (0.6%), while SLIMCAT significantly overestimates $ClONO_2$ outside the vortex. It should be noted that $ClONO_2$ columns outside the vortex are generally small (Fig. 5.2d), and so the relative differences are large, even for small absolute differences. $ClONO_2$ differences appear related to lower stratospheric temperature, with increasing differences for increasing temperatures (slope of $\sim 1.1\ \%\ K^{-1}$ for differences inside the vortex). SLIMCAT generally underestimates HNO_3 both inside and outside the vortex (by 18.2% and 11.0%, respectively). This is expected given the simple equilibrium denitrification scheme included in the model (e.g., Feng et al., 2011). The scatter in the differences increases as temperatures approach T_{NAT}. The large spike in the comparisons around 18 March corresponds to the record low HNO_3 columns measured by the Bruker FTIR in 2020 (Fig. 5.2e), and indicates strong and localized PSC activity.

The SLIMCAT comparisons presented here are in broad agreement with Lindenmaier et al. (2012), who compared SLIMCAT data to Bruker FTIR measurements for 2011. The differences between measurements inside and outside the vortex are consistent, and the underestimation of HNO_3 is present in both studies. Direct comparisons are difficult, however, since the model simulations in Lindenmaier et al. (2012) used an older version of SLIMCAT, with lower resolution and different reanalysis input.

The comparison results indicate that SLIMCAT reproduces the measurements well. For the ozone loss estimates, however, only passive ozone is relevant, which (unlike the trace gases discussed above) is not affected by the model chemistry. Passive ozone cannot be directly compared to springtime measurements, since chemical processes would have already affected the ozone column. In order to assess the agreement passive ozone with measurements, the SLIMCAT simulations were compared to ozonesonde total columns from December of each year. Ozone depletion does not typically start by December in

---

[1] M. Chipperfield, personal communication.

the Arctic, and 2019 data were excluded, since chlorine activation was apparent by late November 2019 (Manney et al., 2020). Considering 2000-2018 data, the mean difference between passive ozone and the ozonesonde columns is 4.8 ± 9.6 DU (2.0 ± 2.7%, mean and standard error), indicating that SLIMCAT successfully simulates observed ozone before chemical depletion starts.

5.4.2 Estimates of Chemical Ozone Loss

The passive ozone time series inside the vortex for 2020 is shown in Figure 5.9a. Passive ozone hovered around 300-350 DU for all of March, well below typical springtime values when the vortex is not present over Eureka (gray shading in Fig. 5.9a). This indicates that dynamical mechanisms, as discussed in Section 5.3, are in part responsible for the exceptionally low column values observed in the spring. Passive transport of ozone alone would have caused a year with ozone minima that were surpassed only by 2011, as indicated by the very low values of out-of-vortex ozone measured in early April (gray points in Fig. 5.1a). Passive ozone in 2011 was as low as in 2020 until early March, but the two time series start to diverge after 10 March. Passive ozone in 2011 increased sharply in late March, and again in early April. These increases correspond well to the increases in the measured ozone columns (Fig. 5.1a).

Figure 5.9b and c show daily averages of absolute and relative ozone loss for all the instruments. SLIMCAT passive ozone was linearly interpolated to the measurement times, using only the datapoints that were inside the vortex based on vertical DMPs corresponding to the SLIMCAT ozone columns. Ozone loss values were taken to be inside the vortex only if both the measurement and the corresponding SLIMCAT column were inside the vortex. In 2020, chemical ozone loss was apparent by the end of February, and its magnitude gradually increased until the end of March. Loss estimates for individual instruments show some scatter, in accordance with the differences between ozone columns (Sect. 5.2). The GBS instruments measured the lowest ozone column values (Fig 5.1a), and therefore differences from passive ozone are most pronounced for this dataset. Absolute differences fell below 100 DU by mid-March, and reached 150 DU in April (maximum of 157 DU on 18 April). Relative differences show a similar pattern, with values well below 30% in the second half of March and in April. The maximum relative difference of 38% was reached on 18 March. SAOZ measurements are irregular past 14 March, and the last in-vortex measurement was on 29 March. The maximum difference of 95 DU (29%) occurred on the second to last measurement day, 26 March. Bruker FTIR measurement coverage is weather-dependent, and the in-vortex measurements ended on 26 March. The maximum

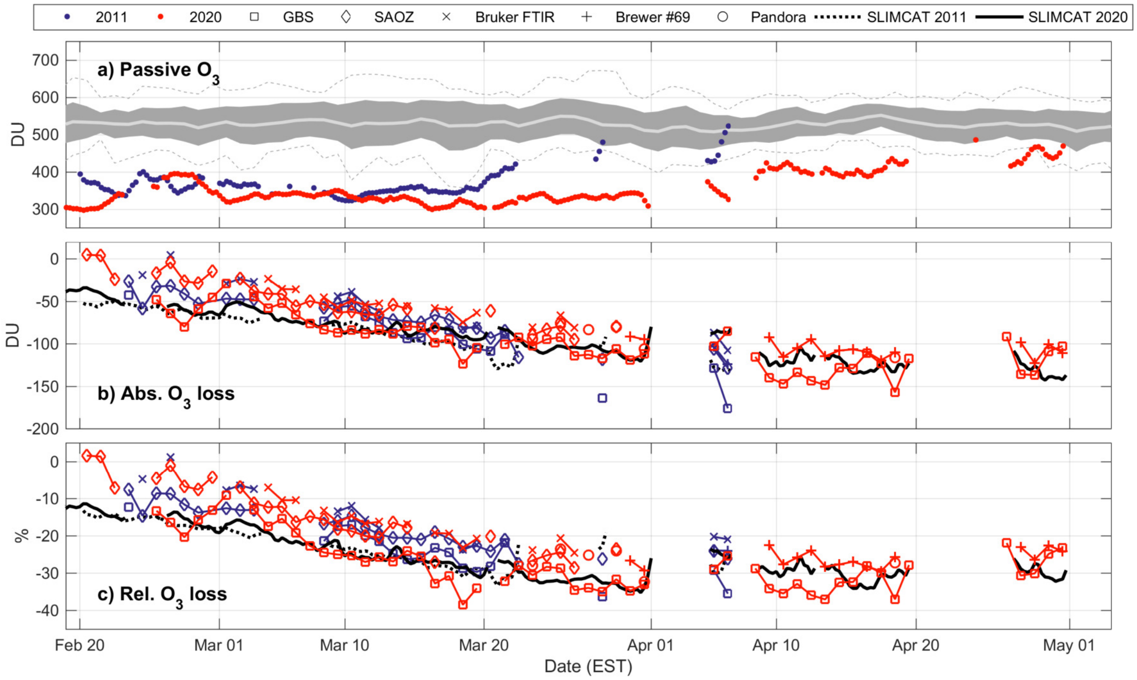

Figure 5.9: **a)** SLIMCAT passive ozone. The gray shaded area shows statistics of passive ozone (after Fig. 5.1) for years when the vortex was not present over Eureka. The colored points show in-vortex data for 2011 and 2020. **b)** Absolute and **c)** relative ozone loss inside the vortex for 2011 and 2020, calculated as described in the text. The datapoints show daily average loss for the measurements, and the black lines show 6-hourly values using SLIMCAT active ozone.

difference of 81 DU (25%) was reached on that day. Brewer measurements started on 30 March, and consistently measured ozone more than 100 DU smaller than SLIMCAT passive ozone. The maximum absolute difference of 123 DU occurred on 28 April, while 29% relative difference was observed on both 31 March and 17 April. The Pandora instrument has only six days of in-vortex measurements. The maximum absolute and relative differences of 117 DU and 32% were observed on 18 April and 31 March, respectively.

The loss estimates are generally similar for 2020 and 2011. Results using SLIMCAT active ozone (black lines in Fig. 5.9b and c) show that absolute loss was slightly higher in 2011. Relative loss was very similar, although ozone loss continued longer (to the end of March) in 2020, resulting in more overall relative loss. The measurements tell a similar story. The absolute differences generally overlap for 2011 and 2020, but the peak losses are greater for 2011. The daily peak loss from the GBS, SAOZ, Bruker FTIR and Brewer datasets was 176, 129, 108, and 124 DU, respectively, compared to 157, 95, 81, and 123 DU in 2020. Peak relative loss, on the other hand, was smaller in 2011 for all instruments, with values of 36, 28, 24, and 24%, compared to 38, 29, 25, and 29% in 2020. Overall, column ozone loss was similar between 2011 and 2020 despite the smaller VMRs reached in 2020 ozonesonde profiles (Manney et al., 2020; Wohltmann et al., 2020). This is largely explained by the higher passive ozone simulated by SLIMCAT for 2011 (Fig. 5.9a).

For the spring of 2011, previous studies report a range of ozone loss estimates. Adams et al. (2012b) and Lindenmaier et al. (2012) used data from Eureka with methods similar to this study. Adams et al. (2012b) estimated a mean ozone loss of 99-108 DU (27-29%) for 12-20 March (GBS and SAOZ data), while Lindenmaier et al. (2012) estimated 35% for all in-vortex measurements (Bruker FTIR data). The corresponding values for 2011 in this study are 92-77 DU (26-21%), and 13%, respectively. The large differences are due in part to the updated chemistry and transport in the SLIMCAT simulations used here. Adams et al. (2012b) corrected SLIMCAT passive ozone to December ozonesonde columns, while Lindenmaier et al. (2012) did not implement a correction. Given the updated SLIMCAT simulations, and because of the diversity of methods (and sampling of datasets) used in previous studies, loss estimates presented here are not necessarily directly comparable to the literature. Estimates of ozone loss from the present dataset are therefore a better basis of comparison. Using equivalent periods in March for 2011 and 2020, estimates of absolute loss are generally similar or smaller, while relative loss is greater, in 2020 than in 2011, for all instruments. This is consistent with the peak daily loss results discussed above.

Quantifying overall chemical ozone loss from a single ground station is challenging, given the variability of both vortex location and measurement coverage. For the best estimate, the vortex should be stable, and remain above the station, after chemical ozone destruction ceased. This was not the case in 2011, while the spring of 2020 fits these requirements best among all winters in the measurement record presented here. According to all indicators (trace gas measurements, correlation of ozone with temperature, SLIMCAT simulations), ozone depletion stopped by late March 2020. The GBS and Brewer instruments measured inside the vortex for the majority of April. Mean ozone loss in April is then a good indicator of overall chemical ozone loss inside the vortex above Eureka. The mean loss calculated from the GBS measurements is 126 DU (31%), while the same value is 111 DU (27%) using measurements from Brewer #69. Some of these differences are likely related to the different viewing geometries, since DOAS path lengths in the 16-20 km altitude region are several times longer than those for direct-sun measurements. The ozone loss estimate of 111-126 DU (27-31%) is consistent with values of 125-135 DU from Wohltmann et al. (2020) and Grooß and Müller (2020), who also used the passive tracer method, but with different CTMs.

5.5 Summary

This chapter used the long-term datasets at Eureka to assess the exceptional stratospheric ozone depletion in 2020. The unusually cold, strong, and persistent polar vortex over the winter and spring created the greatest potential for ozone depletion ever observed in the Arctic. Accordingly, ozone columns across the Arctic reached record lows, surpassing previous records set in 2011. The GBS, SAOZ, Bruker FTIR, Pandora, and Brewer instruments all observed record low ozone columns (187, 221, 240, 222, and 218 DU) in their respective time series. Persistent enhancements of BrO and OClO dSCDs in the GBS dataset indicate that chlorine activation was ongoing until late March, and consistently low HCl and $ClONO_2$ columns from the Bruker FTIR point to heterogeneous chemistry on PSC particles. HNO_3 columns, on the other hand, were not as low as in 2011, and lower stratospheric temperatures were slightly above T_{NAT} for most of the spring. This is consistent with a less denitrified stratosphere above Eureka indicated by the NO_2 measurements. The smallest ozone column values were observed on 16-19 March, coincident with a significant drop in temperatures and HNO_3 columns. CRL measurements indicated the presence of PSCs (at 14-16 km altitude) during the same period. Ozonesondes measured ozone mixing ratios below 0.5 ppmv (with minima below 0.2 ppmv) in the 16-20 km altitude range in late March and throughout April. These values are unprecedented in the Arctic, and are more similar to values commonly observed in the Antarctic ozone hole. While the vortex remained cold and stable throughout April, chlorine activation largely stopped by the end of March, as evidenced by increasing concentrations of chlorine reservoirs and NO_2.

Dynamical contributions to ozone variability must be considered for an accurate assessment of chemical ozone loss. Passive ozone from SLIMCAT indicates that ozone column values in 2020 would likely have been unusually low even without chemical processing. Ozone columns are usually smaller in cold winters, and Eureka ozone measurements inside the vortex generally show good correlation with lower stratospheric temperature. This relationship, however, was substantially different in 2020 (and in 2011) compared to what is observed for more typical years. This indicates that chemical ozone depletion played an exceptionally large role, and contributed to significant additional ozone loss, in 2020 when compared to compared to typical Arctic winters. Bruker FTIR measurements normalized by HF total columns confirm the major role of chemistry in shaping the 2020 trace gas time series.

Chemical loss inside the vortex was estimated using measurements at Eureka and SLIMCAT simulations of passive ozone. With consistent datasets for the entire time series, all instruments observed smaller daily peak absolute loss in 2020 (81-157 DU) than in 2011 (108-176 DU). The absolute loss time series generally overlap, but the daily peaks were higher in 2011. Daily peak relative loss, on the other hand, was greater in 2020 (25-38%) than in 2011 (24-36%) for all instruments. While overall ozone loss is difficult to estimate from a single ground station due to the variable position of the vortex, spring 2020 measurements have good coverage inside the vortex after chemical depletion stopped. Using Brewer and GBS measurements throughout April, the mean chemical ozone loss inside the vortex was estimated to be 111-126 DU (27-31%) over Eureka.

Chapter 6

Measurements of BrO over Four Halogen Activation Seasons

This chapter presents four years (2016-2019) of MAX-DOAS BrO measurements from the PEARL-GBS. Retrieved partial columns from four bromine activation seasons (March through May) are used to investigate the environmental controls on BrO in Eureka. Due to the elevation of the PEARL Ridge Lab, the PEARL-GBS often measures BrO in the free troposphere, except during strong wind episodes and storms that generate a deep boundary layer. Enhanced vertical mixing due to strong winds leads to increasing BrO values and reduced ozone depletion. BrO enhancements show two modes differentiated by local wind direction and air mass history. Longer time spent by the airmass in first-year sea ice areas corresponds to increased BrO for one of these modes only, and it appears that snow on multi-year ice could also contribute to bromine release. The other mode in the BrO enhancements corresponds to storms that bring bromine-enriched air to Eureka. Regardless of the source of BrO, high aerosol optical depth is required to maintain high BrO concentrations, since the measurements often correspond to BrO layers decoupled form the surface. Investigating the aerosols in more detail reveals that the presence of coarse mode aerosols (>0.5 μm, likely SSA) is a necessary and sufficient condition for observing BrO. This indicates that SSA plays an active role in bromine activation at Eureka. The study presented in this chapter has been published in the *Journal of Geophysical Research: Atmospheres* (Bognar et al., 2020b).

6.1 Methods and Datasets

6.1.1 Measurement Site and Local Meteorology

The MAX-DOAS measurements in this chapter were made by the PEARL-GBS in the PEARL Ridge Lab. The Ridge Lab is located approximately 15 km from the EWS, at an altitude of 610 m above sea level. The aerosol instruments are also located in the PEARL Ridge Lab, while the surface ozone monitor is located at the 0PAL, within the EWS at 10 m altitude. The EWS facilities are located on the shore of small fjord, while the PEARL Ridge Lab is somewhat further from the coast, as shown in Figure 6.1. The region is characterized by mountainous terrain typical for Ellesmere Island. Fjords cutting through the island provide natural channels for airflow in the stable atmospheric conditions of winter and spring. While Eureka is around 200 km away from the Arctic Ocean, the wide Nansen Sound (Fig. 6.1) often guides airmasses from the Arctic Ocean directly to the site. During winter and spring, the fjords around Eureka and the waters near Ellesmere Island are covered by FYI. The Arctic Ocean just north of Ellesmere Island is usually covered by multi-year ice (MYI). The EWS and the PEARL Ridge Lab might not always sample the same air masses, due to reasons discussed below.

Radiosondes are launched twice daily from the EWS. While temperature (especially in stable conditions) is a poor indicator of mixing depth in the Arctic boundary layer (Anderson and Neff, 2008), temperature profiles can be used to gain qualitative information about vertical mixing. Radiosonde profiles indicate that a strong inversion is present at Eureka most of the time from March through May. Every sonde from the four spring seasons considered here shows a temperature difference between the surface and the altitude of the PEARL Ridge Lab that is less than the dry adiabatic lapse rate. The exceptions to these stable conditions include stormy days with near-zero temperature gradients, signifying a well-mixed atmosphere. It is likely that aside from storms, remote sensing instruments located in the PEARL Ridge Lab measure above the boundary layer in the spring. The impact of atmospheric stability on in situ measurements is less clear, due to the unknown impact of local terrain on the boundary layer. The comparison of in situ temperature measurements from the EWS and the PEARL Ridge Lab, however, show temperature differences similar to the radiosonde measurements.

Figure 6.2 shows the distribution of springtime (March-May) winds for 2016-2019, measured at the PEARL Ridge Lab (610 m altitude). The wind rose shows a clear bimodal distribution, where winds come from the north close to 50% of the time, and southeasterly winds account for another quarter of the observations. The southeasterly winds show a larger fraction of strong winds compared to northerly winds, due to storms

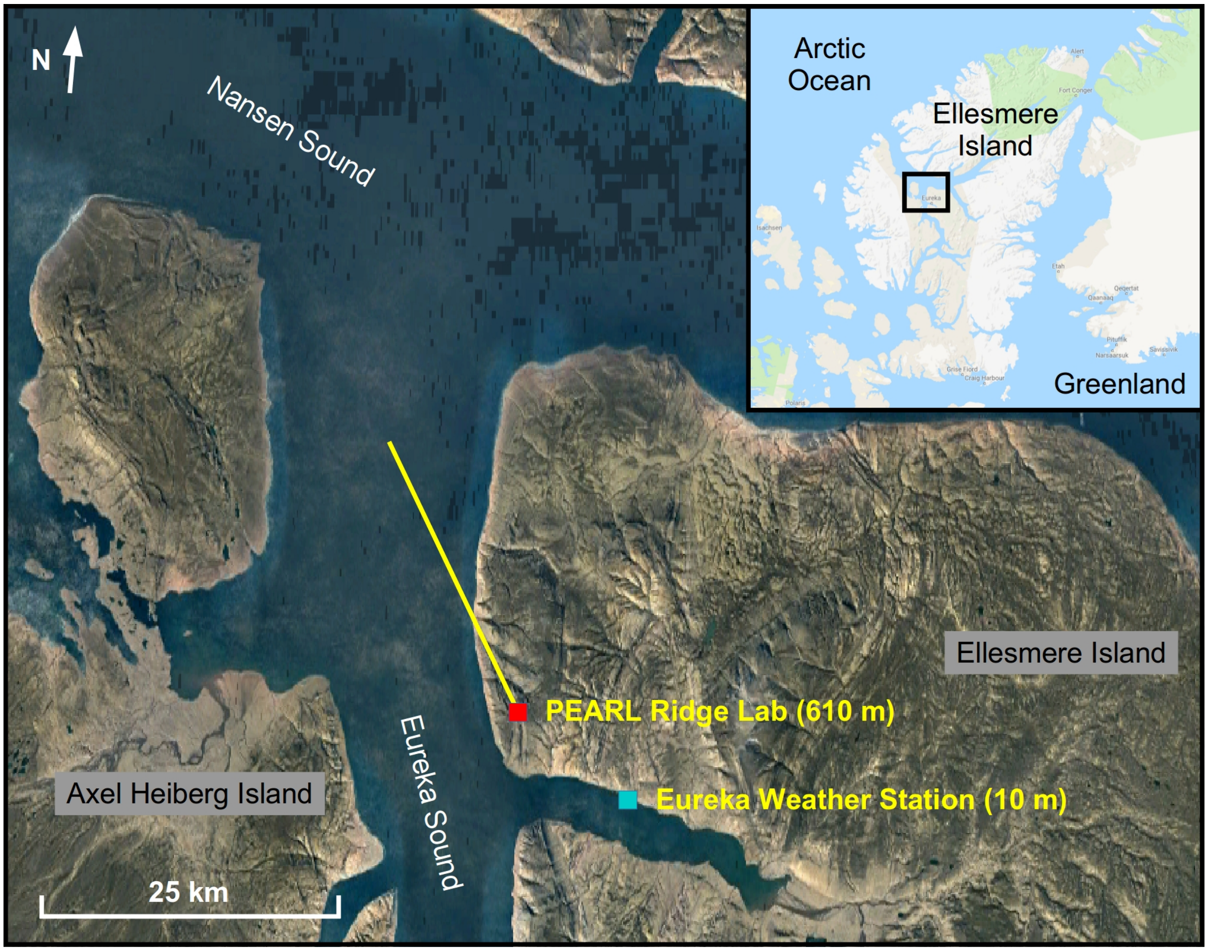

Figure 6.1: Location of the PEARL Ridge Lab and the Eureka Weather Station. The small insert shows the location of the main map on Ellesmere Island, Canada. The yellow line (25 km in length) represents the MAX-DOAS viewing direction of 330°. Images: Google Earth/Google Maps.

that usually come in from the southeast. The same wind patterns appear in the wind data from the EWS at 10 m altitude as well (data not shown). To examine the effect of wind direction on bromine activation, all data were analyzed as a function of wind direction. The wind direction bins were selected as 354° ± 30° for northerly (N) winds, and 123° ± 30° for southeasterly (SE) winds, with the remaining wind directions categorized as 'other'. The mean wind direction of each bin was determined using a Gaussian fit to the wind direction histogram.

6.1.2 MAX-DOAS Measurements

PEARL-GBS measurements from 2016 to 2019 (spring data only) were used in this study, with elevation angles of -1°, 0°, 1°, 2°, 5°, 10°, 15°, 30°, and 90° in each MAX-

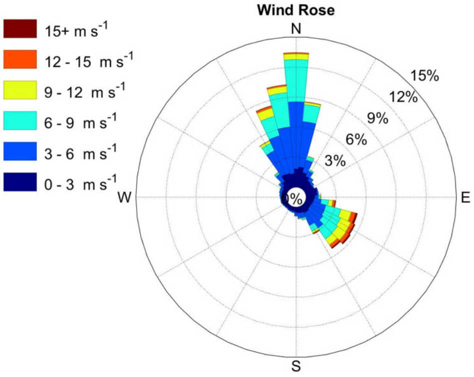

Figure 6.2: Wind rose for March-May using wind speed and wind direction measured at the PEARL Ridge Lab (610 m altitude) from 2016 to 2019.

DOAS scan. Measurements at 0° were excluded from the profile retrievals due to potential discontinuities in the RTM for elevation angles exactly equal to zero. Measurements prior to 2016 (Zhao, 2017) were excluded due to the variable sets of elevation and azimuth angles used. The current azimuth viewing direction of 330° (clockwise from north, see Fig. 6.1) points down a valley that extends from the PEARL Ridge Lab to the nearby fjord, therefore allowing an unobstructed line-of-sight for the low elevation angle measurements. Spectra were recorded for solar elevations above 4°, and so the daily measurement window varies from a few hours in early March to nearly 20 hours by May. Spectra are not recorded while the solar azimuth is close to the azimuth viewing direction of the instrument.

Examples of BrO and O_4 dSCDs are shown in Figure 6.3. The data correspond to 9 May 2018, a measurement day with variable weather conditions. The grey shading in Figure 6.3a and c indicates that retrievals using the highlighted dSCDs were rejected due to low information content of the profiles. This period corresponds to snow and blowing snow around the PEARL Ridge Lab. Weather conditions improved markedly during the day, as evidenced by the clear separation of the O_4 dSCDs. The clear increase of O_4 dSCDs with decreasing elevation angles indicate that the PEARL-GBS line-of-sight is indeed unobstructed.

6.1.3 BrO Profile Retrieval

Aerosol extinction and BrO profiles were retrieved using the HeiPro retrieval algorithm (Chapter 2) in the lowest 4 km of the atmosphere, on a 200 m altitude grid. Following Frieß et al. (2011), two iteration runs were used in the aerosol extinction retrieval, with five iteration steps in each. The retrieved state from the first iteration run was used as the starting point of the second iteration run. Using a larger number of iteration

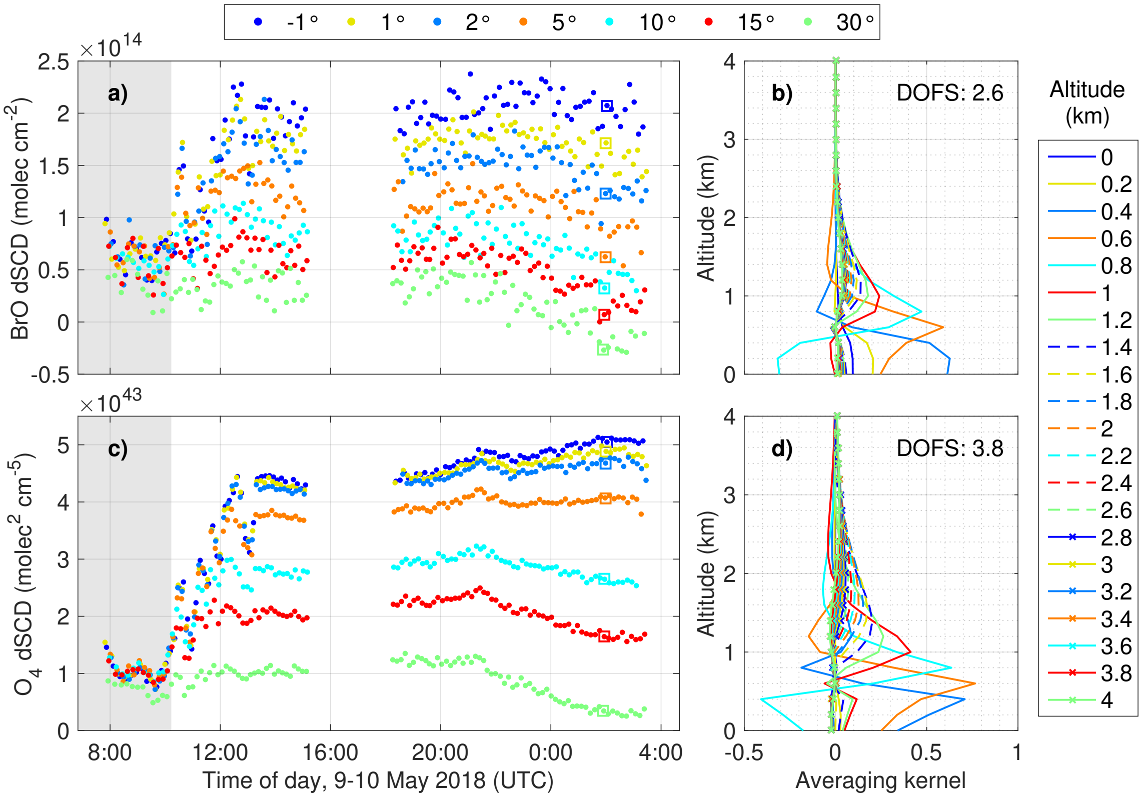

Figure 6.3: MAX-DOAS dSCDs of **a)** BrO and **c)** O_4 measured on 9-10 May 2018. The grey shading around 8:00 indicates that profiles retrieved from these dSCDs were rejected due to low information content. The gap around 16:00 is due to instrument downtime. The right panels show averaging kernels and corresponding DOFS for a selected **b)** BrO and **d)** aerosol extinction profile. The dSCDs used in these profiles are highlighted with the colored squares in subplots a) and c).

steps sometimes resulted in unrealistic profiles. For the retrievals, the single scattering albedo was fixed at 0.95, and the asymmetry parameter (for the Henyey-Greenstein phase function) was set to 0.72, to account for a variety of aerosol conditions. For the aerosol retrieval, the a priori extinction profile was set to an exponential function, with surface extinction of 0.05 km^{-1}, and a scale height of 2 km (Zhao et al., 2016b). The BrO profiles were retrieved in a single iteration run (10 iteration steps). The BrO a priori profile was set to an exponential, with a surface concentration of 5 pptv, and a scale height of 0.5 or 1 km, (similar to Zhao et al., 2016b). The scale height was set according to conditions of atmospheric stability: 0.5 km for strong inversions (inversion strength at 610 m $\geq$ 7 °C), and 1 km for weaker inversions. The diagonal elements of the a priori error covariance matrix (in both the extinction and the BrO retrievals) were set to twice the values in the a priori profile, and the off-diagonal elements were set to decrease exponentially with a correlation length of 500 m. Retrievals were performed using fixed a priori conditions for each (UTC) day, and variable a priori parameters (scale height of the BrO a priori profile, temperature and pressure profiles from radiosonde data, ozone profiles from ozonesonde data) were recalculated for each day.

Only the 0-4 km BrO partial columns and the retrieved AODs were used in this study. Profile information was not included due to the potential impacts of retrieval parameters on the BrO profile shape. Like in previous studies (Peterson et al., 2015; Zhao et al., 2016b), the retrieved BrO profiles were sensitive to the selection of the a priori profile scale height. The BrO concentrations were largest in the lowest few hundred meters for a priori profiles with a scale height of 0.5 km, while BrO was more evenly distributed for a priori profiles with a 1 km scale height. The partial columns, on the other hand, are relatively insensitive to changes in the retrieved vertical distribution of BrO. Sensitivity tests showed that changing the value of the scale height (0.5 to 1 km, and vice versa) only has a 5-10% influence on the partial column results. Given these results, for the present study the 0-4 km partial column values are the best representation of the amount and variability of BrO detected by the PEARL-GBS.

Given the list of elevation angles and the altitude of the measurement site, the PEARL-GBS is likely mostly sensitive to lofted BrO layers. Averaging kernels (Fig. 6.3b and d) show maximum sensitivity in the 600 m layer (near the altitude of the instrument). The BrO averaging kernels show little sensitivity above 1.5-2 km, regardless of the a priori scale height used. This sensitivity range is similar to results from Frieß et al. (2011) and Peterson et al. (2015). Estimating a lower limit for the sensitivity of BrO partial columns is less straightforward. Assuming a maximum horizontal sensitivity range of 10-15 km in the UV (e.g., Wagner et al., 2011), the -1° elevation angle line-of-sight would reach down to 350-450 m above sea level (or ~100 m lower when accounting for the ~1° FOV of the instrument). This is in general agreement with the averaging kernels, which usually show a broad peak between the 200 and 400 m levels. It's important to note that the retrieval considers an instrument floating at 610 m over flat terrain, and the topography around the measurement site is not taken into account. The -1° measurement looks down a valley that extends 9 km from the measurement site to the frozen Arctic Ocean. Given the bright snow cover over the valley, part of the light in the low elevation angle measurements is likely reflected from the floor and walls of the valley, enhancing the sensitivity to layers below the instrument altitude. Much of the valley, however, is significantly above sea level (the first ~6 km along the line-of-sight is above 300 m), and is covered by only a thin (few cm) layer of snow. Some of the reflected light might come from the sea ice farther along the line-of-sight, but the exact sources of reflected light cannot be quantified here. Given the variable viewing conditions and the unknown effects of topography on the radiative transfer calculations, the BrO partial columns are likely most sensitive to altitudes above 300-500 m and below 1.5-2 km. As a result, the retrievals likely miss shallow BrO events, and detect distributed and lofted events only.

Typical DOFS for the BrO retrievals were between 2 and 3, while aerosol DOFS were often between 3 and 4. To preserve information content, retrievals where either the aerosol or BrO DOFS were smaller than 0.7 were discarded (Payne et al., 2009; Peterson et al., 2015). In addition, a few remaining retrievals with AOD > 5 were removed (likely whiteout conditions, or snow on the dome obstructing the input optics). After applying these filters, the mean DOFS for BrO partial columns is 2.27, with a standard deviation of 0.45, while the mean DOFS for AODs is 3.28, with a standard deviation of 0.70. The mean absolute uncertainty on the BrO partial columns is 4.7×10^{12} molec cm^{-2} (45.7% mean relative uncertainty). The mean relative uncertainty is heavily weighted by the smaller partial columns. The mean uncertainties for measurements above and below the median are 5.0×10^{12} molec cm^{-2} (24.4%) and 4.4×10^{12} molec cm^{-2} (66.9%), respectively. The mean uncertainty on the AOD values is 0.036 (38.5% mean relative uncertainty). To estimate an approximate detection limit for the BrO partial columns, BrO profiles were retrieved for ten days in August 2018 (with variable aerosol conditions). Using a Gaussian fit to the distribution of partial columns, the 3σ detection limit was estimated to be 6.6×10^{12} molec cm^{-2}. This is a conservative estimate, assuming that no BrO is present in August. This assumption is reasonable in light of late summer conditions (temperatures above freezing, small sea ice extent), but ignores any potential free tropospheric BrO background. In fact, slight enhancements of BrO (up to 8-10$\times10^{12}$ molec cm^{-2}) appear even in the August partial columns.

6.1.4 Complementary Data Sets

Weather observations were recorded at the EWS (hourly) and at the PEARL Ridge Lab (every minute). For most comparisons, weather data from the PEARL Ridge Lab was used, since those are higher frequency measurements colocated with the aerosol measurements, and to a lesser extent, with the MAX-DOAS measurements. Throughout this chapter, references to meteorological variables indicate data from the PEARL Ridge Lab, unless specified otherwise. Ozonesondes (used in the BrO retrievals) were launched once per week from the EWS, with increased launch frequency in early March. Radiosondes were launched twice daily from the EWS. Surface ozone measurement were made by a TFS 49i ozone analyzer located at 0PAL (10 m altitude). Hourly mean surface ozone data are available for 2017-2019, since the instrument was installed in late 2016.

In situ aerosol measurements were made by several instruments located in the PEARL Ridge Lab (Tremblay et al., 2019; Vicente-Luis et al., 2020). Coarse mode aerosol particles, defined here as diameters (d_p) greater than 0.5 μm, were measured by an Optical Particle Counter (OPC, 3 minute resolution, data available for 2016-2018), and an Aerodynamic Particle Sizer (APS, 1 minute resolution, data available for 2019). The OPC measures the number concentration of particles with d_p between 0.3 μm and 20 μm in six size bins, while the APS measures aerodynamic particle diameters between 0.5 μm and 20 μm in 52 size bins. To combine the coarse mode aerosol data into one time series, the OPC diameter was assumed to be equal to the physical diameter (Tremblay et al., 2019), and merged integrated APS number concentrations with integrated OPC data for $d_p > 0.5$ μm. Owing to the lack of information about the shape and density of the particles measured by the APS, the aerodynamic diameter was assumed to be equal to the physical diameter. Accumulation mode aerosols were measured using a Scanning Mobility Particle Sizer (SMPS, data available for 2016-2019). Number concentrations were integrated for $0.1\ \mu\text{m} < d_p < 0.5\ \mu\text{m}$ (hereafter this range is referred to as the accumulation mode). Black carbon concentrations were measured by two Photoacoustic Extinctiometer instruments (PAX, 1 hour resolution, data available for 2017-2018), one with a 405 nm laser (PAX405), and the other with a 870 nm laser (PAX870) (Vicente-Luis et al., 2020). PAX405 is sensitive to both black and organic carbon, while PAX870 is sensitive to black carbon only.

Back trajectories and surface sensitivities were calculated using the FLEXible PARTicle (FLEXPART) model (Stohl et al., 1998; Pisso et al., 2019). FLEXPART is a Lagrangian particle dispersion model that can be used to simulate the transport and mixing of gases and aerosols in the atmosphere, both forward and backward in time. For this study, 3-day back trajectories were calculated by initializing FLEXPART at approximately 3-hour intervals during the periods when BrO partial columns were available. Passive tracer particles were released instantaneously in a 3° longitude by 0.8° latitude by 2 km altitude box, approximately centered on the sensitivity region of the MAX-DOAS measurements. The simulations used 6-hourly meteorological fields ($0.5° \times 0.5°$ spatial resolution) from the Climate Forecast System (CFS V2) model simulations (Saha et al., 2011, updated daily) provided by NCEP to calculate back trajectories.

The output of the backward FLEXPART simulations is sensitivity to emissions at the surface, at 1-hour time steps along the 3-day back trajectory. For each back trajectory, the total sensitivity in each grid cell was calculated as the sum of the sensitivities for each time step. The mean trajectory, calculated using a clustering algorithm (Stohl et al., 2002) was also recorded. Since the surface sensitivities are calculated for the entire domain (Northern Hemisphere, 0.5° × 0.5° resolution), they can be used to obtain a measure of the amount of contact between the air masses and snow on FYI or MYI. For this purpose, the weekly Equal-Area Scalable Earth (EASE) Grid (12.5 km × 12.5 km) sea ice age data (Tschudi et al., 2019) was used, provided by the National Snow and Ice Data Center at the the National Aeronautics and Space Administration (NASA). To calculate FYI or MYI sensitivity for each back trajectory, the FLEXPART sensitivities were linearly interpolated to a fine grid (0.01° × 0.025°, approx. 1 km × 1 km or better in the Arctic), and the fine grid coordinates were converted to the equal area projection of the sea ice data. Using this converted grid, the mean sensitivity within each sea ice cell can be calculated. The weekly sea ice data were not interpolated, and back trajectories that spanned parts of two weeks were split up for the sea ice sensitivity calculations (and merged again later). Since the sea ice grid cells preserve area, the sea ice sensitivity for each back trajectory is then the sum of the sensitivities in each sea ice cell tagged as FYI or MYI.

To match high-frequency wind data and aerosol measurements to the BrO columns, average values were calculated for the mean measurement time of each BrO column, using the time interval of the MAX-DOAS measurements used in each profile retrieval (10-25 minutes). Note that wind speed and wind direction measurements are not available for approximately 4% of the BrO partial columns. These gaps were not filled with EWS data, because while the overall statistics of wind measurements are similar at the EWS and at the PEARL Ridge Lab, wind directions (as defined in Sect. 6.1) calculated for individual BrO partial columns differ between the two for 70% of the dataset. Low-frequency datasets, such as hourly measurements or the radiosonde data, were linearly interpolated to the time of the BrO partial columns. Sea ice sensitivity values calculated from FLEXPART back trajectories (one value every ~3 h) were linearly interpolated by day, with the values just before (after) the first (last) FLEXPART time of the day held constant. This was done in order to avoid interpolating between sea ice sensitivity values from separate days.

6.2 Overview of the Dataset

6.2.1 Four Years of Springtime BrO Measurements

To understand the environmental controls on BrO variability, it is useful to first take a look at the time series of BrO and other closely related measurements. The four years of

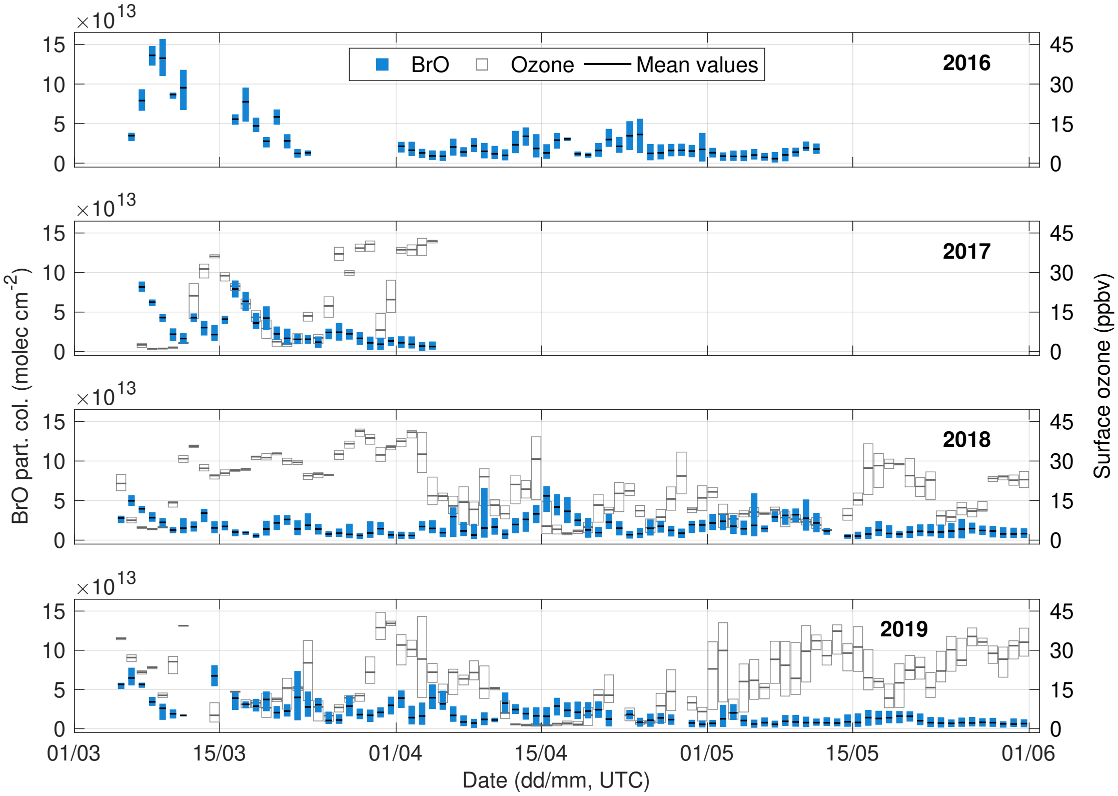

Figure 6.4: Daily range of retrieved 0-4 km BrO partial columns (blue rectangles) and paired surface ozone values (empty rectangles) for March to May 2016-2019. The rectangles represent the full range of values for each day, and the black lines show the daily mean.

springtime observations presented here (254 days and over 10 000 partial columns) provide enough data to examine the month-to-month and year-to-year variability of bromine activation in Eureka.

Figure 6.4 shows the daily mean and range of BrO partial columns for the entire dataset (March-May measurements) used in this study. Missing days (e.g., in March 2016 or 2019) typically indicate that the retrievals failed due to unfavorable weather (blizzards, whiteout conditions), while longer missing periods (e.g., April-May 2017) are due to instrument downtime. The largest BrO partial columns are observed in March, with some bromine activation in April, and generally small BrO partial columns by May. The May measurements are often near or below the approximate detection limit, but all measurements up to 31 May (or the last measurement date) were included here (unlike Burd et al., 2017, for example, who defined end dates for each season). Excluding the typically low BrO partial columns in late May does not have a significant impact on the results presented here. On the other hand, May measurements provide a useful test

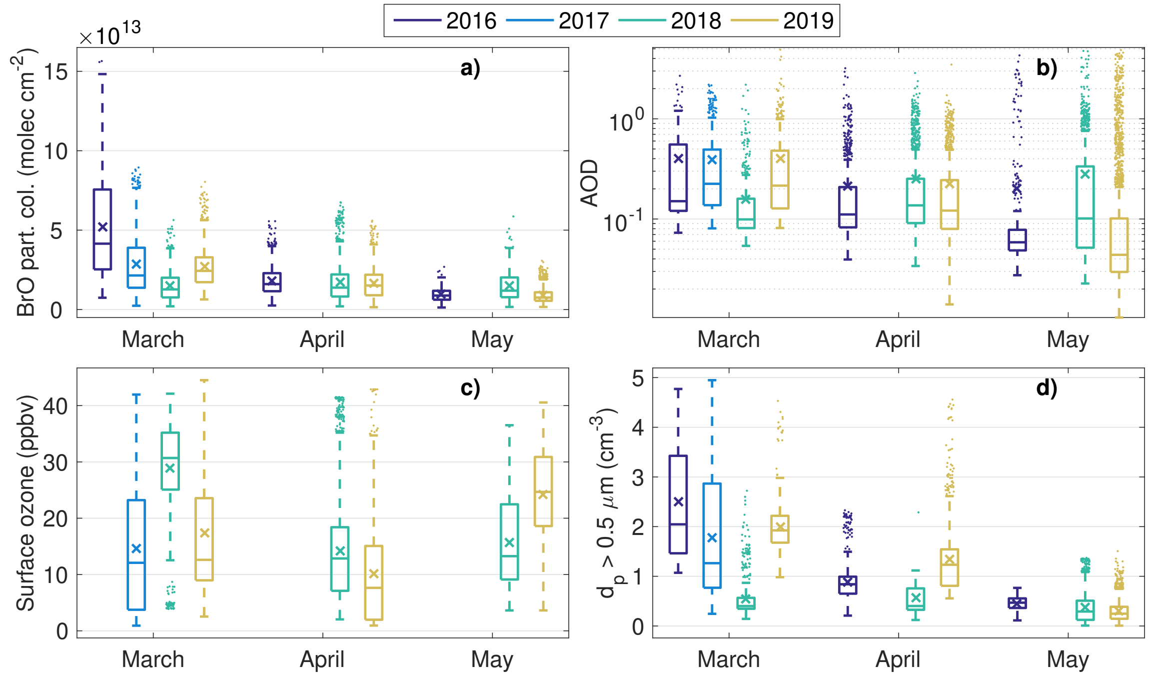

Figure 6.5: Monthly statistics of **a)** 0-4 km MAX-DOAS BrO partial columns, **b)** MAX-DOAS AOD, **c)** surface ozone measurements at the EWS, and **d)** in situ measurements of coarse mode aerosols at the PEARL Ridge Lab. The height of the boxes indicates the 25^{th} and 75^{th} percentiles of the data, with the median marked by the horizontal line, and the mean shown by the x symbols. The whiskers indicate approximately 2.7σ, and the outliers are marked by dots. Note that surface ozone and aerosol measurements were only included for dates when MAX-DOAS data were also available, and there are no MAX-DOAS data for April-May 2017. In addition, no surface ozone measurements are available for 2016.

to determine whether the observed relationships of BrO and other variables hold for background BrO conditions as well.

The month-to-month variability of the BrO partial columns is more readily apparent in Figure 6.5a. The mean and median, as well as the largest BrO partial columns, generally decrease from March through May, with March data showing the greatest variability. These patterns are typical for the bromine activation season. The year 2018 stands out: BrO concentrations were very low in March, and several BrO enhancements were observed in May. The low BrO partial columns in March 2018 correspond to low AOD and low coarse mode aerosol concentrations (Fig. 6.5b and d, respectively), as well as unusually high surface ozone measurements (Fig. 6.5c). The year-to-year variability of BrO (especially in March) is in line with Swanson et al. (2020), who showed that springtime BrO in the Arctic exhibits significant interannual variability.

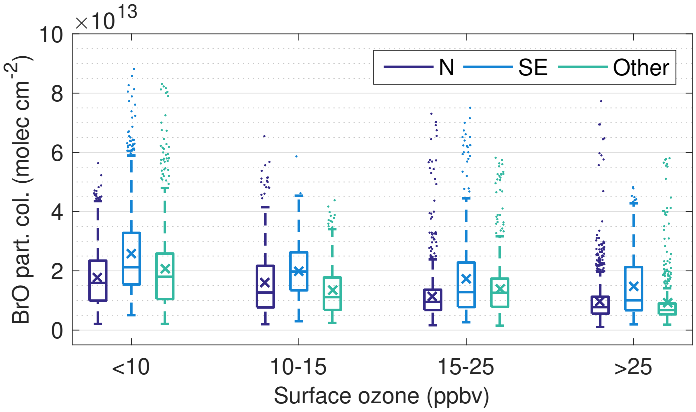

Figure 6.6: Statistics of 0-4 km BrO partial columns as a function of surface ozone concentrations and wind direction. Box plots as in Figure 6.5. Note that surface ozone measurements are only available for 2017-2019.

Ozone measurements (Fig. 6.5c) indicate that more than half of the measurements in March and April (with the exception of March 2018) show at least moderate ODEs (<15 ppbv), and a large fraction of the air samples are strongly depleted in ozone (<10 ppbv; after Halfacre et al., 2014). ODEs are still common in May. During the rest of the year, moderate ODEs occur only in August and September (2% and 0.7% of measurements per month, respectively), and there are only six samples of strongly ozone-depleted air. There are no clear enhancements in the August and September BrO dSCDs, but some BrO might still be present. Excluding March to May data, the overall mean surface ozone concentration measured by the in situ instrument at 0PAL is 33 ppbv, with a 7 ppbv standard deviation (2017-2019 data). The mean value for the March to May measurements is 19 ± 12 ppbv.

Variations in surface ozone do not show a clear relationship to BrO columns (Fig. 6.4). This is not surprising since the MAX-DOAS measurements are not sensitive to the surface layers (Sect. 6.1.3), and some bromine explosions likely terminate before the ozone-depleted airmass arrives in Eureka. Overall, strong and moderate ODEs in the surface ozone data correspond to higher mean and median BrO partial columns than air masses with high surface ozone, as shown in Figure 6.6. This pattern applies to all wind directions, but BrO partial columns for SE winds are usually higher than for other wind directions, especially in non-ODE conditions. The data also show large scatter, with the largest BrO values are observed at similar frequencies for strong ODEs and background ozone conditions. ODEs are often observed in background BrO conditions as well. This is consistent with the literature, where it has often been noted that the relationship of ozone and BrO is complex even for colocated measurements, due to transport and mixing (e.g., Pöhler et al., 2010; Frieß et al., 2011), and the partitioning of reactive bromine (e.g., Wang et al., 2019).

The AOD values retrieved from MAX-DOAS measurements (Fig. 6.5b) show significant month-to-month and year-to-year variation. While the mean AODs are similar from month to month, the median values and the lowest AOD values show a slight decrease for April and May, when compared to March. Coarse mode aerosol concentrations (Fig. 6.5d) show a clear decrease from March through May as well. Accumulation mode aerosol concentrations (not shown), on the other hand, stay relatively constant throughout the spring. The in situ measurements are consistent with the Arctic aerosol cycle (Croft et al., 2016). Ice crystals, common in the spring, also appear less frequently as temperatures increase (EWS observations, not shown). The retrieved AOD likely reflects these variable aerosol conditions, combined with blowing snow events that lead to high AOD values.

6.2.2 Air Mass History

The next step in characterizing the observed bromine events is understanding the source of the air masses. As discussed in Section 6.1.3, the BrO retrievals are likely not sensitive to the surface layers, and so the observed events are probably often related to transport. The air mass histories then likely play an important role. Since the wind directions observed at the PEARL Ridge Lab are clearly bi-modal (see Sect. 6.1.1), air mass histories might vary as a function of local wind direction.

Indeed, FLEXPART back trajectories indicate that the main wind directions correspond to distinct air mass histories. For northerly (N) winds, the majority of air masses arrive at Eureka directly from the Arctic Ocean, and some back trajectories show airmass sources over northern Greenland and the Canadian Arctic Archipelago (Fig. 6.7a, d, and g). Sensitivity to the surface is weighted towards the Arctic Ocean. For southeasterly (SE) winds, back trajectories are typically ‘comma-shaped’ (indicating the presence of storms or low-pressure systems), and cluster towards the south and west of Eureka (Fig. 6.7b, e, and h). The sensitivity is also more heavily weighted towards the Canadian Archipelago and the western Arctic. Other wind directions correspond to a mix of conditions, with back trajectories mostly from the east of Eureka (Fig. 6.7c, f, and i). It should be noted that the back trajectory dataset was not filtered based on local wind speed, since back trajectory lengths do not correlate well with local winds ($R^2 < 0.1$ for 3-day back trajectories). This indicates that local wind speed is not a good indicator of whether the current airmasses are local or transported.

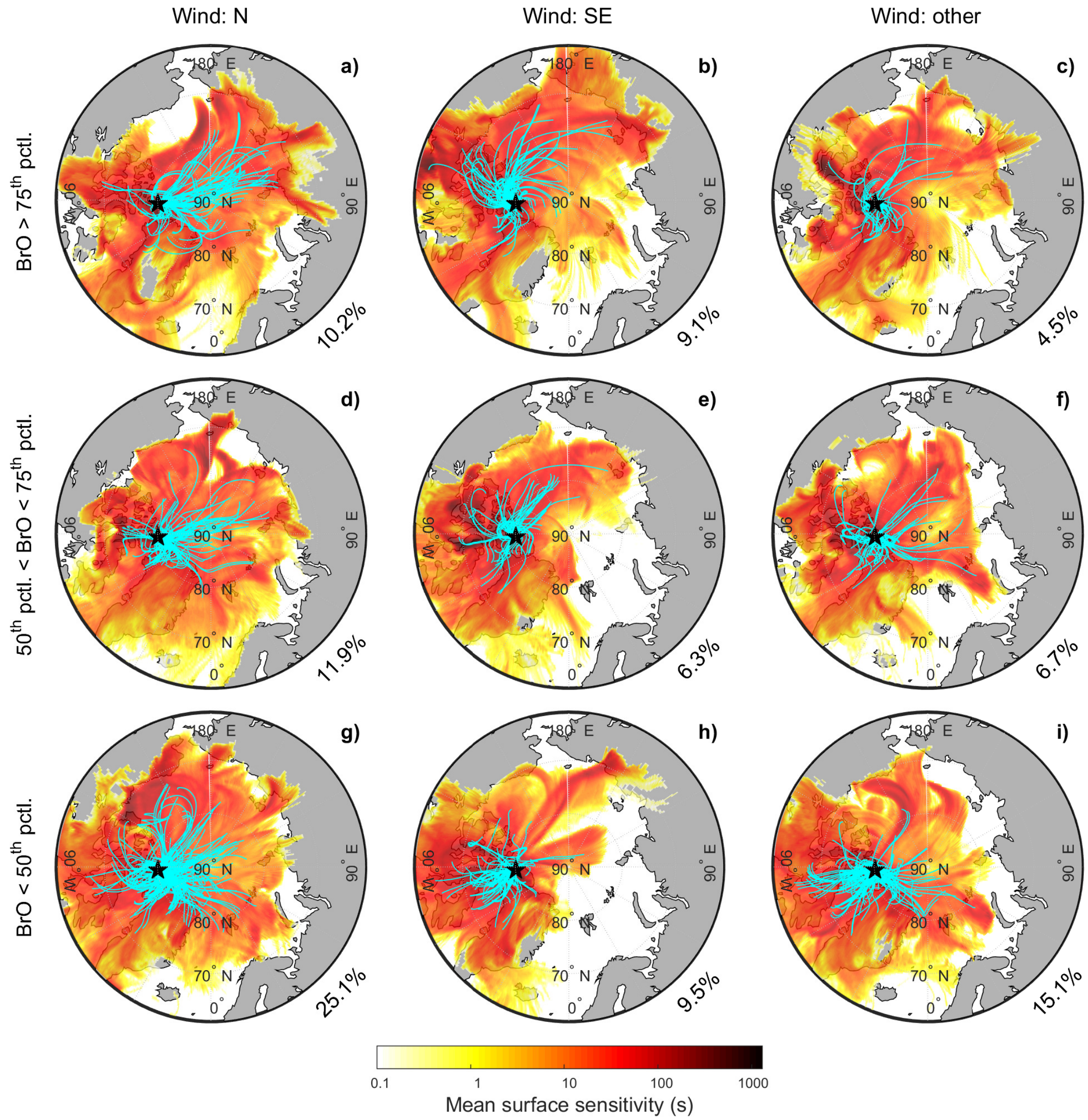

Figure 6.7: Mean surface sensitivities (log scale color map) and individual trajectories (solid lines) for subsets of the FLEXPART back trajectory dataset. The location of Eureka is indicated by the black star. The top row shows FLEXPART runs where the corresponding mean BrO was above the 75th percentile of the BrO partial column dataset (2.1×10^{13} molec cm^{-2}), the middle row shows back trajectories with BrO partial columns between the median (1.3×10^{13} molec cm^{-2}) and the 75th percentile, and the bottom row shows FLEXPART runs with BrO below the median. The back trajectories are grouped by local wind direction in each column. The percentages in the bottom right of each map show the portion of back trajectories that fall into the categories defined by the rows and columns. Note that the percentages add up to less than 100% since back trajectories with no wind data were excluded.

Considering only BrO partial columns of specific magnitudes (from the statistics of the mean BrO partial columns corresponding to each FLEXPART run), the back trajectories differentiate even further. Looking at N winds, BrO partial columns in the top quartile ($>2.1\times10^{13}$ molec cm^{-2}) correspond to reasonably straight back trajectories that connect the central Arctic Ocean to Eureka (Fig. 6.7a). Very few trajectories come from other regions, indicating that contact with sea ice likely plays an important role for N winds. This connection is examined further in Section 6.3.2. When looking at N winds with BrO above the median (1.3×10^{13} molec cm^{-2}), but below the 75th percentile, the back trajectories tell a similar story, but most of them are shorter, originating less than 1000 km from Eureka (Fig. 6.7d). Finally, BrO events below the median show no clear patterns in the back trajectories for N winds (Fig. 6.7g). This category accounts for one quarter of the entire dataset.

For SE winds, the storm-related trajectories discussed earlier correspond mostly to BrO partial columns in the top quartile of the dataset (Fig. 6.7b). These storms often originate in the western Arctic, and travel over sea ice, or over the Canadian Arctic Archipelago. This observation is further supported by the fact that SE winds correspond to a larger fraction of high wind speeds when compared to N winds (Fig. 6.2). BrO events above the median for SE winds show fewer storm-like trajectories, and as for northerly winds, the back trajectories are shorter and indicate more localized influences (Fig. 6.7e). Finally, BrO partial columns below the median show a very different set of air mass histories, with most back trajectories originating to the southeast of Eureka (Fig. 6.7h). From these observations it appears that storms from the western Arctic almost always bring high BrO concentrations to Eureka (see e.g., Blechschmidt et al., 2016; Zhao et al., 2016b, for an exemplary case). While a few comma-shaped trajectories appear for wind directions other than SE, most of these still correspond to high BrO partial columns. Sections 6.3.2 and 6.3.3 shed more light on how storms might contribute to observed BrO enhancements.

6.3 The Relationship between BrO and Environmental Variables

From the back trajectory analysis, it is clear that different wind directions correspond to distinct air mass histories. The observed bromine events, then, might also show different characteristics as a function of wind direction. Principal component analysis (PCA) is a useful tool to highlight the statistical relationships between the observed variables, and

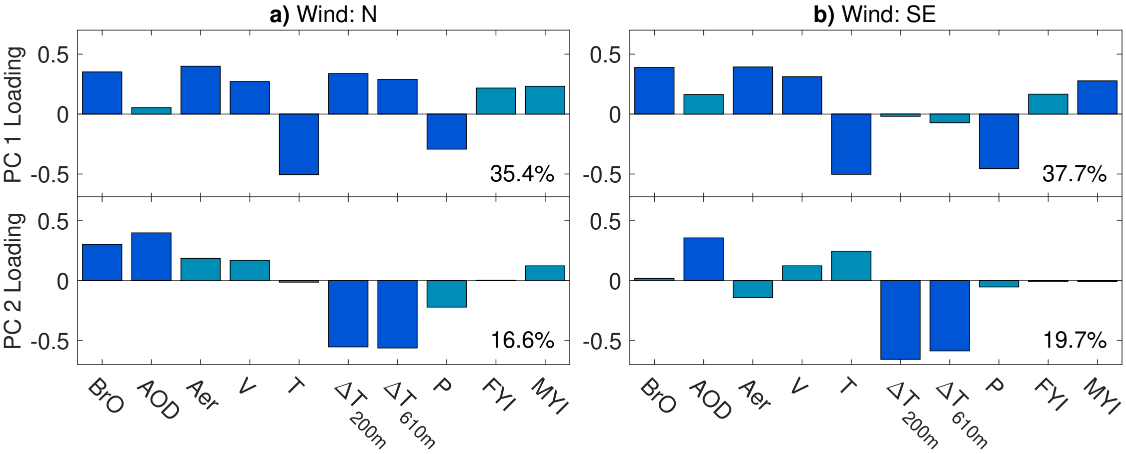

Figure 6.8: Principal component analysis results for **a)** N winds and **b)** SE winds. Variables as described in the text. Only the first two principal components are shown, and the variance corresponding to each PC are indicated on the plots. Loadings greater than 0.25 are highlighted in blue for emphasis.

examine how changing air mass histories affect those statistics. PCA was performed on the dataset composed of the following variables: the BrO partial columns and the AOD retrieved from the PEARL-GBS measurements, the coarse mode aerosol concentrations from the merged OPC and APS dataset ('Aer'), the wind speed (V), temperature (T), and pressure (P) measured at the PEARL Ridge Lab, the temperature differences between 200 or 610 m and sea level (ΔT_{200m} and ΔT_{610m}) calculated from radiosonde data, and the FYI and MYI contact calculated from FLEXPART back trajectories and sea ice age data. Surface ozone concentrations were excluded since data were not available for 2016. The dataset was grouped by wind direction, and the PCA was performed separately on the partial datasets after centering and standardization.

The first two principal components (PC) for N and SE winds are shown in Figure 6.8. The first PC for both N and SE winds accounts for more than one third (35% and 38%, respectively) of the variability in the datasets. For both wind directions, the first PC shows that wind speed, sea ice sensitivity, and coarse mode aerosol concentrations correlate positively with BrO, while temperature is strongly anticorrelated. These relationships are examined in more detail in the following sections. The main difference between the two wind directions according to PCA is the role of atmospheric stability. For N winds, an increase in BrO partial columns is correlated with an increase in the inversion strength between the EWS and the PEARL Ridge Lab, while for SE winds, an increase in BrO correlates with a slight decrease in the temperature difference. Intuitively, these two PCs resemble the two general conditions for bromine activation: shallow BrO enhancements in a stable boundary later, and vertically distributed BrO enhancements during storms. For SE winds, the impact of storms is exemplified by the second PC: this component is not related to BrO, but highlights the correlation of AOD values with decreasing atmospheric stability. For N winds, the second PC is similar to the first PC for SE winds, but explains a smaller portion of the variance in the dataset.

These results are in agreement with Swanson et al. (2020), who analyzed a multi-year dataset of BrO gathered in coastal Alaska (Utqiaġvik) and over the Arctic Ocean. Using PCA with a slightly different set of variables, Swanson et al. (2020) identified two distinct meteorological factors associated with BrO enhancements, similar to the two PCs described above. Here, both of these factors are associated with BrO enhancements, but their importance varies as a function of wind direction and air mass history. In addition, as discussed previously, the BrO partial columns have limited sensitivity to the surface. This is also supported by the observation that the inversion strength at 200 m shows the same results as ΔT_{610m} in Figure 6.8. The fact that the PCA still detects the statistical signature of strong inversions, which Swanson et al. (2020) also associate with surface (0-200 m) BrO enhancements, indicates that transport and topography are important factors for the PEARL-GBS BrO dataset.

6.3.1 Wind Speed, Stability, and Temperature

Wind speed, temperature, and temperature gradients are known to be important factors in bromine chemistry, largely due to their role in determining the vertical structure of BrO (e.g., Peterson et al., 2015). As shown in Figure 6.9a-c, the mean BrO partial columns show a slight increase for wind speeds greater than 5 m s^{-1} for N winds, and a gradual increase across all wind speeds for SE winds. Other wind directions appear similar to N winds, but there are too few stronger wind events to draw any conclusions. It's important to note, however, that averaging all BrO values might obscure important details. BrO partial columns above the median occur across a range of wind speeds, with no clear pattern. It is the low BrO values that appear to be related to wind speed. For N winds, low BrO events become much less frequent for winds above 7-8 m s^{-1}, as indicated by the density of the points in Figure 6.9a. BrO events for SE winds exhibit similar tendencies, and minimum BrO values clearly increase past the same threshold as well (Fig. 6.9b). These trends are likely related to vertical mixing, as explained below.

The majority of studies examining the relationship of BrO to wind speed use data from Utqiaġvik, Alaska. Frieß et al. (2011) and Liao et al. (2012) found that enhanced surface BrO corresponded to episodes of high winds (>5-6 m s^{-1}) and increased surface

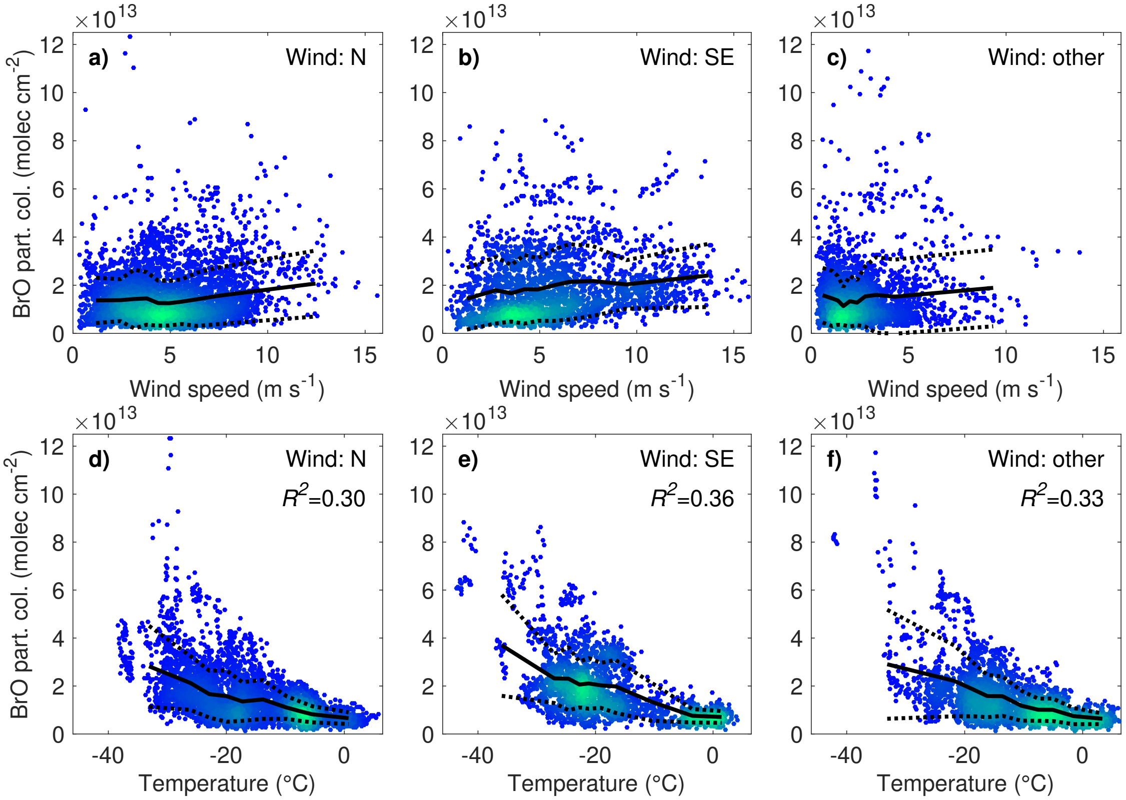

Figure 6.9: 0-4 km BrO partial columns as a function of **a)** to **c)** wind speed, and **d)** to **f)** temperature. The color scaling shows the normalized density of the points. The solid lines show the mean BrO partial column for each decile of the x-data, and the dotted lines indicate the corresponding one standard deviation. The correlation of BrO with temperature is indicated by the R^2 values in panels **d)** to **f)**.

extinction. Peterson et al. (2015), however, found that 0-2 km BrO partial columns showed no clear dependence on wind speed. This is consistent with the observations in this study for BrO partial columns above the median. Peterson et al. (2015) also noted that wind speeds above 8 m s^{-1} almost always led to vertically distributed BrO events and larger column values, which likely explains the observed increase in the minimum BrO values past a similar threshold in this study. Since the retrievals are likely only sensitive to BrO aloft, one might expect to see little to no BrO for shallow boundary layer events, and high BrO for distributed events. If weaker winds correspond to a mix of shallow and distributed events, the retrieved BrO partial columns might show a wide range of values, while wind speeds above 7-8 m s^{-1} would result in larger BrO partial columns only.

The influence of strong winds and vertical mixing highlights the potential impact of atmospheric stability on the BrO partial columns. Here, the temperature differences between the EWS and the PEARL Ridge Lab (ΔT_{610m}, from radiosonde data) are used as a measure of atmospheric stability. Wind speed and ΔT_{610m} do not show a clear relationship. While near-zero ΔT_{610m} are more frequent for strong winds (above 7-8 m s^{-1}), the inversion strength is largely independent of wind speed for weaker winds.

When a temperature inversion is present between the EWS and the PEARL Ridge Lab, the inversion strength appears to have little influence on the BrO partial columns. BrO values above the 90th percentile peak at inversion strengths of approximately 10 °C for N winds, and around 0 °C for SE and other wind directions, although these peaks reflect the most frequent ΔT_{610m} values for each wind direction. BrO values below the 90th percentile are observed across a wide range of ΔT_{610m} values (from -4 to 20 °C), with a decline in the maximum BrO only past $\Delta T_{610m} = 15$ °C. This indicates that BrO aloft is often decoupled from the surface in Eureka, since the atmosphere is expected to be stably stratified for strong inversions, and the measurements here are likely not sensitive to BrO in the surface layer. These results contrast with Peterson et al. (2015), who found that stronger inversions lead to higher near-surface BrO concentrations and reduced column amounts. The large BrO partial columns during strong inversions might be related to long-range transport or to local activation of bromine on aerosol particles (examined in more detail in Sect. 6.3.3). An important caveat is the unknown effect of topography on the measurements presented here: Utqiaġvik is located on flat terrain, while the PEARL Ridge Lab is surrounded by ridges and valleys. Winds blowing over ridges could potentially inject ‘surface’ air into layers hundreds of meters above the open fjords. In addition, the MAX-DOAS instrument is looking down a valley (Fig. 6.1, Sect. 6.1.3), and so the low elevation angle light paths are always closer to the surface than the retrieval algorithm assumes. Surface air masses could therefore still influence the BrO concentrations even when strong inversions are present.

While low wind speeds or atmospheric stability do not have a clear direct influence on BrO partial columns, the mean surface ozone values from the EWS show an increase with wind speed for very weak winds (colocated wind data from the EWS, Fig. 6.10a), and a decrease with increasing ΔT_{610m} (not shown). Samples strongly depleted in ozone are observed most often for wind speeds below 2 m s^{-1}. These events correspond to a wide range of temperature inversion strengths (mean $\Delta T_{610m} = 6.9 \pm 4.5$ °C) and BrO partial column values, which is likely related to the fact that, due to the effects of topography, calm conditions at the EWS do not necessarily correspond to calm weather at the PEARL Ridge Lab. Only events with complete depletion of surface ozone (concentrations below 2 ppbv) occur preferentially during strong inversions (mean $\Delta T_{610m} = 8.0 \pm 3.5$ °C), possibly representing local bromine release from the snowpack. This is in agreement

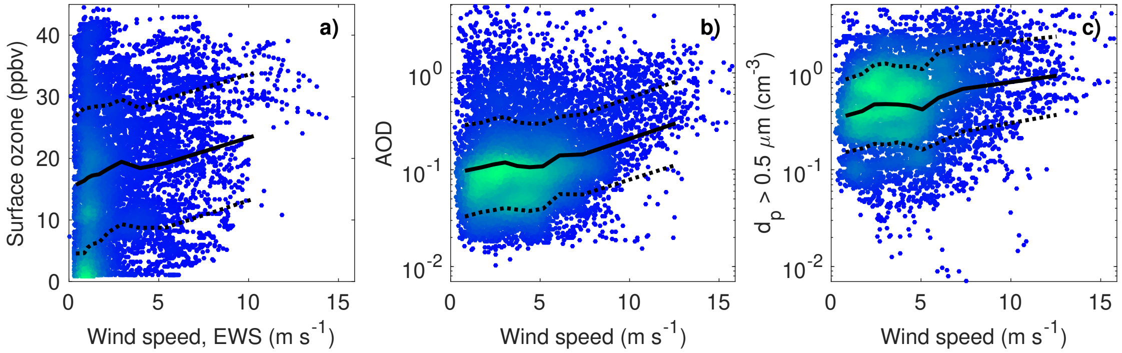

Figure 6.10: **a)** Surface ozone concentrations as a function of wind speed measured at the EWS, alongside **b)** MAX-DOAS AOD and **c)** coarse mode aerosol concentrations as a function of wind speed measured in the PEARL Ridge Lab. The color scaling shows the normalized density of the points. The solid lines show the mean BrO partial column for each decile of the x-data, and the dotted lines indicate the corresponding one standard deviation. Note that the aerosol concentrations are plotted on a logarithmic scale to highlight the change in the minimum values.

with Helmig et al. (2012), who found that ODEs in Utqiaġvik occurred primarily in calm conditions, and Halfacre et al. (2014), who came to the same conclusion using measurements from buoys across the Arctic Ocean.

Strong winds, on the other hand, represent a different regime. Helmig et al. (2012) argued that the increased mixing by stronger winds might replenish ozone fast enough to counteract any potential increase in bromine concentrations. As shown in Figure 6.10a, minimum hourly ozone concentrations show a clear increase for wind speeds greater than approximately 5 m s^{-1}, and ODEs become increasingly rare as wind speeds increase. As described above, stronger winds are more likely to coincide with near-zero $\Delta T_{610\mathrm{m}}$ values (signifying a deeper boundary layer), as well as increasing BrO partial columns (Fig. 6.9a-c). Take strong SE winds as an example: when EWS wind speeds are greater than 8 m s^{-1}, 85% of the BrO partial columns are above the overall median of the BrO dataset. SE winds are commonly associated with storms and good mixing, and large BrO partial columns are commonly observed in non-ODE conditions (see Fig. 6.6). In fact, for SE winds with EWS wind speeds greater than 8 m s^{-1}, surface ozone concentrations generally increase with BrO values, with a corresponding R^2 value of 0.25. These results indicate that for strong winds, mixing of ozone-rich air from above is sufficient to maintain background ozone concentrations even in high BrO conditions. The observation that BrO partial columns are apparently not diluted by the same mixing that replenishes ozone indicates that BrO is either continuously mixed up from the snowpack, or that recycling and/or release from aerosol particles is more efficient in strong winds.

It is known that bromine release occurs predominantly at lower temperatures (e.g., Burd et al., 2017). BrO partial columns show a clear decrease as temperature increases, as seen in Figure 6.9d-f. The relationship is not linear, but R^2 values indicate that temperature (at 610 m) alone can explain a third of the variance in the BrO dataset, independent of wind direction. Minimum BrO partial columns also show an upward trend with decreasing temperatures below approximately -25 °C, likely related to the fact that very cold weather at the PEARL Ridge Lab (which is usually above the inversion layer) often corresponds to strong winds, weak inversions, and good mixing. When considering the temperatures at the EWS, this feature disappears. The strong downward trend of the maximum BrO with temperature, however, is present regardless of the altitude of the temperature measurements. Enhanced BrO is observed up to temperatures just below freezing, and the partial columns decrease to near the approximate detection limit for temperatures around or above 0 °C. The largest BrO partial columns are observed at temperatures below -10 °C.

Tarasick and Bottenheim (2002) argued, based on ozonesonde measurements, that ODEs require temperatures below -20 °C. More recent studies, however, observed ODEs at temperatures well above this threshold (Bottenheim et al., 2009; Jacobi et al., 2010; Halfacre et al., 2014). Jacobi et al. (2010) and Halfacre et al. (2014) both argued that the relationship of ozone and temperature needs to be interpreted with caution due to the role of transport in determining local ozone levels. The results in this study are consistent with Burd et al. (2017), who reported enhancements of 1° elevation BrO dSCDs up to, but not above, freezing temperatures in Utqiaġvik, Alaska. The authors noted that peak dSCDs increased from 0 to -10 °C, and dSCDs showed a relatively flat envelope below -10 °C. Using partial columns from a subset of the same dataset, Peterson et al. (2015) found no clear relationship between BrO and temperature. That dataset, however, only included measurements up to -5 °C, and so the results are not inconsistent with Burd et al. (2017) and the present study. Using long-path DOAS measurements in the Amundsen Gulf, Pöhler et al. (2010) observed a similarly strong negative trend in the maximum near-surface BrO, but sloping to a high threshold of -15 °C (the highest observed temperature) instead of 0 °C. It should be noted however, that those measurements did not extend into May, and thus did not experience the higher temperatures associated with the end of the bromine activation season.

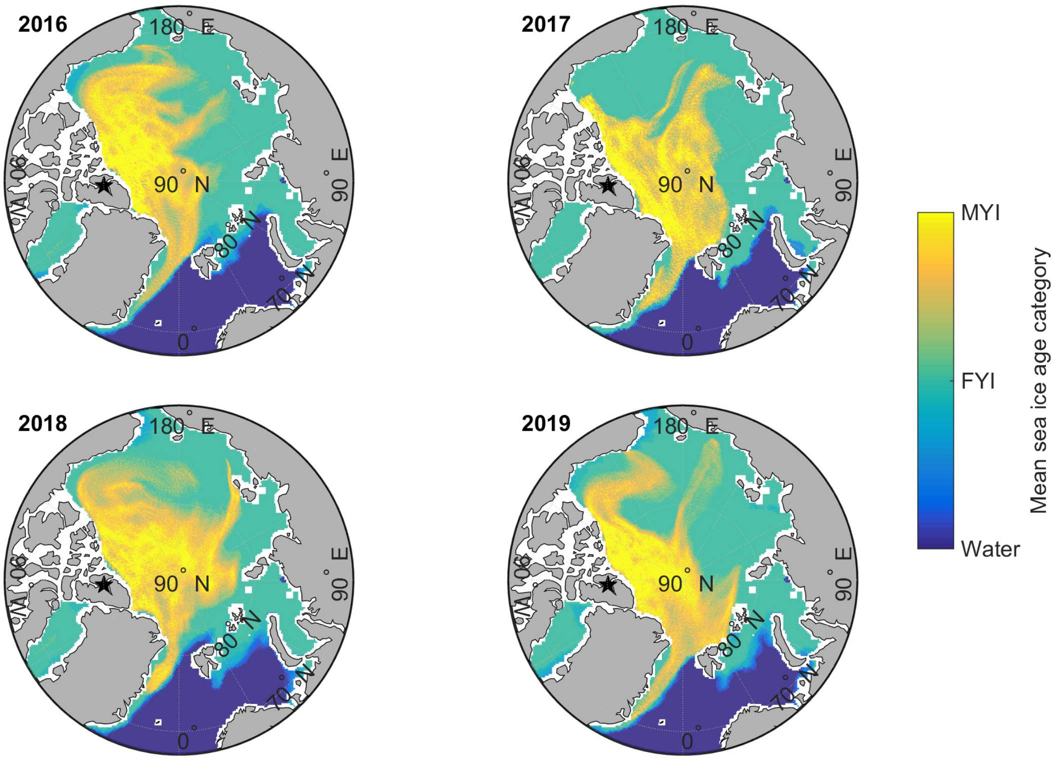

Figure 6.11: Mean sea ice age for spring 2016-2019 using weekly EASE-Grid sea ice age data. The averages for each year correspond to the measurement period of the MAX-DOAS instrument. White shading indicate areas where ice age was not calculated in the EASE-Grid dataset. The location of Eureka is indicated by the black star.

6.3.2 Relationship to Sea Ice Sensitivity

If the lofted BrO in the dataset is related to transport, a correlation might be expected with time spent in areas covered by sea ice, as snow over FYI is commonly considered a major source of bromine to the atmosphere (e.g., Peterson et al., 2016). Maps of the distribution of FYI and MYI for the measurement period in each year are shown in Figure 6.11. Sea ice age data from the weekly EASE-Grid dataset were averaged using age categories of water = 0, FYI = 1, and MYI = 2. This simple method was chosen to highlight the general distribution of FYI and MYI in each spring, as movement of sea ice in the 2-3 month periods considered here is not significant from an Arctic-wide viewpoint. While the distribution of FYI and MYI varied significantly from year to year, the sector of the Arctic Ocean near Ellesmere Island was covered in MYI in all four years. White areas on Figure 6.11 (e.g., in the Canadian Arctic Archipelago) indicate locations where the EASE-Grid ice age was not calculated. Most of these areas were likely covered by FYI during the study period.

BrO partial columns show a clear relationship to FYI sensitivity for N winds only (Fig. 6.12a). The maximum BrO partial columns increase with increasing FYI sensitivity, and the mean BrO partial columns show an increase as well. For N winds, air masses with enhanced BrO mostly come from over the Arctic Ocean (Fig. 6.7), and so they likely transport bromine that was released from the snow over the sea ice. The lack of local influences is further supported by the fact that the largest BrO partial columns were observed when strong temperature inversions were also present (Sect. 6.3.1).

For SE and other wind directions, the largest BrO partial columns still tend to coincide with high FYI sensitivity, but the mean BrO values are largely independent of time spent in FYI areas (Fig. 6.12b and c). Since for SE winds, BrO events above the median often correspond to storms, this indicates that the snowpack over FYI is likely not the only source of storm-related BrO. Enhanced BrO events coincided with air masses that originated in a variety of regions, including over the Canadian Arctic Archipelago, where the inland snowpack might play a larger role than FYI (Peterson et al., 2018). The role of local BrO sources (snowpack and locally generated aerosol) might also be important. Other wind directions do not show a close relationship to FYI sensitivity, as most back trajectories originated to the south or east of Eureka.

Good correlation between air mass contact with FYI and measured BrO has been reported by several studies (Simpson et al., 2007; Nghiem et al., 2012; Peterson et al., 2016). Frieß et al. (2011), however, found that time spent in FYI areas was not in itself a good predictor of BrO concentrations. The authors noted that simple characterizations might not be sufficient to capture the complex influences of air mass history, meteorology, and micro physical parameters. The approach in this study still utilizes a relatively simple parametrization, and it is evident that FYI sensitivity alone does not explain the local BrO variability. The different impact of FYI sensitivity as a function of wind direction highlights the importance of meteorology at sites that experience distinct weather regimes. Furthermore, FYI is not necessarily the best metric to compare to BrO measurements in Eureka.

When considering all sea ice sensitivity (FYI and MYI, Fig. 6.12d-f), the relationship to the highest BrO values is similar to the FYI case discussed above. The mean BrO partial columns, however, now show at least a modest increase as a function of sea ice sensitivity for all wind directions. While the sea ice sensitivity metric is only weakly correlated to BrO, the correlation coefficients might be used as a more tangible measure of the changes in the relationship. R values improve from 0.28, 0.07, and -0.01 (for N, SE and other wind directions, respectively) to 0.32, 0.11, and 0.09 when all sea ice

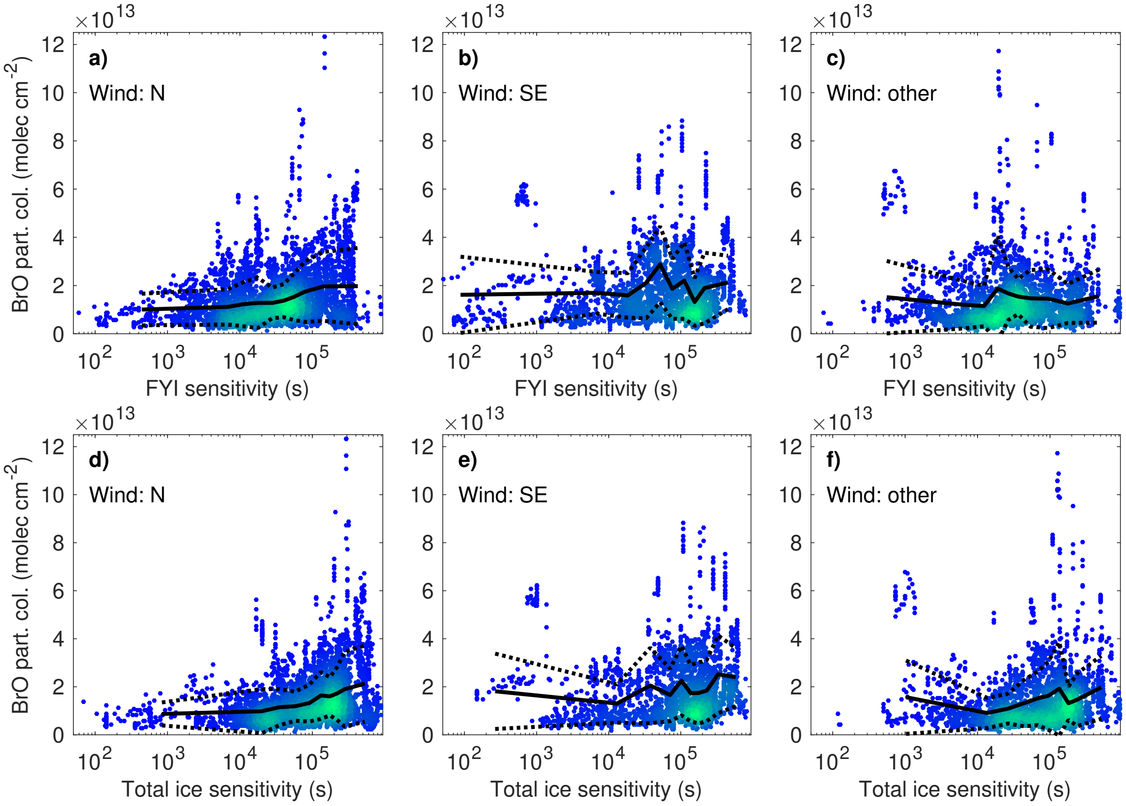

Figure 6.12: 0-4 km BrO partial columns as a function of **a)** to **c)** FYI sensitivity and **d)** to **f)** all sea ice sensitivity. The color scaling shows the normalized density of the points. The solid lines show the mean BrO partial column for each decile of the sensitivity data, and the dotted lines indicate the corresponding one standard deviation.

is considered. It appears that considering FYI and MYI together is a slightly better indicator of bromine activation than FYI sensitivity only. Extending the back trajectory durations to 5 days (instead of 3 days) does not change the results. Compared to other sites, sensitivity to MYI might be more prominent in Eureka, since the Arctic Ocean off the coast of Ellesmere Island is usually covered by perennial ice. It should be noted that the observed sensitivity to different sea ice areas is not independent. The maximum MYI sensitivity values increase with FYI sensitivity, although low MYI sensitivity values occur across a wide range of FYI sensitivity values. Even so, it is possible that new snow on MYI also contributes to bromine release.

Seasonal ice (FYI) contributes to the snow salinity required for bromine release via upward migration of brine into the snowpack, through the influence of frost flowers, and via atmospheric processes such as sea spray SSA from leads and polynyas (e.g., Domine et al., 2004; Hara et al., 2017; Frey et al., 2020). On the other hand, sea ice that survives the summer (MYI) has much lower salinity, and MYI areas are more consolidated, with fewer areas of open water. As a result, snow on FYI is commonly considered a much more likely source of bromine than MYI. Atmospheric processes, however, might still create favorable conditions for bromine release on MYI. Arctic haze (pollution transported from northern Eurasia) is ubiquitous over the Arctic Ocean in the winter and spring. The haze consists of aged and acidic accumulation mode (approx. $0.1\ \mu m < d_p < 0.5\ \mu m$) particles, composed mainly of sulfate, black carbon, and sea salt (e.g., Quinn et al., 2007; Croft et al., 2016). Haze aerosols are deposited onto the surface of the snowpack, and can be scavenged by falling and blowing snow as well (e.g., Sharp et al., 2002; Nawrot et al., 2016). It has been shown that acidity and markers of halogen activation (Br^-, Hg) in the snowpack correlate with exposure to Arctic haze (Toom-Sauntry and Barrie, 2002; Douglas and Sturm, 2004; Nawrot et al., 2016). While this process impacts snow on all sea ice, as well as snow on land, the additional bromine source from MYI areas might be detectable at sites like Eureka, situated near the perennially ice-covered regions of the Arctic Ocean.

Identifying the source regions of transported BrO events is challenging, and it is outside the scope of this project. Using 3-day back trajectories, there are several enhanced BrO events with high MYI to all sea ice sensitivity ratios (4% of the dataset has a ratio of 0.9 or greater), but even the small fraction of FYI sensitivity is always sufficient to explain the observed BrO. For example, most of these events correspond to easily identifiable BrO plumes that originate over FYI in the western Arctic (data from the University of Bremen GOME-2 data browser[1]). The most probable case for MYI bromine release is a single event (16 May 2019) that maintains the 90% MYI sensitivity even when the back trajectories are extended to 5 days. BrO concentrations on 16 May were in the top quartile of the May 2019 BrO measurements ($\sim 1.6 \times 10^{13}$ molec cm^{-2}, see Fig. 6.5), and surface ozone was in the 15-20 ppbv range. The corresponding back trajectories indicate that the mean mixing layer height for all particles was less than 280 m during the 5-day FLEXPART runs. This is below the mean and median mixing layer height for all FLEXPART runs, indicating fairly calm conditions along the back trajectories, ideal for snowpack bromine release. The timing of this event might also play a role. The influence of Arctic haze (as well as bromine plumes that pass over MYI) would accumulate during the course of the spring, and the potentially increasing salinity and bromide content (Toom-Sauntry and Barrie, 2002; Douglas and Sturm, 2004) of snow over MYI could create favorable conditions for bromine release in May.

Previous studies have noted the potential role of MYI in bromine chemistry. Peterson et al. (2016) found that time spent in all ice areas correlated slightly better with BrO

---

[1] `http://www.iup.uni-bremen.de/doas/scia_data_browser.htm`

than FYI contact only, and the authors reported R values similar to those seen in this study for N winds. Gilman et al. (2010) came to similar conclusions using ozone as a tracer for the presence of halogens. The authors of both studies noted, however, that all ice contact is highly correlated with FYI contact. More recently, Peterson et al. (2019) analyzed bulk snow samples collected over FYI and MYI in the central Arctic, and found that surface snow over MYI was frequently depleted in bromide, indicating that MYI acts as a source of bromine to the atmosphere. Based on snowpack salinity and depth measurements, the authors concluded that atmospheric processes, as opposed to upward migration of brine, are likely the key factors in determining halogen concentrations in surface snow. In addition to direct bromine release, the snowpack on sea ice is also a source of blowing snow, which then may generate SSA particles (Giordano et al., 2018; Huang et al., 2018; Frey et al., 2020). While investigating the role of SSA in bromine release, Choi et al. (2018) found that bromine explosion frequency correlated better with modeled SSA emission flux over all sea ice than with SSA emissions over FYI only (although given the results of Peterson et al., 2019, SSA from snow on MYI might not be an ideal source of bromine). These results lend support to the idea that bromine chemistry is active in MYI areas. Determining the exact contribution of MYI (either through the snowpack or via SSA production) requires further research.

6.3.3 The Role of Aerosol Particles

Transport of BrO over long distances by storms (Begoin et al., 2010; Sihler et al., 2012; Blechschmidt et al., 2016; Zhao et al., 2016b) indicates that aerosols are important for recycling and maintaining lofted BrO concentrations. As discussed in Section 6.2.2, SE winds often correspond to storms passing over Eureka, and these air masses show little correlation between sea ice sensitivity and BrO partial columns (Sect. 6.3.2). Aerosols might then be the key for the observed large BrO partial columns. Furthermore, since the BrO partial columns presented here have limited sensitivity to local snowpack sources, aerosols likely play an important role regardless of wind direction.

The mean BrO partial columns show a clear increase with increasing AOD values (Fig. 6.13a-c). As anticipated, this increase is most pronounced for SE winds, and this wind direction sees the largest ratio of high to low AOD observations as well. 70% of AODs are above 0.1 for SE winds, while the same statistic is 45% for N and other wind directions. High AOD values don't necessarily correspond to large BrO partial columns, but the largest BrO partial columns are observed for AOD > 0.1, and mean BrO remains high past this value as well. Frieß et al. (2011), Peterson et al. (2015), Simpson et al.

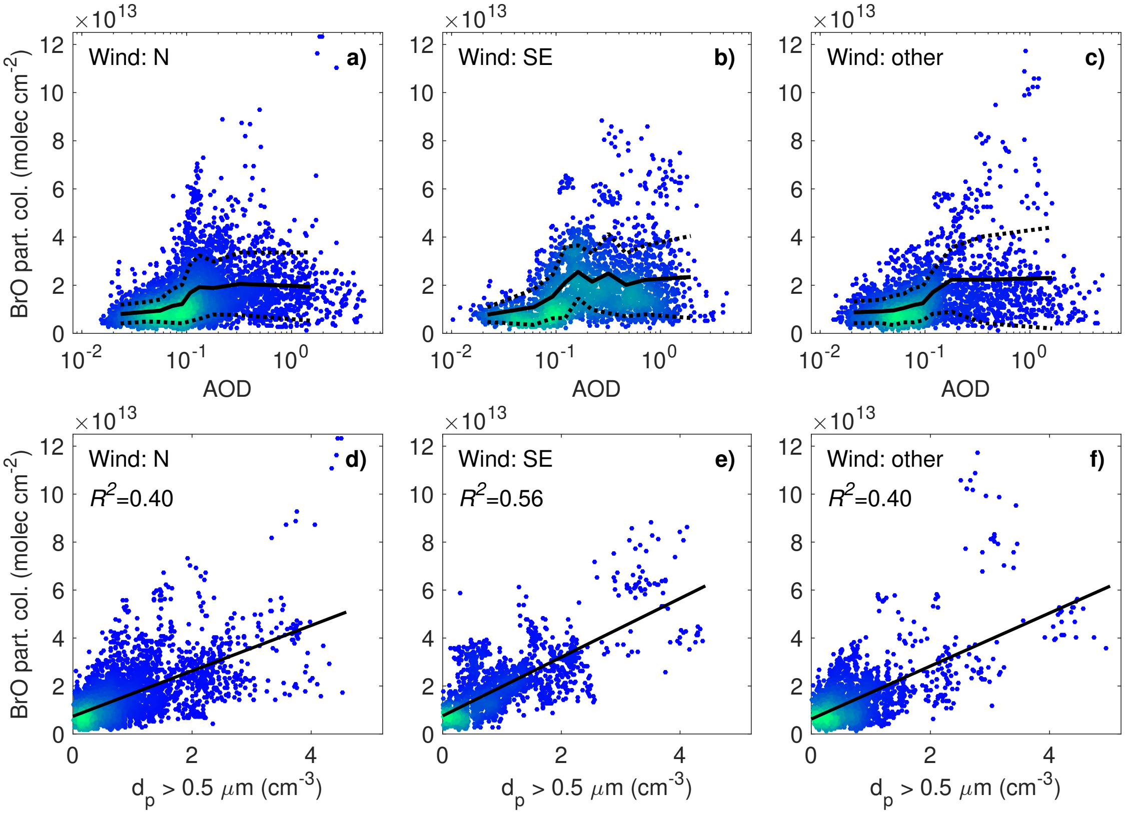

Figure 6.13: 0-4 km BrO partial columns as a function of **a)** to **c)** retrieved AOD, and **d)** to **f)** coarse mode aerosol number concentrations. The color scaling shows the normalized density of the points. For panels a-c, the solid lines show the mean BrO partial column for each decile of the x-data, and the dotted lines indicate the corresponding one standard deviation. For panels **d)** to **f)**, the solid lines show the linear least squares fit, with the R^2 values indicated on the plots.

(2017), and Swanson et al. (2020) all found that increasing extinction and high AOD corresponded to larger BrO values. Simpson et al. (2017) concluded that high extinction was necessary, but not sufficient, for BrO layers to migrate aloft, in agreement with the results presented here. The aerosol extinction retrieval, however, does not separate the sources of extinction (aerosols, ice crystals, blowing snow). High AOD corresponds to a wide range of aerosol concentrations (for both accumulation and coarse mode). In situ aerosol measurements, therefore, might be a more appropriate base of comparison.

Indeed, BrO values show good correlation to coarse mode aerosol concentrations (>0.5 μm, Fig. 6.13d-f). The relationship is approximately linear, with the highest R^2 value for SE winds (0.56), and lower R^2 values (0.4) for other wind directions. Both minimum and maximum BrO values show a linear increase with increasing coarse mode aerosol concentrations, and this envelope is the tightest for SE winds. Interestingly, accu-

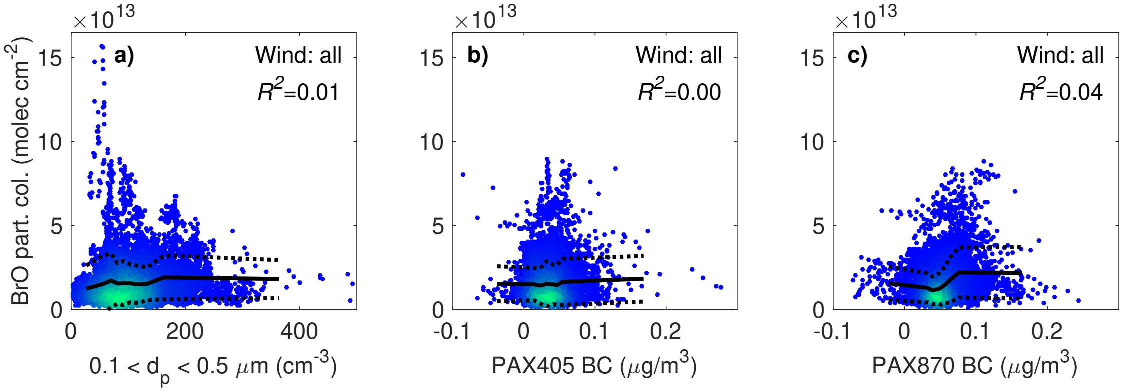

Figure 6.14: 0-4 km BrO partial columns as a function of **a)** accumulation mode aerosol concentrations, and black carbon concentrations from **b)** PAX405 and **c)** PAX870. The color scaling shows the normalized density of the points. The solid lines show the mean BrO partial column for each decile of the data, and the dotted lines indicate the corresponding one standard deviation. Note that PAX measurements are only available for 2017-2019.

mulation mode aerosols (0.1-0.5 µm, Fig. 6.14a) are not at all correlated to BrO partial columns ($R^2 \approx 0$). From this dataset, it appears that coarse mode aerosols play a crucial role in bromine chemistry, and the presence of these aerosols is a necessary and sufficient condition for observing high BrO values at the elevation of the PEARL Ridge Lab.

These results are in good agreement with Peterson et al. (2017), who observed a BrO plume sustained on, and transported with, a layer of supermicron aerosol particles. The authors also noted that submicron aerosol particles were likely not a controlling factor in BrO recycling. While a different diameter cutoff (0.5 µm instead of 1 µm) is used here, the conclusions do not change when using supermicron particles following Peterson et al. (2017). For this dataset, aerosols larger than 0.5 µm correlate better with BrO (R^2 values improve by 8% and 40% for N and SE winds, respectively). In situ measurements support the role of aerosols in bromine chemistry. Hara et al. (2002) found that aerosol particles larger than 2 µm were generally depleted in Br^-. In Antarctica, Legrand et al. (2016) observed Br^- depletion in coarse mode aerosols in the spring, and Br^- enhancement in accumulation mode particles. These conclusions were supported by the results of Giordano et al. (2018) as well. Hara et al. (2018), however, found that Br^- was depleted in all aerosols, regardless of size. Frey et al. (2020) came to similar conclusions, although they only measured aerosols with $d_p > 0.36$ µm.

There are no composition measurements available for springtime aerosol in Eureka for 2016-2019. The limited number of coarse mode aerosol sources in the Arctic spring implies that the aerosol instruments most likely observe SSA, which might be generated by blowing snow (Zhao et al., 2017; Giordano et al., 2018; Huang et al., 2018; Frey et al., 2020), or released from leads in the sea ice (Nilsson et al., 2001; Leck et al., 2002; May et al., 2016; Kirpes et al., 2019). SSA generated from local blowing snow would correspond to high aerosol load for wind speeds above the blowing snow threshold. Figure 6.10b and c show that both minimum AOD values and minimum coarse mode aerosol concentrations clearly increase with wind speed for strong winds.

The wind speed threshold for blowing snow during the measurement period was estimated using the empirical model of Li and Pomeroy (1997). The model describes the wind speed threshold (U) for blowing snow as a function of temperature (T):

$$U = 9.43 + 0.18\,T + 0.0033\,T^2, \tag{6.1}$$

where the parameters were calculated to best fit the blowing snow thresholds observed across the prairies of western Canada. Using temperature data from the PEARL Ridge Lab, the mean blowing snow threshold for the study period was calculated to be 7.8 m s^{-1}. Since the threshold varies with temperature, the mean values were lower in March and April (7.1 and 7.3 m s^{-1}, respectively) than in May (8.5 m s^{-1}). Using temperature data from the EWS, the mean threshold was 7.7 m s^{-1} (7.3, 7.1, and 8.3 m s^{-1} for March, April, and May, respectively). Estimates using this model likely have large uncertainties, given that 2 m temperatures (as specified by Li and Pomeroy, 1997) are not available here, and snow properties in Eureka might differ from those observed in the prairies. Manual weather observations from the EWS provide an independent estimate of the blowing snow threshold. Weather conditions are reported hourly, 24 hours a day. Using March to May data, the mean wind speed corresponding to observations of 'Blowing Snow' was 7.4 m s^{-1}, remarkably similar to the estimates using the Li and Pomeroy (1997) model. Given these estimates, it is likely that the commonly accepted blowing snow threshold of 7-8 m s^{-1} (Li and Pomeroy, 1997; Giordano et al., 2018; Frey et al., 2020) applies to springtime conditions in Eureka.

Considering data with wind speeds below the calculated blowing snow threshold, coarse mode aerosol concentrations are 0.68 ± 0.65 cm^{-3} (mean and standard deviation). For wind speeds above the threshold, the mean value is 1.32 ± 0.98 cm^{-3}, indicating that coarse mode aerosol load increases significantly ($p < 0.001$) for wind speeds above the blowing snow threshold. High aerosol concentrations, on the other hand, occur over a range of wind speeds, with only a slight preference for stronger winds. This indicates that most of the aerosols are likely not produced locally, but transported to the measurement location. The increased aerosol load for strong winds is also consistent with the threshold for lead-based SSA production (4-5 m s^{-1}, e.g., Leck et al., 2002; May et al., 2016), although local wind speed is not necessarily representative of wind speed along the back trajectories.

To investigate the potential contribution of leads-sourced SSA to the measurements, Moderate Resolution Imaging Spectroradiometer (MODIS)/Aqua and MODIS/Terra L3 daily sea ice data (Hall and Riggs, 2015a,b) were used to examine sea ice coverage near Eureka. The sea ice maps indicate that during the study period there were no clearly identifiable leads or areas of open water within 600-800 km to the north and west of Eureka, where most of the air masses pass through (Sect. 6.2.2). However, cloud cover often obscures much of the sea ice near Eureka, and so the presence of leads cannot be ruled out. Leads further along the back trajectories (e.g., in the western Arctic, where the storms that reach Eureka typically originate) likely also contribute to the measured aerosol concentrations. A potential nearby source of lead-sourced SSA is northern Baffin Bay, which often contains polynyas as early as March, and becomes largely ice-free by early May. Back trajectories, however, show little sensitivity to this area, especially when BrO concentrations are high. Overall, the measurements presented here are consistent with some local SSA production from blowing snow. The proportion and sources of transported aerosols, however, cannot be determined based on the data used in this study.

Accumulation mode aerosols are likely dominated by the Arctic haze (Sect. 6.3.2), with some potential contribution from SSA. Frey et al. (2020) noted that less saline blowing snow would create smaller particles, potentially as small as d_p on the order of 1 nm. To separate the impact of the Arctic haze, BrO partial columns were compared to black carbon concentrations (another haze tracer) from the PAX405 and PAX870 instruments at the PEARL Ridge Lab (Vicente-Luis et al., 2020). The results (Fig. 6.14b and c) indicate a similar lack of correlation as seen in the accumulation mode comparisons, and the structure in the correlation plots largely reflects the underlying distribution of BrO partial columns. The two PAX instruments show a slightly different relationship to BrO, likely due to the different sensitivity of the PAX instruments, but neither correlate with BrO. This suggests that Arctic haze does not play a direct role in bromine activation in Eureka. It is possible, however, that these particles participate in bromine recycling once BrO is already present, as haze aerosols are composed partly of sea salt (e.g., Quinn et al., 2007; Croft et al., 2016).

It is still unclear to what extent SSA contributes to direct bromine release, as opposed to recycling of bromine released elsewhere. The recent results of Legrand et al. (2016) and Hara et al. (2018) indicate that SSA is a major source of tropospheric bromine in

Antarctica. Frey et al. (2020) came to the same conclusion, and showed that bromine release from SSA took place between 2 and 29 m above the sea ice surface. While these results can likely be generalized to all polar regions, similar measurements are needed in the Arctic to confirm the role of SSA. Satellite measurements of BrO by Choi et al. (2018) showed good correlation to simulated SSA emission flux in the Arctic, and no correlation to FYI areas, indicating that SSA is responsible for at least part of the bromine release in the Arctic. The very good correlation between coarse mode aerosols and BrO observed in this study supports this conclusion. Given that the coarse mode aerosols are most likely SSA, and the observation that high coarse mode aerosol concentrations always correspond to high BrO values, these results strongly suggest that coarse mode aerosols play an active role in bromine release at Eureka.

6.4 Summary

This chapter used BrO partial columns and AOD values retrieved from PEARL-GBS measurements to characterize bromine activation during four activation seasons in Eureka. Local wind directions show two distinct modes (N and SE), and the observed BrO events show different characteristics for each of these wind directions. Air mass histories for enhanced BrO events (inferred from FLEXPART back trajectory simulations) show two modes as well: N winds transport air masses from over the Arctic Ocean, while SE winds generally correspond to storms that originate in the western Arctic or over the Canadian Arctic Archipelago.

It appears that temperature alone accounts for a third of the variance in the BrO dataset, and enhanced BrO was observed at temperatures up to 0 °C. Maximum BrO values increase almost linearly with decreasing temperatures. Due to the elevation of the measurement site (610 m), the retrieved BrO partial columns are likely not sensitive to the surface (sea level), and the PEARL-GBS measures above the boundary layer most of the time. As a result, the strength of the temperature inversion has a limited impact on the BrO values presented here, since the retrievals do not capture the shallow bromine events that typically show a strong dependence on atmospheric stability. When the boundary layer is deep, however, the effects of the enhanced vertical mixing manifest as an increase in the minimum BrO values for wind speeds of 7-8 m s^{-1} or greater. Minimum surface ozone concentrations increase even in moderate wind speeds, and ODEs become less and less frequent as wind speeds increase past 7-8 m s^{-1}. While these high-wind events most often correspond to enhanced BrO, mixing of ozone-rich air from higher altitudes is sufficient to counteract ozone destruction.

While air masses have similar sensitivity to FYI areas regardless of wind direction, BrO partial columns increase with FYI sensitivity for N winds only. On the other hand, when all sea ice sensitivity (FYI+MYI) is considered, the relationship to BrO improves for all wind directions. Snow on MYI is often neglected as a source of bromine because of its lower salinity compared to FYI. It is possible, however, that atmospheric processes (e.g., exposure to Arctic haze) could create favorable conditions for bromine release from snow on MYI.

Since the observed BrO enhancements are likely often decoupled from the surface, high aerosol load (as indicated by the retrieved AOD values) was necessary to maintain high BrO concentrations. The contribution of accumulation mode (0.1-0.5 μm) and coarse mode (>0.5 μm) aerosols was examined using in situ measurements. The accumulation mode is likely dominated by the Arctic haze, and these particles show no direct relationship to BrO. The presence of coarse mode aerosols, however, was a necessary and sufficient condition for observing large BrO partial columns with an instrument located above the boundary layer. It is most likely that these particles are SSA. The strongest correlation ($R^2 = 0.56$) was observed for SE winds that often correspond to storms and favorable conditions for both transport and local production of SSA. The good correlation between BrO and coarse mode aerosols supports the view that SSA is a direct source of bromine to the polar troposphere, but more measurements of the composition and vertical distribution of aerosols would be required to quantify the exact contribution of SSA to the Arctic halogen budget.

Chapter 7

NO_2 Profiling in Toronto

This chapter describes a NO_2 profile dataset retrieved from 2018-2020 Pandora measurements in Toronto using the MAPA retrieval code. MAPA results generally agree well with retrievals using HeiPro, although HeiPro systematically overestimates MAPA NO_2 at higher altitudes. Comparisons indicate that MAPA partial columns correlate better with direct-sun total columns, while HeiPro surface concentrations show a closer relationship to in situ measurements. MAPA was selected to process the entire time series of the Pandora instruments on the basis of computational efficiency. The retrieved partial columns show good correlation to direct-sun data for all measurement modes, while the relationship to in situ surface concentrations varies depending on the wavelength range of the measurements. The MAPA results are used to assess the variability of NO_2 in Toronto, both in normal conditions and during the COVID-19 lockdown in 2020. Seasonal and diurnal variability is apparent in both the partial column and surface concentration datasets, and the main impact of the COVID-19 lockdown appears to be a reduction in the peak NO_2 values.

7.1 Introduction

NO_2 is important for ozone destruction and chlorine deactivation in the stratosphere, and it is also present in the troposphere, where it is often a pollutant. While some NO_x is produced from natural sources (lightning, biomass burning, soils), most tropospheric NO_x is released from fossil fuel combustion and industrial processes (Jacob, 1999). As a result, NO_x is a marker of anthropogenic activity, and NO_2 is commonly used as an indicator of air quality, since it is detectable by remote sensing. High NO_x concentrations are harmful to human health (e.g., Andersen et al., 2011; Anenberg et al., 2018), and NO_x is a precursor for acid rain and secondary pollutants like tropospheric ozone. NO_2 is produced mainly by the oxidation of NO, which happens within a few minutes of emission (Burkholder et al., 2015). High NO_2 concentrations are typically confined to industrial areas or roads with heavy traffic, due to the short lifetime (a few hours in the summer to ∼1 day in the winter, e.g., Leue et al., 2001; Martin et al., 2003; Kenagy et al., 2018) of NO_2 in the boundary layer.

NO_2 is commonly measured using DOAS, both from the ground and from space. Nadir-viewing satellite instruments, such as OMI, GOME, GOME-2, the Scanning Imaging Absorption Spectrometer for Atmospheric Cartography (SCIAMACHY), and the TROPOspheric Monitoring Instrument (TROPOMI), provide global coverage of NO_2 columns (Richter and Burrows, 2002; Richter et al., 2005; Boersma et al., 2007; Valks et al., 2011; van Geffen et al., 2020). The spatial resolution of satellite measurements, however, is generally too coarse to resolve pollution much below the city scale, and the conversion of satellite columns to surface concentrations (a more useful quality for air pollution metrics) is not straightforward (Lamsal et al., 2008; Dieudonné et al., 2013; Gu et al., 2017; Qin et al., 2020). Furthermore, the satellites (in near-polar, sun-synchronous orbits) generally provide one measurement per day for a given location. Ground-based DOAS instruments are ideal for continuous monitoring of NO_2 concentrations. Zenith-sky and direct-sun measurements provide total columns of NO_2 (Brewer et al., 1973; Noxon, 1975; Lee et al., 1994; Van Roozendael et al., 1997; Cede et al., 2006; Herman et al., 2009), and tropospheric columns (Spinei et al., 2014) or surface concentrations (Zhao et al., 2019b) might be retrieved from these measurements as well.

The best tropospheric sensitivity, however, is provided by off-axis viewing geometries (e.g., MAX-DOAS). MAX-DOAS measurements have good sensitivity to NO_2 in the lowest 1-1.5 km of the atmosphere (Vlemmix et al., 2011), and the horizontal sensitivity of the measurements is on the order of a few to tens of km (Tirpitz et al., 2021). A large number of algorithms have been developed to retrieve tropospheric columns, profiles, and surface concentrations of NO_2 from MAX-DOAS measurements. Some studies use geometrical approximations or simple radiative transfer calculations to retrieve partial columns (Ma et al., 2013; Vlemmix et al., 2015; Jin et al., 2016; Drosoglou et al., 2017). Profile retrievals require more detailed simulations using RTMs, and most algorithms follow the parametric or OEM approaches, as described in Chapter 2. Profile datasets from a variety of measurement sites and MAX-DOAS instruments have been described in the literature (Peters et al., 2012; Hendrick et al., 2014; Chan et al., 2015; Wang et al., 2017b; Bösch et al., 2018; Chan et al., 2018; Ryan et al., 2018; Beirle et al., 2019; Wang et al., 2019; Blechschmidt et al., 2020; Davis et al., 2020; Tirpitz et al., 2021). These results are frequently used for satellite validation (e.g., Wang et al., 2017a; Drosoglou et al., 2018; Chan et al., 2019; Verhoelst et al., 2021), and air quality studies (e.g., Hendrick et al., 2014; Wang et al., 2019; Blechschmidt et al., 2020).

In addition to the range of retrieval algorithms, the MAX-DOAS instruments themselves are just as variable (Kreher et al., 2020). Standardized, high-performance instruments provide numerous benefits, including reliable data quality and consistency across multiple sites. The Pandora spectrometers, developed at the NASA Goddard Space Flight Center, were designed to be such high-performance instruments, with the aim to provide standardized and calibrated datasets for satellite validation and air quality monitoring. Pandoras were first deployed in 2006 (Herman et al., 2009; Tzortziou et al., 2012), and the instruments have since been deployed to more than 50 sites globally. The PGN, launched in 2019, coordinates the Pandora measurements, and aims to provide central processing of the data. The current official data products include total columns of ozone and NO_2 retrieved from direct-sun measurements, and the NO_2 data are frequently used for satellite validation (Lamsal et al., 2014; Ialongo et al., 2016; Griffin et al., 2019b; Herman et al., 2019; Ialongo et al., 2020; Verhoelst et al., 2021; Zhao et al., 2020b).

Pandora direct-sun measurements can be used to derive tropospheric columns of NO_2 (Spinei et al., 2014), and NO_2 surface concentrations have been retrieved from Pandora zenith-sky measurements (Zhao et al., 2019b). Direct-sun measurements, however, are not available in cloudy weather, and zenith-sky measurements have limited sensitivity to the near-surface layers. Pandora off-axis measurements are ideal for NO_2 retrievals, but these data are currently underutilized. A quick-look algorithm developed by NASA (used in Frieß et al., 2019; Tirpitz et al., 2021) uses the off-axis measurements to provide partial columns, surface concentrations, and partial profiles based on trigonometric considerations and simplified radiative transport. Currently, however, there are no full NO_2 profiles available from Pandora measurements.

7.2 Instruments and Data Processing

7.2.1 Pandora Measurements

The Pandora instruments (described briefly in Chapter 5) use a temperature-stabilized symmetric Czerny-Turner grating spectrometer with a 0.05 mm entrance slit and a 1200 gr mm^{-1} grating (Herman et al., 2009; Tzortziou et al., 2012; Herman et al., 2015). Spectra are recorded with an uncooled, 2048×64 pixel back-thinned Hamamatsu CCD detector, in the 280-530 nm wavelength range at 0.6 nm resolution. While multiple Pandora configurations exist, only the typical single-spectrometer design is described here. As opposed to the GBS instruments which use mirrors for pointing (Chapter 2), the Pandora instruments point with the optical fibre directly. The Pandora input optics (described below) are mounted on a suntracker assembly to allow multiple viewing geometries. Light enters the input optics through a collimator tube, and the light passes through an entrance window and two filter wheels before it is focused onto an optical fibre by a lens. The first filter wheel contains band pass filters and diffusers, while the second filter wheel contains a set of neutral density filters (generally used for direct-sun measurements only). Both filter wheels contain empty slots as well. The input optics are coupled to the spectrometer using a single-strand silica fibre. The spectrometer is located in a purpose-built box that also contains the instrument computer and the suntracker motor controllers. The box is typically located indoors, while the input optics and the suntracker assembly are mounted outdoors.

Pandora measurements are either made across the entire 280-530 nm wavelength range, or in the UV using the band pass filters in the first filter wheel (280-320 nm or 280-380 nm). The band pass filters reduce stray light for measurements in the UV spectral range. Wavelength calibration for each instrument is performed in the laboratory at several spectrometer temperatures to accurately characterize the spectrometer slit function. Measured spectra are then corrected for a number of effects, including dark current, stray light, temperature changes, nonlinearity effects, and others (Cede, 2019). The exact spatial orientation of the input optics is calculated using the apparent position of the sun from sun-searches performed throughout each day, ensuring excellent pointing accuracy.

The Pandora instruments perform a combination of zenith-sky, direct-sun, and off-axis measurements, alternating between measurements with and without UV band pass filters. The typical measurement sequence includes two types of off-axis elevation scans. 'Long' scans include a full set of 11 elevation angles (1°, 2°, 3°, 5°, 8°, 10°, 15°, 20°, 30°, 40°, and 50°), plus a zenith-sky measurement, while 'quick' scans feature a set of 4 elevation angles (1°, 2°, 15°, and 30°) plus a zenith-sky measurement. Each measurement sequence consists of a U-shaped scan, from 90° to 1°, and back to 90° (the 1° measurement is not repeated). Quick scans account for approximately three quarters of all elevation scans in the typical Pandora measurement sequence.

The two Pandora instruments used here, #103 and #104, have been deployed at ECCC's Downsview location in Toronto since 2013. Elevation scans from the two instruments are available for February 2018 - May 2020 for #103, and for April 2018 - May 2020 for #104. During this period, the main azimuth viewing angles of the two instruments were 255° and 250°, respectively. The line-of-sight of the instruments mostly covers urban

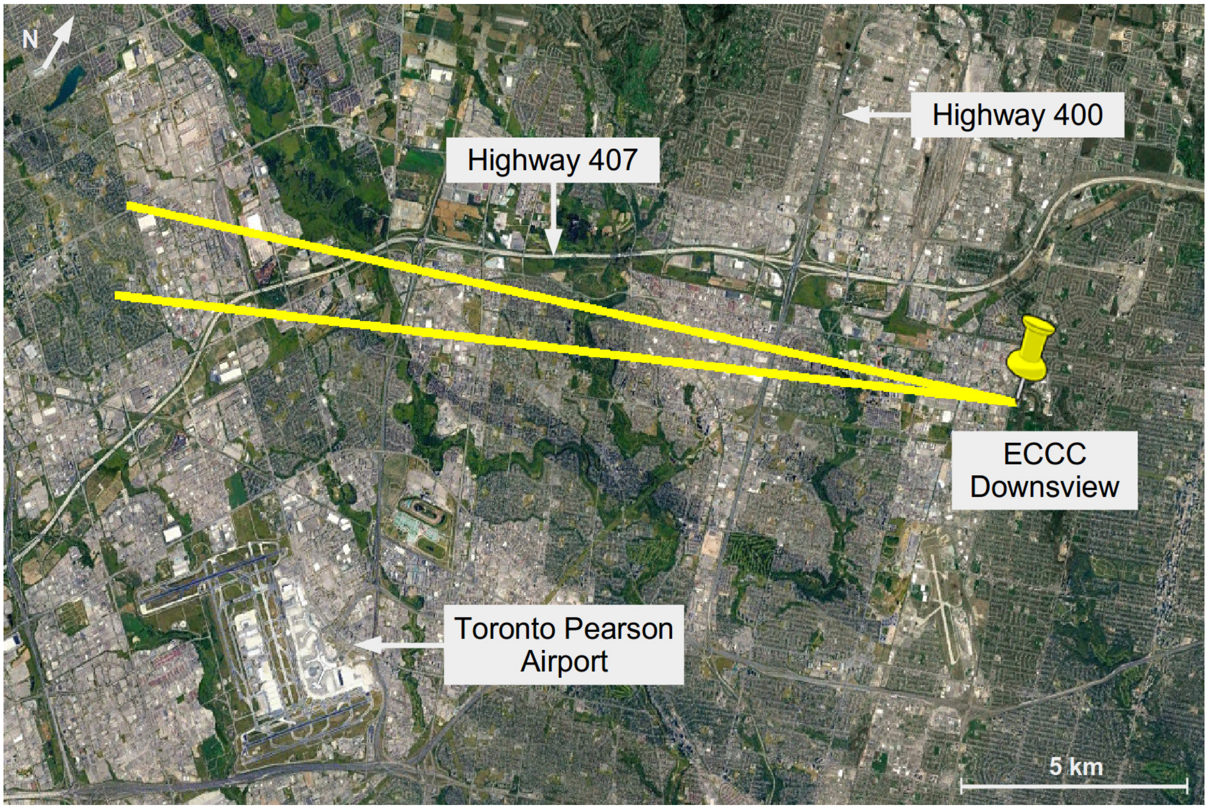

Figure 7.1: Location of Pandoras #103 and #104 in Toronto. The azimuth viewing angles of the instruments (255° and 250°, respectively) are indicated by the yellow lines (20 km in length). Image: Google Earth.

terrain, as shown in Figure 7.1. Major pollution sources include Highways 407 and 400, which run approximately parallel to and across the viewing directions, respectively, and Toronto Pearson Airport, which is only a few km to the south of the line-of-sight of both instruments.

Spectra from the Pandora elevation scans were processed as MAX-DOAS data with sequential references, using the methods outlined in Chapter 2. The QDOAS fit parameters for the data products are shown in Table 7.1. The settings were identical to the fit settings used for CINDI-2 (Appendix A of Kreher et al., 2020, see also Chapter 3). The O_4-UV and NO_2-UV products used the 338-370 nm wavelength window, and only the measurements taken with the UV band pass filters were included. The O_4-vis and NO_2-vis retrievals used only the measurements without the UV band pass filters, and the fits were performed in the 425-490 nm range. The same cross-sections of NO_2 (at 294 and 220 K) (Vandaele et al., 1998), O_4 (at 293 K) (Thalman and Volkamer, 2013), and ozone (at 223 K in the visible and at 223 and 243 K for the UV) (Serdyuchenko et al., 2014) were included for both fitting windows. In addition, the 338-370 nm window included cross-

Table 7.1: QDOAS fit parameters for the Pandora MAX-DOAS measurements.

	O_4-UV and NO_2-UV	O_4-vis and NO_2-vis
Fitting window	338-370 nm	425-490 nm
Cross-section		
Ozone	Serdyuchenko et al. (2014) at 223 and 243 K	Serdyuchenko et al. (2014) at 223 K
NO_2	Vandaele et al. (1998) at 294 and 220 K	Vandaele et al. (1998) at 294 and 220 K
O_4	Thalman and Volkamer (2013) at 293 K	Thalman and Volkamer (2013) at 293 K
H_2O	–	HITEMP (Rothman et al., 2010)
BrO	Fleischmann et al. (2004) at 223 K	–
HCHO	Meller and Moortgat (2000) at 297 K	–
Ring	Chance and Spurr (1997)	Chance and Spurr (1997)
Polynomial	5th order	5th order
Offset correction	Constant	Constant
Shift and stretch	1st order	1st order

sections of HCHO (Meller and Moortgat, 2000) and BrO (Fleischmann et al., 2004), while the 425-490 nm window included a H_2O cross-section (Rothman et al., 2010). A 5th order polynomial and a constant offset correction was used for both wavelength ranges. A uniform RMS threshold of 0.003 was applied to all four dSCD datasets.

7.2.2 Aerosol and NO_2 Retrievals

Aerosol extinction and NO_2 profiles were retrieved using the MAPA and HeiPro retrieval algorithms (Chapter 2). Retrievals were performed separately for the UV and visible wavelength ranges, at the standard RTM wavelengths of 360 nm for both O_4-UV and NO_2-UV, and at 477 and 460 nm for O_4-vis and NO_2-vis, respectively. Both algorithms employ the two-step approach (Chapter 2), where profiles of aerosol extinction retrieved from O_4 dSCDs are used as inputs in the NO_2 retrievals. The MAPA retrievals were performed on the full time series of both Pandoras #103 and #104, while HeiPro retrievals were performed on a subset (June-July 2019) of the Pandora #103 dataset. The general retrieval procedure for MAPA and HeiPro (illustrated in Figure 7.2) is described below.

The MAPA retrievals are performed by elevation scan, and so each U-shaped long and quick scan was separated into two elevation scans (with the 1° elevation angle measurement duplicated). One profile was retrieved for each of these separated elevation scans. HeiPro considers dSCDs in specific time intervals, and so a different approach was necessary. Since the Pandora elevation scans do not follow a strict schedule, the retrieval start times and time intervals were selected to maximize the number of time periods that contain exactly one full U-shaped scan. One profile was then retrieved for each time period, and profiles corresponding to incomplete U-shaped scans (or more than one such scan) were filtered. With HeiPro, the long and quick scans were retrieved separately, due to the different duration and distribution of the scans.

For both the MAPA and the HeiPro retrievals, a priori temperature and pressure profiles were provided by ERA5 reanalysis data (Hersbach et al., 2018, 2020). Daily profiles were calculated for the location of the instruments from the average of daytime (11:00, 14:00, 17:00, 20:00, 23:00 UTC) temperature and pressure profiles. For MAPA, no other a priori information was necessary. For HeiPro, a priori profiles of extinction and NO_2 were selected to be exponentially-decreasing profiles with a scale height of 1 km, with a corresponding AOD and NO_2 column of 0.18 and 9×10^{15} molec cm^{-2}, respectively (after Tirpitz et al., 2021, see also Chapter 3).

HeiPro profiles were retrieved on a 0-4 km altitude grid, using a 200 m vertical resolution. The value in the lowest retrieval layer (0-200 m) is taken to represent surface concentrations (e.g., Tirpitz et al., 2021). For MAPA, only three parameters are retrieved: the integrated column, the layer height, and a shape parameter. The profiles are constructed from a combination of a box profile and an exponential profile. The possible combinations are simple box profiles, box profiles with exponentially decreasing concentrations above, and elevated box profiles. When elevated profiles are retrieved, concentrations below the layer are zero, which might result in a low bias in comparisons to in situ measurements. The MAPA altitude grid is arbitrary, and profiles were output on the same 0-4 km grid as for HeiPro. Surface concentrations correspond to the 0-200 m layer.

OEM algorithms generally converge over a broader range of atmospheric conditions compared to parametric algorithms, as shown by Tirpitz et al. (2021). This is because any lack of information is filled with a priori knowledge, resulting in plausible profiles even when the measurements contain limited information. To limit the influence of such results, HeiPro profiles where DOFS for either NO_2 or aerosols were smaller than 0.7

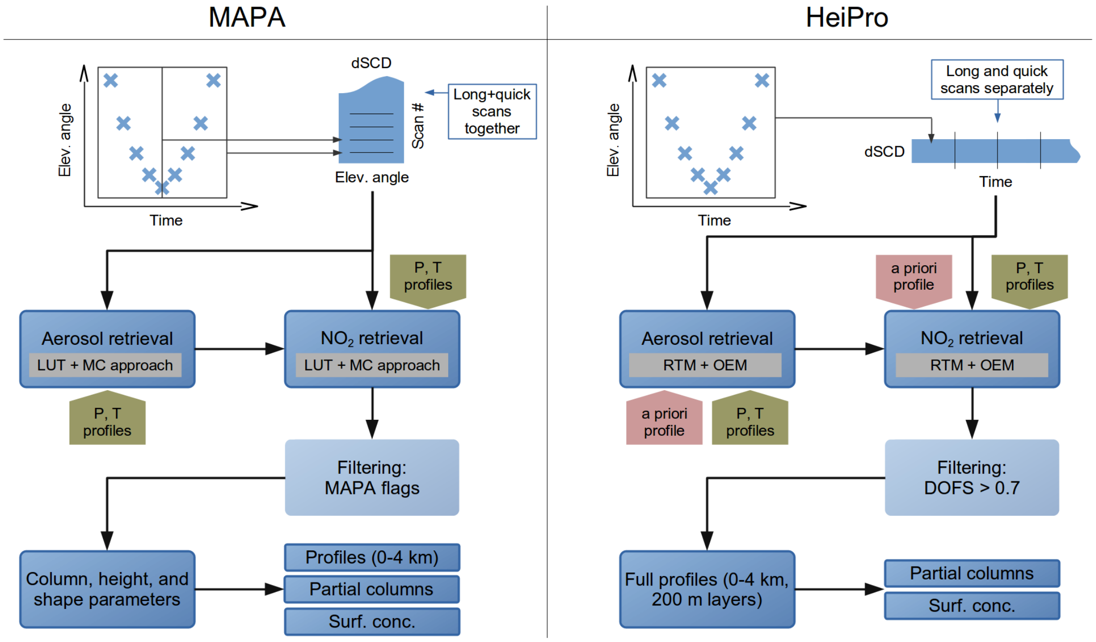

Figure 7.2: Flowchart of the MAPA and HeiPro retrieval procedure for NO$_2$, from the Pandora dSCD processing to the final data products. See text for full descriptions of each algorithm.

were discarded (Payne et al., 2009).

Parametric approaches, on the other hand, often retrieve ambiguous solutions when the limited number of parameters is not adequate to describe the vertical profile. In the case of MAPA, unrealistic profiles are filtered using an elaborate flagging scheme (Beirle et al., 2019). For each flag, warning and error thresholds are defined according to Table 2 of Beirle et al. (2019). Flags are based on the agreement of measured and modelled dSCDs, the consistency of the retrieved parameter ensembles, the shape of the retrieved profile, and other miscellaneous parameters. Profiles with any error or warning flags were excluded from the analysis in this study. Notably, profiles with a corresponding AOD of 2 or higher are flagged as unreliable, since MAX-DOAS sensitivity decreases in the presence of high aerosol load. Using measurements from CINDI-2, Tirpitz et al. (2021) confirmed that this flagging scheme reliably identifies unrealistic profiles, and the filtered MAPA dataset performed well in the algorithm intercomparison (MAPA achieved the overall best results for NO$_2$). To characterize the retrieval uncertainties, the RMS-weighted mean and standard deviation of the parameter ensembles are taken as the final MAPA results (Beirle et al., 2019).

7.3 Supporting Data and Comparison Methodology

The direct-sun NO_2 total columns measured by the Pandoras themselves provide an excellent dataset for comparison to the retrieved partial columns, since the total column is dominated by the tropospheric component in urban settings. Direct-sun measurements provide accurate measurements of the total column, as the light path is well defined, and no RTM calculations are necessary to calculate AMFs. For the direct-sun data product, Pandora spectra are analyzed in the 400-440 nm range using a TOAS technique (Cede, 2019), and NO_2 total columns are produced using the centralized processing algorithm implemented by the PGN. The Pandora NO_2 total columns have been validated in several field studies (Herman et al., 2009; Wang et al., 2010; Piters et al., 2012; Flynn et al., 2014; Reed et al., 2015; Martins et al., 2016; Lamsal et al., 2017), and Herman et al. (2009) found that the columns have an accuracy of 2.7×10^{15} molec cm^{-2} in clear-sky conditions. Pandora #103 direct-sun NO_2 for 2018-2019 is used here.

To validate the retrieved NO_2 surface concentrations, in situ measurements from the National Air Pollution Surveillance (NAPS) Program are used[1]. The NAPS station at Downsview provides hourly averages of NO_2 mixing ratios. The mixing ratios were converted to NO_2 concentrations using colocated weather station data. NAPS NO_2 data are available for 2018-2019.

Since MAPA and HeiPro handle input dSCDs in different ways, additional processing was required for the comparisons between the algorithms. For HeiPro, profiles were only accepted if they corresponded to exactly one U-shaped elevation scan. For MAPA, new profiles were calculated as the average of the two halves of each U-shaped scan, when both halves were marked as valid by the flagging scheme. The resulting profiles were then compared to each other, and to direct-sun and NAPS measurements.

For comparisons of data with similar temporal resolutions, coincidences were generated by pairing measurements from both datasets to the nearest measurement in the other dataset, within a ±10 minute time window. This approach was applied to the comparisons to direct-sun data, the comparisons between UV and visible measurements, and the comparisons between the two Pandora instruments. For the comparisons with NAPS data, the hourly in situ NO_2 concentrations were linearly interpolated to the time of each retrieved value. To assess the systematic differences between various datasets, the mean absolute differences and the $RMSD$ values were used (Chapter 4). The statistical dependency of the datasets was evaluated using the R^2 value, and the linear relationship between the datasets was assessed using orthogonal distance regression (ODR) (Boggs

---

[1] `https://open.canada.ca/data/en/dataset/1b36a356-defd-4813-acea-47bc3abd859b`

Table 7.2: Mean relative uncertainties for the full MAPA NO_2 dataset, with data from Pandoras #103 and #104 combined for each wavelength range and scan type.

Retrieved value	Scan type	Mean uncertainty (%)	
		NO_2-UV	NO_2-vis
Partial column	Long	5.8	4.7
	Quick	5.2	3.9
Surface concentration	Long	43.4	55.2
	Quick	56.8	85.5

and Rogers, 1990). Since the ODR solution is symmetrical, it doesn't require the assignment of one dataset as the independent variable. While the ODR method can handle uncertainties on both datasets included in the fits, uncertainties were not included here, since not all datasets provide uncertainty estimates.

7.4 MAPA Retrieval Results

The full MAPA dataset is comprised of close to 10 000 valid profiles for NO_2-UV and more than 20 000 valid profiles for NO_2-vis, for both Pandoras #103 and #104. The valid profiles represent 17% and 24% of all profiles for NO_2-UV and NO_2-vis, respectively, while the remaining profiles were filtered out by the flagging scheme. The mean relative uncertainties for the retrieved partial columns and surface concentrations are shown in Table 7.2 for both wavelength ranges and scan types. Since the uncertainties for Pandoras #103 and #104 are very similar, the two datasets were combined for the table. Uncertainties for partial columns are smaller for NO_2-vis than for NO_2-UV, while the opposite is true for surface concentrations. The largest difference between long and quick scans appear for the NO_2-vis surface concentrations, and possible reasons for this are discussed further on. Uncertainties are much larger for surface concentrations than for partial columns, reflecting the variability of the parametric profiles in the near-surface layers. The following sections compare a subset of the MAPA results to retrievals using HeiPro, and assess the full MAPA dataset using supporting observations.

7.4.1 Comparisons to HeiPro

MAPA results for Pandora #103 were compared to HeiPro retrievals from the same dataset for June-July 2019. To assess the performance of long and quick scans, these results were compared separately for both NO_2-UV and NO_2-vis. The number of coinci-

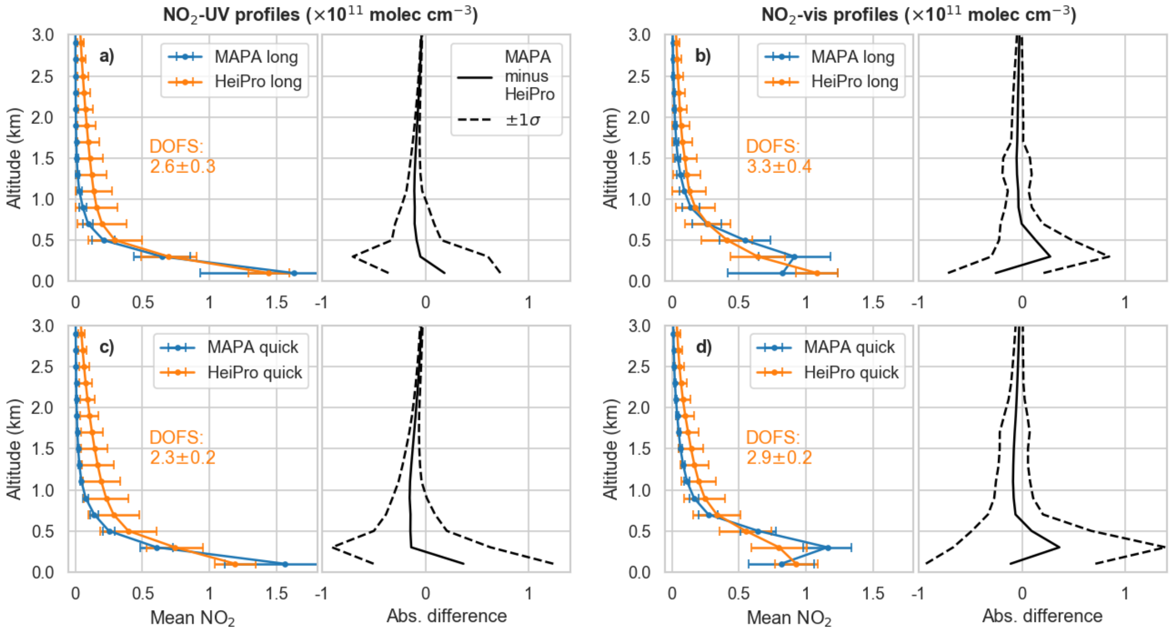

Figure 7.3: Mean NO_2 profiles and mean absolute differences, using MAPA and HeiPro profiles retrieved from **a)**, **c)** UV spectra and **b)**, **d)** visible spectra. The top row shows results from long scans, and the bottom row shows results from quick scans. For the mean profiles, the error bars show the mean of the uncertainties on the individual profiles. The dashed lines in the difference plots show one standard deviation of the absolute differences. The mean and standard deviation of the DOFS for the HeiPro results are indicated in each panel. Note that the profiles are plotted on the 0-3 km range, while the retrieval grid extends up to 4 km.

dent profiles was 182 and 903 for long and quick scans in the UV, and 253 and 1246 in the visible range, respectively. Based on the HeiPro results, DOFS for both the UV and visible wavelength ranges are similar to the findings of Tirpitz et al. (2021). The mean DOFS (shown in Fig. 7.3) are higher for the visible range (3.3 for long and 2.9 for quick scans) than in the UV (2.6 for long and 2.3 for quick scans). As expected, long scans (11 elevation angles) have higher DOFS than quick scans (four elevation angles), but the distributions overlap, and long and quick scans provide a similar amount of information about the NO_2 profile.

The mean retrieved NO_2-UV profiles are shown in Figure 7.3a and c for long and quick scans, respectively. On average, both MAPA and HeiPro retrieve exponentially decreasing NO_2 profiles. The error bars on the mean profiles show the mean of the retrieval uncertainties for each layer, to illustrate the confidence intervals each algorithm derives for various altitudes. The mean profiles agree within the mean uncertainties at all altitude levels. Mean uncertainties are generally larger for MAPA near the surface, while above 500 m, HeiPro uncertainties are larger. A clear difference between the mean profiles is the retrieved NO_2 at higher altitudes, as shown by the mean absolute difference plots in Figure 7.3. Above the 300 m layer, HeiPro generally retrieves more NO_2, with larger uncertainties. This is due to the larger contribution of the a priori profile to the HeiPro results at higher altitudes (Frieß et al., 2019). While averaging kernels show that sensitivity to the true state only becomes negligible above 2 km, each row of the averaging kernels peaks below 1 km. MAPA, on the other hand, does not rely on a priori information, and so concentrations at higher altitudes approach zero much quicker than for HeiPro. Above ∼2 km, the differences converge to a roughly constant small value. This is expected since MAX-DOAS measurements have minimal sensitivity at those altitudes, and while MAPA allows zero concentrations, HeiPro returns the small but non-zero a priori value. The behavior for higher altitudes described above is consistent between long and quick scans, even though quick scans have a slightly reduced vertical sensitivity given the limited number of large elevation angles. The results of Tirpitz et al. (2021) indicate that given the conditions during CINDI-2, the HeiPro results might be more realistic than MAPA at higher altitudes.

The lowest retrieval layers for NO_2-UV show good agreement between MAPA and HeiPro. There is more scatter for quick scans, as shown by the standard deviation of the absolute differences. Surface concentrations (0-200 layer) retrieved from the same elevation scans show good agreement between MAPA and HeiPro, with R^2 values of 0.95 and 0.90 for long and quick scans, respectively. As shown by the mean profiles in Figure 7.3a and c, MAPA surface concentrations are generally larger than those retrieved by HeiPro, especially for larger values.

Figure 7.3b and d show the mean NO_2 profiles for the visible wavelength range. Compared to the UV retrievals, the NO_2-vis results distribute NO_2 differently, with smaller concentrations in the bottom layers and more NO_2 aloft. This is likely related to the increased MAX-DOAS path lengths at visible wavelengths. Averaging kernels from HeiPro show that sensitivities become negligible only above ∼3 km, and individual rows peak as high as 1.1-1.4 km. The differences are especially apparent for the mean MAPA profile, which no longer shows an exponential shape, and has smaller mean uncertainties than in the UV. For long scans, MAPA results show approximately constant concentrations in the bottom two retrieval layers, while for quick scans, elevated layers are more often retrieved. HeiPro results for quick scans also show a deviation from the exponential profile, with more of a well-mixed layer below 400 m. Surface concentrations show more scatter between MAPA and HeiPro, with R^2 values of 0.84 and 0.72 for long and quick scans, respectively. Part of the reason is the prevalence of elevated layers in the MAPA profiles,

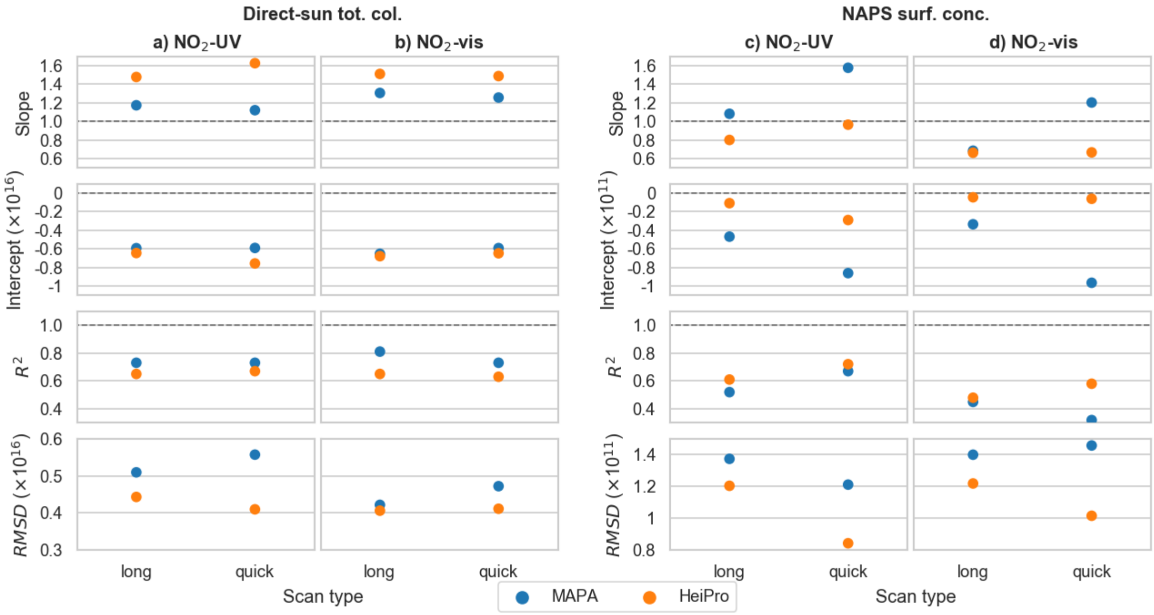

Figure 7.4: Correlation of **a)**, **c)** NO_2-UV and **b)**, **d)** NO_2-vis partial columns and surface concentrations from MAPA and HeiPro (Pandora #103 data, June-July 2019) to direct-sun total columns and in situ surface concentrations of NO_2. Results for long and quick scans are plotted separately.

which correspond to zero surface concentrations when the layers start above 200 m. The differences between the MAPA and HeiPro profiles at higher altitudes are similar to the UV results, but the offset is generally smaller, and only appears above the 700-900 m layers.

The NO_2 partial columns retrieved by MAPA and HeiPro show good agreement, with R^2 values of 0.89 for NO_2-UV (both long and quick scans), and 0.85 and 0.91 for NO_2-vis (long and quick scans, respectively). MAPA partial columns are generally smaller than those from HeiPro, mainly due to the larger NO_2 concentrations retrieved by HeiPro at higher altitudes. The profile differences are larger in the UV, and so the partial column differences are larger for the UV results as well. To test which of these results agree better with supporting datasets, the MAPA and HeiPro results were compared to direct-sun total columns and in situ NAPS NO_2.

The correlation between retrieval results and direct-sun NO_2 is shown in Figure 7.4a for NO_2-UV, and in Figure 7.4b for NO_2-vis. The results from the long and quick scans are overall similar, showing that both scan types retrieve the partial column similarly well. The results from the linear fits show that all retrieved partial columns show a slope greater than 1, with a negative intercept, when compared to the direct-sun data. This is expected given that the direct-sun data are total columns. MAX-DOAS measurements have greater sensitivity to the near-surface layers, and so when tropospheric NO$_2$ concentrations are large, the retrieval results might detect more NO$_2$. Conversely, when tropospheric NO$_2$ is minimal, the stratospheric column becomes significant, and stratospheric NO$_2$ is not detected by the MAX-DOAS measurements. The MAPA partial columns show a smaller slope for both the UV and the visible results, while the intercept values are similar for MAPA and HeiPro. The R^2 values are higher for MAPA across all wavelength ranges and scan types. The $RMSD$ values, on the other hand, are smaller for HeiPro than for MAPA, especially for the UV results.

The comparison results of NO$_2$-UV and NO$_2$-vis surface concentrations to NAPS data are shown in Figure 7.4c and d, respectively. Since the NAPS data are in situ measurements, and the retrieved surface concentrations represent 0-200 m layer averages, the R^2 values are quite low. MAPA and HeiPro perform similarly for most products (with slightly higher R^2 values for HeiPro), with the exception of quick scans in the visible range, for which HeiPro compares much better to NAPS data. This could be related to cloud cover, as cloudy conditions might affect NO$_2$-vis surface concentrations more for MAPA than for HeiPro (Tirpitz et al., 2021). As for the partial column results, $RMSD$ values are greater for MAPA than for HeiPro. Slopes are generally on either side of unity with a significant offset in between MAPA and HeiPro, except for long scans in the visible range, where the two values are almost identical. Intercepts are uniformly negative, with smaller values for MAPA for all scan types and wavelength ranges.

Overall, the profiles retrieved using MAPA and HeiPro show some systematic differences, especially at altitudes where the measurement sensitivity is limited. These differences are consistent with MAPA and HeiPro profile differences shown in the supplement of Tirpitz et al. (2021). The retrieved partial columns correlate better with direct-sun data for MAPA, while HeiPro surface concentrations show a closer relationship to NAPS measurements. While these results are not directly comparable to Tirpitz et al. (2021), who used tropospheric columns and LP-DOAS surface concentrations for the comparisons, the $RMSD$ and R^2 values presented here are similar to those in that study. Compared to long scans, results for quick scans show larger differences between the two retrieval algorithms, as might be expected given that only four elevation angles are available to constrain the retrievals. Interestingly, the highest R^2 values for the NAPS comparisons are observed for the UV quick scans for both MAPA and HeiPro. This might be related to the higher number of coincidences for quick scans, combined with shorter MAX-DOAS path lengths in the UV. $RMSD$ values are generally larger for MAPA than for HeiPro, likely reflecting the fundamental differences between the parametric and OEM approaches. These differences also manifest in the retrieval uncertainties, which are larger (smaller) for MAPA

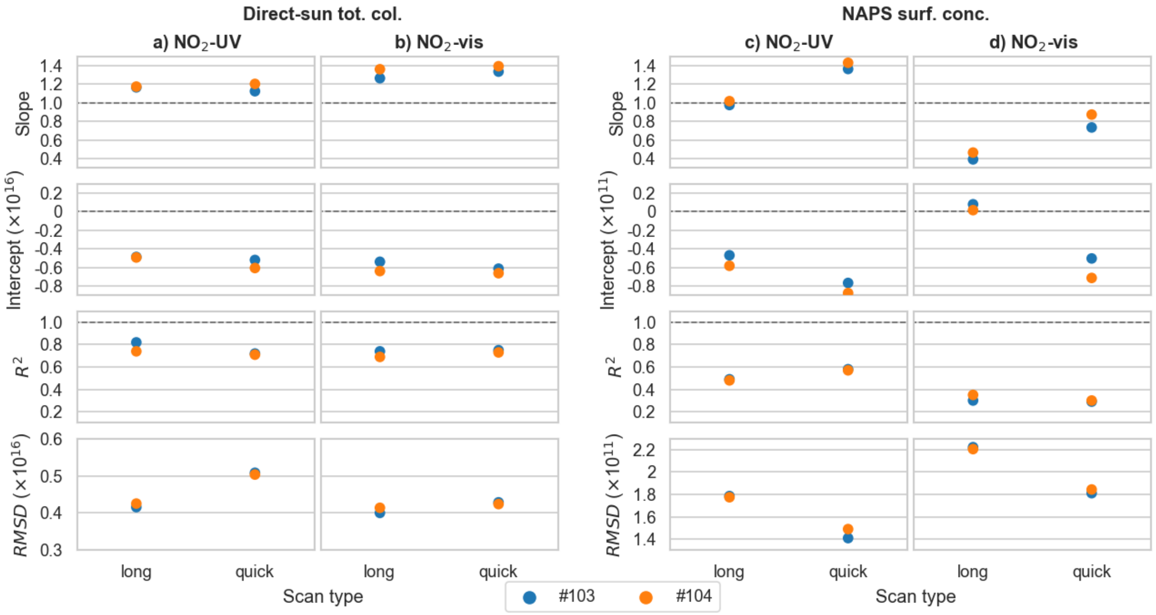

Figure 7.5: Same as Figure 7.4, with MAPA results from Pandoras #103 and #104 (2018-2019 data).

in the near-surface layers (at higher altitudes).

While the comparison results indicate that both algorithms have their strengths and disadvantages, MAPA has a clear advantage in terms of processing times. On a per-profile basis, MAPA is faster than HeiPro by a factor of 9 for NO_2 and by a factor of ∼17 for aerosols (Frieß et al., 2019), since no live RTM calculations are required for MAPA retrievals. This presents a serious advantage for the large Pandora datasets. The retrieval of the combined NO_2-UV and NO_2-vis dataset for Pandoras #103 and #104 takes ∼17 days on a single processor using MAPA, while the same retrievals would require nearly 8 months using HeiPro.

7.4.2 Comparisons to Direct-Sun and In Situ Measurements

The full MAPA NO_2 datasets for both Pandoras were compared to direct-sun and in situ measurements, as in the previous section. The results, for 2018-2019, are shown in Figure 7.5. The two Pandoras show very good agreement across all comparison metrics, as might be expected for colocated instruments. The slightly different azimuth viewing directions (difference of 5°) likely contribute to small differences, especially in the visible range, and for surface concentrations.

The correlation of MAPA partial columns to direct-sun total columns are shown in Figure 7.5a and b for NO_2-UV and NO_2-vis, respectively. Long and quick scans show

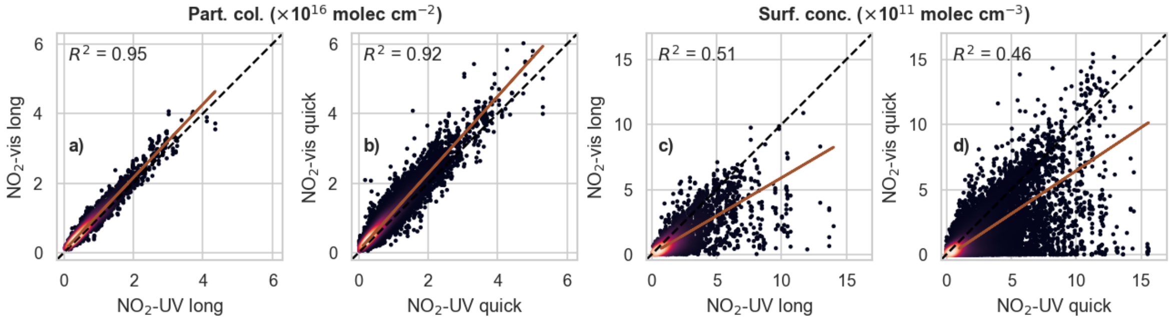

Figure 7.6: Correlation of **a)**, **b)** NO$_2$ partial columns and **c)**, **d)** NO$_2$ surface concentrations retrieved from UV and visible measurements. Data from Pandoras #103 and #104 have been merged for each scan type and wavelength range.

very similar agreement. The only major difference is the $RMSD$ for NO$_2$-UV, which is larger for quick scans. Slopes are larger, and intercepts are slightly smaller, for NO$_2$-vis compared to NO$_2$-UV, but R^2 values are similarly high (between 0.7 and 0.8) for all scan types and wavelength ranges. The correlation of the UV and visible partial columns is shown in Figure 7.6a and b. Given the very good agreement between Pandoras #103 and #104, the two datasets were combined into a single Pandora dataset for each scan type and wavelength range. The UV and visible partial columns agree very well, with similar R^2 values for long and quick scans (0.95 and 0.92, respectively). The slight overestimation of the partial columns in the visible range is consistent with the comparison results of Tirpitz et al. (2021) (see Fig. 3.13). Comparisons between long and quick scans show uniformly good correlation ($R^2 = 0.91$) for both UV and visible results.

The correlation to NAPS surface concentrations show different agreement for long and quick scans (Fig. 7.5c and d, respectively). For NO$_2$-UV, the linear relationship between retrieved values and NAPS data is better for long scans, while quick scans show higher R^2 and smaller $RMSD$ values. For NO$_2$-vis, the linear relationships are inconclusive, and R^2 values are uniformly low for both long and quick scans. MAPA generally underestimates in situ surface concentrations, in part as a consequence of the profile parametrization scheme, where elevated NO$_2$ layers correspond to zero surface concentrations. Given the R^2 and $RMSD$ values, the UV surface concentrations show a closer relationship to NAPS data. The correlation between the UV and visible surface concentrations is shown in Figure 7.6c and d. R^2 values are quite low for both long and quick scans (0.51 and 0.46, respectively), and the UV retrievals often return larger surface concentrations. This is in part a consequence of the different shapes of the UV and visible profiles, as discussed in Section 7.4.1. The same behavior is apparent for both long and quick scans. The general underestimation of the surface concentrations in the visible range was also observed by

Tirpitz et al. (2021), although the range of surface concentrations was smaller in that study (see Fig. 3.13). When comparing long and quick scans to each other, the UV results show more consistent results ($R^2 = 0.83$) than the retrievals in the visible range ($R^2 = 0.61$). This is in agreement with the larger differences in the uncertainties for long and quick scans in the visible range (Table 7.2).

Overall, NO_2 partial columns show good agreement with each other and with direct-sun total columns. This indicates that the partial column is successfully retrieved by MAPA regardless of the scan types or wavelength ranges used. For surface concentrations, the results are less clear, although the retrieved values (0-200 m layer, up to tens of km of horizontal sensitivity) are not necessarily directly comparable to the NAPS in situ measurements. NO_2-UV surface concentrations show a better correlation to NAPS data, since the horizontal viewing distance is significantly shorter in the UV than in the visible wavelength range (Tirpitz et al., 2021). Long and quick scans show variable agreement with NAPS data. Overall, both scan types seem to provide similar quality data for NO_2-UV, while long scans might be more reliable for NO_2-vis.

7.5 NO_2 Variability and the Impact of COVID-19

Given the results discussed above, only the NO_2-UV dataset was used to examine NO_2 variability in the entire time series. For this section, UV results from Pandoras #103 and #104 (both long and quick scans) have been merged into a single dataset. Since the dataset starts in 2018 and stretches into 2020, the impact of Toronto's lockdown in response to the COVID-19 pandemic must be considered when interpreting the time series. The lockdown started on 17 March 2020, when Ontario entered a state of emergency. The stay-at-home orders and closure of businesses resulted in a significant reduction of road traffic, which then led to reductions of NO_2 pollution in Toronto (e.g., Griffin et al., 2020; Adams, 2020), similar to cities worldwide (e.g., Bauwens et al., 2020; Bera et al., 2020; Berman and Ebisu, 2020; Feng et al., 2020; Pacheco et al., 2020; Parker et al., 2020). To show 'normal' conditions when examining NO_2 seasonality, only data up to (and including) February 2020 are used. For diurnal variability, April-May data from 2018-2019 are shown, which provide a useful base of comparison for the lockdown conditions in April-May 2020.

The month-to-month variability of the NO_2-UV partial columns is shown in Figure 7.7a. There is a clear seasonal cycle, with the largest mean and median values in winter, and the smallest values in the summer. This is expected given the much longer lifetime of NO_2 in the winter ($\sim$1 day) compared to the summer (few hours) (Kenagy et al.,

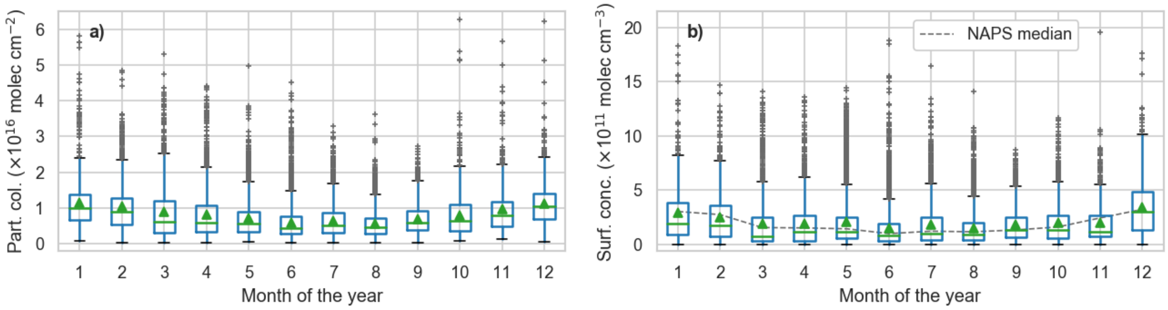

Figure 7.7: Monthly box plots of **a)** NO_2-UV partial columns and **b)** NO_2-UV surface concentrations retrieved using MAPA. The plots combine long and quick scan data from both Pandoras #103 and #104, for February 2018 - February 2020, and panel **b)** also shows monthly median values of NAPS data for the same time period. The height of the boxes indicates the 25th and 75th percentiles of the data, with the median marked by the horizontal lines, and the mean shown by the green triangles. The whiskers extend to 1.5× the interquantile range, and outliers are shown by the gray crosses. When there are no outliers, the whiskers extend to the largest/smallest data point.

2018). The extreme values show less of a clear cycle, but the largest partial columns (as indicated by the top whiskers in Fig. 7.7a) are generally observed in the colder months. The NO_2-UV surface concentrations (Fig. 7.7b) show a seasonal cycle somewhat similar to the partial column values, but with more variability. The winter months (December, January, February; DJF) show the highest mean, median, and peak surface concentrations, consistent with the longer lifetime of NO_2 in the winter. The other months show statistics similar to each other, and the smallest mean and median values occur in the summer. This is in agreement with the seasonal cycle in the NAPS data (monthly median values shown in Fig. 7.7b), which also shows the largest values in DJF, and similar monthly statistics for the rest of the year. The surface concentrations are affected by the increasing height of the boundary layer during the day, which shows seasonal variability, as discussed below.

The diurnal variability of NO_2-UV partial columns during weekdays for April-May 2018-2019 is shown in Figure 7.8a. There is a clear diurnal cycle, where partial columns peak in the morning, decrease in the afternoon, and show a weak peak in the evening. The daily cycle is controlled by weekday commuter traffic on nearby roads and highways (morning and evening rush hour), as well as by variability in photochemistry and meteorology (e.g., Harkey et al., 2015; Amin et al., 2017; Seo et al., 2018; Wang et al., 2018). The April-May data shown in Figure 7.8a are typical for spring and summer measurements in the Pandora dataset. The fall and winter partial columns show reduced variability, with morning and evening peaks that are similar in magnitude. Partial columns are larger

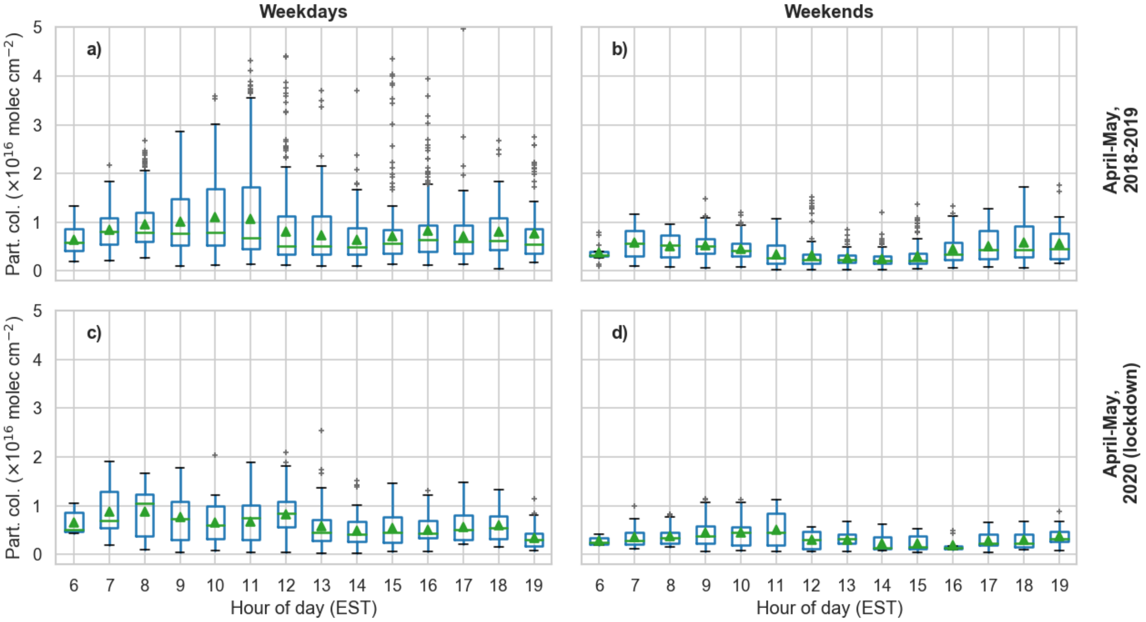

Figure 7.8: Diurnal variability of NO_2-UV partial columns, during **a)**, **c)** weekdays and **b)**, **d)** weekends. The top row shows data for April-May 2018-2019, while the bottom row shows the same time period for 2020. The plots combine long and quick scan data from both Pandoras #103 and #104. Box plots as in Figure 7.7.

throughout the weekdays, consistent with the larger monthly mean values for those seasons (Fig. 7.7a). The weekend NO_2-UV partial columns for April-May 2018-2019, shown in Figure 7.8b, are much smaller than weekday values. The morning and evening peaks are still present, but mean and extreme NO_2 values are greatly reduced compared to weekdays. This is in part due to reduced heavy-duty diesel truck traffic on the weekends, as these vehicles are a significant source of NO_x (e.g., Dreher and Harley, 1998; Wang et al., 2018). The drop in NO_2 partial columns from weekday to weekend is consistent across all seasons, although the values remain higher on weekends as well in the winter.

The daily cycle of NO_2-UV surface concentrations is shown in Figure 7.9a for weekdays. As for partial columns, surface concentrations peak in the morning, then decrease significantly, and then increase again to a smaller evening peak. The morning peak occurs a few hours earlier compared to partial columns, consistent with the gradual mixing and lifting of surface-sourced NO_2 to higher altitudes. The surface concentrations are strongly affected by the changing height of the boundary layer throughout the day, in addition to the other factors discussed above. As the boundary layer deepens in the afternoon, the NO_2 is diluted and the surface concentrations decrease. The expanding boundary layer is captured by the layer height parameter retrieved by MAPA. The daily change

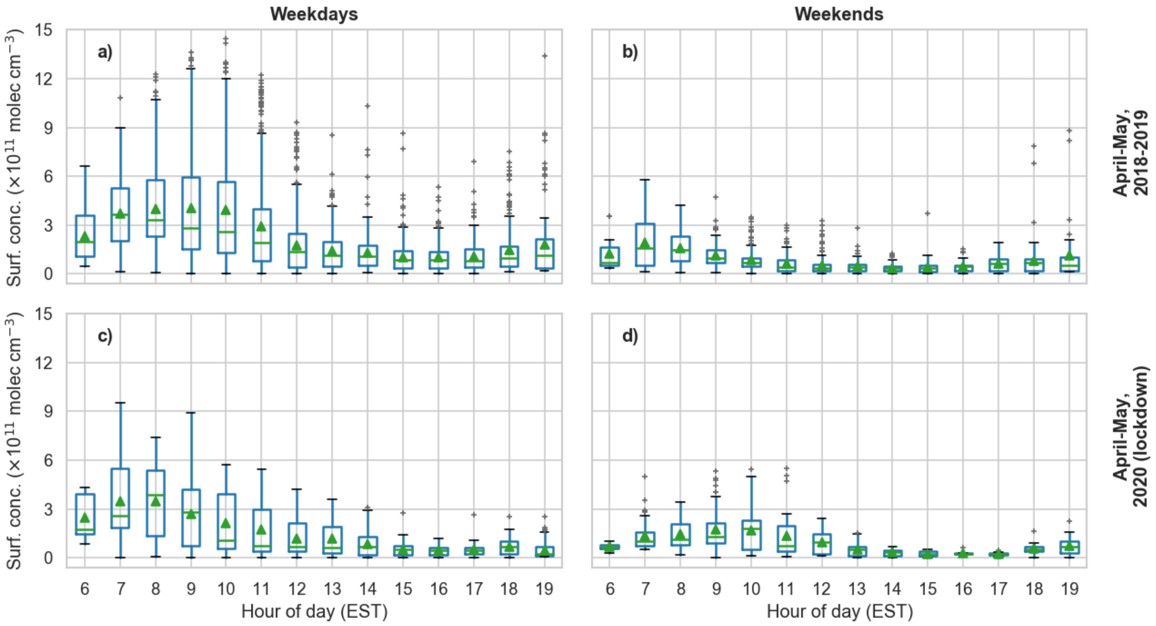

Figure 7.9: Same as Figure 7.8, with NO_2-UV surface concentrations.

in layer height is largest in the spring and summer, and the surface NO_2 variability for those months is similar to the patterns shown in Figure 7.9a. In the winter, shorter days and colder weather correspond to smaller retrieved layer heights. Accordingly, the NO_2 surface concentrations in the winter remain high throughout the day, while the morning and evening peaks show similar concentrations as in the summer months. As for partial columns, the surface concentrations (Fig. 7.9b) are significantly reduced on the weekends, but the morning and evening peaks are still apparent.

To highlight the impact of the COVID-19 lockdown on NO_2 concentrations, April-May partial columns and surface concentrations from 2020 are plotted alongside the 2018-2019 values in Figures 7.8 and 7.9. Data from March 2020 were excluded to avoid any transition period between the full lockdown and pre-lockdown conditions.

During lockdown, the mean partial columns were slightly reduced on weekdays, and the morning NO_2 peak was much less clear (Fig. 7.8c), as might be expected from reduced commuter traffic. The median partial columns, on the other hand, were similar to 2018-2019 values. Weekday partial columns were still clearly larger than normal weekend values, and the weekday to weekend reduction is also present, with weekend partial columns that were similar to 2018-2019 values. This is possibly due to heavy-duty vehicle traffic on weekdays generated by essential services that were exempt from the lockdown. The most striking impact of the lockdown appears to be the drastic reduction of extreme weekday pollution episodes. Only three individual profiles result in partial columns above

2×10^{16} molec cm^{-2} for April and May 2020, while values between 2-4$\times10^{16}$ molec cm^{-2} were common in the preceding years, especially in the mornings.

Surface NO_2 concentrations in April-May 2020 show slight reductions in the mean and median values on weekdays, when compared to 2018-2019 values (Fig. 7.9c). The morning peak is still present, but it is shifted 2-3 hours earlier, perhaps as another sign of the larger fraction of commercial traffic during lockdown. In the afternoons, surface NO_2 is reduced to near-zero concentrations, similar to normal weekend afternoons. Weekend surface concentrations in 2020 appear similar to 2018-2019 values, but the morning peak is shifted later. A similar shift might be present for the weekend partial column values as well, although the those data are more variable. As is the case for the partial columns, the most obvious impact of the lockdown is the reduction in extreme surface concentrations on weekdays. Only a single datapoint exceeds 9×10^{11} molec cm^{-3}, while values up to 15×10^{11} molec cm^{-3} often occur in the 2018-2019 data.

Using TROPOMI measurements and air quality model simulations, Griffin et al. (2020) showed that NO_2 columns over Toronto were reduced by nearly 60% during the lockdown. Adams (2020) found similar reductions in surface concentrations using in situ measurements. Both studies, however, emphasized that meteorological variability played a significant role in these reductions. Griffin et al. (2020) estimated that a third of the NO_2 reductions might be due to seasonal changes and TROPOMI sampling variability, while Adams (2020) noted that surface concentrations were already unusually low before the lockdown period. Goldberg et al. (2020) used TROPOMI observations and ERA5 data to show that meteorological conditions were especially favorable for low NO_2 in much of North America (including Toronto) in spring 2020.

NO_2 reductions unrelated to the lockdown are present in the Pandora dataset as well. January-February 2020 mean partial columns and surface concentrations from the NO_2-UV dataset are 0.16×10^{16} molec cm^{-2} and 0.51×10^{11} molec cm^{-3} smaller, respectively, than corresponding two-month averages using 2018-2019 data. When considering February data only, the differences increase to 0.29×10^{16} molec cm^{-2} and 1.17×10^{11} molec cm^{-3}. Assuming that these differences carry over to April and May, the year-to-year variability would explain any changes in the mean and median values discussed above. On the other hand, changes in the timing of the daily NO_2 peaks, and the reductions of extreme values, are still apparent in the dataset. This is in general agreement with Griffin et al. (2020) and Goldberg et al. (2020), who argued that even after accounting for interannual variability, NO_2 columns over Toronto were reduced by as much as 30-40%. While such large reductions are not apparent in the Pandora dataset, differences in spatial coverage likely play a role. The Pandora measurements are sensitive to emissions from major highways, while the TROPOMI results represent city-wide averages. To accurately isolate the impact of the COVID-19 lockdowns on NO_2 concentrations, and on air quality in general, more detailed follow-up studies will be required.

7.6 Summary

This chapter describes a two-year dataset of NO_2 profiles retrieved using a parametric profile retrieval algorithm (MAPA) from two Pandora instruments in Toronto. NO_2-UV and NO_2-vis results from MAPA were compared to retrievals using the HeiPro OEM algorithm for June-July 2019. The profiles from HeiPro are systematically larger at higher altitudes (>300-700 m), since HeiPro results tend to the a priori as MAX-DOAS vertical sensitivity decreases, whereas MAPA does not rely on a priori profiles. These result are consistent for all wavelengths and scan types. As a consequence, while NO_2-UV and NO_2-vis partial columns from the two algorithms show good correlation ($R^2 > 0.85$), HeiPro partial columns are generally larger. When compared to Pandora direct-sun total columns, MAPA partial columns show a better correlation for both wavelength ranges. Retrieved 0-200 m surface concentrations from MAPA and HeiPro show better agreement for NO_2-UV ($R^2 > 0.90$) than for NO_2-vis ($R^2 > 0.72$). The retrieved NO_2 distribution is somewhat variable, with a more even distribution of NO_2 in the lowest 400-600 m in the visible range, compared to the UV profiles. Comparisons to NAPS in situ NO_2 surface concentrations indicate that the UV retrievals perform better for both algorithms, likely due to the shorter path lengths in the UV. HeiPro results generally agree better with NAPS data.

For the full MAPA dataset, results from Pandoras #103 and #104 show very good agreement, and data from the two instruments were merged into a single dataset. Retrieved partial columns show similarly good correlation to direct-sun total columns for all wavelength ranges and scan types, and UV and visible partial columns show good correlation with each other ($R^2 > 0.92$). Comparisons to NAPS data corroborate the better performance of the UV retrievals for surface concentrations. UV and visible surface concentrations show relatively weak correlation to each other ($R^2 > 0.46$), likely due to the tendency of the visible MAPA retrievals to return elevated NO_2 layers with zero surface concentrations. Overall, long and quick elevation scans provide similar quality data. Partial columns from both scan types agree well with each other, and with direct-sun data, for both NO_2-UV and NO_2-vis. Surface concentrations show better agreement between the scan types for NO_2-UV, while comparisons to NAPS in situ data show similar agreement for long and quick scans for each wavelength range. The HeiPro dataset shows that

DOFS for profiles retrieved from quick scans are only slightly lower than those for long scans.

The variability of NO_2 in Toronto was examined using the full NO_2-UV dataset, including both instruments and both long and quick scans. Partial columns and surface concentrations show a seasonal cycle with peak monthly mean values in the winter, following the seasonal changes in the lifetime of NO_2. Morning and evening peaks are observed in the diurnal distribution of both partial columns and surface concentrations, and weekend values are significantly smaller than those on weekdays. Variability in surface concentrations is greater due to the dilution of near-surface NO_2 by the expanding boundary layer throughout the day. During the COVID-19 lockdown in Toronto, NO_2 concentrations were lower than during the equivalent period in 2018-2019. While meteorological variability likely contributed to reduced NO_2, the reduction in peak NO_2 partial columns and surface concentrations appears to be a direct consequence of reduced road traffic during the lockdown.

Chapter 8

Conclusions

8.1 Summary and Contributions of the Thesis

Ozone and related trace gases play important roles in both the stratosphere and the troposphere, with far-reaching impacts on climate, the environment, and human health. Evaluating the processes that affect ozone concentrations in the Arctic is important to understand how these processes will evolve in response to climate change. To study ozone and related species, this thesis uses long-term datasets of ozone, NO_2, BrO, and OClO, retrieved from ground-based UV-vis spectrometers. In Eureka, the combined UT-GBS and PEARL-GBS dataset now includes 20 years of measurements (1999-2020, excluding 2001 and 2002). The full time series of zenith-sky ozone and NO_2 VCDs were reprocessed with consistent retrieval settings, and the results were submitted to the NDACC archive in HDF format. A rapid delivery retrieval was also implemented, and data are regularly submitted to CAMS in HDF format. The GBS MAX-DOAS dataset was extended to eleven years (2010-2020), and profiles of aerosol extinction and BrO were retrieved from PEARL-GBS MAX-DOAS dSCDs for four spring seasons (2016-2019). In Toronto, a NO_2 profile dataset was retrieved from 2018-2020 Pandora MAX-DOAS measurements in order to study urban NO_2 pollution.

The PEARL-GBS was successfully deployed as a 2D MAX-DOAS instrument for the CINDI-2 campaign in September 2016. The pointing stability of the instrument was excellent throughout the campaign (Donner et al., 2020). The retrieved dSCDs of O_4, NO_2, and ozone were found to agree well with other instruments, and the PEARL-GBS met most of the campaign performance criteria (Kreher et al., 2020). Profiles of aerosol extinction and NO_2, retrieved both from the measurements and a median dSCD dataset, were consistent with other instruments and with supporting datasets (Tirpitz et al., 2021).

The following sections summarize the findings of Chapters 4, 5, 6, and 7, organized around the science questions raised in Chapter 1.

8.1.1 Contributions to the Validation of Satellite Datasets

The Eureka GBS ozone and NO_2 datasets were combined with SAOZ, Bruker FTIR, PARIS-IR, and Brewer data in order to validate measurements from the OSIRIS, ACE-FTS and ACE-MAESTRO satellite instruments. This project, described in Chapter 4 and in Bognar et al. (2019), addressed the following science questions:

- How consistent are the ozone and NO_2 columns retrieved from the aging OSIRIS, ACE-FTS, and ACE-MAESTRO satellite instruments when compared to each other, and to ground-based measurements? How do the results compare to previous validation efforts, and what are the reasons for any changes in the results?

Ozone partial columns (14-52 km) from the three satellite instruments show reasonable agreement. OSIRIS and ACE-FTS agree to within 1.2%, while ACE-MAESTRO ozone shows a 6.7% and 5.9% low bias when compared to OSIRIS and ACE-FTS, respectively. Profile comparisons show that relative to the OSIRIS and ACE-FTS, ACE-MAESTRO underestimates the peak ozone concentrations within 500 km of PEARL. This bias was not apparent in previous ACE-MAESTRO data versions, and is likely related to changes in the v3.13 processing. Satellite ozone profiles were extended to the surface using ozonesonde data, and the resulting columns were compared to five ground-based datasets. OSIRIS ozone columns agree with ground-based total columns with a maximum mean relative difference of 4.4%. The agreement is better than 7.5% for ACE-FTS ozone, while ACE-MAESTRO columns show a maximum relative difference of 12%, reflecting the low bias indicated by the satellite comparisons. The largest differences were observed for the ACE minus Bruker FTIR and PARIS-IR comparisons (the agreement is better than 4.4% for all other instrument pairs). Satellite NO_2 partial columns were compared to four ground-based datasets. OSIRIS partial columns agree with ground-based partial columns to within 19.9%, and the differences show significant seasonal variation, with the largest negative values in the summer. ACE-FTS partial columns show a maximum mean relative difference of 33.2%, that improves to better than 15.3% when excluding the Bruker FTIR comparison.

The results presented here are generally consistent with previous validation efforts that used the same instruments. Changes in the differences between various instrument pairs were found to be related to 1) updated data versions, 2) changing seasonal distribution of the coincidences, combined with seasonal effects in the difference time series, and 3) longer time series that provide better comparison statistics.

- Is there any drift over time in the differences between the various satellite and ground-based instruments?

Drifts in the daily mean relative difference time series for each instrument pair were evaluated using robust linear regression. None of the satellite-plus-sonde ozone columns or satellite NO_2 partial columns show a significant drift when compared to the ground-based datasets. While some of the calculated drifts were significant based on the linear regression only, most of these values were found to be related to the changing seasonal distribution of the coincidences, as discussed above. In addition, none of the time series are long enough for confident detection of drifts of the magnitude given by the linear regression. These results confirm that the observed low bias of ACE-MAESTRO ozone is related to data processing, and not to instrument effects. Overall, the lack of significant drift in any of the comparison time series indicates that OSIRIS, ACE-FTS and ACE-MAESTRO continue to provide reliable measurements of ozone and NO_2 in the Arctic.

- Does the location of the polar vortex have a significant impact on springtime comparisons? Can these impacts be quantified using dynamical parameters derived from reanalysis data?
- Can the validation results be improved by implementing a cloud screening algorithm for the ground-based DOAS instruments?

Springtime ozone comparisons are affected by ozone depletion inside the polar vortex. This additional variability is most significant for the ACE minus Bruker FTIR and PARIS-IR comparisons, since most of those coincidences (all for PARIS-IR) occur during the spring. Using stricter dynamical coincidence criteria in the spring, ACE minus Bruker FTIR and PARIS-IR comparisons improved by 2.3-4.7%, in line with previous validation studies. Results for the other instrument pairs showed modest to no improvements, likely due to the lack of precise line-of-sight information for the scattered-light measurements. This indicates that the polar vortex introduces significant uncertainty in the springtime ozone comparisons, and accounting for these effects requires precise knowledge of the measurement light path. Comparisons of satellite-plus-sonde ozone with a cloud-filtered ZSL-DOAS dataset indicate that the underlying agreements in the ozone comparisons are likely different due to a positive bias in the ZSL-DOAS measurements in cloudy conditions. Since direct-sun measurements have a natural clear-sky bias, comparison results across multiple datasets have to be interpreted with care. Dynamical coincidence criteria did not improve the NO_2 comparison results, likely due to the large uncertainties in the NO_2 measurements. Implementing a ±1° latitude coincidence criterion modestly improved spring and fall comparison results for most instrument pairs, suggesting that while the latitudinal gradient of NO_2 has a significant impact on validation exercises, a 500 km radius for coincidences is adequate for comparisons of NO_2 measurements.

8.1.2 Contributions to the Study of Stratospheric Ozone Depletion

The Eureka GBS, SAOZ, Bruker FTIR, and Brewer datasets, with the addition of Pandora ozone measurements, lidar data, and SLIMCAT simulations, were used to assess the unprecedented stratospheric ozone depletion in the spring of 2020. This work, described in Chapter 5 and in Bognar et al. (2020a, submitted), addressed the following science questions:

- How did trace gas concentrations evolve inside the polar vortex during the unusual spring in 2020? What were the key differences between ozone depletion in 2020 and 2011?

The unusually cold, strong, and persistent polar vortex over the winter and spring of 2019/2020 created the greatest potential for ozone depletion ever observed in the Arctic. Accordingly, every instrument used in this study measured record low ozone column values in spring 2020. The GBS, SAOZ, Bruker FTIR, Pandora, and Brewer instruments all observed record low ozone columns (187, 221, 240, 222, and 218 DU) in their respective time series, well below previous records set in 2011. Persistent enhancements of BrO and OClO dSCDs in the GBS dataset indicate that chlorine activation was ongoing until late March (perhaps slightly later than in 2011), and consistently low HCl and $ClONO_2$ columns from the Bruker FTIR point to heterogeneous chemistry on PSC particles. HNO_3 columns, on the other hand, were not as low as in 2011, and lower stratospheric temperatures were slightly above T_{NAT} for most of the spring. This is consistent with a less denitrified stratosphere above Eureka indicated by the NO_2 measurements. The smallest ozone column values were observed on 16-19 March, coincident with a significant drop in temperatures and HNO_3 columns. CRL measurements indicated the presence of PSCs (at 14-16 km altitude) during the same period. Ozonesondes measured ozone mixing ratios below 0.5 ppmv (with minima below 0.2 ppmv) in the 16-20 km altitude range in late March and throughout April. These values are unprecedented in the Arctic, and are more similar to values commonly observed in the Antarctic ozone hole. Even after chemical depletion stopped in late March, the vortex remained cold and stable, and so ozone columns in 2020 remained well below seasonal averages until the end of April, much longer than in 2011.

- What was the contribution of dynamical factors to the exceptionally low ozone columns measured in spring 2020? How did stratospheric dynamics contribute to the recovery of ozone inside the polar vortex?

Passive ozone from SLIMCAT indicates that ozone column values in 2020 would likely have been unusually low even without chemical processing. Ozone columns are usually smaller in cold winters due to dynamical factors, and Eureka ozone measurements inside the vortex generally show good correlation with lower stratospheric temperature. This relationship, however, was substantially different in 2020 (and in 2011) compared to what is observed for more typical years. This indicates that chemical ozone depletion played an exceptionally large role, and contributed to significant additional ozone loss, in 2020 when compared to compared to typical Arctic winters. After chlorine activation stopped in late March 2020, ozone inside the vortex recovered with increasing temperatures as expected, but with an offset of 84-93 DU compared to typical winters. This offset, which was smaller in 2011, can be interpreted as the approximate amount of additional chemical ozone destruction in 2020 compared to more typical Arctic winters. Bruker FTIR measurements normalized by HF total columns confirm the major role of chemistry in shaping the 2020 trace gas time series.

- What is the agreement of modeled ozone and related trace gases with measurements at Eureka? Is this agreement consistent inside and outside the polar vortex?

Comparisons indicate that trace gas columns from SLIMCAT generally agree well with springtime ground-based measurements for the entire time series (2000-2020). Considering active ozone inside the vortex, SLIMCAT slightly underestimates measurements, with mean relative differences of 1.4% to -8.9%. The largest differences are observed in the early spring, when the spatial mismatch between the measurements and the modeled vertical columns is the greatest. Outside the vortex, SLIMCAT generally overestimates ozone, with a consistent offset of 10-11% (40-45 DU) between inside and outside comparisons across all instruments. This difference is likely related to model dynamics. Columns of HCl from SLIMCAT agree well with Bruker FTIR measurements inside and outside the vortex, while $ClONO_2$ columns show good agreement inside the vortex only. HNO_3 is underestimated by SLIMCAT both inside and outside the vortex, due to the relatively simple equilibrium denitrification scheme included in the model. Passive ozone agrees with December ozonesonde columns to within 2%, indicating that SLIMCAT successfully simulates observed ozone before chemical depletion starts.

- What are the estimates of chemical ozone loss when comparing measurements to modeled passive ozone? Can these estimates be generalized to assess overall ozone loss inside the vortex over Eureka?

Chemical loss inside the vortex was estimated using measurements and SLIMCAT passive ozone. All instruments observed smaller daily peak absolute loss in 2020 (81-157 DU) than in 2011 (108-176 DU). The absolute loss time series generally overlap, but the daily peaks were higher in 2011. Daily peak relative loss, on the other hand, was greater in 2020 (25-38%) than in 2011 (24-36%) for all instruments. SLIMCAT active ozone shows consistent results, with more absolute loss in 2011, and relative loss that was similar, but continued longer, in 2020. While overall ozone loss is difficult to estimate from a single ground station due to the variable position of the vortex, spring 2020 measurements have good coverage inside the vortex after chemical depletion stopped. Using Brewer and GBS measurements throughout April, the mean chemical ozone loss inside the vortex was estimated to be 111-126 DU (27-31%) over Eureka.

8.1.3 Contributions to the Study of Tropospheric Bromine Activation

The four-year time series of springtime BrO partial columns retrieved from PEARL-GBS MAX-DOAS measurements represents a rare long-term BrO dataset in the Arctic. Combined with in situ observations of aerosols and ozone, the dataset was used to study bromine activation and ODEs in Eureka, as presented in Chapter 6 and in Bognar et al. (2020b). The study addressed the following science questions:

- How do wind speed and atmospheric stability influence bromine activation? What is the role of vertical mixing and topography in determining BrO values observed from an elevated measurement site?

Due to the elevation of the PEARL Ridge Lab (610 m), the retrieved BrO partial columns are likely not sensitive to the surface (sea level), and the PEARL-GBS measures above the boundary layer most of the time. As a result, the strength of the temperature inversion has a limited impact on the BrO partial columns, since the retrievals do not capture the shallow bromine events that typically show a strong dependence on atmospheric stability. BrO is commonly observed above the boundary layer, indicating that bromine is often transported to the measurement site. It is possible, however, that BrO aloft is never fully decoupled from the surface, due to the uncertain effects of topography on the boundary layer. When the boundary layer is deep, the effects of the enhanced vertical mixing manifest as an increase in the minimum BrO values for wind speeds of 7-8 m s^{-1} or greater. Minimum surface ozone concentrations increase even in moderate wind speeds, and ODEs become less and less frequent as wind speeds increase past 7-8 m s^{-1}. While these high-wind events most often correspond to enhanced BrO, mixing of ozone-rich air from higher altitudes is sufficient to counteract ozone destruction.

- What is the relative importance of the snowpack and aerosols in bromine release? Can the effects of transport and local sources be separated using measurements at Eureka?

Local wind directions show two distinct modes (N and SE), and the observed BrO events show different characteristics for each of these wind directions. Air mass histories for enhanced BrO events (inferred from FLEXPART back trajectory simulations) show two modes as well: N winds transport air masses from over the Arctic Ocean, while SE winds generally correspond to storms that originate in the western Arctic or over the Canadian Arctic Archipelago. Increased sensitivity to FYI corresponds to increases in the BrO partial columns for N winds only, even though air masses have similar sensitivity to FYI areas regardless of wind direction. This indicates that air reaching Eureka directly from the Arctic Ocean likely transports bromine released from snow on FYI. Evidence for local release of bromine from the snowpack is provided by in situ ozone measurements. Strong ODEs (<10 ppbv) are observed most often for surface wind speeds below 2 m s^{-1}, and complete ODEs (<2 ppbv) occur preferentially in calm conditions with strong temperature inversions.

Since bromine needs to be recycled on aerosol particles in order to maintain lofted BrO plumes, high aerosol load (as indicated by the retrieved AOD values) was necessary to maintain enhanced BrO concentrations for all wind directions. AOD shows the closest link to BrO for SE winds that often correspond to storms. These storms almost always bring BrO enhancements to Eureka, and the strong winds during storms create favorable conditions for both transport and local production of aerosols, as discussed below.

- Is the snowpack on first-year sea ice the only source of snowpack-related bromine? Does the snowpack on the multi-year ice areas near Eureka contribute to the observed BrO values?

When sensitivity to all sea ice (FYI+MYI) is considered instead of just FYI sensitivity, the relationship to BrO improves for all wind directions. This indicates the possible release of bromine from snow on MYI. The BrO dataset contains at least one enhanced BrO event that maintains a high MYI to all sea ice sensitivity ratio (>0.9) even for 5-day back trajectories, with no clear alternative bromine source. Snow on MYI is often neglected as a source of bromine because of its lower salinity compared to FYI. It is possible, however, that atmospheric processes (e.g., exposure to Arctic haze) could create favorable conditions for bromine release from snow on MYI.

- What are the likely sources of springtime aerosol in Eureka? Can the importance of aerosol particles for bromine activation be categorized based on size distribution and chemical composition?

The contribution of accumulation mode (0.1-0.5 μm) and coarse mode (>0.5 μm) aerosols was examined using in situ measurements. The accumulation mode is likely dominated by the Arctic haze, and these particles show no direct relationship to BrO. The presence of coarse mode aerosols, however, was a necessary and sufficient condition for observing large BrO partial columns with an instrument located above the boundary layer. The strongest correlation ($R^2 = 0.56$) was observed for SE winds. It is most likely that the observed coarse mode aerosols are SSA, generated in part from the sublimation of blowing snow. The mean blowing snow threshold was estimated to be 7.7-7.8 m s^{-1} for the EWS and the PEARL Ridge Lab, and coarse mode aerosol concentrations were significantly higher for wind speeds above the blowing snow threshold. High aerosol concentrations, on the other hand, occur over a range of wind speeds, indicating that most of the aerosols are likely not produced locally, but transported to the measurement location. The sources of these transported aerosols might be blowing snow or leads in the sea ice along the back trajectories, although no leads were identified near Eureka for the study period.

Overall, the good correlation between BrO and coarse mode aerosols supports the view that SSA is a direct source of bromine to the polar troposphere. More measurements of the composition and vertical distribution of aerosols would be required to quantify the exact contribution of SSA to the Arctic halogen budget.

8.1.4 Contributions to the Study of Urban NO_2 Pollution

A two-year dataset of NO_2 profiles, in both the UV and visible wavelength ranges, was retrieved from MAX-DOAS measurements made by Pandoras #103 and #104 in Toronto. Results using a parametric algorithm (MAPA) were compared to an OEM retrieval (HeiPro) and to supporting datasets. The MAPA NO_2-UV time series was used to assess NO_2 variability in Toronto. The study, presented in Chapter 7, addressed the following science questions:

- Do Pandora MAX-DOAS measurements have sufficient sensitivity to retrieve profiles of tropospheric NO_2? How do results from parametric and optimal estimation retrieval methods compare?

- How consistent are the retrieved partial columns when compared to the standard Pandora NO_2 total columns? What is the relationship between the retrieved surface NO_2 concentrations and those measured by in-situ measurements in Toronto?

HeiPro results for Pandora #103 (June-July 2019) indicate that both the long and quick scans in the regular measurement sequence provide a similar amount of information about the NO_2 profile, and DOFS for quick scans are only slightly lower than those for long scans. Comparison results, described below, are generally similar for long and quick scans. HeiPro profiles are systematically larger than MAPA at higher altitudes (>300-700 m), since HeiPro results tend to the a priori as MAX-DOAS vertical sensitivity decreases, whereas MAPA does not rely on a priori profiles. As a consequence, while partial columns from the two algorithms show good correlation ($R^2 > 0.85$), HeiPro partial columns are generally larger. MAPA partial columns show a better correlation when compared to Pandora direct-sun total columns. For the full MAPA dataset (2018-2020), retrieved partial columns show similarly good correlation to direct-sun total column for both instruments, wavelength ranges and scan types, and UV and visible partial columns show good correlation with each other ($R^2 > 0.92$). This indicates that the NO_2 partial column is successfully retrieved regardless of the input dataset.

Retrieved 0-200 m surface concentrations from MAPA and HeiPro show better agreement for NO_2-UV ($R^2 > 0.90$) than for NO_2-vis ($R^2 > 0.72$). The retrieved NO_2 profiles are somewhat variable, with a more even distribution of NO_2 in the lowest 400-600 m in the visible range, compared to the UV profiles. Comparisons to NAPS in situ NO_2 surface concentrations indicate that the UV retrievals perform better for both algorithms, likely due to the shorter path lengths in the UV. HeiPro results generally agree better with NAPS data. For the full MAPA dataset, comparisons to NAPS data corroborate the better performance of the UV retrievals for surface concentrations. UV and visible surface concentrations show weaker correlation to each other ($R^2 > 0.46$), likely due to the tendency of the visible MAPA retrievals to return elevated NO_2 layers with zero surface concentrations.

- What are the patterns of temporal variability in the retrieved NO_2 dataset? What are the patterns in the vertical distribution of NO_2?

- What was the effect of the 2020 COVID-19 lockdown on NO_2 columns and surface concentrations in Toronto?

The variability of NO_2 in Toronto was examined using the full NO_2-UV dataset retrieved using MAPA, including both Pandora instruments and both long and quick scans. Partial columns and surface concentrations show a seasonal cycle with peak monthly mean values in the winter, following the seasonal changes in the lifetime of NO_2. Morning and evening maxima are observed in the diurnal distribution of both partial columns and surface concentrations, and weekend values are significantly smaller than those on weekdays. Variability in surface concentrations is greater due to the dilution of near-surface NO_2 by the expanding boundary layer throughout the day.

During the COVID-19 lockdown in Toronto, NO_2 concentrations were lower than during the equivalent period in 2018-2019. While meteorological variability likely contributed to reduced NO_2, the reduction in peak NO_2 partial columns and surface concentrations appears to be a direct consequence of reduced road traffic during the lockdown.

8.2 Suggested Future Work

The GBS dataset of ozone and NO_2 VCDs now includes 20 years of measurements. As the dataset continues to be extended, detection of stratospheric trends will become possible. There is significant uncertainty in the timeline for the return of pre-CFC ozone concentrations in the stratosphere (Chipperfield et al., 2020). The GBS dataset could be used to assess changes in ozone concentrations above Eureka, as the measurements now cover almost two decades since the expected peak of ozone loss around 2000 (WMO, 2014). In addition, the longer dataset would aid in assessing drifts between satellite and ground-based datasets with increased confidence. The OSIRIS and ACE satellite instruments have been measuring trace gases in the Arctic stratosphere since 2001 and 2003, respectively, and monitoring the quality of these datasets becomes more and more important as the instruments continue to age and potentially degrade. To aid these projects, the feasibility of retrieving zenith-sky dSCDs and VCDs using fixed yearly reference spectra should be investigated. A large portion of the uncertainty in the ozone and NO_2 datasets arises from the use of daily reference spectra, and a fixed reference would reduce the uncertainty of the VCDs both in high-SZA conditions (early spring and late fall) and during the polar day.

The feasibility of using fixed reference spectra for OClO and BrO dSCDs should also be evaluated, and Ramina Alwarda is working on this. The GBS OClO data are being used for the validation of TROPOMI measurements (Pinardi et al., 2020). The BrO data could also be used to validate satellite measurements, including stratospheric columns from the GOME, GOME-2, OMI, and TROPOMI instruments. Stratospheric columns of BrO have been retrieved from GBS measurements before, by Adams (2012) and Zhao (2017), and their approach could be extended to the entire BrO time series to create and excellent dataset for validation purposes.

The elevation calibration of MAX-DOAS instruments is critical for accurate profile retrievals, as confirmed by the CINDI-2 campaign. While the CINDI-2 results indicate that the pointing stability of the GBS trackers is adequate for high quality MAX-DOAS measurements, the initial elevation calibration could be improved. Tests have been performed using the PEARL-GBS by measuring the light of a laser level at multiple azimuth angles. These tests were successful in the TAO, but did not adapt well to conditions in Eureka. These methods could be improved and implemented as part of the yearly tests for the GBS instruments. By calculating elevation offsets at multiple azimuth angles for each suntracker, the elevation offset for the MAX-DOAS viewing directions (pointing off the roof of the PEARL Ridge Lab) could be determined. To monitor the pointing stability of the instrument, daily horizon scans could be incorporated into the MAX-DOAS measurement sequence.

To further improve the elevation stability of the PEARL-GBS suntracker, modifications to the tracker box could be considered, to reduce warping and vibrations of internal components. This would be most beneficial for direct sun measurements. The software and hardware components are available to perform active solar tracking, and with improvements to the stability of the camera mount, direct-sun measurements could be performed reliably.

A 2D MAX-DOAS measurement sequence was implemented for CINDI-2 by Zhao (2017). This could be implemented for the GBS measurements in Eureka, to study the horizontal distribution of BrO, for example. However, a careful evaluation of the dataset will be required. Light reflected from the local snowpack likely has a significant influence on measurements at small (and negative) elevation angles. These effects could be highly variable as a function of viewing direction, given the complex topography around the PEARL Ridge Lab. Since the RTM simulations used in the BrO retrievals do not account for topography or variability in surface albedo, the effects of reflected light need to be evaluated to accurately interpret the retrieval results. Such a study would be highly valuable for improving MAX-DOAS measurements in the polar regions, and the study might involve radiative transfer modelling, or analysis of dSCDs in a range of conditions.

The springtime BrO and aerosol dataset retrieved from PEARL-GBS MAX-DOAS data covers four years (2016-2019). Retrievals are available for 2015 as well, but the smaller number of elevation angles measured in 2015 limit the usefulness of the profiles. The elevation angles have been consistent since 2016, and so the dataset should be extended to include spring seasons past 2019. Alongside the current retrieval approach using the OEM algorithm HeiPro, the feasibility of using parametric retrieval algorithms, such as MAPA, should be examined as well. The parametric approach provides good quality data with greatly increased computational efficiency, and this would be beneficial for retrieving more trace gases from (and utilizing a larger portion of) the MAX-DOAS dataset. A current limitation of MAPA for Eureka retrievals is the lack of nodes for negative elevation angles in the LUTs.

Regardless of the retrieval method, the BrO dataset is ideal for the validation of satellite and model datasets. Initial comparisons have been performed between pTOMCAT 3D CTM simulations (Yang et al., 2005) and PEARL-GBS retrievals for 2015-2018. Modeled BrO from pTOMCAT (which considers only bromine release from SSA) generally reproduces the retrieved BrO partial columns, but the model tends to overestimate BrO concentrations, likely due to the coarse horizontal resolution (2.8° × 2.8°) of pTOMCAT. This work could be extended to include long-term model validation of pTOMCAT BrO, ozone, and aerosols at Eureka. In addition to model validation, the BrO partial columns should be used to validate tropospheric BrO columns retrieved from GOME-2, OMI, and TROPOMI measurements. The detection of shallow boundary layer BrO events (typical for snowpack bromine release) is not straightforward for nadir-viewing satellite instruments, given the need to separate the tropospheric BrO column from the total column (e.g., Sihler et al., 2012). As a result, discrepancies arise between satellite measurements and MAX-DOAS data when the MAX-DOAS instruments are located at sea level. Since the PEARL Ridge Lab is located at 610 m altitude, the PEARL-GBS dataset likely has a vertical sensitivity that is more similar to satellite instruments compared to other MAX-DOAS datasets. This presents a unique opportunity to assess satellite BrO measurements in the Arctic.

In addition to the BrO retrievals, the PEARL-GBS MAX-DOAS data could be used to retrieve profiles of NO_2 in the UV, and UT-GBS MAX-DOAS measurements (available since 2015) could be used to retrieve NO_2 in the visible wavelength range. NO_2 is emitted from the snowpack (e.g., Grannas et al., 2007), and the presence of NO_2 could extend bromine explosions in low ozone conditions (Wang et al., 2019). Combined with the results from a snow sampling project completed by Xin Yang during the 2018 and 2019 Canadian Arctic ACE/OSIRIS Validation Campaigns, the NO_2 and BrO profile datasets could be used to investigate snow photochemistry and its effects on bromine activation.

Efforts are underway in the MAX-DOAS community to standardize analysis and retrieval practices, similar to the NDACC guidelines for VCD processing. The FRM4DOAS project aims to eventually provide centralized data processing and profile retrievals for participating instruments. Integrating the GBS instruments into the FRM4DOAS network would provide additional quality checks and data products to complement the work being done by the GBS team.

The Pandora MAX-DOAS NO_2 dataset in Toronto is ideal for satellite validation. Pandora direct-sun NO_2 columns are used to validate NO_2 total columns measured by TROPOMI, and the retrieved NO_2 partial columns could be used to validate the tropospheric NO_2 product from the same satellite instrument. Furthermore, the dataset could be extended to include ECCC Pandoras at multiple locations across the Greater Toronto Area (Zhao et al., 2020b), and to study the spatial variability of tropospheric and surface NO_2. Retrievals of HCHO have also been performed for the UV Pandora measurements. This dataset, however, requires careful evaluation, since some components of older Pandora head sensors emit HCHO, leading to a temperature-dependent bias in the measured spectra (Spinei et al., 2021).

In addition to the Pandoras in Toronto, a Pandora instrument has been installed at the PEARL Ridge Lab since 2019. Direct-sun and zenith-sky data from this instrument could be used to compare to GBS VCD results, while retrievals using the Pandora MAX-DOAS data could provide a useful addition to the BrO and NO_2 profile datasets retrieved from GBS data.

Overall, this thesis presents a 20-year time series of ground-based UV-visible measurements in the Arctic. As the dataset continues to extend, the long-term measurements can be used, in conjunction with satellite and model datasets, to examine ozone variability and trends in the stratosphere, and to improve our understanding of the processes that affect ozone in the troposphere. The continuation of the long-term data record at Eureka is essential in order to understand and evaluate the consequences of a changing Arctic atmosphere.

References

Abbatt, J. P. D., Thomas, J. L., Abrahamsson, K., Boxe, C., Granfors, A., Jones, A. E., King, M. D., Saiz-Lopez, A., Shepson, P. B., Sodeau, J., et al.: Halogen activation via interactions with environmental ice and snow in the polar lower troposphere and other regions, Atmospheric Chemistry and Physics, 12(14), 6237–6271, doi: 10.5194/acp-12-6237-2012, 2012.

Adams, C.: Measurements of Atmospheric Ozone, NO_2, OClO, and BrO at 80 °N using UV Visible Spectroscopy, Ph.D. thesis, University of Toronto, 2012.

Adams, C., McLinden, C. A., Strong, K., and Umlenski, V.: Ozone and NO_2 variations measured during the 1 August 2008 solar eclipse above Eureka, Canada with a UV-visible spectrometer, Journal of Geophysical Research: Atmospheres, 115(D19), doi:10.1029/2010JD014424, 2010.

Adams, C., Strong, K., Batchelor, R. L., Bernath, P. F., Brohede, S., Boone, C., Degenstein, D., Daffer, W. H., Drummund, J. R., Fogal, P. F., Farahani, E., Fayt, C., Fraser, A., Goutail, F., Hendrick, F., Kolonjari, F., Lindenmaier, R., Manney, G., McElroy, C. T., McLinden, C. A., Mendonca, J., Park, J.-H., Pavlovic, B., Pazmino, A., Roth, C., Savastiouk, V., Walker, K. A., Weaver, D., and Zhao, X.: Validation of ACE and OSIRIS Ozone and NO_2 Measurements Using Ground Based Instruments at 80 °N, Atmospheric Measurement Techniques, 5(5), 927–953, doi:10.5194/amt-5-927-2012, 2012a.

Adams, C., Strong, K., Zhao, X., Bassford, M. R., Chipperfield, M. P., Daffer, W., Drummond, J. R., Farahani, E. E., Feng, W., Fraser, A., Goutail, F., Manney, G. L., McLinden, C. A., Pazmino, A., Rex, M., and Walker, K. A.: Severe 2011 ozone depletion assessed with 11 years of ozone, NO_2, and OClO measurements at 80 °N, Geophysical Research Letters, 39(5), doi:10.1029/2011GL050478, 2012b.

Adams, C., Strong, K., Zhao, X., Bourassa, A. E., Daffer, W. H., Degenstein, D., Drummond, J. R., Farahani, E. E., Fraser, A., Lloyd, N. D., Manney, G. L., McLinden, C. A., Rex, M., Roth, C., Strahan, S. E., Walker, K. A., and Wohltmann, I.: The spring 2011 final stratospheric warming above Eureka: anomalous dynamics and chemistry, Atmospheric Chemistry and Physics, 13(2), 611–624, doi:10.5194/acp-13-611-2013, 2013.

Adams, C., Bourassa, A. E., Sofieva, V., Froidevaux, L., McLinden, C. A., Hubert, D., Lambert, J.-C., Sioris, C. E., and Degenstein, D. A.: Assessment of Odin-OSIRIS ozone measurements from 2001 to the present using MLS, GOMOS, and ozonesondes, Atmospheric Measurement Techniques, 7(1), 49–64, doi:doi:10.5194/amt-7-49-2014, 2014.

Adams, M. D.: Air pollution in Ontario, Canada during the COVID-19 State of Emergency, Science of the Total Environment, 742, 140516, doi:10.1016/j.scitotenv.2020.140516, 2020.

Aliwell, S. R., Van Roozendael, M., Johnston, P. V., Richter, A., Wagner, T., Arlander, D. W., Burrows, J. P., Fish, D. J., Jones, R. L., Tørnkvist, K. K., Lambert, J.-C., Pfeilsticker, K., and Pundt, I.: Analysis for BrO in zenith-sky spectra: An intercomparison exercise for analysis improvement, Journal of Geophysical Research: Atmospheres, 107(D14), ACH 10–1–ACH 10–20, doi:10.1029/2001JD000329, 2002.

Amin, R. S., Tamima, U., and Amador Jimenez, L.: Understanding air pollution from induced traffic during and after the construction of a new highway: Case study of highway 25 in Montreal, Journal of Advanced Transportation, 2017, doi:10.1155/2017/5161308, 2017.

Andersen, Z. J., Hvidberg, M., Jensen, S. S., Ketzel, M., Loft, S., Sørensen, M., Tjønneland, A., Overvad, K., and Raaschou-Nielsen, O.: Chronic Obstructive Pulmonary Disease and Long-Term Exposure to Traffic-related Air Pollution, American Journal of Respiratory and Critical Care Medicine, 183(4), 455–461, doi:10.1164/rccm.201006-0937OC, 2011.

Anderson, P. S. and Neff, W. D.: Boundary layer physics over snow and ice, Atmospheric Chemistry and Physics, 8(13), 3563–3582, doi:10.5194/acp-8-3563-2008, 2008.

Anenberg, S. C., Henze, D. K., Tinney, V., Kinney, P. L., Raich, W., Fann, N., Malley, C. S., Roman, H., Lamsal, L., Duncan, B., Martin, R. V., van Donkelaar, A., Brauer, M., Doherty, R., Jonson, J. E., Davila, Y., Sudo, K., and Kuylenstierna, J. C. I.: Estimates of the global burden of ambient PM2.5, ozone, and NO_2 on asthma incidence and emergency room visits, Environmental Health Perspectives, 126(10), 107004, doi:10.1289/EHP3766, 2018.

Balis, D., Isaksen, I. S. A., Zerefos, C., Zyrichidou, I., Eleftheratos, K., Tourpali, K., Bojkov, R., Rognerud, B., Stordal, F., Svde, O. A., and Orsolini, Y.: Observed and modelled record ozone decline over the Arctic during winter/spring 2011, Geophysical Research Letters, 38(23), doi:10.1029/2011GL049259, 2011.

Barber, D. G., Ehn, J. K., Puko, M., Rysgaard, S., Deming, J. W., Bowman, J. S., Papakyriakou, T., Galley, R. J., and Sgaard, D. H.: Frost flowers on young Arctic sea ice: The climatic, chemical, and microbial significance of an emerging ice type, Journal of Geophysical Research: Atmospheres, 119(20), 11593–11612, doi:10.1002/2014JD021736, 2014.

Barrie, L. A., Bottenheim, J. W., Schnell, R. C., Crutzen, P. J., and Rasmussen, R. A.: Ozone destruction and photochemical reactions at polar sunrise in the lower Arctic atmosphere, Nature, 334(6178), 138–141, doi:doi.org/10.1038/334138a0, 1988.

Bassford, M. R., Strong, K., and Rebello, J.: An Automated Spectrometer for Monitoring Arctic Ozone Depletion-The authors discuss the construction of a portable spectrometer system developed for performing stand-alone measurements, Spectroscopy, 15(10), 42–47, 2000.

Bassford, M. R., McLinden, C. A., and Strong, K.: Zenith-sky observations of stratospheric gases: the sensitivity of air mass factors to geophysical parameters and the influence of tropospheric clouds, Journal of Quantitative Spectroscopy and Radiative Transfer, 68(6), 657–677, doi:10.1016/S0022-4073(00)00052-2, 2001.

Bassford, M. R., Strong, K., McLinden, C. A., and McElroy, C. T.: Ground-based measurements of ozone and NO_2 during MANTRA 1998 using a Zenith-sky spectrometer, Atmosphere-ocean, 43(4), 325–338, doi:10.3137/ao.430404, 2005.

Batchelor, R. L., Strong, K., Lindenmaier, R., Mittermeier, R. L., Fast, H., Drummond, J. R., and Fogal, P. F.: A new Bruker IFS 125HR FTIR spectrometer for the polar environment atmospheric research laboratory at Eureka, Nunavut, Canada: measurements and comparison with the existing Bomem DA8 spectrometer, Journal of Atmospheric and Oceanic Technology, 26(7), 1328–1340, doi:10.1175/2009JTECHA1215.1, 2009.

Batchelor, R. L., Kolonjari, F., Lindenmaier, R., Mittermeier, R. L., Daffer, W., Fast, H., Manney, G., Strong, K., and Walker, K. A.: Four Fourier transform spectrometers and the Arctic polar vortex: instrument intercomparison and ACE-FTS validation at Eureka during the IPY springs of 2007 and 2008, Atmospheric Measurement Techniques, 3(1), 51–66, doi:10.5194/amt-3-51-2010, 2010.

Bauwens, M., Compernolle, S., Stavrakou, T., Mller, J.-F., van Gent, J., Eskes, H., Levelt, P. F., van der A, R., Veefkind, J. P., Vlietinck, J., Yu, H., and Zehner, C.: Impact of Coronavirus Outbreak on NO_2 Pollution Assessed Using TROPOMI and OMI Observations, Geophysical Research Letters, 47(11), e2020GL087978, doi:10.1029/2020GL087978, 2020.

Begoin, M., Richter, A., Weber, M., Kaleschke, L., Tian-Kunze, X., Stohl, A., Theys, N., and Burrows, J. P.: Satellite observations of long range transport of a large BrO plume in the Arctic, Atmospheric Chemistry and Physics, 10(14), 6515–6526, doi:10.5194/acp-10-6515-2010, 2010.

Beirle, S., Dörner, S., Donner, S., Remmers, J., Wang, Y., and Wagner, T.: The Mainz profile algorithm (MAPA), Atmospheric Measurement Techniques, 12(3), 1785–1806, doi:10.5194/amt-12-1785-2019, 2019.

Bera, B., Bhattacharjee, S., Shit, P. K., Sengupta, N., and Saha, S.: Significant impacts of COVID-19 lockdown on urban air pollution in Kolkata (India) and amelioration of environmental health, Environment, Development and Sustainability, 1–28, doi:10.1007/s10668-020-00898-5, 2020.

Berg, T., Pfaffhuber, K. A., Cole, A. S., Engelsen, O., and Steffen, A.: Ten-year trends in atmospheric mercury concentrations, meteorological effects and climate variables at Zeppelin, Ny-Ålesund, Atmospheric Chemistry and Physics, 13(13), 6575–6586, doi:10.5194/acp-13-6575-2013, 2013.

Berman, J. D. and Ebisu, K.: Changes in US air pollution during the COVID-19 pandemic, Science of the Total Environment, 739, 139864, doi:10.1016/j.scitotenv.2020.139864, 2020.

Bernath, P. F., McElroy, C. T., Abrams, M. C., Boone, C. D., Butler, M., Camy-Peyret, C., Carleer, M., Clerbaux, C., Coheur, P.-F., Colin, R., DeCola, P., DeMaziére, M., Drummond, J. R., Dufour, D., Evans, W. F. J., Fast, H., Fussen, D., Gilbert, K., Jennings, D. E., Llewellyn, E. J., Lowe, R. P., Mahieu, E., McConnell, J. C., McHugh, M., McLeod, S. D., Michaud, R., Midwinter, C., Nassar, R., Nichitiu, F., Nowlan, C., Rinsland, C. P., Rochon, Y. J., Rowlands, N., Semeniuk, K., Simon, P., Skelton, R., Sloan, J. J., Soucy, M.-A., Strong, K., Tremblay, P., Turnbull, D., Walker, K. A., Walkty, I., Wardle, D. A., Wehrle, V., Zander, R., and Zou, J.: Atmospheric Chemistry Experiment (ACE): Mission overview, Geophysical Research Letters, 32(15), L15S01, doi:10.1029/2005GL022386, 2005.

Bernhard, G. H., Fioletov, V. E., Grooß, J.-U., Ialongo, I., Johnsen, B., Lakkala, K., Manney, G. L., Müller, R., and Svendby, T.: Record-Breaking Increases in Arctic Solar Ultraviolet Radiation Caused by Exceptionally Large Ozone Depletion in 2020, Geophysical Research Letters, 47(24), e2020GL090844, doi:10.1029/2020GL090844, 2020.

Bhartia, P. K., Wellemeyer, C. G., Taylor, S. L., Nath, N., and Gopolan, A.: Solar Backscatter Ultraviolet (SBUV) version 8 profile algorithm, in: Zerefos, C. (editor), *Proceedings of the Quadrennial Ozone Symposium*, 295–296, 2004.

Blechschmidt, A.-M., Richter, A., Burrows, J. P., Kaleschke, L., Strong, K., Theys, N., Weber, M., Zhao, X., and Zien, A.: An exemplary case of a bromine explosion event linked to cyclone development in the Arctic, Atmospheric Chemistry and Physics, 16(3), 1773–1788, doi:10.5194/acp-16-1773-2016, 2016.

Blechschmidt, A.-M., Arteta, J., Coman, A., Curier, L., Eskes, H., Foret, G., Gielen, C., Hendrick, F., Marécal, V., Meleux, F., Parmentier, J., Peters, E., Pinardi, G., Piters, A. J. M., Plu, M., Richter, A., Segers, A., Sofiev, M., Valdebenito, Á. M., Van Roozendael, M., Vira, J., Vlemmix, T., and Burrows, J. P.: Comparison of tropospheric NO_2 columns from MAX-DOAS retrievals and regional air quality model simulations, Atmospheric Chemistry and Physics, 20(5), 2795–2823, doi:10.5194/acp-20-2795-2020, 2020.

Bocquet, F., Helmig, D., Van Dam, B. A., and Fairall, C. W.: Evaluation of the flux gradient technique for measurement of ozone surface fluxes over snowpack at Summit, Greenland, Atmospheric Measurement Techniques, 4(10), 2305–2321, doi:10.5194/amt-4-2305-2011, 2011.

Boersma, K. F., Eskes, H. J., Veefkind, J. P., Brinksma, E. J., van der A, R. J., Sneep, M., van den Oord, G. H. J., Levelt, P. F., Stammes, P., Gleason, J. F., and Bucsela, E. J.: Near-real time retrieval of tropospheric NO_2 from OMI, Atmospheric Chemistry and Physics, 7(8), 2103–2118, doi:10.5194/acp-7-2103-2007, 2007.

Boggs, P. T. and Rogers, J. E.: Orthogonal distance regression, in: Brown, P. J. and Wayne, A. F. (editors), *Statistical analysis of measurement error models and applications: proceedings of the AMS-IMS-SIAM joint summer research conference held June 10-16, 1989*, 183–194, American Mathematical Society, 1990.

Bognar, K., Zhao, X., Strong, K., Boone, C. D., Bourassa, A. E., Degenstein, D. A., Drummond, J. R., Duff, A., Goutail, F., Griffin, D., Jeffery, P. S., Lutsch, E., Manney, G. L., McElroy, C. T., McLinden, C. A., Millán, L. F., Pazmino, A., Sioris, C. E., Walker,

K. A., and Zou, J.: Updated validation of ACE and OSIRIS ozone and NO_2 measurements in the Arctic using ground-based instruments at Eureka, Canada, Journal of Quantitative Spectroscopy and Radiative Transfer, 238, 106571, doi:10.1016/j.jqsrt.2019.07.014, 2019.

Bognar, K., Alwarda, R., Strong, K., Chipperfield, M. P., Dhomse, S. S., Drummond, J. R., Feng, W., Fioletov, V., Goutail, F., Herrera, B., Manney, G. L., McCullough, E. M., Millán, L. F., Pazmino, A., Walker, K. A., Wizenberg, T., and Zhao, X.: Unprecedented spring 2020 ozone depletion in the context of 20 years of measurements at Eureka, Canada, Submitted to: Journal of Geophysical Research: Atmospheres, doi: 10.1002/essoar.10505235.1, 2020a.

Bognar, K., Zhao, X., Strong, K., Chang, R. Y.-W., Frieß, U., Hayes, P. L., McClure-Begley, A., Morris, S., Tremblay, S., and Vicente-Luis, A.: Measurements of Tropospheric Bromine Monoxide Over Four Halogen Activation Seasons in the Canadian High Arctic, Journal of Geophysical Research: Atmospheres, 125(18), e2020JD033015, doi:10.1029/2020JD033015, 2020b.

Bogumil, K., Orphal, J., Homann, T., Voigt, S., Spietz, P., Fleischmann, O., Vogel, A., Hartmann, M., Kromminga, H., Bovensmann, H., Frerick, J., and Burrows, J. P.: Measurements of molecular absorption spectra with the SCIAMACHY pre-flight model: instrument characterization and reference data for atmospheric remote-sensing in the 230–2380 nm region, Journal of Photochemistry and Photobiology A: Chemistry, 157(2-3), 167–184, doi:10.1016/S1010-6030(03)00062-5, 2003.

Boone, C. D., Nassar, R., Walker, K. A., Rochon, Y., McLeod, S. D., Rinsland, C. P., and Bernath, P. F.: Retrievals for the atmospheric chemistry experiment Fourier-transform spectrometer, Applied Optics, 44(33), 7218–7231, doi:10.1364/AO.44.007218, 2005.

Boone, C. D., Walker, K. A., and Bernath, P. F.: Version 3 Retrievals for the Atmospheric Chemistry Experiment Fourier Transform Spectrometer (ACE-FTS), in: Bernath, P. F. (editor), *The Atmospheric Chemistry Experiment ACE at 10: a solar occultation anthology*, 103–127, A. Deepak Publishing, 2013.

Bösch, T., Rozanov, V., Richter, A., Peters, E., Rozanov, A., Wittrock, F., Merlaud, A., Lampel, J., Schmitt, S., de Haij, M., Berkhout, S., Henzing, B., Apituley, A., den Hoed, M., Vonk, J., Tiefengraber, M., Müller, M., and Burrows, J. P.: BOREAS – a new MAX-DOAS profile retrieval algorithm for aerosols and trace gases, Atmospheric Measurement Techniques, 11(12), 6833–6859, doi:10.5194/amt-11-6833-2018, 2018.

Bottenheim, J. W., Gallant, A. G., and Brice, K. A.: Measurements of NO_y species and O_3 at 82 °N latitude, Geophysical Research Letters, 13(2), 113–116, doi:10.1029/GL013i002p00113, 1986.

Bottenheim, J. W., Netcheva, S., Morin, S., and Nghiem, S. V.: Ozone in the boundary layer air over the Arctic Ocean: measurements during the TARA transpolar drift 2006–2008, Atmospheric Chemistry and Physics, 9(14), 4545–4557, doi:10.5194/acp-9-4545-2009, 2009.

Bourassa, A. E., Roth, C. Z., Zawada, D. J., Rieger, L. A., McLinden, C. A., and Degenstein, D. A.: Drift-corrected Odin-OSIRIS ozone product: algorithm and updated stratospheric ozone trends, Atmospheric Measurement Techniques, 11(1), 489–498, doi:10.5194/amt-11-489-2018, 2018.

Brewer, A. W.: Evidence for a world circulation provided by the measurements of helium and water vapour distribution in the stratosphere, Quarterly Journal of the Royal Meteorological Society, 75(326), 351–363, doi:10.1002/qj.49707532603, 1949.

Brewer, A. W.: A replacement for the Dobson spectrophotometer?, Pure and Applied Geophysics, 106(1), 919–927, doi:10.1007/BF00881042, 1973.

Brewer, A. W., McElroy, C. T., and Kerr, J. B.: Nitrogen dioxide concentrations in the atmosphere, Nature, 246(5429), 129–133, doi:10.1038/246129a0, 1973.

Brohede, S., McLinden, C. A., Berthet, G., Haley, C. S., Murtagh, D., and Sioris, C. E.: A stratospheric NO_2 climatology from Odin/OSIRIS limb-scatter measurements, Canadian Journal of Physics, 85(11), 1253–1274, doi:10.1139/p07-141, 2007a.

Brohede, S. M., Haley, C. S., Mclinden, C. A., Sioris, C. E., Murtagh, D. P., Petelina, S. V., Llewellyn, E. J., Bazureau, A., Goutail, F., Randall, C. E., Lumpe, J. D., Taha, G., Thomasson, L. W., and Gordley, L. L.: Validation of Odin/OSIRIS stratospheric NO_2 profiles, Journal of Geophysical Research: Atmospheres, 112(D7), doi:10.1029/2006JD007586, 2007b.

Burd, J. A., Peterson, P. K., Nghiem, S. V., Perovich, D. K., and Simpson, W. R.: Snowmelt onset hinders bromine monoxide heterogeneous recycling in the Arctic, Journal of Geophysical Research: Atmospheres, 122(15), 8297–8309, doi:10.1002/2017JD026906, 2017.

Burkholder, J. B., Sander, S. P., Abbatt, J. P. D., Barker, J. R., Huie, R. E., Kolb, C. E., Kurylo, M. J., Orkin, V. L., Wilmouth, D. M., and Wine, P. H.: Chemical kinetics and photochemical data for use in atmospheric studies: evaluation number 18, Jet Propulsion Laboratory, National Aeronautics and Space Administration, Pasadena, CA, 2015.

Cao, L., Sihler, H., Platt, U., and Gutheil, E.: Numerical analysis of the chemical kinetic mechanisms of ozone depletion and halogen release in the polar troposphere, Atmospheric Chemistry and Physics, 14(7), 3771–3787, doi:10.5194/acp-14-3771-2014, 2014.

Cao, L., He, M., Jiang, H., Grosshans, H., and Cao, N.: Sensitivity of the reaction mechanism of the ozone depletion events during the Arctic spring on the initial atmospheric composition of the troposphere, Atmosphere, 7(10), 124, doi:10.3390/atmos7100124, 2016.

Cede, A.: *Manual for Blick Software Suite 1.7*, LuftBlick, 2019.

Cede, A., Herman, J., Richter, A., Krotkov, N., and Burrows, J.: Measurements of nitrogen dioxide total column amounts using a Brewer double spectrophotometer in direct Sun mode, Journal of Geophysical Research: Atmospheres, 111(D5), doi:10.1029/2005JD006585, 2006.

Chan, K. L., Hartl, A., Lam, Y. F., Xie, P. H., Liu, W. Q., Cheung, H. M., Lampel, J., Pöhler, D., Li, A., Xu, J., Zhou, H. J., Ning, Z., and Wenig, M. O.: Observations of tropospheric NO_2 using ground based MAX-DOAS and OMI measurements during the Shanghai World Expo 2010, Atmospheric Environment, 119, 45–58, doi:10.1016/j.atmosenv.2015.08.041, 2015.

Chan, K. L., Wiegner, M., Wenig, M., and Pöhler, D.: Observations of tropospheric aerosols and NO_2 in Hong Kong over 5 years using ground based MAX-DOAS, Science of the total environment, 619, 1545–1556, doi:10.1016/j.scitotenv.2017.10.153, 2018.

Chan, K. L., Wang, Z., Ding, A., Heue, K.-P., Shen, Y., Wang, J., Zhang, F., Shi, Y., Hao, N., and Wenig, M.: MAX-DOAS measurements of tropospheric NO_2 and HCHO in Nanjing and a comparison to ozone monitoring instrument observations, Atmospheric Chemistry and Physics, 19(15), 10051–10071, doi:10.5194/acp-19-10051-2019, 2019.

Chance, K. V. and Spurr, R. J. D.: Ring effect studies: Rayleigh scattering, including molecular parameters for rotational Raman scattering, and the Fraunhofer spectrum, Applied optics, 36(21), 5224–5230, doi:10.1364/AO.36.005224, 1997.

Chapman, S.: XXXV. On ozone and atomic oxygen in the upper atmosphere, The London, Edinburgh, and Dublin Philosophical Magazine and Journal of Science, 10(64), 369–383, doi:10.1080/14786443009461588, 1930.

Charlton, A. J. and Polvani, L. M.: A New Look at Stratospheric Sudden Warmings. Part I: Climatology and Modeling Benchmarks, Journal of Climate, 20(3), 449–469, doi:10.1175/JCLI3996.1, 2007.

Chipperfield, M. P.: New version of the TOMCAT/SLIMCAT off-line chemical transport model: Intercomparison of stratospheric tracer experiments, Quarterly Journal of the Royal Meteorological Society, 132(617), 1179–1203, doi:10.1256/qj.05.51, 2006.

Chipperfield, M. P. and Jones, R. L.: Relative influences of atmospheric chemistry and transport on Arctic ozone trends, Nature, 400(6744), 551–554, doi:10.1038/22999, 1999.

Chipperfield, M. P., Dhomse, S. S., Feng, W., McKenzie, R. L., Velders, G. J. M., and Pyle, J. A.: Quantifying the ozone and ultraviolet benefits already achieved by the Montreal Protocol, Nature Communications, 6(1), 1–8, doi:10.1038/ncomms8233, 2015.

Chipperfield, M. P., Hossaini, R., Montzka, S. A., Reimann, S., Sherry, D., and Tegtmeier, S.: Renewed and emerging concerns over the production and emission of ozone-depleting substances, Nature Reviews Earth and Environment, 1–13, doi:10.1038/s43017-020-0048-8, 2020.

Choi, S., Theys, N., Salawitch, R. J., Wales, P. A., Joiner, J., Canty, T. P., Chance, K., Suleiman, R. M., Palm, S. P., Cullather, R. I., Darmenov, A. S., da Silva, A., Kurosu, T. P., Hendrick, F., and Van Roozendael, M.: Link Between Arctic Tropospheric BrO Explosion Observed From Space and Sea-Salt Aerosols From Blowing Snow Investigated Using Ozone Monitoring Instrument BrO Data and GEOS-5 Data Assimilation System, Journal of Geophysical Research: Atmospheres, 123(13), 6954–6983, doi:10.1029/2017JD026889, 2018.

Cole, A. S. and Steffen, A.: Trends in long-term gaseous mercury observations in the Arctic and effects of temperature and other atmospheric conditions, Atmospheric Chemistry and Physics, 10(10), 4661–4672, doi:10.5194/acp-10-4661-2010, 2010.

Coy, L., Nash, E. R., and Newman, P. A.: Meteorology of the polar vortex: Spring 1997, Geophysical Research Letters, 24(22), 2693–2696, doi:10.1029/97GL52832, 1997.

Croft, B., Martin, R. V., Leaitch, W. R., Tunved, P., Breider, T. J., D'Andrea, S. D., and Pierce, J. R.: Processes controlling the annual cycle of Arctic aerosol number and size distributions, Atmospheric Chemistry and Physics, 16(6), 3665–3682, doi:10.5194/acp-16-3665-2016, 2016.

Custard, K. D., Thompson, C. R., Pratt, K. A., Shepson, P. B., Liao, J., Huey, L. G., Orlando, J. J., Weinheimer, A. J., Apel, E., Hall, S. R., Flocke, F., Mauldin, L., Hornbrook, R. S., Pöhler, D., General, S., Zielcke, J., Simpson, W. R., Platt, U., Fried, A., Weibring, P., Sive, B. C., Ullmann, K., Cantrell, C., Knapp, D. J., and Montzka, D. D.: The NO_x dependence of bromine chemistry in the Arctic atmospheric boundary layer, Atmospheric Chemistry and Physics, 15(18), 10799–10809, doi:10.5194/acp-15-10799-2015, 2015.

Custard, K. D., Raso, A. R. W., Shepson, P. B., Staebler, R. M., and Pratt, K. A.: Production and release of molecular bromine and chlorine from the Arctic coastal snowpack, ACS Earth and Space Chemistry, 1(3), 142–151, doi:10.1021/acsearthspacechem.7b00014, 2017.

Danckaert, T., Fayt, C., Van Roozendael, M., De Smedt, I., Letocart, V., Merlaud, A., and Pinardi, G.: *QDOAS Software user manual*, Belgian Institute for Space Aeronomy, 3.2 edition, 2017.

Davis, Z. Y. W., Frieß, U., Strawbridge, K. B., Aggarwaal, M., Baray, S., Schnitzler, E. G., Lobo, A., Fioletov, V. E., Abboud, I., McLinden, C. A., Whiteway, J., Willis, M. D., Lee, A. K. Y., Brook, J., Olfert, J., O'Brien, J., Staebler, R., Osthoff, H. D., Mihele, C., and McLaren, R.: Validation of MAX-DOAS retrievals of aerosol extinction, SO_2, and NO_2 through comparison with lidar, sun photometer, active DOAS, and aircraft measurements in the Athabasca oil sands region, Atmospheric Measurement Techniques, 13(3), 1129–1155, doi:10.5194/amt-13-1129-2020, 2020.

De Mazière, M., Thompson, A. M., Kurylo, M. J., Wild, J. D., Bernhard, G., Blumenstock, T., Braathen, G. O., Hannigan, J. W., Lambert, J.-C., Leblanc, T., McGee, T. J., Nedoluha, G., Petropavlovskikh, I., Seckmeyer, G., Simon, P. C., Steinbrecht, W., and Strahan, S. E.: The Network for the Detection of Atmospheric Composition Change (NDACC): history, status and perspectives, Atmospheric Chemistry and Physics, 18(7), 4935–4964, doi:10.5194/acp-18-4935-2018, 2018.

Degenstein, D. A., Bourassa, A. E., Roth, C. Z., and Llewellyn, E. J.: Limb scatter ozone retrieval from 10 to 60 km using a multiplicative algebraic reconstruction technique, Atmospheric Chemistry and Physics, 9(17), 6521–6529, doi:10.5194/acp-9-6521-2009, 2009.

DeLand, M. T., Bhartia, P. K., Kramarova, N., and Chen, Z.: OMPS LP Observations of PSC Variability During the NH 2019-2020 Season, Geophysical Research Letters, 47(20), e2020GL090216, doi:10.1029/2020GL090216, 2020.

Deutschmann, T., Beirle, S., Frieß, U., Grzegorski, M., Kern, C., Kritten, L., Platt, U., Prados-Román, C., Puķı, J., Wagner, T., Werner, B., and Pfeilsticker, K.: The Monte Carlo atmospheric radiative transfer model McArtim: Introduction and validation of Jacobians and 3D features, Journal of Quantitative Spectroscopy and Radiative Transfer, 112(6), 1119–1137, doi:10.1016/j.jqsrt.2010.12.009, 2011.

Dhomse, S. S., Chipperfield, M. P., Feng, W., Ball, W. T., Unruh, Y. C., Haigh, J. D., Krivova, N. A., Solanki, S. K., and Smith, A. K.: Stratospheric O_3 changes during 2001–2010: the small role of solar flux variations in a chemical transport model, Atmospheric Chemistry and Physics, 13(19), 10113–10123, doi:10.5194/acp-13-10113-2013, 2013.

Dhomse, S. S., Feng, W., Montzka, S. A., Hossaini, R., Keeble, J., Pyle, J. A., Daniel, J. S., and Chipperfield, M. P.: Delay in recovery of the Antarctic ozone hole from unexpected CFC-11 emissions, Nature Communications, 10(1), 1–12, 2019.

Dieudonné, E., Ravetta, F., Pelon, J., Goutail, F., and Pommereau, J.-P.: Linking NO_2 surface concentration and integrated content in the urban developed atmospheric boundary layer, Geophysical Research Letters, 40(6), 1247–1251, doi:10.1002/grl.50242, 2013.

Dobson, G. M. B.: Origin and distribution of the polyatomic molecules in the atmosphere, Proceedings of the Royal Society of London. Series A, Mathematical and Physical Sciences, 236(1205), 187–193, doi:10.1098/rspa.1956.0127, 1956.

Dobson, G. M. B.: Forty Years' Research on Atmospheric Ozone at Oxford: a History, Applied Optics, 7(3), 387–405, doi:10.1364/AO.7.000387, 1968.

Dobson, G. M. B. and Harrison, D. N.: Measurements of the amount of ozone in the earth's atmosphere and its relation to other geophysical conditions, Proceedings of the Royal Society of London. Series A, Containing Papers of a Mathematical and Physical Character, 110(756), 660–693, doi:10.1098/rspa.1926.0040, 1926.

Domine, F., Sparapani, R., Ianniello, A., and Beine, H. J.: The origin of sea salt in snow on Arctic sea ice and in coastal regions, Atmospheric Chemistry and Physics, 4(9/10), 2259–2271, doi:10.5194/acp-4-2259-2004, 2004.

Domine, F., Taillandier, A. S., Simpson, W. R., and Severin, K.: Specific surface area, density and microstructure of frost flowers, Geophysical Research Letters, 32(13), doi:10.1029/2005GL023245, 2005.

Donner, S., Kuhn, J., Van Roozendael, M., Bais, A., Beirle, S., Bösch, T., Bognar, K., Bruchkouski, I., Chan, K. L., Dörner, S., Drosoglou, T., Fayt, C., Frieß, U., Hendrick, F., Hermans, C., Jin, J., Li, A., Ma, J., Peters, E., Pinardi, G., Richter, A., Schreier, S. F., Seyler, A., Strong, K., Tirpitz, J.-L., Wang, Y., Xie, P., Xu, J., Zhao, X., and Wagner, T.: Evaluating different methods for elevation calibration of MAX-DOAS (Multi AXis Differential Optical Absorption Spectroscopy) instruments during the CINDI-2 campaign, Atmospheric Measurement Techniques, 13(2), 685–712, doi:10.5194/amt-13-685-2020, 2020.

Douglas, T. A. and Sturm, M.: Arctic haze, mercury and the chemical composition of snow across northwestern Alaska, Atmospheric Environment, 38(6), 805–820, doi: 10.1016/j.atmosenv.2003.10.042, 2004.

Douglas, T. A., Domine, F., Barret, M., Anastasio, C., Beine, H. J., Bottenheim, J., Grannas, A., Houdier, S., Netcheva, S., Rowland, G., Staebler, R., and Steffen, A.: Frost flowers growing in the Arctic ocean-atmosphere-sea ice-snow interface: 1 Chemical composition, Journal of Geophysical Research: Atmospheres, 117(D14), doi: 10.1029/2011JD016460, 2012.

Dreher, D. B. and Harley, R. A.: A Fuel-Based Inventory for Heavy-Duty Diesel Truck Emissions, Journal of the Air and Waste Management Association, 48(4), 352–358, doi: 10.1080/10473289.1998.10463686, 1998.

Drosoglou, T., Bais, A. F., Zyrichidou, I., Kouremeti, N., Poupkou, A., Liora, N., Giannaros, C., Koukouli, M. E., Balis, D., and Melas, D.: Comparisons of ground-based tropospheric NO_2 MAX-DOAS measurements to satellite observations with the aid of an air quality model over the Thessaloniki area, Greece, Atmospheric Chemistry and Physics, 17(9), 5829–5849, doi:10.5194/acp-17-5829-2017, 2017.

Drosoglou, T., Koukouli, M. E., Kouremeti, N., Bais, A. F., Zyrichidou, I., Balis, D., van der A, R. J., Xu, J., and Li, A.: MAX-DOAS NO_2 observations over Guangzhou, China; ground-based and satellite comparisons, Atmospheric Measurement Techniques, 11(4), 2239–2255, doi:10.5194/amt-11-2239-2018, 2018.

Dunkerton, T. J. and Delisi, D. P.: Evolution of potential vorticity in the winter stratosphere of January-February 1979, Journal of Geophysical Research: Atmospheres, 91(D1), 1199–1208, doi:10.1029/JD091iD01p01199, 1986.

Dupuy, E., Walker, K. A., Kar, J., Boone, C. D., McElroy, C. T., Bernath, P. F., Drummond, J. R., Skelton, R., McLeod, S. D., Hughes, R. C., Nowlan, C. R., Dufour, D. G., Zou, J., Nichitiu, F., Strong, K., Baron, P., Bevilacqua, R. M., Blumenstock, T., Bodeker, G. E., Borsdorff, T., Bourassa, A. E., Bovensmann, H., Boyd, I. S., Bracher, A., Brogniez, C., Burrows, J. P., Catoire, V., Ceccherini, S., Chabrillat, S., Christensen, T., Coffey,

M. T., Cortesi, U., Davies, J., De Clercq, C., Degenstein, D. A., De Mazière, M., Demoulin, P., Dodion, J., Firanski, B., Fischer, H., Forbes, G., Froidevaux, L., Fussen, D., Gerard, P., Godin-Beekmann, S., Goutail, F., Granville, J., Griffith, D., Haley, C. S., Hannigan, J. W., Höpfner, M., Jin, J. J., Jones, A., Jones, N. B., Jucks, K., Kagawa, A., Kasai, Y., Kerzenmacher, T. E., Kleinböhl, A., Klekociuk, A. R., Kramer, I., Küllmann, H., Kuttippurath, J., Kyrölä, E., Lambert, J.-C., Livesey, N. J., Llewellyn, E. J., Lloyd, N. D., Mahieu, E., Manney, G. L., Marshall, B. T., McConnell, J. C., McCormick, M. P., McDermid, I. S., McHugh, M., McLinden, C. A., Mellqvist, J., Mizutani, K., Murayama, Y., Murtagh, D. P., Oelhaf, H., Parrish, A., Petelina, S. V., Piccolo, C., Pommereau, J.-P., Randall, C. E., Robert, C., Roth, C., Schneider, M., Senten, C., Steck, T., Strandberg, A., Strawbridge, K. B., Sussmann, R., Swart, D. P. J., Tarasick, D. W., Taylor, J. R., Tétard, C., Thomason, L. W., Thompson, A. M., Tully, M. B., Urban, J., Vanhellemont, F., Vigouroux, C., von Clarmann, T., von der Gathen, P., von Savigny, C., Waters, J. W., Witte, J. C., Wolff, M., and Zawodny, J. M.: Validation of ozone measurements from the Atmospheric Chemistry Experiment (ACE), Atmospheric Chemistry and Physics, 9(2), 287–343, doi:10.5194/acp-9-287-2009, 2009.

Efron, B. and Tibshirani, R.: Bootstrap methods for standard errors, confidence intervals, and other measures of statistical accuracy, Statistical Science, 1(1), 54–75, doi:10.2307/2245500, 1986.

Eigen, M. and Kustin, K.: The kinetics of halogen hydrolysis, Journal of the American Chemical Society, 84(8), 1355–1361, doi:10.1021/ja00867a005, 1962.

Eskes, H. J. and Boersma, K. F.: Averaging kernels for DOAS total-column satellite retrievals, Atmospheric Chemistry and Physics, 3(5), 1285–1291, doi:10.5194/acp-3-1285-2003, 2003.

Eyring, V., Waugh, D. W., Bodeker, G. E., Cordero, E., Akiyoshi, H., Austin, J., Beagley, S. R., Boville, B. A., Braesicke, P., Brühl, C., Butchart, N., Chipperfield, M. P., Dameris, M., Deckert, R., Deushi, M., Frith, S. M., Garcia, R. R., Gettelman, A., Giorgetta, M. A., Kinnison, D. E., Mancini, E., Manzini, E., Marsh, D. R., Matthes, S., Nagashima, T., Newman, P. A., Nielsen, J. E., Pawson, S., Pitari, G., Plummer, D. A., Rozanov, E., Schraner, M., Scinocca, J. F., Semeniuk, K., Shepherd, T. G., Shibata, K., Steil, B., Stolarski, R. S., Tian, W., and Yoshiki, M.: Multimodel projections of stratospheric ozone in the 21^{st} century, Journal of Geophysical Research: Atmospheres, 112(D16), doi:10.1029/2006JD008332, 2007.

Eyring, V., Arblaster, J. M., Cionni, I., Sedláček, J., Perlwitz, J., Young, P. J., Bekki, S., Bergmann, D., Cameron-Smith, P., Collins, W. J., Faluvegi, G., Gottschaldt, K.-D., Horowitz, L. W., Kinnison, D. E., Lamarque, J.-F., Marsh, D. R., Saint-Martin, D., Shindell, D. T., Sudo, K., Szopa, S., and Watanabe, S.: Long-term ozone changes and associated climate impacts in CMIP5 simulations, Journal of Geophysical Research: Atmospheres, 118(10), 5029–5060, doi:10.1002/jgrd.50316, 2013.

Fabry, C. and Buisson, H.: Étude de l'extrémité ultra-violette du spectre solaire, Journal de Physique et Le Radium, 2(7), 197–226, doi:10.1051/jphysrad:0192100207019700, 1921.

Fan, S.-M. and Jacob, D. J.: Surface ozone depletion in Arctic spring sustained by bromine reactions on aerosols, Nature, 359, 522–524, doi:10.1038/359522a0, 1992.

Farahani, E.: Stratospheric Composition Measurements in the Arctic and at Mid-latitudes and Comparison with Chemical Fields from Atmospheric Models, Ph.D. thesis, University of Toronto, 2006.

Farman, J. C., Gardiner, B. G., and Shanklin, J. D.: Large losses of total ozone in Antarctica reveal seasonal ClO_x/NO_x interaction, Nature, 315, 207–210, doi:doi.org/10.1038/315207a0, 1985.

Feng, S., Jiang, F., Wang, H., Wang, H., Ju, W., Shen, Y., Zheng, Y., Wu, Z., and Ding, A.: NO_x Emission Changes Over China During the COVID-19 Epidemic Inferred From Surface NO_2 Observations, Geophysical Research Letters, 47(19), e2020GL090080, doi:10.1029/2020GL090080, 2020.

Feng, W., Chipperfield, M. P., Davies, S., von der Gathen, P., Kyrö, E., Volk, C. M., Ulanovsky, A., and Belyaev, G.: Large chemical ozone loss in 2004/2005 Arctic winter/spring, Geophysical Research Letters, 34(9), doi:10.1029/2006GL029098, 2007.

Feng, W., Chipperfield, M. P., Davies, S., Mann, G. W., Carslaw, K. S., Dhomse, S., Harvey, L., Randall, C., and Santee, M. L.: Modelling the effect of denitrification on polar ozone depletion for Arctic winter 2004/2005, Atmospheric Chemistry and Physics, 11(13), 6559–6573, doi:10.5194/acp-11-6559-2011, 2011.

Fish, D. J., Jones, R. L., and Strong, E. K.: Midlatitude observations of the diurnal variation of stratospheric BrO, Journal of Geophysical Research: Atmospheres, 100(D9), 18863–18871, doi:10.1029/95JD01944, 1995.

Fleischmann, O. C., Hartmann, M., Burrows, J. P., and Orphal, J.: New ultraviolet absorption cross-sections of BrO at atmospheric temperatures measured by time-windowing

Fourier transform spectroscopy, Journal of Photochemistry and Photobiology A: Chemistry, 168(1-2), 117–132, doi:10.1016/j.jphotochem.2004.03.026, 2004.

Flynn, C. M., Pickering, K. E., Crawford, J. H., Lamsal, L., Krotkov, N., Herman, J., Weinheimer, A., Chen, G., Liu, X., Szykman, J., Tsay, S.-C., Loughner, C., Hains, J., Lee, P., Dickerson, R. R., Stehr, J. W., and Brent, L.: Relationship between column-density and surface mixing ratio: Statistical analysis of O_3 and NO_2 data from the July 2011 Maryland DISCOVER-AQ mission, Atmospheric Environment, 92, 429–441, doi:10.1016/j.atmosenv.2014.04.041, 2014.

Fogal, P. F., LeBlanc, L. M., and Drummond, J. R.: The Polar Environment Atmospheric Research Laboratory (PEARL): sounding the atmosphere at 80° North, Arctic, 66(3), 377–386, doi:10.2307/23594645, 2013.

Foster, K. L., Plastridge, R. A., Bottenheim, J. W., Shepson, P. B., Finlayson-Pitts, B. J., and Spicer, C. W.: The role of Br_2 and BrCl in surface ozone destruction at polar sunrise, Science, 291(5503), 471–474, doi:10.1126/science.291.5503.471, 2001.

Franklin, J. E.: Solar Absorption Spectroscopy at the Dalhousie Atmospheric Observatory, Ph.D. thesis, Dalhousie University, 2015.

Fraser, A., Bernath, P. F., Blatherwick, R. D., Drummond, J. R., Fogal, P. F., Fu, D., Goutail, F., Kerzenmacher, T. E., McElroy, C. T., Midwinter, C., Olson, J. R., Strong, K., Walker, K. A., Wunch, D., and Young, I. J.: Intercomparison of ground-based ozone and NO_2 measurements during the MANTRA 2004 campaign, Atmospheric Chemistry and Physics, 7(21), 5489–5499, doi:10.5194/acp-7-5489-2007, 2007a.

Fraser, A., Goutail, F., McLinden, C. A., Melo, S. M. L., and Strong, K.: Lightning-produced NO_2 observed by two ground-based UV-visible spectrometers at Vanscoy, Saskatchewan in August 2004, Atmospheric Chemistry and Physics, 7(6), 1683–1692, doi:10.5194/acp-7-1683-2007, 2007b.

Fraser, A., Goutail, F., Strong, K., Bernath, P. F., Boone, C., Daffer, W. H., Drummond, J. R., Dufour, D. G., Kerzenmacher, T. E., Manney, G. L., McElroy, C. T., Midwinter, C., McLinden, C. A., Nichitiu, F., Nowlan, C. R., Walker, J., Walker, K. A., Wu, H., and Zou, J.: Intercomparison of UV-visible measurements of ozone and NO_2 during the Canadian Arctic ACE validation campaigns: 2004–2006, Atmospheric Chemistry and Physics, 8(6), 1763–1788, doi:10.5194/acp-8-1763-2008, 2008.

Fraser, A., Adams, C., Drummond, J. R., Goutail, F., Manney, G., and Strong, K.: The Polar Environment Atmospheric Research Laboratory UV–visible Ground-Based Spectrometer: First measurements of O_3, NO_2, BrO, and OClO columns, Journal of Quantitative Spectroscopy and Radiative Transfer, 110(12), 986–1004, doi:10.1016/j.jqsrt.2009.02.034, 2009.

Fraser, A. C.: Arctic and Midlatitude Stratospheric Trace Gas Measurements Using Ground-based UV-visible Spectroscopy, Ph.D. thesis, University of Toronto, 2008.

Frey, M. M., Norris, S. J., Brooks, I. M., Anderson, P. S., Nishimura, K., Yang, X., Jones, A. E., Nerentorp Mastromonaco, M. G., Jones, D. H., and Wolff, E. W.: First direct observation of sea salt aerosol production from blowing snow above sea ice, Atmospheric Chemistry and Physics, 20(4), 2549–2578, doi:10.5194/acp-20-2549-2020, 2020.

Frieß, U., Monks, P. S., Remedios, J. J., Rozanov, A., Sinreich, R., Wagner, T., and Platt, U.: MAX-DOAS O_4 measurements: A new technique to derive information on atmospheric aerosols: 2. Modeling studies, Journal of Geophysical Research: Atmospheres, 111(D14), doi:10.1029/2005JD006618, 2006.

Frieß, U., Sihler, H., Sander, R., Pöhler, D., Yilmaz, S., and Platt, U.: The vertical distribution of BrO and aerosols in the Arctic: Measurements by active and passive differential optical absorption spectroscopy, Journal of Geophysical Research: Atmospheres, 116(D14), D00R04, doi:10.1029/2011JD015938, 2011.

Frieß, U., Beirle, S., Alvarado B, L., Bösch, T., Friedrich, M. M., Hendrick, F., Piters, A., Richter, A., van Roozendael, M., Rozanov, V. V., Spinei, E., Tirpitz, J.-L., Vlemmix, T., Wagner, T., and Wang, Y.: Intercomparison of MAX-DOAS vertical profile retrieval algorithms: studies using synthetic data, Atmospheric Measurement Techniques, 12(4), 2155–2181, doi:10.5194/amt-12-2155-2019, 2019.

Fu, D., Walker, K. A., Sung, K., Boone, C. D., Soucy, M.-A., and Bernath, P. F.: The portable atmospheric research interferometric spectrometer for the infrared, PARIS-IR, Journal of Quantitative Spectroscopy and Radiative Transfer, 103(2), 362–370, doi:10.1016/j.jqsrt.2006.05.006, 2007.

Fu, D., Walker, K. A., Mittermeier, R. L., Strong, K., Sung, K., Fast, H., Bernath, P. F., Boone, C. D., Daffer, W. H., Fogal, P., Kolonjari, F., Loewen, P., Manney, G. L., Mikhailov, O., and Drummond, J. R.: Simultaneous trace gas measurements using two Fourier transform spectrometers at Eureka, Canada during spring 2006, and comparisons with the ACE-FTS, Atmospheric Chemistry and Physics, 11(11), 5383–5405, doi:10.5194/acp-11-5383-2011, 2011.

Gardiner, T., Forbes, A., de Mazière, M., Vigouroux, C., Mahieu, E., Demoulin, P., Velazco, V., Notholt, J., Blumenstock, T., Hase, F., Kramer, I., Sussmann, R., Stremme, W., Mellqvist, J., Strandberg, A., Ellingsen, K., and Gauss, M.: Trend analysis of greenhouse gases over Europe measured by a network of ground-based remote FTIR instruments, Atmospheric Chemistry and Physics, 8(22), 6719–6727, doi:10.5194/acp-8-6719-2008, 2008.

Gelaro, R., McCarty, W., Suárez, M. J., Todling, R., Molod, A., Takacs, L., Randles, C. A., Darmenov, A., Bosilovich, M. G., Reichle, R., Wargan, K., Coy, L., Cullather, R., Draper, C., Akella, S., Buchard, V., Conaty, A., da Silva, A. M., Gu, W., Kim, G., Koster, R., Lucchesi, R., Merkova, D., Nielsen, J. E., Partyka, G., Pawson, S., Putman, W., Rienecker, M., Schubert, S. D., Sienkiewicz, M., and Zhao, B.: The modern-era retrospective analysis for research and applications, version 2 (MERRA-2), Journal of Climate, 30(14), 5419–5454, doi:10.1175/JCLI-D-16-0758.1, 2017.

Gielen, C., Van Roozendael, M., Hendrick, F., Pinardi, G., Vlemmix, T., De Bock, V., De Backer, H., Fayt, C., Hermans, C., Gillotay, D., and Wang, P.: A simple and versatile cloud-screening method for MAX-DOAS retrievals, Atmospheric Measurement Techniques, 7(10), 3509–3527, doi:10.5194/amt-7-3509-2014, 2014.

Gilman, J. B., Burkhart, J. F., Lerner, B. M., Williams, E. J., Kuster, W., Goldan, P. D., Murphy, P. C., Warneke, C., Fowler, C., Montzka, S. A., Miller, B. R., Miller, L., Oltmans, S. J., Ryerson, T. B., Cooper, O. R., Stohl, A., and de Gouw, J. A.: Ozone variability and halogen oxidation within the Arctic and sub-Arctic springtime boundary layer, Atmospheric Chemistry and Physics, 10(21), 10223–10236, doi:10.5194/acp-10-10223-2010, 2010.

Giordano, M. R., Kalnajs, L. E., Goetz, J. D., Avery, A. M., Katz, E., May, N. W., Leemon, A., Mattson, C., Pratt, K. A., and DeCarlo, P. F.: The importance of blowing snow to halogen-containing aerosol in coastal Antarctica: influence of source region versus wind speed, Atmospheric Chemistry and Physics, 18(22), 16689–16711, doi:10.5194/acp-18-16689-2018, 2018.

GMAO: MERRA-2 inst3_3d_asm_Nv: 3d,3-Hourly,Instantaneous,Model-Level,Assimilation,Assimilated Meteorological Fields V5.12.4, Goddard Earth Sciences Data and Information Services Center (GES DISC), Greenbelt, MD, USA, doi:10.5067/WWQSXQ8IVFW8, accessed: 2020/08/01, 2015.

Goldberg, D. L., Anenberg, S. C., Griffin, D., McLinden, C. A., Lu, Z., and Streets, D. G.: Disentangling the Impact of the COVID-19 Lockdowns on Urban NO_2 From Natural Variability, Geophysical Research Letters, 47(17), e2020GL089269, doi:10.1029/2020GL089269, 2020.

Grainger, J. F. and Ring, J.: Anomalous Fraunhofer line profiles, Nature, 193, 762, doi:10.1038/193762a0, 1962.

Grannas, A. M., Jones, A. E., Dibb, J., Ammann, M., Anastasio, C., Beine, H. J., Bergin, M., Bottenheim, J., Boxe, C. S., Carver, G., Chen, G., Crawford, J. H., Dominé, F., Frey, M. M., Guzmán, M. I., Heard, D. E., Helmig, D., Hoffmann, M. R., Honrath, R. E., Huey, L. G., Hutterli, M., Jacobi, H. W., Klán, P., Lefer, B., McConnell, J., Plane, J., Sander, R., Savarino, J., Shepson, P. B., Simpson, W. R., Sodeau, J. R., von Glasow, R., Weller, R., Wolff, E. W., and Zhu, T.: An overview of snow photochemistry: evidence, mechanisms and impacts, Atmospheric Chemistry and Physics, 7(16), 4329–4373, doi:10.5194/acp-7-4329-2007, 2007.

Greenblatt, G. D., Orlando, J. J., Burkholder, J. B., and Ravishankara, A. R.: Absorption measurements of oxygen between 330 and 1140 nm, Journal of Geophysical Research: Atmospheres, 95(D11), 18577–18582, doi:10.1029/JD095iD11p18577, 1990.

Griffin, D., Walker, K. A., Conway, S., Kolonjari, F., Strong, K., Batchelor, R., Boone, C. D., Lin, D., Drummond, J. R., Fogal, P. F., Fu, D., Lindenmaier, R., Manney, G. L., and Weaver, D.: Multi-year comparisons of ground-based and space-borne Fourier transform spectrometers in the high Arctic between 2006 and 2013, Atmospheric Measurement Techniques, 10(9), 3273–3294, doi:10.5194/amt-10-3273-2017, 2017.

Griffin, D., Walker, K. A., Wohltmann, I., Dhomse, S. S., Rex, M., Chipperfield, M. P., Feng, W., Manney, G. L., Liu, J., and Tarasick, D.: Stratospheric ozone loss in the Arctic winters between 2005 and 2013 derived with ACE-FTS measurements, Atmospheric Chemistry and Physics, 19(1), 577–601, doi:10.5194/acp-19-577-2019, 2019a.

Griffin, D., Zhao, X., McLinden, C. A., Boersma, F., Bourassa, A., Dammers, E., Degenstein, D., Eskes, H., Fehr, L., Fioletov, V., Hayden, K., Kharol, S. K., Li, S.-M., Makar, P., Martin, R. V., Mihele, C., Mittermeier, R. L., Krotkov, N., Sneep, M., Lamsal, L. N., Linden, M. t., van Geffen, J., Veefkind, P., and Wolde, M.: High-Resolution Mapping of Nitrogen Dioxide With TROPOMI: First Results and Validation Over the Canadian Oil Sands, Geophysical Research Letters, 46(2), 1049–1060, doi:10.1029/2018GL081095, 2019b.

Griffin, D., McLinden, C., Racine, J., Moran, M., Fioletov, V., Pavlovic, R., and Eskes, H.: Assessing the impact of Corona-virus-19 on nitrogen dioxide levels over southern Ontario, Canada, Submitted to: Geophysical Research Letters, doi:10.1002/essoar.10503538.2, 2020.

Grooß, J.-U. and Müller, R.: Simulation of the record Arctic stratospheric ozone depletion in 2020, Submitted to: Journal of Geophysical Research: Atmospheres, doi: 10.1002/essoar.10503569.1, 2020.

Gruber, A., Su, C.-H., Zwieback, S., Crow, W., Dorigo, W., and Wagner, W.: Recent advances in (soil moisture) triple collocation analysis, International Journal of Applied Earth Observation and Geoinformation, 45, 200–211, doi:10.1016/j.jag.2015.09.002, 2016.

Gu, J., Chen, L., Yu, C., Li, S., Tao, J., Fan, M., Xiong, X., Wang, Z., Shang, H., and Su, L.: Ground-level NO_2 concentrations over China inferred from the satellite OMI and CMAQ model simulations, Remote Sensing, 9(6), 519, doi:10.3390/rs9060519, 2017.

Halfacre, J. W., Knepp, T. N., Shepson, P. B., Thompson, C. R., Pratt, K. A., Li, B., Peterson, P. K., Walsh, S. J., Simpson, W. R., Matrai, P. A., Bottenheim, J. W., Netcheva, S., Perovich, D. K., and Richter, A.: Temporal and spatial characteristics of ozone depletion events from measurements in the Arctic, Atmospheric Chemistry and Physics, 14(10), 4875–4894, doi:10.5194/acp-14-4875-2014, 2014.

Hall, D. K. and Riggs, G. A.: MODIS/Aqua Sea Ice Extent Daily L3 Global 1km EASE-Grid Day, Version 6 [March to May, 2016 to 2019], NASA National Snow and Ice Data Center, Boulder, Colorado USA, doi:10.5067/MODIS/MYD29P1D.006, accessed: 09/09/2019, 2015a.

Hall, D. K. and Riggs, G. A.: MODIS/Terra Sea Ice Extent Daily L3 Global 1km EASE-Grid Day, Version 6 [March to May, 2016 to 2019], NASA National Snow and Ice Data Center, Boulder, Colorado USA, doi:10.5067/MODIS/MOD29P1D.006, accessed: 09/09/2019, 2015b.

Hara, K., Osada, K., Matsunaga, K., Iwasaka, Y., Shibata, T., and Furuya, K.: Atmospheric inorganic chlorine and bromine species in Arctic boundary layer of the winter/spring, Journal of Geophysical Research: Atmospheres, 107(D18), AAC 4–1–AAC 4–15, doi:10.1029/2001JD001008, 2002.

Hara, K., Matoba, S., Hirabayashi, M., and Yamasaki, T.: Frost flowers and sea-salt aerosols over seasonal sea-ice areas in northwestern Greenland during winter–spring., Atmospheric Chemistry and Physics, 17(13), 8577–8598, doi:10.5194/acp-17-8577-2017, 2017.

Hara, K., Osada, K., Yabuki, M., Takashima, H., Theys, N., and Yamanouchi, T.: Important contributions of sea-salt aerosols to atmospheric bromine cycle in the Antarctic coasts, Scientific Reports, 8(1), 13852, doi:10.1038/s41598-018-32287-4, 2018.

Harkey, M., Holloway, T., Oberman, J., and Scotty, E.: An evaluation of CMAQ NO_2 using observed chemistry-meteorology correlations, Journal of Geophysical Research: Atmospheres, 120(22), 11775–11797, doi:10.1002/2015JD023316, 2015.

Hartley, W. N.: XXI.On the absorption of solar rays by atmospheric ozone, Journal of the Chemical Society, Transactions, 39, 111–128, doi:10.1039/CT8813900111, 1881a.

Hartley, W. N.: X.On the absorption spectrum of ozone, Journal of the Chemical Society, Transactions, 39, 57–60, doi:10.1039/CT8813900057, 1881b.

Helmig, D., Bocquet, F., Cohen, L., and Oltmans, S. J.: Ozone uptake to the polar snowpack at Summit, Greenland, Atmospheric Environment, 41(24), 5061–5076, doi:10.1016/j.atmosenv.2006.06.064, 2007a.

Helmig, D., Oltmans, S. J., Morse, T. O., and Dibb, J. E.: What is causing high ozone at Summit, Greenland?, Atmospheric Environment, 41(24), 5031–5043, doi:10.1016/j.atmosenv.2006.05.084, 2007b.

Helmig, D., Cohen, L. D., Bocquet, F., Oltmans, S., Grachev, A., and Neff, W.: Spring and summertime diurnal surface ozone fluxes over the polar snow at Summit, Greenland, Geophysical Research Letters, 36(8), doi:10.1029/2008GL036549, 2009.

Helmig, D., Boylan, P., Johnson, B., Oltmans, S., Fairall, C., Staebler, R., Weinheimer, A., Orlando, J., Knapp, D. J., Montzka, D. D., Flocke, F., Frieß, U., Sihler, H., and Shepson, P. B.: Ozone dynamics and snow-atmosphere exchanges during ozone depletion events at Barrow, Alaska, Journal of Geophysical Research: Atmospheres, 117(D20), doi:10.1029/2012JD017531, 2012.

Hendrick, F., Van Roozendael, M., Kylling, A., Petritoli, A., Rozanov, A., Sanghavi, S., Schofield, R., von Friedeburg, C., Wagner, T., Wittrock, F., Fonteyn, D., and De Maziére, M.: Intercomparison exercise between different radiative transfer models used for the interpretation of ground-based zenith-sky and multi-axis DOAS observations, Atmos Chem Phys, 6(1), 93–108, doi:10.5194/acp-6-93-2006, 2006.

Hendrick, F., Pommereau, J.-P., Goutail, F., Evans, R. D., Ionov, D., Pazmino, A., Kyrö, E., Held, G., Eriksen, P., Dorokhov, V., Gil, M., and Van Roozendael, M.: NDACC/SAOZ UV-visible total ozone measurements: improved retrieval and comparison with correlative ground-based and satellite observations, Atmospheric Chemistry and Physics, 11(12), 5975–5995, doi:10.5194/acp-11-5975-2011, 2011.

Hendrick, F., Müller, J.-F., Clémer, K., Wang, P., De Mazière, M., Fayt, C., Gielen, C., Hermans, C., Ma, J. Z., Pinardi, G., Stavrakou, T., Vlemmix, T., and Van Roozendael, M.: Four years of ground-based MAX-DOAS observations of HONO and NO_2 in the Beijing area, Atmospheric Chemistry and Physics, 14(2), 765–781, doi:10.5194/acp-14-765-2014, 2014.

Hendrick, F., Pinardi, G., Van Roozendael, M., Apituley, A., Piters, A., Richter, A., Wagner, T., Kreher, K., Frieß, U., and Lampel, J.: Deliverable D13: Intercomparison Campaign Planning Document, Fiducial Reference Measurements for Ground-Based DOAS Air-Quality Observations, URL `https://frm4doas.aeronomie.be/ProjectDir/Deliverables/FRM4DOAS_D13_Campaign_Planning_Document_20161021_final.pdf`, accessed: 2020/11/10, 2016.

Herman, J., Cede, A., Spinei, E., Mount, G., Tzortziou, M., and Abuhassan, N.: NO_2 column amounts from ground-based Pandora and MFDOAS spectrometers using the direct-sun DOAS technique: Intercomparisons and application to OMI validation, Journal of Geophysical Research: Atmospheres, 114(D13), doi:10.1029/2009JD011848, 2009.

Herman, J., Evans, R., Cede, A., Abuhassan, N., Petropavlovskikh, I., and McConville, G.: Comparison of ozone retrievals from the Pandora spectrometer system and Dobson spectrophotometer in Boulder, Colorado, Atmospheric Measurement Techniques, 8(8), 3407–3418, doi:10.5194/amt-8-3407-2015, 2015.

Herman, J., Abuhassan, N., Kim, J., Kim, J., Dubey, M., Raponi, M., and Tzortziou, M.: Underestimation of column NO_2 amounts from the OMI satellite compared to diurnally varying ground-based retrievals from multiple PANDORA spectrometer instruments, Atmospheric Measurement Techniques, 12(10), 5593–5612, doi:10.5194/amt-12-5593-2019, 2019.

Hermans, C., Vandaele, A. C., Fally, S., Carleer, M., Colin, R., Coquart, B., Jenouvrier, A., and Merienne, M.-F.: Absorption cross-section of the collision-induced bands of oxygen from the UV to the NIR, in: Camy-Peyret, C. and Vigasin, A. A. (editors), *Weakly* *interacting molecular pairs: unconventional absorbers of radiation in the atmosphere*, 193–202, Springer, 2003.

Hersbach, H., Bell, B., Berrisford, P., Biavati, G., Horányi, A., Muñoz Sabater, J., Nicolas, J., Peubey, C., Radu, R., Rozum, I., Schepers, D., Simmons, A., Soci, C., Dee, D., and Thépaut, J.-N.: ERA5 hourly data on pressure levels from 1979 to present, Copernicus Climate Change Service (C3S) Climate Data Store (CDS), doi:10.24381/cds.bd0915c6, accessed: 01/06/2020, 2018.

Hersbach, H., Bell, B., Berrisford, P., Hirahara, S., Hor/'anyi, A., Muñoz-Sabater, J., Nicolas, J., Peubey, C., Radu, R., Schepers, D., Simmons, A., Soci, C., Abdalla, S., Abellan, X., Balsamo, G., Bechtold, P., Biavati, G., Bidlot, J., Bonavita, M., De Chiara, G., Dahlgren, P., Dee, D., Diamantakis, M., Dragani, R., Flemming, J., Forbes, R., Fuentes, M., Geer, A., Haimberger, L., Healy, S., Hogan, R. J., Hólm, E., Janisková, M., Keeley, S., Laloyaux, P., Lopez, P., Lupu, C., Radnoti, G., de Rosnay, P., Rozum, I., Vamborg, F., Villaume, S., and Thépaut, J.-N.: The ERA5 global reanalysis, Quarterly Journal of the Royal Meteorological Society, 146(730), 1999–2049, doi:10.1002/qj.3803, 2020.

Holland, P. W. and Welsch, R. E.: Robust regression using iteratively reweighted least-squares, Communications in Statistics, 6(9), 813–827, doi:10.1080/03610927708827533, 1977.

Hommel, R., Eichmann, K.-U., Aschmann, J., Bramstedt, K., Weber, M., von Savigny, C., Richter, A., Rozanov, A., Wittrock, F., Khosrawi, F., Bauer, R., and Burrows, J. P.: Chemical ozone loss and ozone mini-hole event during the Arctic winter 2010/2011 as observed by SCIAMACHY and GOME-2, Atmospheric Chemistry and Physics, 14(7), 3247–3276, doi:10.5194/acp-14-3247-2014, 2014.

Hönninger, G., von Friedeburg, C., and Platt, U.: Multi axis differential optical absorption spectroscopy (MAX-DOAS), Atmospheric Chemistry and Physics, 4(1), 231–254, doi: 0.5194/acp-4-231-2004, 2004.

Honrath, R. E., Lu, Y., Peterson, M. C., Dibb, J. E., Arsenault, M. A., Cullen, N. J., and Steffen, K.: Vertical fluxes of NO_x, HONO, and HNO_3 above the snowpack at Summit, Greenland, Atmospheric Environment, 36(15-16), 2629–2640, doi: 10.1016/S1352-2310(02)00132-2, 2002.

Horiba: *TRIAX 180/190 Spectrometer Operation Manual*, Jobin Yvon Technology/Horiba Scientific, 2014.

Hossaini, R., Chipperfield, M. P., Montzka, S. A., Rap, A., Dhomse, S., and Feng, W.: Efficiency of short-lived halogens at influencing climate through depletion of stratospheric ozone, Nature Geoscience, 8(3), 186–190, doi:10.1038/ngeo2363, 2015.

Huang, J. and Jaeglé, L.: Wintertime enhancements of sea salt aerosol in polar regions consistent with a sea ice source from blowing snow, Atmospheric Chemistry and Physics, 17(5), 3699–3712, doi:10.5194/acp-17-3699-2017, 2017.

Huang, J., Jaeglé, L., and Shah, V.: Using CALIOP to constrain blowing snow emissions of sea salt aerosols over Arctic and Antarctic sea ice., Atmospheric Chemistry and Physics, 18(22), doi:10.5194/acp-18-16253-2018, 2018.

Hubert, D., Lambert, J.-C., Verhoelst, T., Granville, J., Keppens, A., Baray, J.-L., Cortesi, U., Degenstein, D. A., Froidevaux, L., Godin-Beekmann, S., Hoppel, K. W., Johnson, B. J., Kyrölä, E., Leblanc, T., Lichtenberg, G., Marchand, M., McElroy, C. T., Murtagh, D., Nakane, H., Portafaix, T., Querel, R., Russell III, J. M., Salvador, J., Smit, H. G. J., Stebel, K., Steinbrecht, W., Strawbridge, K. B., Stübi, R., Swart, D. P. J., Taha, G., Tarasick, D. W., Thompson, A. M., Urban, J., van Gijsel, J. A. E., Van Malderen, R., von der Gathen, P., Walker, K. A., Wolfram, E., and Zawodny, J. M.: Ground-based assessment of the bias and long-term stability of 14 limb and occultation ozone profile data records, Atmospheric Measurement Techniques, 9(6), 2497–2534, doi:10.5194/amt-9-2497-2016, 2016.

Ialongo, I., Herman, J., Krotkov, N., Lamsal, L., Boersma, K. F., Hovila, J., and Tamminen, J.: Comparison of OMI NO_2 observations and their seasonal and weekly cycles with ground-based measurements in Helsinki, Atmospheric Measurement Techniques, 9(10), 5203–5212, doi:10.5194/amt-9-5203-2016, 2016.

Ialongo, I., Virta, H., Eskes, H., Hovila, J., and Douros, J.: Comparison of TROPOMI/Sentinel-5 Precursor NO_2 observations with ground-based measurements in Helsinki, Atmospheric Measurement Techniques, 13(1), 205–218, doi:10.5194/amt-13-205-2020, 2020.

Inness, A., Chabrillat, S., Flemming, J., Huijnen, V., Langenrock, B., Nicolas, J., Polichtchouk, I., and Razinger, M.: Exceptionally Low Arctic Stratospheric Ozone in Spring 2020 as Seen in the CAMS Reanalysis, Journal of Geophysical Research: Atmospheres, 125(23), e2020JD033563, doi:10.1029/2020JD033563, 2020.

IPCC: Climate Change 2013: The Physical Science Basis. Contribution of Working Group

I to the Fifth Assessment Report of the Intergovernmental Panel on Climate Change, 2013.

Jacob, D. J.: *Introduction to Atmospheric Chemistry*, Princeton University Press, 1999.

Jacobi, H.-W., Morin, S., and Bottenheim, J. W.: Observation of widespread depletion of ozone in the springtime boundary layer of the central Arctic linked to mesoscale synoptic conditions, Journal of Geophysical Research: Atmospheres, 115(D17), doi: 10.1029/2010JD013940, 2010.

Jin, J., Ma, J., Lin, W., Zhao, H., Shaiganfar, R., Beirle, S., and Wagner, T.: MAX-DOAS measurements and satellite validation of tropospheric NO_2 and SO_2 vertical column densities at a rural site of North China, Atmospheric Environment, 133, 12–25, doi:10.1016/j.atmosenv.2016.03.031, 2016.

Jones, A. E., Weller, R., Anderson, P. S., Jacobi, H.-W., Wolff, E. W., Schrems, O., and Miller, H.: Measurements of NO_x emissions from the Antarctic snowpack, Geophysical Research Letters, 28(8), 1499–1502, doi:10.1029/2000GL011956, 2001.

Jones, A. E., Anderson, P. S., Begoin, M., Brough, N., Hutterli, M. A., Marshall, G. J., Richter, A., Roscoe, H. K., and Wolff, E. W.: BrO, blizzards, and drivers of polar tropospheric ozone depletion events, Atmospheric Chemistry and Physics, 9(14), 4639–4652, doi:10.5194/acp-9-4639-2009, 2009.

Jones, A. E., Anderson, P. S., Wolff, E. W., Roscoe, H. K., Marshall, G. J., Richter, A., Brough, N., and Colwell, S. R.: Vertical structure of Antarctic tropospheric ozone depletion events: characteristics and broader implications, Atmospheric Chemistry and Physics, 10(16), 7775–7794, doi:10.5194/acp-10-7775-2010, 2010.

Kaleschke, L., Richter, A., Burrows, J., Afe, O., Heygster, G., Notholt, J., Rankin, A. M., Roscoe, H. K., Hollwedel, J., Wagner, T., and Jacobi, H.-W.: Frost flowers on sea ice as a source of sea salt and their influence on tropospheric halogen chemistry, Geophysical Research Letters, 31(16), doi:10.1029/2004GL020655, 2004.

Kalnajs, L. E. and Avallone, L. M.: Frost flower influence on springtime boundary-layer ozone depletion events and atmospheric bromine levels, Geophysical Research Letters, 33(10), doi:10.1029/2006GL025809, 2006.

Kenagy, H. S., Sparks, T. L., Ebben, C. J., Wooldrige, P. J., Lopez-Hilfiker, F. D., Lee, B. H., Thornton, J. A., McDuffie, E. E., Fibiger, D. L., Brown, S. S., Montzka, D. D., Weinheimer, A. J., Schroder, J. C., Campuzano-Jost, P., Day, D. A., Jimenez, J. L., Dibb, J. E., Campos, T., Shah, V., Jaeglé, L., and Cohen, R. C.: NO_x Lifetime and NO_y Partitioning During WINTER, Journal of Geophysical Research: Atmospheres, 123(17), 9813–9827, doi:10.1029/2018JD028736, 2018.

Kerr, J., McElroy, C., and Olafson, R.: Measurements of ozone with the Brewer ozone spectrophotometer, in: London, J. (editor), *Proceedings of the Quadrennial Ozone Symposium*, 74–79, 1981.

Kerr, J. B.: New methodology for deriving total ozone and other atmospheric variables from Brewer spectrophotometer direct sun spectra, Journal of Geophysical Research: Atmospheres, 107(D23), ACH 22–1–ACH 22–17, doi:10.1029/2001JD001227, 2002.

Kerzenmacher, T., Wolff, M. A., Strong, K., Dupuy, E., Walker, K. A., Amekudzi, L. K., Batchelor, R. L., Bernath, P. F., Berthet, G., Blumenstock, T., Boone, C. D., Bramstedt, K., Brogniez, C., Brohede, S., Burrows, J. P., Catoire, V., Dodion, J., Drummond, J. R., Dufour, D. G., Funke, B., Fussen, D., Goutail, F., Griffith, D. W. T., Haley, C. S., Hendrick, F., Höpfner, M., Huret, N., Jones, N., Kar, J., Kramer, I., Llewellyn, E. J., López-Puertas, M., Manney, G., McElroy, C. T., McLinden, C. A., Melo, S., Mikuteit, S., Murtagh, D., Nichitiu, F., Notholt, J., Nowlan, C., Piccolo, C., Pommereau, J.-P., Randall, C., Raspollini, P., Ridolfi, M., Richter, A., Schneider, M., Schrems, O., Silicani, M., Stiller, G. P., Taylor, J., Tétard, C., Toohey, M., Vanhellemont, F., Warneke, T., Zawodny, J. M., and Zou, J.: Validation of NO_2 and NO from the Atmospheric Chemistry Experiment (ACE), Atmospheric Chemistry and Physics, 8(19), 5801–5841, doi:10.5194/acp-8-5801-2008, 2008.

Kerzenmacher, T. E., Walker, K. A., Strong, K., Berman, R., Bernath, P. F., Boone, C. D., Drummond, J. R., Fast, H., Fraser, A., MacQuarrie, K., Midwinter, C., Sung, K., McElroy, C. T., Mittermeier, R. L., Walker, J., and Wu, H.: Measurements of O_3, NO_2 and temperature during the 2004 Canadian Arctic ACE Validation Campaign, Geophysical Research Letters, 32(16), L16S07, doi:10.1029/2005GL023032, 2005.

Kinzel, J., Fennig, K., Schröder, M., Andersson, A., Bumke, K., and Hollmann, R.: Decomposition of random errors inherent to HOAPS-3.2 near-surface humidity estimates using multiple triple collocation analysis, Journal of Atmospheric and Oceanic Technology, 33(7), 1455–1471, doi:10.1175/JTECH-D-15-0122.1, 2016.

Kirpes, R. M., B, D., May, N. W., Fraund, M., Barget, A. J., Moffet, R. C., Ault, A. P., and Pratt, K. A.: Wintertime Arctic Sea Spray Aerosol Composition Controlled by Sea

Ice Lead Microbiology, ACS Central Science, 5(11), 1760–1767, doi:10.1021/acscentsci.9b00541, 2019.

Koelemeijer, R. B. A., de Haan, J. F., and Stammes, P.: A database of spectral surface reflectivity in the range 335-772 nm derived from 5.5 years of GOME observations, Journal of Geophysical Research: Atmospheres, 108(D2), doi:10.1029/2002JD002429, 2003.

Kreher, K., Van Roozendael, M., Hendrick, F., Apituley, A., Dimitropoulou, E., Frieß, U., Richter, A., Wagner, T., Lampel, J., Abuhassan, N., Ang, L., Anguas, M., Bais, A., Benavent, N., Bösch, T., Bognar, K., Borovski, A., Bruchkouski, I., Cede, A., Chan, K. L., Donner, S., Drosoglou, T., Fayt, C., Finkenzeller, H., Garcia-Nieto, D., Gielen, C., Gómez-Martín, L., Hao, N., Henzing, B., Herman, J. R., Hermans, C., Hoque, S., Irie, H., Jin, J., Johnston, P., Khayyam Butt, J., Khokhar, F., Koenig, T. K., Kuhn, J., Kumar, V., Liu, C., Ma, J., Merlaud, A., Mishra, A. K., Müller, M., Navarro-Comas, M., Ostendorf, M., Pazmino, A., Peters, E., Pinardi, G., Pinharanda, M., Piters, A., Platt, U., Postylyakov, O., Prados-Roman, C., Puentedura, O., Querel, R., Saiz-Lopez, A., Schönhardt, A., Schreier, S. F., Seyler, A., Sinha, V., Spinei, E., Strong, K., Tack, F., Tian, X., Tiefengraber, M., Tirpitz, J.-L., van Gent, J., Volkamer, R., Vrekoussis, M., Wang, S., Wang, Z., Wenig, M., Wittrock, F., Xie, P. H., Xu, J., Yela, M., Zhang, C., and Zhao, X.: Intercomparison of NO_2, O_4, O_3 and HCHO slant column measurements by MAX-DOAS and zenith-sky UV–visible spectrometers during CINDI-2, Atmospheric Measurement Techniques, 13(5), 2169–2208, doi:10.5194/amt-13-2169-2020, 2020.

Kremser, S., Thomason, L. W., von Hobe, M., Hermann, M., Deshler, T., Timmreck, C., Toohey, M., Stenke, A., Schwarz, J. P., Weigel, R., Fueglistaler, S., Prata, F. J., Vernier, H., J.-Pand Schlager, Barnes, J. E., Antuña-Marrero, J.-C., Fairlie, D., Palm, M., Mahieu, E., Notholt, J., Rex, M., Bingen, C., Vanhellemont, F., Bourassa, A., Plane, J. M. C., Klocke, D., Carn, S. A., Clarisse, L., Trickl, T., Neely, R., James, A. D., Rieger, L., Wilson, J. C., and Meland, B.: Stratospheric aerosol – Observations, processes, and impact on climate, Reviews of Geophysics, 54(2), 278–335, doi:10.1002/2015RG000511, 2016.

Kurucz, R. L.: Solar Flux Atlas from 296 to 1300 nm, National Solar Observatory Atlas, 1, 1984.

Kuttippurath, J., Godin-Beekmann, S., Lefèvre, K., Nikulin, G., Santee, M. L., and Froidevaux, L.: Record-breaking ozone loss in the Arctic winter 2010/2011: comparison with 1996/1997, Atmospheric Chemistry and Physics, 12(15), 7073–7085, doi:10.5194/acp-12-7073-2012, 2012.

Kwok, R.: Arctic sea ice thickness, volume, and multiyear ice coverage: losses and coupled variability (1958–2018), Environmental Research Letters, 13(10), 105005, doi:10.1088/1748-9326/aae3ec, 2018.

Lambert, J.-C., Granville, J., Van Roozendael, M., Sarkissian, A., Goutail, F., Müller, J.-F., Pommereau, J.-P., and Russel, J. M.: A climatology of NO_2 profile for improved air mass factors for ground-based vertical column measurements, in: Harris, N. R. P., Guirlet, M., and Amanatidis, G. T. (editors), *Stratospheric Ozone 1999, Air Pollution Research Report 73 (CEC DG XII)*, 703–706, 1999.

Lambert, J.-C., Granville, J., Van Roozendael, M., Müller, J.-F., Goutail, F., Pommereau, J.-P., Sarkissian, A., Johnston, P. V., and Russell III, J. M.: Global behavior of atmospheric NO_2 as derived from the integrated use of satellite, ground-based network and balloon observations, in: *Atmospheric Ozone - 19th Quadrennial Ozone Symposium, Sapporo, Japan*, 201–202, 2000.

Lamsal, L. N., Martin, R. V., van Donkelaar, A., Steinbacher, M., Celarier, E. A., Bucsela, E., Dunlea, E. J., and Pinto, J. P.: Ground-level nitrogen dioxide concentrations inferred from the satellite-borne Ozone Monitoring Instrument, Journal of Geophysical Research: Atmospheres, 113(D16), doi:10.1029/2007JD009235, 2008.

Lamsal, L. N., Krotkov, N. A., Celarier, E. A., Swartz, W. H., Pickering, K. E., Bucsela, E. J., Gleason, J. F., Martin, R. V., Philip, S., Irie, H., Cede, A., Herman, J., Weinheimer, A., Szykman, J. J., and Knepp, T. N.: Evaluation of OMI operational standard NO_2 column retrievals using in situ and surface-based NO_2 observations, Atmospheric Chemistry and Physics, 14(21), 11587–11609, doi:10.5194/acp-14-11587-2014, 2014.

Lamsal, L. N., Janz, S. J., Krotkov, N. A., Pickering, K. E., Spurr, R. J. D., Kowalewski, M. G., Loughner, C. P., Crawford, J. H., Swartz, W. H., and Herman, J. R.: High-resolution NO_2 observations from the Airborne Compact Atmospheric Mapper: Retrieval and validation, Journal of Geophysical Research: Atmospheres, 122(3), 1953–1970, doi:10.1002/2016JD025483, 2017.

Lary, D. J.: Catalytic destruction of stratospheric ozone, Journal of Geophysical Research: Atmospheres, 102(D17), 21515–21526, doi:10.1029/97JD00912, 1997.

Lawrence, Z. D., Perlwitz, J., Butler, A. H., Manney, G. L., Newman, P. A., Lee, S. H., and Nash, E. R.: The Remarkably Strong Arctic Stratospheric Polar Vortex of Winter 2020: Links to Record-Breaking Arctic Oscillation and Ozone Loss, Journal of Geophysical Research: Atmospheres, 125(22), e2020JD033271, doi:10.1029/2020JD033271, 2020.

Leck, C., Norman, M., Bigg, E. K., and Hillamo, R.: Chemical composition and sources of the high Arctic aerosol relevant for cloud formation, Journal of Geophysical Research: Atmospheres, 107(D12), AAC 1–1–AAC 1–17, doi:10.1029/2001JD001463, 2002.

Lee, A., Roscoe, H., Oldham, D., Squires, J., Sarkissian, A., Pommereau, J.-P., and Gardiner, B.: Improvements to the accuracy of measurements of NO_2 by zenith-sky visible spectrometers, Journal of Quantitative Spectroscopy and Radiative Transfer, 52(5), 649–657, doi:0022-4073(94)90031-0, 1994.

Legrand, M., Yang, X., Preunkert, S., and Theys, N.: Year-round records of sea salt, gaseous, and particulate inorganic bromine in the atmospheric boundary layer at coastal (Dumont d'Urville) and central (Concordia) East Antarctic sites, Journal of Geophysical Research: Atmospheres, 121(2), 997–1023, doi:10.1002/2015JD024066, 2016.

Leue, C., Wenig, M., Wagner, T., Klimm, O., Platt, U., and Jähne, B.: Quantitative analysis of NO_x emissions from Global Ozone Monitoring Experiment satellite image sequences, Journal of Geophysical Research: Atmospheres, 106(D6), 5493–5505, doi:10.1029/2000JD900572, 2001.

Li, L. and Pomeroy, J. W.: Estimates of threshold wind speeds for snow transport using meteorological data, Journal of Applied Meteorology, 36(3), 205–213, doi:10.1175/1520-0450(1997)036⟨0205:EOTWSF⟩2.0.CO;2, 1997.

Liao, J., Huey, L. G., Tanner, D. J., Flocke, F. M., Orlando, J. J., Neuman, J. A., Nowak, J. B., Weinheimer, A. J., Hall, S. R., Smith, J. N., Fried, A., Staebler, R. M., Wang, Y., Koo, J.-H., Cantrell, C. A., Weibring, P., Walega, J., Knapp, D. J., Shepson, P. B., and Stephens, C. R.: Observations of inorganic bromine (HOBr, BrO, and Br_2) speciation at Barrow, Alaska, in spring 2009, Journal of Geophysical Research: Atmospheres, 117(D14), D00R16, doi:10.1029/2011JD016641, 2012.

Liao, J., Huey, L. G., Liu, Z., Tanner, D. J., Cantrell, C. A., Orlando, J. J., Flocke, F. M., Shepson, P. B., Weinheimer, A. J., Hall, S. R., Ullmann, K., Beine, H. J., Wang, Y., Ingall, E. D., Stephens, C. R., Hornbrook, R. S., Apel, E. C., Riemer, D., Fried, A., Mauldin, R. L., Smith, J. N., Staebler, R. M., Neuman, J. A., and Nowak, J. B.: High levels of molecular chlorine in the Arctic atmosphere, Nature Geoscience, 7(2), 91–94, doi:10.1038/ngeo2046, 2014.

Lieb-Lappen, R. M. and Obbard, R. W.: The role of blowing snow in the activation of bromine over first-year Antarctic sea ice, Atmospheric Chemistry and Physics, 15(13), 7537–7545, doi:10.5194/acp-15-7537-2015, 2015.

Lindenmaier, R., Strong, K., Batchelor, R. L., Bernath, P. F., Chabrillat, S., Chipperfield, M. P., Daffer, W. H., Drummond, J. R., Feng, W., Jonsson, A. I., Kolonjari, F., Manney, G. L., McLinden, C., Ménard, R., and Walker, K. A.: A study of the Arctic NO_y budget above Eureka, Canada, Journal of Geophysical Research: Atmospheres, 116(D23302), doi:10.1029/2011JD016207, 2011.

Lindenmaier, R., Strong, K., Batchelor, R. L., Chipperfield, M. P., Daffer, W. H., Drummond, J. R., Duck, T. J., Fast, H., Feng, W., Fogal, P. F., Kolonjari, F., Manney, G. L., Manson, A., Meek, C., Mittermeier, R. L., Nott, G. J., Perro, C., and Walker, K. A.: Unusually low ozone, HCl, and HNO_3 column measurements at Eureka, Canada during winter/spring 2011, Atmospheric Chemistry and Physics, 12(8), 3821–3835, doi:10.5194/acp-12-3821-2012, 2012.

Llewellyn, E. J., Lloyd, N. D., Degenstein, D. A., Gattinger, R. L., Petelina, S. V., Bourassa, A. E., Wiensz, J. T., Ivanov, E. V., McDade, I. C., Solheim, B. H., McConnell, J. C., Haley, C. S., von Savigny, C., Sioris, C. E., McLinden, C. A., Griffioen, E., Kaminski, J., Evans, W. F. J., Puckrin, E., Strong, K., Wehrle, V., Hum, R. H., Kendall, D. J. W., Matsushita, J., Murtagh, D. P., Brohede, S., Stegman, J., Witt, G., Barnes, G., Payne, W. F., Piche, L., Smith, K., Warshaw, G., Deslauniers, D. L., Marchand, P., Richardson, E. H., King, R. A., Wevers, I., McCreath, W., Kyrola, E., Oikarinen, L., Leppelmeier, G. W., Auvinen, H., Megie, G., Hauchecorne, A., Lefevre, F., de La Noe, J., Ricaud, P., Frisk, U., Sjoberg, F., von Scheele, F., and Nordh, L.: The OSIRIS instrument on the Odin spacecraft, Canadian Journal of Physics, 82(6), 411–422, doi:10.1139/p04-005, 2004.

Loew, A. and Schlenz, F.: A dynamic approach for evaluating coarse scale satellite soil moisture products, Hydrology and Earth System Sciences, 15(1), 75–90, doi:10.5194/hess-15-75-2011, 2011.

Loew, A., Bell, W., Brocca, L., Bulgin, C. E., Burdanowitz, J., Calbet, X., Donner, R. V., Ghent, D., Gruber, A., Kaminski, T., Kinzel, J., Klepp, C., Lambert, J.-C., Schaepman-Strub, G., Schröder, M., and Verhoelst, T.: Validation practices for satellite-based Earth observation data across communities, Reviews of Geophysics, 55(3), 779–817, doi:10.1002/2017RG000562, 2017.

Lovelock, J. E., Maggs, R. J., and Wade, R. J.: Halogenated hydrocarbons in and over the Atlantic, Nature, 241(5386), 194–196, doi:10.1038/241194a0, 1973.

Ma, J. Z., Beirle, S., Jin, J. L., Shaiganfar, R., Yan, P., and Wagner, T.: Tropospheric NO_2 vertical column densities over Beijing: results of the first three years of ground-based MAX-DOAS measurements (2008-2011) and satellite validation, Atmospheric Chemistry and Physics, 13(3), 1547–1567, doi:10.5194/acp-13-1547-2013, 2013.

Mankin, W. G., Coffey, M. T., Goldman, A., Schoeberl, M. R., Lait, L. R., and Newman, P. A.: Airborne measurements of stratospheric constituents over the Arctic in the winter of 1989, Geophysical Research Letters, 17(4), 473–476, doi:10.1029/GL017i004p00473, 1990.

Manney, G. L. and Lawrence, Z. D.: The major stratospheric final warming in 2016: dispersal of vortex air and termination of Arctic chemical ozone loss, Atmospheric Chemistry and Physics, 16(23), 15371–15396, doi:10.5194/acp-16-15371-2016, 2016.

Manney, G. L., Zurek, R. W., O'Neill, A., and Swinbank, R.: On the Motion of Air through the Stratospheric Polar Vortex, Journal of the Atmospheric Sciences, 51(20), 2973–2994, doi:10.1175/1520-0469(1994)051\$⟨\$2973:OTMOAT\$⟩\$2.0.CO;2, 1994.

Manney, G. L., Froidevaux, L., Santee, M. L., Zurek, R. W., and Waters, J. W.: MLS observations of Arctic ozone loss in 1996-97, Geophysical Research Letters, 24(22), 2697–2700, doi:10.1029/97GL52827, 1997.

Manney, G. L., Santee, M. L., Froidevaux, L., Hoppel, K., Livesey, N. J., and Waters, J. W.: EOS MLS observations of ozone loss in the 2004-2005 Arctic winter, Geophysical Research Letters, 33(4), doi:10.1029/2005GL024494, 2006.

Manney, G. L., Daffer, W. H., Zawodny, J. M., Bernath, P. F., Hoppel, K. W., Walker, K. A., Knosp, B. W., Boone, C., Remsberg, E. E., Santee, M. L., Harvey, V. L., Pawson, S., Jackson, D. R., Deaver, L., McElroy, C. T., McLinden, C. A., Drummond, J. R., Pumphrey, H. C., Lambert, A., Schwartz, M. J., Froidevaux, L., McLeod, S., Takacs, L. L., Suarez, M. J., Trepte, C. R., Cuddy, D. C., Livesey, N. J., Harwood, R. S., and Waters, J. W.: Solar occultation satellite data and derived meteorological products: Sampling issues and comparisons with Aura Microwave Limb Sounder, Journal of Geophysical Research: Atmospheres, 112(D24), doi:10.1029/2007JD008709, 2007.

Manney, G. L., Hegglin, M. I., Daffer, W. H., Santee, M. L., Ray, E. A., Pawson, S., Schwartz, M. J., Boone, C. D., Froidevaux, L., Livesey, N. J., Read, W. G., and Walker, K. A.: Jet characterization in the upper troposphere/lower stratosphere (UTLS): applications to climatology and transport studies, Atmospheric Chemistry and Physics, 11(12), 6115–6137, doi:10.5194/acp-11-6115-2011, 2011a.

Manney, G. L., Santee, M. L., Rex, M., Livesey, N. J., Pitts, M. C., Veefkind, P., Nash, E. R., Wohltmann, I., Lehmann, R., Froidevaux, L., Poole, L. R., Schoeberl, M. R., Haffner, D. P., Davies, J., Dorokhov, V., Gernandt, H., Johnson, B., Kivi, R., Kyrö, E. N., Larsen, Levelt, P. F., Makshtas, A., McElroy, C. T., Nakajima, H., Parrondo, M. C., Tarasick, D. W., von der Gathen, P., Walker, K. A., and Zinoviev, N. S.: Unprecedented Arctic ozone loss in 2011, Nature, 478(7370), 469–475, doi:10.1038/nature10556, 2011b.

Manney, G. L., Lawrence, Z. D., Santee, M. L., Read, W. G., Livesey, N. J., Lambert, A., Froidevaux, L., Pumphrey, H. C., and Schwartz, M. J.: A minor sudden stratospheric warming with a major impact: Transport and polar processing in the 2014/2015 Arctic winter, Geophysical Research Letters, 42(18), 7808–7816, doi:10.1002/2015GL065864, 2015.

Manney, G. L., Hegglin, M. I., Lawrence, Z. D., Wargan, K., Millán, L. F., Schwartz, M. J., Santee, M. L., Lambert, A., Pawson, S., Knosp, B. W., Fuller, R. A., and Daffer, W. H.: Reanalysis comparisons of upper tropospheric–lower stratospheric jets and multiple tropopauses, Atmospheric Chemistry and Physics, 17(18), 11541–11566, doi: 10.5194/acp-17-11541-2017, 2017.

Manney, G. L., Livesey, N. J., Santee, M. L., Froidevaux, L., Lambert, A., Lawrence, Z., Millán, L. F., Neu, J. L., Read, W. G., Schwartz, M. J., and Fuller, R. A.: Record-low Arctic stratospheric ozone in 2020: MLS observations of chemical processes and comparisons with previous extreme winters, Geophysical Research Letters, 47(16), e2020GL089063, doi:10.1029/2020GL089063, 2020.

Martin, R. V., Jacob, D. J., Chance, K., Kurosu, T. P., Palmer, P. I., and Evans, M. J.: Global inventory of nitrogen oxide emissions constrained by space-based observations of NO_2 columns, Journal of Geophysical Research: Atmospheres, 108(D17), doi:10.1029/2003JD003453, 2003.

Martins, D. K., Najjar, R. G., Tzortziou, M., Abuhassan, N., Thompson, A. M., and Kollonige, D. E.: Spatial and temporal variability of ground and satellite column measurements of NO_2 and O_3 over the Atlantic Ocean during the Deposition of Atmospheric Nitrogen to Coastal Ecosystems Experiment, Journal of Geophysical Research: Atmospheres, 121(23), 14175–14187, doi:10.1002/2016JD024998, 2016.

Matthias, V., Dörnbrack, A., and Stober, G.: The extraordinarily strong and cold polar vortex in the early northern winter 2015/2016, Geophysical Research Letters, 43(23), 12,287–12,294, doi:10.1002/2016GL071676, 2016.

May, N. W., Quinn, P. K., McNamara, S. M., and Pratt, K. A.: Multiyear study of the dependence of sea salt aerosol on wind speed and sea ice conditions in the coastal Arctic, Journal of Geophysical Research: Atmospheres, 121(15), 9208–9219, doi:10.1002/2016JD025273, 2016.

Mayer, B. and Kylling, A.: Technical note: The libRadtran software package for radiative transfer calculations - description and examples of use, Atmospheric Chemistry and Physics, 5(7), 1855–1877, doi:10.5194/acp-5-1855-2005, 2005.

McColl, K. A., Vogelzang, J., Konings, A. G., Entekhabi, D., Piles, M., and Stoffelen, A.: Extended triple collocation: Estimating errors and correlation coefficients with respect to an unknown target, Geophysical Research Letters, 41(17), 6229–6236, doi:10.1002/2014GL061322, 2014.

McCullough, E. M., Sica, R. J., Drummond, J. R., Nott, G., Perro, C., Thackray, C. P., Hopper, J., Doyle, J., Duck, T. J., and Walker, K. A.: Depolarization calibration and measurements using the CANDAC Rayleigh–Mie–Raman lidar at Eureka, Canada, Atmospheric Measurement Techniques, 10(11), 4253–4277, doi:10.5194/amt-10-4253-2017, 2017.

McCullough, E. M., Drummond, J. R., and Duck, T. J.: Lidar measurements of thin laminations within Arctic clouds, Atmospheric Chemistry and Physics, 19(7), 4595–4614, doi:10.5194/acp-19-4595-2019, 2019.

McElroy, C. T., Nowlan, C. R., Drummond, J. R., Bernath, P. F., Barton, D. V., Dufour, D. G., Midwinter, C., Hall, R. B., Ogyu, A., Ullberg, A., Wardle, D. I., Kar, J., Zou, J., Nichitiu, F., Boone, C. D., Walker, K. A., and Rowlands, N.: The ACE-MAESTRO instrument on SCISAT: description, performance, and preliminary results, Applied Optics, 46(20), 4341–4356, doi:10.1364/AO.46.004341, 2007.

McElroy, M. B., Salawitch, R. J., Wofsy, S. C., and Logan, J. A.: Reductions of Antarctic ozone due to synergistic interactions of chlorine and bromine, Nature, 321(6072), 759–762, doi:10.1038/321759a0, 1986.

McLinden, C. A., Olsen, S. C., Hannegan, B., Wild, O., Prather, M. J., and Sundet, J.: Stratospheric ozone in 3-D models: A simple chemistry and the cross-tropopause flux, Journal of Geophysical Research: Atmospheres, 105(D11), 14653–14665, doi:10.1029/2000JD900124, 2000.

McLinden, C. A., Haley, C. S., and Sioris, C. E.: Diurnal effects in limb scatter observations, J Geophys Res Atmos, 111(D14302), doi:10.1029/2005JD006628, 2006.

Meller, R. and Moortgat, G. K.: Temperature dependence of the absorption cross sections of formaldehyde between 223 and 323 K in the wavelength range 225-375 nm, Journal of Geophysical Research: Atmospheres, 105(D6), 7089–7101, doi:10.1029/1999JD901074, 2000.

Melo, S. M. L., Farahani, E., Strong, K., Bassford, M. R., Preston, K. E., and McLinden, C. A.: NO_2 vertical profiles retrieved from ground-based measurements during spring 1999 in the Canadian Arctic, Advances in Space Research, 34(4), 786–792, doi:10.1016/j.asr.2003.08.065, 2004.

Melo, S. M. L., Strong, K., Bassford, M. R., Preston, K. E., McElroy, C. T., Rozanov, E. V., and Egorova, T.: Retrieval of stratospheric NO_2 vertical profiles from ground-based zenith-sky DOAS measurements: Results for the MANTRA 1998 field campaign, Atmosphere-Ocean, 43(4), 339–350, doi:10.3137/ao.430405, 2005.

Merten, A., Tschritter, J., and Platt, U.: Design of differential optical absorption spectroscopy long-path telescopes based on fiber optics, Applied Optics, 50(5), 738–754, doi:10.1364/AO.50.000738, 2011.

Molina, L. T. and Molina, M. J.: Production of chlorine oxide (Cl_2O_2) from the self-reaction of the chlorine oxide (ClO) radical, Journal of Physical Chemistry, 91(2), 433–436, doi:10.1021/j100286a035, 1987.

Molina, M. J. and Rowland, F. S.: Stratospheric sink for chlorofluoromethanes: chlorine atom-catalysed destruction of ozone, Nature, 249(28), 810–812, doi:doi.org/10.1038/249810a0, 1974.

Montzka, S. A., Dutton, G. S., Yu, P., Ray, E., Portmann, R. W., Daniel, J. S., Kuijpers, L., Hall, B. D., Mondeel, D., Siso, C., Nance, J. D., Rigby, M., Manning, A. J., Hu, L., Moore, F., Miller, B. R., and Elkins, J. W.: An unexpected and persistent increase in global emissions of ozone-depleting CFC-11, Nature, 557(7705), 413–417, doi:10.1038/s41586-018-0106-2, 2018.

Murtagh, D., Frisk, U., Merino, F., Ridal, M., Jonsson, A., Stegman, J., Witt, G., Eriksson, P., Jimnez, C., Megie, G., de La Noe, J., Ricaud, P., Baron, P., Pardo, J. R., Hauchcorne, A., Llewellyn, E. J., Degenstein, D. A., Gattinger, R. L., Lloyd, N. D., Evans,

W. F. J., McDade, I. C., Haley, C. S., Sioris, C., von Savigny, C., Solheim, B. H., McConnell, J. C., Strong, K., Richardson, E. H., Leppelmeier, G. W., Kyrola, E., Auvinen, H., and Oikarinen, L.: An overview of the Odin atmospheric mission, Canadian Journal of Physics, 80(4), 309–319, doi:10.1139/p01-157, 2002.

Nasse, J.-M., Eger, P. G., Pöhler, D., Schmitt, S., Frieß, U., and Platt, U.: Recent improvements of long-path DOAS measurements: impact on accuracy and stability of short-term and automated long-term observations, Atmospheric Measurement Techniques, 12(8), 4149–4169, doi:10.5194/amt-12-4149-2019, 2019.

Nawrot, A. P., Migała, K., Luks, B., Pakszys, P., and Głowacki, P.: Chemistry of snow cover and acidic snowfall during a season with a high level of air pollution on the Hans Glacier, Spitsbergen, Polar Science, 10(3), 249–261, doi:10.1016/j.polar.2016.06.003, 2016.

Newchurch, M. J., Allen, M., Gunson, M. R., Salawitch, R. J., Collins, G. B., Huston, K. H., Abbas, M. M., Abrams, M. C., Chang, A. Y., Fahey, D. W., Gao, R. S., Irion, F. W., Loewenstein, M., Manney, G. L., Michelsen, H. A., Podolske, J. R., Rinsland, C. P., and Zander, R.: Stratospheric NO and NO_2 abundances from ATMOS Solar-Occultation Measurements, Geophysical Research Letters, 23(17), 2373–2376, doi:10.1029/96GL01196, 1996.

Newman, P. A., Gleason, J. F., McPeters, R. D., and Stolarski, R. S.: Anomalously low ozone over the Arctic, Geophysical Research Letters, 24(22), 2689–2692, doi:10.1029/97GL52831, 1997.

Nghiem, S. V., Rigor, I. G., Richter, A., Burrows, J. P., Shepson, P. B., Bottenheim, J., Barber, D. G., Steffen, A., Latonas, J., Wang, F., Stern, G., Clemente-Coln, P., Martin, S., Hall, D. K., Kaleschke, L., Tackett, P., Neumann, G., and Asplin, M. G.: Field and satellite observations of the formation and distribution of Arctic atmospheric bromine above a rejuvenated sea ice cover, Journal of Geophysical Research: Atmospheres, 117(D17), doi:10.1029/2011JD016268, 2012.

Nilsson, E. D., Rannik, U., Swietlicki, E., Leck, C., Aalto, P. P., Zhou, J., and Norman, M.: Turbulent aerosol fluxes over the Arctic Ocean: 2. Wind-driven sources from the sea, Journal of Geophysical Research: Atmospheres, 106(D23), 32139–32154, doi:10.1029/2000JD900747, 2001.

Nott, G. J., Duck, T. J., Doyle, J. G., Coffin, M. E. W., Perro, C., Thackray, C. P., Drummond, J. R., Fogal, P. F., McCullough, E., and Sica, R. J.: A remotely operated lidar for aerosol, temperature, and water vapor profiling in the High Arctic, Journal of Atmospheric and Oceanic Technology, 29(2), 221–234, doi:10.1175/JTECH-D-11-00046.1, 2012.

Noxon, J. F.: Nitrogen dioxide in the stratosphere and troposphere measured by ground-based absorption spectroscopy, Science, 189(4202), 547–549, doi:10.1126/science.189.4202.547, 1975.

Obbard, R. W., Roscoe, H. K., Wolff, E. W., and Atkinson, H. M.: Frost flower surface area and chemistry as a function of salinity and temperature, Journal of Geophysical Research: Atmospheres, 114(D20), doi:10.1029/2009JD012481, 2009.

Oltmans, S. J.: Climatology of Arctic and Antarctic tropospheric ozone, in: *The tropospheric chemistry of ozone in the polar regions*, 25–40, Springer, 1993.

Oltmans, S. J. and Komhyr, W. D.: Surface ozone distributions and variations from 1973–1984: Measurements at the NOAA Geophysical Monitoring for Climatic Change Baseline Observatories, Journal of Geophysical Research: Atmospheres, 91(D4), 5229–5236, doi:10.1029/JD091iD04p05229, 1986.

Pacheco, H., Díaz-López, S., Jarre, E., Pacheco, H., Méndez, W., and Zamora-Ledezma, E.: NO_2 levels after the COVID-19 lockdown in Ecuador: A trade-off between environment and human health, Urban Climate, 34, 100674, doi:10.1016/j.uclim.2020.100674, 2020.

Parker, H. A., Hasheminassab, S., Crounse, J. D., Roehl, C. M., and Wennberg, P. O.: Impacts of Traffic Reductions Associated With COVID-19 on Southern California Air Quality, Geophysical Research Letters, 47(23), e2020GL090164, doi:10.1029/2020GL090164, 2020.

Payne, V. H., Clough, S. A., Shephard, M. W., Nassar, R., and Logan, J. A.: Information-centered representation of retrievals with limited degrees of freedom for signal: Application to methane from the Tropospheric Emission Spectrometer, Journal of Geophysical Research: Atmospheres, 114(D10), doi:10.1029/2008JD010155, 2009.

Perner, D. and Platt, U.: Detection of nitrous acid in the atmosphere by differential optical absorption, Geophysical Research Letters, 6(12), 917–920, doi:10.1029/GL006i012p00917, 1979.

Perrin, F. H.: Whose absorption law?, Journal of the Optical Society of America A, 38(1), 72–74, 1948.

Peters, E., Wittrock, F., Großmann, K., Frieß, U., Richter, A., and Burrows, J. P.: Formaldehyde and nitrogen dioxide over the remote western Pacific Ocean: SCIAMACHY and GOME-2 validation using ship-based MAX-DOAS observations, Atmospheric Chemistry and Physics, 12(22), 11179–11197, doi:10.5194/acp-12-11179-2012, 2012.

Peterson, P. K., Simpson, W. R., Pratt, K. A., Shepson, P. B., Frieß, U., Zielcke, J., Platt, U., Walsh, S. J., and Nghiem, S. V.: Dependence of the vertical distribution of bromine monoxide in the lower troposphere on meteorological factors such as wind speed and stability, Atmospheric Chemistry and Physics, 15(4), 2119–2137, doi: 10.5194/acp-15-2119-2015, 2015.

Peterson, P. K., Simpson, W. R., and Nghiem, S. V.: Variability of bromine monoxide at Barrow, Alaska, over four halogen activation (March–May) seasons and at two on-ice locations, Journal of Geophysical Research: Atmospheres, 121(3), 1381–1396, doi: 10.1002/2015JD024094, 2016.

Peterson, P. K., Pöhler, D., Sihler, H., Zielcke, J., General, S., Frieß, U., Platt, U., Simpson, W. R., Nghiem, S. V., Shepson, P. B., Stirm, B. H., Dhaniyala, S., Wagner, T., Caulton, D. R., Fuentes, J. D., and Pratt, K. A.: Observations of bromine monoxide transport in the Arctic sustained on aerosol particles, Atmospheric Chemistry and Physics, 17(12), 7567–7579, doi:10.5194/acp-17-7567-2017, 2017.

Peterson, P. K., Pöhler, D., Zielcke, J., General, S., Frieß, U., Platt, U., Simpson, W. R., Nghiem, S. V., Shepson, P. B., Stirm, B. H., and Pratt, K. A.: Springtime Bromine Activation over Coastal and Inland Arctic Snowpacks, ACS Earth and Space Chemistry, 2(10), 1075–1086, doi:10.1021/acsearthspacechem.8b00083, 2018.

Peterson, P. K., Hartwig, M., May, N. W., Schwartz, E., Rigor, I., Ermold, W., Steele, M., Morison, J. H., Nghiem, S. V., and Pratt, K. A.: Snowpack measurements suggest role for multi-year sea ice regions in Arctic atmospheric bromine and chlorine chemistry, Elementa (Washington, DC), 7(14), doi:10.1525/elementa.352, 2019.

Pinardi, G., Van Roozendael, M., Abuhassan, N., Adams, C., Cede, A., Clémer, K., Fayt, C., Frieß, U., Gil, M., Herman, J., Hermans, C., Hendrick, F., Irie, H., Merlaud, A., Navarro Comas, M., Peters, E., Piters, A. J. M., Puentedura, O., Richter, A., Schönhardt, A., Shaiganfar, R., Spinei, E., Strong, K., Takashima, H., Vrekoussis, M., Wagner, T., Wittrock, F., and Yilmaz, S.: MAX-DOAS formaldehyde slant column measurements during CINDI: intercomparison and analysis improvement, Atmospheric Measurement Techniques, 6(1), 167–185, doi:10.5194/amt-6-167-2013, 2013.

Pinardi, G., Richter, A., Meier, A., and Van Roozendael, M.: Monitoring Stratospheric OClO with Sentinel-5p (S5pOClO), European Space Agency, 2020.

Pisso, I., Sollum, E., Grythe, H., Kristiansen, N. I., Cassiani, M., Eckhardt, S., Arnold, D., Morton, D., Thompson, R. L., Groot Zwaaftink, C. D., Evangeliou, N., Sodemann, H., Haimberger, L., Henne, S., Brunner, D., Burkhart, J. F., Fouilloux, A., Brioude, J., Philipp, A., Seibert, P., and Stohl, A.: The Lagrangian particle dispersion model FLEXPART version 10.4, Geoscientific Model Development, 12(12), 4955–4997, doi:10.5194/gmd-12-4955-2019, 2019.

Piters, A. J. M., Boersma, K. F., Kroon, M., Hains, J. C., Van Roozendael, M., Wittrock, F., Abuhassan, N., Adams, C., Akrami, M., Allaart, M. A. F., Apituley, A., Beirle, S., Bergwerff, J. B., Berkhout, A. J. C., Brunner, D., Cede, A., Chong, J., Clémer, K., Fayt, C., Frieß, U., Gast, L. F. L., Gil-Ojeda, M., Goutail, F., Graves, R., Griesfeller, A., Großmann, K., Hemerijckx, G., Hendrick, F., Henzing, B., Herman, J., Hermans, C., Hoexum, M., van der Hoff, G. R., Irie, H., Johnston, P. V., Kanaya, Y., Kim, Y. J., Klein Baltink, H., Kreher, K., de Leeuw, G., Leigh, R., Merlaud, A., Moerman, M. M., Monks, P. S., Mount, G. H., Navarro-Comas, M., Oetjen, H., Pazmino, A., Perez-Camacho, M., Peters, E., du Piesanie, A., Pinardi, G., Puentedura, O., Richter, A., Roscoe, H. K., Schönhardt, A., Schwarzenbach, B., Shaiganfar, R., Sluis, W., Spinei, E., Stolk, A. P., Strong, K., Swart, D. P. J., Takashima, H., Vlemmix, T., Vrekoussis, M., Wagner, T., Whyte, C., Wilson, K. M., Yela, M., Yilmaz, S., Zieger, P., and Zhou, Y.: The Cabauw Intercomparison campaign for Nitrogen Dioxide measuring Instruments (CINDI): design, execution, and early results, Atmospheric Measurement Techniques, 5(2), 457–485, doi:10.5194/amt-5-457-2012, 2012.

Pitts, M. C., Poole, L. R., and Gonzalez, R.: Polar stratospheric cloud climatology based on CALIPSO spaceborne lidar measurements from 2006 to 2017, Atmospheric Chemistry and Physics, 18(15), 10881–10913, doi:10.5194/acp-18-10881-2018, 2018.

Platt, U. and Stutz, J.: *Differential Optical Absorption Spectroscopy*, Springer, 2008.

Platt, U., Perner, D., and Pätz, H. W.: Simultaneous measurement of atmospheric CH_2O, O_3, and NO_2 by differential optical absorption, Journal of Geophysical Research: Oceans, 84(C10), 6329–6335, doi:10.1029/JC084iC10p06329, 1979.

Pöhler, D., Vogel, L., Frieß, U., and Platt, U.: Observation of halogen species in the Amundsen Gulf, Arctic, by active long-path differential optical absorption spectroscopy, Proceedings of the National Academy of Sciences, 107(15), 6582–6587, doi:10.1073/pnas.0912231107, 2010.

Pommereau, J. P. and Goutail, F.: O_3 and NO_2 ground-based measurements by visible spectrometry during Arctic winter and spring 1988, Geophysical Research Letters, 15(8), 891–894, doi:10.1029/GL015i008p00891, 1988.

Pommereau, J.-P., Goutail, F., Lefèvre, F., Pazmino, A., Adams, C., Dorokhov, V., Eriksen, P., Kivi, R., Stebel, K., Zhao, X., and van Roozendael, M.: Why unprecedented ozone loss in the Arctic in 2011? Is it related to climate change?, Atmospheric Chemistry and Physics, 13(10), 5299–5308, doi:10.5194/acp-13-5299-2013, 2013.

Pougatchev, N. S., Connor, B. J., and Rinsland, C. P.: Infrared measurements of the ozone vertical distribution above Kitt Peak, Journal of Geophysical Research: Atmospheres, 100(D8), 16689–16697, doi:10.1029/95JD01296, 1996.

Pratt, K. A., Custard, K. D., Shepson, P. B., Douglas, T. A., Pöhler, D., General, S., Zielcke, J., Simpson, W. R., Platt, U., Tanner, D. J., Huey, L. G., Carlsen, M., and Stirm, B. H.: Photochemical production of molecular bromine in Arctic surface snowpacks, Nature Geoscience, 6(5), 351–356, doi:10.1038/NGEO1779, 2013.

Qin, K., Han, X., Li, D., Xu, J., Loyola, D., Xue, Y., Zhou, X., Li, D., Zhang, K., and Yuan, L.: Satellite-based estimation of surface NO_2 concentrations over east-central China: A comparison of POMINO and OMNO2d data, Atmospheric Environment, 224, 117322, 2020.

Quinn, P. K., Shaw, G., Andrews, E., Dutton, E. G., Ruoho-Airola, T., and Gong, S. L.: Arctic haze: current trends and knowledge gaps, Tellus B: Chemical and Physical Meteorology, 59(1), 99–114, doi:10.1111/j.1600-0889.2006.00236.x, 2007.

Rankin, A. M., Wolff, E. W., and Martin, S.: Frost flowers: Implications for tropospheric chemistry and ice core interpretation, Journal of Geophysical Research: Atmospheres, 107(D23), AAC 4–1–AAC 4–15, doi:10.1029/2002JD002492, 2002.

Raso, A. R. W., Custard, K. D., May, N. W., Tanner, D., Newburn, M. K., Walker, L., Moore, R. J., Huey, L. G., Alexander, L., Shepson, P. B., and Pratt, K. A.: Active molecular iodine photochemistry in the Arctic, Proceedings of the National Academy of Sciences, 114(38), 10053–10058, doi:10.1073/pnas.1702803114, 2017.

Reed, A. J., Thompson, A. M., Kollonige, D. E., Martins, D. K., Tzortziou, M. A., Herman, J. R., Berkoff, T. A., Abuhassan, N. K., and Cede, A.: Effects of local meteorology and aerosols on ozone and nitrogen dioxide retrievals from OMI and pandora spectrometers in Maryland, USA during DISCOVER-AQ 2011, Journal of atmospheric chemistry, 72(3-4), 455–482, doi:10.1007/s10874-013-9254-9, 2015.

Rex, M., Salawitch, R. J., von der Gathen, P., Harris, N. R. P., Chipperfield, M. P., and Naujokat, B.: Arctic ozone loss and climate change, Geophysical Research Letters, 31(4), doi:10.1029/2003GL018844, 2004.

Rex, M., Salawitch, R. J., Deckelmann, H., von der Gathen, P., Harris, N. R. P., Chipperfield, M. P., Naujokat, B., Reimer, E., Allaart, M., Andersen, S. B., Bevilacqua, R., Braathen, G. O., Claude, H., Davies, J., De Backer, H., Dier, H., Dorokhov, V., Fast, H., Gerding, M., Godin-Beekmann, S., Hoppel, K., Johnson, B., Kyrö, E., Litynska, Z., Moore, D., Nakane, H., Parrondo, M. C., Risley Jr., A. D., Skrivankova, P., Stübi, R., Viatte, P., Yushkov, V., and Zerefos, C.: Arctic winter 2005: Implications for stratospheric ozone loss and climate change, Geophysical Research Letters, 33(23), doi:10.1029/2006GL026731, 2006.

Richter, A. and Burrows, J. P.: Tropospheric NO_2 from GOME measurements, Advances in Space Research, 29(11), 1673–1683, 2002.

Richter, A., Burrows, J. P., Nüß, H., Granier, C., and Niemeier, U.: Increase in tropospheric nitrogen dioxide over China observed from space, Nature, 437(7055), 129–132, 2005.

Rigby, M., Park, S., Saito, T., Western, L. M., Redington, A. L., Fang, X., Henne, S., Manning, A. J., Prinn, R. G., Dutton, G. S., Fraser, P. J., Ganesan, A. L., Hall, B. D., Harth, C. M., Kim, J., Kim, K.-R., Krummel, P. B., Lee, T., Li, S., Liang, Q., Lunt, M. F., Montzka, S. A., Mühle, J., O'Doherty, S., Park, M.-K., Reimann, S., Salameh, P. K., Simmonds, P., Tunnicliffe, R. L., Weiss, R. F., Yokouchi, Y., and Young, D.: Increase in CFC-11 emissions from eastern China based on atmospheric observations, Nature, 569(7757), 546–550, doi:10.1038/s41586-019-1193-4, 2019.

Rodgers, C. D.: *Inverse Methods for Atmospheric Sounding: Theory and Practice*, volume 2, World Scientific, ISBN 981-02-2740-X, 2000.

Rodgers, C. D. and Connor, B. J.: Intercomparison of remote sounding instruments, Journal of Geophysical Research: Atmospheres, 108(D3), doi:10.1029/2002JD002299, 2003.

Roscoe, H. K., Van Roozendael, M., Fayt, C., du Piesanie, A., Abuhassan, N., Adams, C., Akrami, M., Cede, A., Chong, J., Clémer, K., Frieß, U., Gil Ojeda, M., Goutail, F., Graves, R., Griesfeller, A., Grossmann, K., Hemerijckx, G., Hendrick, F., Herman, J., Hermans, C., Irie, H., Johnston, P. V., Kanaya, Y., Kreher, K., Leigh, R., Merlaud, A., Mount, G. H., Navarro, M., Oetjen, H., Pazmino, A., Perez-Camacho, M., Peters, E., Pinardi, G., Puentedura, O., Richter, A., Schönhardt, A., Shaiganfar, R., Spinei, E., Strong, K., Takashima, H., Vlemmix, T., Vrekoussis, M., Wagner, T., Wittrock, F., Yela, M., Yilmaz, S., Boersma, F., Hains, J., Kroon, M., Piters, A., and Kim, Y. J.: Intercomparison of slant column measurements of NO_2 and O_4 by MAX-DOAS and zenith-sky UV and visible spectrometers, Atmospheric Measurement Techniques, 3(6), 1629–1646, doi:10.5194/amt-3-1629-2010, 2010.

Rothman, L. S., Jacquemart, D., Barbe, A., Chris Benner, D., Birk, M., Brown, L., Carleer, M., Chackerian Jr, C., Chance, K., Coudert, L. H., Dana, V., Devi, V. M., Flaud, J.-M., Gamache, R. R., Goldman, A., Hartmann, J.-M., Jucks, K. W., G, M. A., Mandin, J.-Y., Massie, S. T., Orphal, J., Perrin, A., Rinsland, C. P., Smith, M. A. H., Tennyson, J., Tolchenov, R. N., Toth, R. A., Vander Auwera, J., Varanasi, P., and Wagner, G.: The HITRAN 2004 molecular spectroscopic database, Journal of quantitative spectroscopy and radiative transfer, 96(2), 139–204, doi:10.1016/j.jqsrt.2004.10.008, 2005.

Rothman, L. S., Gordon, I. E., Barbe, A., Benner, D. C., Bernath, P. F., Birk, M., Boudon, V., Brown, L. R., Campargue, A., Champion, J.-P., Chance, K., Coudert, L. H., Dana, V., Devi, V. M., Fally, S., Flaud, J.-M., Gamache, R. R., Goldman, A., Jacquemart, D., Kleiner, I., Lacome, N., Lafferty, W. J., Mandin, J.-Y., Massie, S. T., Mikhailenko, S. N., Miller, C. E., Moazzen-Ahmadi, N., Naumenko, O. V., Nikitin, A. V., Orphal, J., Perevalov, V. I., Perrin, A., Predoi-Cross, A., Rinsland, C. P., Rotger, M., Simeckova, M., Smith, M. A. H., Sung, K., Tashkun, S. A., Tennyson, J., Toth, R. A., Vandaele, A. C., and Vander Auwera, J.: The HITRAN 2008 molecular spectroscopic database, Journal of Quantitative Spectroscopy and Radiative Transfer, 110(9-10), 533–572, doi: 10.1016/j.jqsrt.2009.02.013, 2009.

Rothman, L. S., Gordon, I. E., Barber, R. J., Dothe, H., Gamache, R. R., Goldman, A., Perevalov, V. I., Tashkun, S. A., and Tennyson, J.: HITEMP, the high-temperature molecular spectroscopic database, Journal of Quantitative Spectroscopy and Radiative Transfer, 111(15), 2139–2150, doi:10.1016/j.jqsrt.2010.05.001, 2010.

Rozanov, A., Rozanov, V., Buchwitz, M., Kokhanovsky, A., and Burrows, J. P.: SCIATRAN 2.0 – A new radiative transfer model for geophysical applications in the 175 – 2400 nm spectral region, Advances in Space Research, 36(5), 1015–1019, doi: 10.1016/j.asr.2005.03.012, 2005.

Ryan, R. G., Rhodes, S., Tully, M., Wilson, S., Jones, N., Frieß, U., and Schofield, R.: Daytime HONO, NO_2 and aerosol distributions from MAX-DOAS observations in Melbourne, Atmospheric Chemistry and Physics, 18(19), 13969–13985, doi:10.5194/acp-18-13969-2018, 2018.

Saha, S., Moorthi, S., Wu, X., Wang, J., Nadiga, S., Tripp, P., Behringer, D., Hou, Y.-T., Chuang, H.-y., Iredell, M., Ek, M., Meng, J., Yang, R., Mendez, M. P., van den Dool, H., Zhang, Q., Wang, W., Chen, M., and Becker, E.: NCEP Climate Forecast System Version 2 (CFSv2) 6-hourly Products, Research Data Archive at the National Center for Atmospheric Research, Computational and Information Systems Laboratory, Boulder, Colorado, USA, doi:10.5065/D61C1TXF, accessed: 05/09/2019, 2011, updated daily.

Saiz-Lopez, A. and von Glasow, R.: Reactive halogen chemistry in the troposphere, Chemical Society Reviews, 41(19), 6448–6472, doi:10.1039/C2CS35208G, 2012.

Salawitch, R. J., Gobbi, G. P., Wofsy, S. C., and McElroy, M. B.: Denitrification in the Antarctic stratosphere, Nature, 339(6225), 525–527, doi:10.1038/339525a0, 1989.

Salby, M. L. and Callaghan, P. F.: On the wintertime increase of Arctic ozone: Relationship to changes of the polar-night vortex, Journal of Geophysical Research: Atmospheres, 112(D6), doi:10.1029/2006JD007948, 2007.

Sander, S. P. and Friedl, R. R.: Kinetics and product studies of the reaction chlorine monoxide+bromine monoxide using flash photolysis-ultraviolet absorption, The Journal of Physical Chemistry, 93(12), 4764–4771, doi:10.1021/j100349a017, 1989.

Schneider, M., Redondas, A., Hase, F., Guirado, C., Blumenstock, T., and Cuevas, E.: Comparison of ground-based Brewer and FTIR total column O_3 monitoring techniques, Atmospheric Chemistry and Physics, 8(18), 5535–5550, doi:10.5194/acp-8-5535-2008, 2008.

Schnell, R. C., Liu, S. C., Oltmans, S. J., Stone, R. S., Hofmann, D. J., Dutton, E. G., Deshler, T., Sturges, W. T., Harder, J. W., Sewell, S. D., Trainer, M., and Harris, J. M.: Decrease of summer tropospheric ozone concentrations in Antarctica, Nature, 351(6329), 726–729, doi:10.1038/351726a0, 1991.

Schroeder, W. H., Anlauf, K. G., Barrie, L. A., Lu, J. Y., Steffen, A., Schneeberger, D. R., and Berg, T.: Arctic springtime depletion of mercury, Nature, 394(6691), 331–332, doi:10.1038/28530, 1998.

Seo, J., Park, D.-S. R., Kim, J. Y., Youn, D., Lim, Y. B., and Kim, Y.: Effects of meteorology and emissions on urban air quality: a quantitative statistical approach to long-term records (1999–2016) in Seoul, South Korea, Atmospheric Chemistry and Physics, 18(21), 16121–16137, doi:10.5194/acp-18-16121-2018, 2018.

Serdyuchenko, A., Gorshelev, V., Weber, M., Chehade, W., and Burrows, J. P.: High spectral resolution ozone absorption cross-sections – Part 2: Temperature dependence, Atmospheric Measurement Techniques, 7(2), 625–636, doi:10.5194/amt-7-625-2014, 2014.

Sharp, M., Skidmore, M., and Nienow, P.: Seasonal and spatial variations in the chemistry of a High Arctic supraglacial snow cover, Journal of Glaciology, 48(160), 149–158, doi:10.3189/172756502781831683, 2002.

Sihler, H., Platt, U., Beirle, S., Marbach, T., Kühl, S., Dörner, S., Verschaeve, J., Frieß, U., Pöhler, D., Vogel, L., Sander, R., and Wagner, T.: Tropospheric BrO column densities in the Arctic derived from satellite: retrieval and comparison to ground-based measurements, Atmospheric Measurement Techniques, 5(11), 2779–2807, doi:10.5194/amt-5-2779-2012, 2012.

Simpson, W. R., von Glasow, R., Riedel, K., Anderson, P., Ariya, P., Bottenheim, J., Burrows, J., Carpenter, L. J., Frieß, U., Goodsite, M. E., Heard, D., Hutterli, M., Jacobi, H.-W., Kaleschke, L., Neff, B., Plane, J., Platt, U., Richter, A., Roscoe, H., Sander, R., Shepson, P., Sodeau, J., Steffen, A., Wagner, T., and Wolff, E.: Halogens and their role in polar boundary-layer ozone depletion, Atmospheric Chemistry and Physics, 7(16), 4375–4418, doi:10.5194/acp-7-4375-2007, 2007.

Simpson, W. R., Brown, S. S., Saiz-Lopez, A., Thornton, J. A., and von Glasow, R.: Tropospheric halogen chemistry: Sources, cycling, and impacts, Chemical reviews, 115(10), 4035–4062, doi:10.1021/cr5006638, 2015.

Simpson, W. R., Peterson, P. K., Frieß, U., Sihler, H., Lampel, J., Platt, U., Moore, C., Pratt, K., Shepson, P., Halfacre, J., and Nghiem, S. V.: Horizontal and vertical structure of reactive bromine events probed by bromine monoxide MAX-DOAS, Atmospheric Chemistry and Physics, 17(15), 9291–9309, doi:10.5194/acp-17-9291-2017, 2017.

Singleton, C. S., Randall, C. E., Chipperfield, M. P., Davies, S., Feng, W., Bevilacqua, R. M., Hoppel, K. W., Fromm, M. D., Manney, G. L., and Harvey, V. L.: 2002-2003 Arctic ozone loss deduced from POAM III satellite observations and the SLIMCAT chemical transport model, Atmospheric Chemistry and Physics, 5(3), 597–609, doi:10.5194/acp-5-597-2005, 2005.

Singleton, C. S., Randall, C. E., Harvey, V. L., Chipperfield, M. P., Feng, W., Manney, G. L., Froidevaux, L., Boone, C. D., Bernath, P. F., Walker, K. A., McElroy, C. T., and Hoppel, K. W.: Quantifying Arctic ozone loss during the 2004-2005 winter using satellite observations and a chemical transport model, Journal of Geophysical Research: Atmospheres, 112(D7), doi:10.1029/2006JD007463, 2007.

Sinnhuber, B.-M., Stiller, G., Ruhnke, R., von Clarmann, T., Kellmann, S., and Aschmann, J.: Arctic winter 2010/2011 at the brink of an ozone hole, Geophysical Research Letters, 38(24), doi:10.1029/2011GL049784, 2011.

Sinreich, R., Frieß, U., Wagner, T., and Platt, U.: Multi axis differential optical absorption spectroscopy (MAX-DOAS) of gas and aerosol distributions, Faraday Discussions, 130, 153–164, 2005.

Sioris, C., Rieger, L., Lloyd, N., Bourassa, A., Roth, C., Degenstein, D., Camy-Peyret, C., Pfeilsticker, K., Berthet, G., Catoire, V., Goutail, F., Pommereau, J.-P., and Mclinden, C. E.: Improved OSIRIS NO_2 retrieval algorithm: description and validation, Atmospheric Measurement Techniques, 10(3), 1155–1168, doi:10.5194/amt-10-1155-2017, 2017.

Solomon, S., Garcia, R. R., Rowland, F. S., and Wuebbles, D. J.: On the depletion of Antarctic ozone, Nature, 321(6072), 755–758, doi:10.1038/321755a0, 1986.

Solomon, S., Haskins, J., Ivy, D. J., and Min, F.: Fundamental differences between Arctic and Antarctic ozone depletion, Proceedings of the National Academy of Sciences, 111(17), 6220–6225, doi:10.1073/pnas.1319307111, 2014.

Solomon, S., Ivy, D. J., Kinnison, D., Mills, M. J., Neely, R. R., and Schmidt, A.: Emergence of healing in the Antarctic ozone layer, Science, 353(6296), 269–274, doi: 10.1126/science.aae0061, 2016.

Spang, R., Hoffmann, L., Müller, R., Grooß, J.-U., Tritscher, I., Höpfner, M., Pitts, M., Orr, A., and Riese, M.: A climatology of polar stratospheric cloud composition between 2002 and 2012 based on MIPAS/Envisat observations, Atmospheric Chemistry and Physics, 18(7), 5089–5113, doi:10.5194/acp-18-5089-2018, 2018.

Spicer, C. W., Plastridge, R. A., Foster, K. L., Finlayson-Pitts, B. J., Bottenheim, J. W., Grannas, A. M., and Shepson, P. B.: Molecular halogens before and during ozone depletion events in the Arctic at polar sunrise: concentrations and sources, Atmospheric Environment, 36(15-16), 2721–2731, doi:10.1016/S1352-2310(02)00125-5, 2002.

Spinei, E., Cede, A., Swartz, W. H., Herman, J., and Mount, G. H.: The use of NO_2 absorption cross section temperature sensitivity to derive NO_2 profile temperature and stratospheric-tropospheric column partitioning from visible direct-sun DOAS measurements, Atmospheric Measurement Techniques, 7(12), 4299–4316, doi:10.5194/amt-7-4299-2014, 2014.

Spinei, E., Tiefengraber, M., Müller, M., Gebetsberger, M., Cede, A., Valin, L., Szykman, J., Whitehill, A., Kotsakis, A., Santos, F., Abbuhasan, N., Zhao, X., Fioletov, V., Lee, S. C., and Swap, R.: Effect of polyoxymethylene (POM-H Delrin) off-gassing within the Pandora head sensor on direct-sun and multi-axis formaldehyde column measurements in 2016–2019, Atmospheric Measurement Techniques, 14(1), 647–663, doi:10.5194/amt-14-647-2021, 2021.

Steffen, A., Douglas, T., Amyot, M., Ariya, P., Aspmo, K., Berg, T., Bottenheim, J., Brooks, S., Cobbett, F., Dastoor, A., Dommergue, A., Ebinghaus, R., Ferrari, C., Gardfeldt, K., Goodsite, M. E., Lean, D., Poulain, A. J., Scherz, C., Skov, H., and Sommar, J.: A synthesis of atmospheric mercury depletion event chemistry in the atmosphere and snow, Atmospheric Chemistry and Physics, 8(6), 1445–1482, doi:10.5194/acp-8-1445-2008, 2008.

Stoffelen, A.: Toward the true near-surface wind speed: Error modeling and calibration using triple collocation, Journal of Geophysical Research: Oceans, 103(C4), 7755–7766, doi:10.1029/97JC03180, 1998.

Stohl, A., Hittenberger, M., and Wotawa, G.: Validation of the Lagrangian particle dispersion model FLEXPART against large-scale tracer experiment data, Atmospheric Environment, 32(24), 4245–4264, doi:10.1016/S1352-2310(98)00184-8, 1998.

Stohl, A., Eckhardt, S., Forster, C., James, P., Spichtinger, N., and Seibert, P.: A replacement for simple back trajectory calculations in the interpretation of atmospheric trace substance measurements, Atmospheric Environment, 36(29), 4635–4648, doi:10.1016/S1352-2310(02)00416-8, 2002.

Strahan, S. E., Douglass, A. R., and Newman, P. A.: The contributions of chemistry and transport to low arctic ozone in March 2011 derived from Aura MLS observations, Journal of Geophysical Research: Atmospheres, 118(3), 1563–1576, doi:10.1002/jgrd.50181, 2013.

Stutz, J., Thomas, J. L., Hurlock, S. C., Schneider, M., von Glasow, R., Piot, M., Gorham, K., Burkhart, J. F., Ziemba, L., Dibb, J. E., and Lefer, B. L.: Longpath DOAS observations of surface BrO at Summit, Greenland, Atmospheric Chemistry and Physics, 11(18), 9899–9910, doi:10.5194/acp-11-9899-2011, 2011.

Style, R. W. and Worster, M. G.: Frost flower formation on sea ice and lake ice, Geophysical Research Letters, 36(11), doi:10.1029/2009GL037304, 2009.

Su, C.-H., Ryu, D., Crow, W. T., and Western, A. W.: Beyond triple collocation: Applications to soil moisture monitoring, Journal of Geophysical Research: Atmospheres, 119(11), 6419–6439, doi:10.1002/2013JD021043, 2014.

Sung, K., Skelton, R., Walker, K. A., Boone, C. D., Fu, D., and Bernath, P. F.: N_2O and O_3 Arctic column amounts from PARIS-IR observations: Retrievals, characterization and error analysis, Journal of Quantitative Spectroscopy and Radiative Transfer, 107(3), 385–406, doi:10.1016/j.jqsrt.2007.03.002, 2007.

Swanson, W. F., Graham, K. A., Halfacre, J. W., Holmes, C. D., Shepson, P. B., and Simpson, W. R.: Arctic Reactive Bromine Events Occur in Two Distinct Sets of Environmental Conditions: A Statistical Analysis of 6 Years of Observations, Journal of Geophysical Research: Atmospheres, 125(10), e2019JD032139, doi:10.1029/2019JD032139, 2020.

Tarasick, D. W. and Bottenheim, J. W.: Surface ozone depletion episodes in the Arctic and Antarctic from historical ozonesonde records, Atmospheric Chemistry and Physics, 2(3), 197–205, doi:10.5194/acp-2-197-2002, 2002.

Tarasick, D. W., Davies, J., Smit, H. G. J., and Oltmans, S. J.: A re-evaluated Canadian ozonesonde record: measurements of the vertical distribution of ozone over Canada from 1966 to 2013, Atmospheric Measurement Techniques, 9(1), 195–214, doi: 10.5194/amt-9-195-2016, 2016.

Tegtmeier, S., Rex, M., Wohltmann, I., and Krüger, K.: Relative importance of dynamical and chemical contributions to Arctic wintertime ozone, Geophysical Research Letters, 35(17), doi:10.1029/2008GL034250, 2008.

Thalman, R. and Volkamer, R.: Temperature dependent absorption cross-sections of O_2–O_2 collision pairs between 340 and 630 nm and at atmospherically relevant pressure, Physical chemistry chemical physics, 15(37), 15371–15381, doi:10.1039/C3CP50968K, 2013.

Theys, N., Van Roozendael, M., Hendrick, F., Yang, X., De Smedt, I., Richter, A., Begoin, M., Errera, Q., Johnston, P. V., Kreher, K., and De Maziére, M.: Global observations of tropospheric BrO columns using GOME-2 satellite data, Atmospheric Chemistry and Physics, 11(4), 1791–1811, doi:10.5194/acp-11-1791-2011, 2011.

Thomas, J. L., Stutz, J., Lefer, B., Huey, L. G., Toyota, K., Dibb, J. E., and von Glasow, R.: Modeling chemistry in and above snow at Summit, Greenland - Part 1: Model description and results, Atmospheric Chemistry and Physics, 11(10), 4899–4914, doi:10.5194/acp-11-4899-2011, 2011.

Thomas, J. L., Dibb, J. E., Huey, L. G., Liao, J., Tanner, D., Lefer, B., von Glasow, R., and Stutz, J.: Modeling chemistry in and above snow at Summit, Greenland - Part 2: Impact of snowpack chemistry on the oxidation capacity of the boundary layer, Atmospheric Chemistry and Physics, 12(14), 6537–6554, doi:10.5194/acp-12-6537-2012, 2012.

Thompson, C. R., Shepson, P. B., Liao, J., Huey, L. G., Apel, E. C., Cantrell, C. A., Flocke, F., Orlando, J., Fried, A., Hall, S. R., Hornbrook, R. S., Knapp, D. J., Mauldin III, R. L., Montzka, D. D., Sive, B. C., Ullmann, K., Weibring, P., and Weinheimer, A.: Interactions of bromine, chlorine, and iodine photochemistry during ozone depletions in Barrow, Alaska, Atmospheric Chemistry and Physics, 15(16), 9651–9679, doi:10.5194/acp-15-9651-2015, 2015.

Thompson, C. R., Shepson, P. B., Liao, J., Huey, L. G., Cantrell, C., Flocke, F., and Orlando, J.: Bromine atom production and chain propagation during springtime Arctic ozone depletion events in Barrow, Alaska, Atmospheric Chemistry and Physics, 17(5), 3401–3421, doi:10.5194/acp-17-3401-2017, 2017.

Tilmes, S., Müller, R., Engel, A., Rex, M., and Russell III, J. M.: Chemical ozone loss in the Arctic and Antarctic stratosphere between 1992 and 2005, Geophysical Research Letters, 33(20), doi:10.1029/2006GL026925, 2006.

Tirpitz, J.-L., Frieß, U., Hendrick, F., Alberti, C., Allaart, M., Apituley, A., Bais, A., Beirle, S., Berkhout, S., Bognar, K., Bösch, T., Bruchkouski, I., Cede, A., Chan, K. L., den Hoed, M., Donner, S., Drosoglou, T., Fayt, C., Friedrich, M. M., Frumau, A., Gast, L., Gielen, C., Gomez-Martín, L., Hao, N., Hensen, A., Henzing, B., Hermans, C., Jin, J., Kreher, K., Kuhn, J., Lampel, J., Li, A., Liu, C., Liu, H., Ma, J., Merlaud, A., Peters, E., Pinardi, G., Piters, A., Platt, U., Puentedura, O., Richter, A., Schmitt, S., Spinei, E., Stein Zweers, D., Strong, K., Swart, D., Tack, F., Tiefengraber, M., van der Hoff, R., van Roozendael, M., Vlemmix, T., Vonk, J., Wagner, T., Wang, Y., Wang, Z., Wenig, M., Wiegner, M., Wittrock, F., Xie, P., Xing, C., Xu, J., Yela, M., Zhang, C., and Zhao, X.: Intercomparison of MAX-DOAS vertical profile retrieval algorithms: studies on field data from the CINDI-2 campaign, Atmospheric Measurement Techniques, 14(1), 1–35, doi:10.5194/amt-14-1-2021, 2021.

Toohey, M. and Strong, K.: Estimating biases and error variances through the comparison of coincident satellite measurements, Journal of Geophysical Research: Atmospheres, 112(D13), doi:10.1029/2006JD008192, 2007.

Toom-Sauntry, D. and Barrie, L. A.: Chemical composition of snowfall in the high Arctic: 1990–1994, Atmospheric Environment, 36(15-16), 2683–2693, doi:10.1016/S1352-2310(02)00115-2, 2002.

Toon, G. C., Farmer, C. B., Schaper, P. W., Lowes, L. L., Norton, R. H., Schoeberl, M. R., Lait, L. R., and Newman, P. A.: Evidence for subsidence in the 1989 Arctic winter stratosphere from airborne infrared composition measurements, Journal of Geophysical Research: Atmospheres, 97(D8), 7963–7970, doi:10.1029/91JD03115, 1992.

Toyota, K., McConnell, J. C., Lupu, A., Neary, L., McLinden, C. A., Richter, A., Kwok, R., Semeniuk, K., Kaminski, J. W., Gong, S.-L., Jarosz, J., Chipperfield, M. P., and Sioris, C. E.: Analysis of reactive bromine production and ozone depletion in the Arctic boundary layer using 3-D simulations with GEM-AQ: inference from synoptic-scale patterns, Atmospheric Chemistry and Physics, 11(8), 3949–3979, doi:10.5194/acp-11-3949-2011, 2011.

Toyota, K., McConnell, J. C., Staebler, R. M., and Dastoor, A. P.: Air-snowpack exchange of bromine, ozone and mercury in the springtime Arctic simulated by the 1-D model PHANTAS – Part 1: In-snow bromine activation and its impact on ozone, Atmospheric Chemistry and Physics, 14(8), 4101–4133, doi:10.5194/acp-14-4101-2014, 2014.

Tremblay, S., Picard, J.-C., Bachelder, J. O., Lutsch, E., Strong, K., Fogal, P., Leaitch, W. R., Sharma, S., Kolonjari, F., Cox, C. J., Chang, R. Y.-W., and Hayes, P. L.: Characterization of aerosol growth events over Ellesmere Island during the summers of 2015 and 2016, Atmospheric Chemistry and Physics, 19(8), 5589–5604, doi:10.5194/acp-19-5589-2019, 2019.

Tschudi, M., Meier, W. N., Stewart, J. S., Fowler, C., and Maslanik, J.: EASE-Grid Sea Ice Age, Version 4 [March to May, 2016 to 2019], NASA National Snow and Ice Data Center, Boulder, Colorado USA, doi:10.5067/UTAV7490FEPB, accessed: 09/09/2019, 2019.

Tung, K.-K., Ko, M. K. W., Rodriguez, J. M., and Sze, N. D.: Are Antarctic ozone variations a manifestation of dynamics or chemistry?, Nature, 322(6082), 811–814, doi:10.1038/322811a0, 1986.

Tzortziou, M., Herman, J. R., Cede, A., and Abuhassan, N.: High precision, absolute total column ozone measurements from the Pandora spectrometer system: Comparisons with data from a Brewer double monochromator and Aura OMI, Journal of Geophysical Research: Atmospheres, 117(D16), doi:10.1029/2012JD017814, 2012.

Valks, P., Pinardi, G., Richter, A., Lambert, J.-C., Hao, N., Loyola, D., Van Roozendael, M., and Emmadi, S.: Operational total and tropospheric NO_2 column retrieval for GOME-2, Atmospheric Measurement Techniques, 4(7), 1491–1514, doi:10.5194/amt-4-1491-2011, 2011.

van Geffen, J., Boersma, K. F., Eskes, H., Sneep, M., ter Linden, M., Zara, M., and Veefkind, J. P.: S5P TROPOMI NO_2 slant column retrieval: method, stability, uncertainties and comparisons with OMI, Atmospheric Measurement Techniques, 13(3), 1315–1335, doi:10.5194/amt-13-1315-2020, 2020.

Van Roozendael, M.: Centralized DOAS processing of CINDI-2 data, 2^{nd} CINDI-2 Workshop, Mutters, Austria, 14-15 March 2018, URL `https://frm4doas.aeronomie.be/ProjectDir/2nd-CINDI2-WS/vanRoozendael_2ndCINDI2_WS_20180314.pdf`, 2018.

Van Roozendael, M., De Mazière, M., Hermans, C., Simon, P. C., Pommereau, J.-P., Goutail, F., Tie, X. X., Brasseur, G., and Granier, C.: Ground-based observations of stratospheric NO_2 at high and midlatitudes in Europe after the Mount Pinatubo eruption, Journal of Geophysical Research: Atmospheres, 102(D15), 19171–19176, doi:10.1029/97JD01098, 1997.

Vandaele, A. C., Hermans, C., Simon, P. C., Carleer, M., Colin, R., Fally, S., Merienne, M.-F., Jenouvrier, A., and Coquart, B.: Measurements of the NO_2 absorption cross-section from 42 000 cm^{-1} to 10 000 cm^{-1} (238–1000 nm) at 220 K and 294 K, Journal of Quantitative Spectroscopy and Radiative Transfer, 59(3-5), 171–184, doi:10.1016/S0022-4073(97)00168-4, 1998.

Verhoelst, T., Granville, J., Hendrick, F., Köhler, U., Lerot, C., Pommereau, J.-P., Redondas, A., Van Roozendael, M., and Lambert, J.-C.: Metrology of ground-based satellite validation: co-location mismatch and smoothing issues of total ozone comparisons, Atmospheric Measurement Techniques, 8(12), 5039–5062, doi:10.5194/amt-8-5039-2015, 2015.

Verhoelst, T., Compernolle, S., Pinardi, G., Lambert, J.-C., Eskes, H. J., Eichmann, K.-U., Fjæraa, A. M., Granville, J., Niemeijer, S., Cede, A., Tiefengraber, M., Hendrick, F., Pazmiño, A., Bais, A., Bazureau, A., Boersma, K. F., Bognar, K., Dehn, A., Donner, S., Elokhov, A., Gebetsberger, M., Goutail, F., Grutter de la Mora, M., Gruzdev, A., Gratsea, M., Hansen, G. H., Irie, H., Jepsen, N., Kanaya, Y., Karagkiozidis, D., Kivi, R., Kreher, K., Levelt, P. F., Liu, C., Müller, M., Navarro Comas, M., Piters, A. J. M., Pommereau, J.-P., Portafaix, T., Prados-Roman, C., Puentedura, O., Querel, R., Remmers, J., Richter, A., Rimmer, J., Rivera Cárdenas, C., Saavedra de Miguel, L., Sinyakov, V. P., Stremme, W., Strong, K., Van Roozendael, M., Veefkind, J. P., Wagner, T., Wittrock, F., Yela González, M., and Zehner, C.: Ground-based validation of the Copernicus Sentinel-5P TROPOMI NO_2 measurements with the NDACC ZSL-DOAS, MAX-DOAS and Pandonia global networks, Atmospheric Measurement Techniques, 14(1), 481–510, doi:10.5194/amt-14-481-2021, 2021.

Vicente-Luis, A., Tremblay, S., Dionne, J., Chang, R. Y.-W., Fogal, P., Leaitch, W. R., Sharma, S., Kolonjari, F., and Hayes, P. L.: In situ aerosol optical properties in the Canadian High Arctic in winter and spring from 2016 to 2019, In Preparation, 2020.

Vlemmix, T., Piters, A. J. M., Berkhout, A. J. C., Gast, L. F. L., Wang, P., and Levelt, P. F.: Ability of the MAX-DOAS method to derive profile information for NO_2: can the boundary layer and free troposphere be separated?, Atmospheric Measurement Techniques, 4(12), 2659–2684, doi:10.5194/amt-4-2659-2011, 2011.

Vlemmix, T., Eskes, H. J., Piters, A. J. M., Schaap, M., Sauter, F. J., Kelder, H., and Levelt, P. F.: MAX-DOAS tropospheric nitrogen dioxide column measurements compared with the Lotos-Euros air quality model, Atmospheric Chemistry and Physics, 15(3), 1313–1330, doi:10.5194/acp-15-1313-2015, 2015.

von Clarmann, T.: Smoothing error pitfalls, Atmospheric Measurement Techniques, 7(9), 3023–3034, doi:10.5194/amt-7-3023-2014, 2014.

Wagner, T., Leue, C., Wenig, M., Pfeilsticker, K., and Platt, U.: Spatial and temporal distribution of enhanced boundary layer BrO concentrations measured by the GOME instrument aboard ERS-2, Journal of Geophysical Research: Atmospheres, 106(D20), 24225–24235, doi:10.1029/2000JD000201, 2001.

Wagner, T., Dix, B., Friedeburg, C. v., Frieß, U., Sanghavi, S., Sinreich, R., and Platt, U.: MAX-DOAS O_4 measurements: A new technique to derive information on atmospheric aerosolsPrinciples and information content, Journal of Geophysical Research: Atmospheres, 109(D22), doi:10.1029/2004JD004904, 2004.

Wagner, T., Beirle, S., Brauers, T., Deutschmann, T., Frieß, U., Hak, C., Halla, J. D., Heue, K. P., Junkermann, W., Li, X., Platt, U., and Pundt-Gruber, I.: Inversion of tropospheric profiles of aerosol extinction and HCHO and NO_2 mixing ratios from MAX-DOAS observations in Milano during the summer of 2003 and comparison with independent data sets, Atmospheric Measurement Techniques, 4(12), 2685–2715, doi:10.5194/amt-4-2685-2011, 2011.

Wagner, T., Apituley, A., Beirle, S., Dörner, S., Frieß, U., Remmers, J., and Shaiganfar, R.: Cloud detection and classification based on MAX-DOAS observations, Atmospheric Measurement Techniques, 7(5), 1289–1320, doi:10.5194/amt-7-1289-2014, 2014.

Wagner, T., Beirle, S., Remmers, J., Shaiganfar, R., and Wang, Y.: Absolute calibration of the colour index and O_4 absorption derived from Multi AXis (MAX-) DOAS measurements and their application to a standardised cloud classification algorithm, Atmospheric Measurement Techniques, 9(9), 4803–4823, doi:10.5194/amt-9-4803-2016, 2016.

Wahner, A., Tyndall, G. S., and Ravishankara, A. R.: Absorption cross sections for symmetric chlorine dioxide as a function of temperature in the wavelength range 240-480 nm, Journal of Physical Chemistry, 91(11), 2734–2738, doi:10.1021/j100295a018, 1987.

Wang, J. M., Jeong, C.-H., Hilker, N., Shairsingh, K. K., Healy, R. M., Sofowote, U., Debosz, J., Su, Y., McGaughey, M., Doerksen, G., Munoz, T., White, L., Herod, D., and Evans, G. J.: Near-Road Air Pollutant Measurements: Accounting for Inter-Site Variability Using Emission Factors, Environmental Science and Technology, 52(16), 9495–9504, doi:10.1021/acs.est.8b01914, 2018.

Wang, S. and Pratt, K. A.: Molecular Halogens Above the Arctic Snowpack: Emissions, Diurnal Variations, and Recycling Mechanisms, Journal of Geophysical Research: Atmospheres, 122(21), 11991–12007, doi:10.1002/2017JD027175, 2017.

Wang, S., Pongetti, T. J., Sander, S. P., Spinei, E., Mount, G. H., Cede, A., and Herman, J.: Direct Sun measurements of NO_2 column abundances from Table Mountain, California: Intercomparison of low- and high-resolution spectrometers, Journal of Geophysical Research: Atmospheres, 115(D13), doi:10.1029/2009JD013503, 2010.

Wang, S., McNamara, S. M., Moore, C. W., Obrist, D., Steffen, A., Shepson, P. B., Staebler, R. M., Raso, A. R. W., and Pratt, K. A.: Direct detection of atmospheric atomic bromine leading to mercury and ozone depletion, Proceedings of the National Academy of Sciences, 116(29), 14479–14484, doi:10.1073/pnas.1900613116, 2019.

Wang, Y., Penning de Vries, M., Xie, P., Beirle, S., Dörner, S., Remmers, J., Li, A., and Wagner, T.: Cloud and aerosol classification for 2.5 years of MAX-DOAS observations in Wuxi (China) and comparison to independent data sets, Atmospheric Measurement Techniques, 8(12), 5133–5156, doi:10.5194/amt-8-5133-2015, 2015.

Wang, Y., Beirle, S., Lampel, J., Koukouli, M., De Smedt, I., Theys, N., Li, A., Wu, D., Xie, P., Liu, C., Van Roozendael, M., Stavrakou, T., Müller, J.-F., and Wagner, T.: Validation of OMI, GOME-2A and GOME-2B tropospheric NO_2, SO_2 and HCHO products using MAX-DOAS observations from 2011 to 2014 in Wuxi, China: investigation of the effects of priori profiles and aerosols on the satellite products, Atmospheric Chemistry and Physics, 17(8), 5007–5033, doi:10.5194/acp-17-5007-2017, 2017a.

Wang, Y., Lampel, J., Xie, P., Beirle, S., Li, A., Wu, D., and Wagner, T.: Ground-based MAX-DOAS observations of tropospheric aerosols, NO_2, SO_2 and HCHO in Wuxi, China, from 2011 to 2014, Atmospheric Chemistry and Physics, 17(3), 2189–2215, doi:10.5194/acp-17-2189-2017, 2017b.

Weatherhead, E. C., Reinsel, G. C., Tiao, G. C., Meng, X.-L., Choi, D., Cheang, W.-K., Keller, T., DeLuisi, J., Wuebbles, D. J., Kerr, J. B., Miller, A. J., Oltmans, S. J., and Frederick, J. E.: Factors affecting the detection of trends: Statistical considerations and applications to environmental data, Journal of Geophysical Research: Atmospheres, 103(D14), 17149–17161, doi:10.1029/98JD00995, 1998.

Wennberg, P.: Bromine explosion, Nature, 397(6717), 299–301, doi:10.1038/16805, 1999.

WMO: Meteorology – A three-dimensional science: Second session of the Commission for Aerology, WMO Bulletin, 4(4), 134–138, 1957.

WMO: Scientific Assessment of Ozone Depletion: 2014, Geneva, Switzerland: Global Ozone Research and Monitoring Project Report 55, 2014.

WMO: Scientific Assessment of Ozone Depletion: 2018, Geneva, Switzerland: Global Ozone Research and Monitoring Project Report 58, 2018.

Wohltmann, I., von der Gathen, P., Lehmann, R., Maturilli, M., Deckelmann, H., Manney, G. L., Davies, J., Tarasick, D., Jepsen, N., Kivi, R., Lyall, N., and Rex, M.: Near-Complete Local Reduction of Arctic Stratospheric Ozone by Severe Chemical Loss in Spring 2020, Geophysical Research Letters, 47(20), e2020GL089547, doi:10.1029/2020GL089547, 2020.

Wren, S. N., Donaldson, D. J., and Abbatt, J. P. D.: Photochemical chlorine and bromine activation from artificial saline snow, Atmospheric Chemistry and Physics, 13(19), 9789–9800, doi:10.5194/acp-13-9789-2013, 2013.

Yang, X., Cox, R. A., Warwick, N. J., Pyle, J. A., Carver, G. D., O'Connor, F. M., and Savage, N. H.: Tropospheric bromine chemistry and its impacts on ozone: A model study, Journal of Geophysical Research: Atmospheres, 110(D23), doi:10.1029/2005JD006244, 2005.

Yang, X., Pyle, J. A., and Cox, R. A.: Sea salt aerosol production and bromine release: Role of snow on sea ice, Geophysical Research Letters, 35(16), L16815, doi:10.1029/2008GL034536, 2008.

Yang, X., Pyle, J. A., Cox, R. A., Theys, N., and Van Roozendael, M.: Snow-sourced bromine and its implications for polar tropospheric ozone, Atmospheric Chemistry and Physics, 10(16), 7763–7773, doi:10.5194/acp-10-7763-2010, 2010.

Yilmaz, S.: Retrieval of atmospheric aerosol and trace gas vertical profiles using multi-axis differential optical absorption spectroscopy, Ph.D. thesis, University of Heilderberg, doi:10.11588/heidok.00013128, 2012.

York, D., Evensen, N. M., Martınez, M. L., and De Basabe Delgado, J.: Unified equations for the slope, intercept, and standard errors of the best straight line, American Journal of Physics, 72(3), 367–375, doi:10.1119/1.1632486, 2004.

Zawada, D. J., Dueck, S. R., Rieger, L. A., Bourassa, A. E., Lloyd, N. D., and Degenstein, D. A.: High-resolution and Monte Carlo additions to the SASKTRAN radiative transfer model, Atmospheric Measurement Techniques, 8(6), 2609–2623, doi:10.5194/amt-8-2609-2015, 2015.

Zhao, X.: Studies of Atmospheric Ozone and Related Constituents in the Arctic and at Mid-latitudes, Ph.D. thesis, University of Toronto, 2017.

Zhao, X., Fioletov, V., Cede, A., Davies, J., and Strong, K.: Accuracy, precision, and temperature dependence of Pandora total ozone measurements estimated from a comparison with the Brewer triad in Toronto, Atmospheric Measurement Techniques, 9(12), 5747–5761, doi:10.5194/amt-9-5747-2016, 2016a.

Zhao, X., Strong, K., Adams, C., Schofield, R., Yang, X., Richter, A., Frieß, U., Blechschmidt, A.-M., and Koo, J.-H.: A case study of a transported bromine explosion event in the Canadian high arctic, Journal of Geophysical Research: Atmospheres, 121(1), 457–477, doi:10.1002/2015JD023711, 2016b.

Zhao, X., Weaver, D., Bognar, K., Manney, G., Millán, L., Yang, X., Eloranta, E., Schneider, M., and Strong, K.: Cyclone-induced surface ozone and HDO depletion in the Arctic, Atmospheric Chemistry and Physics, 17(24), 14955–14974, doi:10.5194/acp-17-14955-2017, 2017.

Zhao, X., Bognar, K., Fioletov, V., Pazmino, A., Goutail, F., Millán, L., Manney, G., Adams, C., and Strong, K.: Assessing the impact of clouds on ground-based UV–visible total column ozone measurements in the high Arctic, Atmospheric Measurement Techniques, 12(4), 2463–2483, doi:10.5194/amt-12-2463-2019, 2019a.

Zhao, X., Griffin, D., Fioletov, V., McLinden, C., Davies, J., Ogyu, A., Lee, S. C., Lupu, A., Moran, M. D., Cede, A., Tiefengraber, M., and Müller, M.: Retrieval of total column and surface NO_2 from Pandora zenith-sky measurements, Atmospheric Chemistry and Physics, 19(16), 10619–10642, doi:10.5194/acp-19-10619-2019, 2019b.

Zhao, X., Fioletov, V., Brohart, M., Savastiouk, V., Abboud, I., Ogyu, A., Davies, J., Sit, R., Lee, S. C., Cede, A., Tiefengraber, M., Müller, M., Griffin, D., and McLinden, C.: The world Brewer reference triad–updated performance assessment and new double triad, Atmospheric Measurement Techniques Discussions, 1–34, doi:10.5194/amt-2020-324, 2020a.

Zhao, X., Griffin, D., Fioletov, V., McLinden, C., Cede, A., Tiefengraber, M., Müller, M., Bognar, K., Strong, K., Boersma, F., Eskes, H., Davies, J., Ogyu, A., and Lee, S. C.: Assessment of the quality of TROPOMI high-spatial-resolution NO_2 data products in the Greater Toronto Area, Atmospheric Measurement Techniques, 13(4), 2131–2159, doi:10.5194/amt-13-2131-2020, 2020b.

Zielcke, J.: Observations of reactive bromine, iodine and chlorine species in the Arctic and Antarctic with differential optical absorption spectroscopy, Ph.D. thesis, University of Heidelberg, doi:10.11588/heidok.00018932, 2015.